NASA TECHNICAL MEMORANDUM

NASA TM X-3489

NASA TM X-3489

AERODYNAMIC CHARACTERISTICS OF A 1/6-SCALE POWERED MODEL OF THE ROTOR SYSTEMS RESEARCH AIRCRAFT

Raymond E. Mineck and Carl E. Freeman

Langley Directorate,
U.S. Army Air Mobility R&D Laboratory

Langley Research Center
Hampton, Va. 23665

NATIONAL AERONAUTICS AND SPACE ADMINISTRATION • WASHINGTON, D. C. • JUNE 1977

1. Report No.
NASA TM X-3489

2. Government Accession No.

3. Recipient's Catalog No.

4. Title and Subtitle
AERODYNAMIC CHARACTERISTICS OF A 1/6-SCALE POWERED MODEL OF THE ROTOR SYSTEMS RESEARCH AIRCRAFT

5. Report Date
June 1977

6. Performing Organization Code

7. Author(s)
Raymond E. Mineck and Carl E. Freeman

8. Performing Organization Report No.
L-11287

9. Performing Organization Name and Address
Langley Directorate, USAAMRDL
NASA Langley Research Center
Hampton, VA 23665

10. Work Unit No.
505-10-21-05

11. Contract or Grant No.

12. Sponsoring Agency Name and Address
National Aeronautics and Space Administration
Washington, DC 20546
and
U.S. Army Air Mobility R&D Laboratory
Moffett Field, CA 94035

13. Type of Report and Period Covered
Technical Memorandum

14. Army Project No.
1F161102AH45

15. Supplementary Notes

16. Abstract

A wind-tunnel investigation was conducted to determine the effects of the main-rotor wake on the aerodynamic characteristics of the rotor systems research aircraft (RSRA). For the investigation, a 1/6-scale model with a four-blade articulated main rotor was used. Tests were conducted with and without the main rotor. Both the helicopter and the compound helicopter were tested. The latter configuration included the auxiliary thrust engines and the variable-incidence wing. Data were obtained over ranges of angle of attack, angle of sideslip, and main-rotor collective pitch angle at several main-rotor advance ratios. Results are presented for the total loads on the airframe as well as the loads on the rotor, the wing, and the tail.

The results indicated that without the effect of the rotor wake, the RSRA had static longitudinal and directional stability and positive effective dihedral. With the effect of the main rotor and its wake, the RSRA exhibited longitudinal instability but retained static directional stability and positive effective dihedral.

17. Key Words (Suggested by Author(s))
RSRA (rotor systems research aircraft)
Compound helicopters

18. Distribution Statement
Unclassified – Unlimited

Subject Category 02

19. Security Classif. (of this report)
Unclassified

20. Security Classif. (of this page)
Unclassified

21. No. of Pages
238

22. Price*
$8.00

*For sale by the National Technical Information Service, Springfield, Virginia 22161

AERODYNAMIC CHARACTERISTICS OF A 1/6-SCALE POWERED MODEL OF THE ROTOR SYSTEMS RESEARCH AIRCRAFT

Raymond E. Mineck* and Carl E. Freeman*
Langley Research Center

SUMMARY

A wind-tunnel investigation was conducted to determine the effects of the main-rotor wake on the aerodynamic characteristics of the rotor systems research aircraft (RSRA). For the investigation, a 1/6-scale model with a four-blade articulated main rotor was used. Tests were conducted with and without the main rotor. Both the helicopter and the compound helicopter were tested. The latter configuration included the auxiliary thrust engines and the variable-incidence wing. Data were obtained over ranges of angle of attack, angle of sideslip, and main-rotor collective pitch angle at several main-rotor advance ratios. Results are presented for the total loads on the airframe as well as the loads on the rotor, the wing, and the tail.

The results indicated that without the effect of the rotor wake, the RSRA had static longitudinal and directional stability and positive effective dihedral. With the effect of the main rotor and its wake, the RSRA exhibited longitudinal instability but retained static directional stability and positive effective dihedral.

INTRODUCTION

Rotor-wake effects complicate the prediction of helicopter stability and performance. The effect of the rotor wake, which alters the flow field around the helicopter, is often very difficult to predict analytically. This report presents the results from a wind-tunnel investigation to determine experimentally the rotor-wake effects on the rotor systems research aircraft (RSRA) developed by NASA and the U.S. Army.

The RSRA is a unique compound helicopter designed to obtain accurate data for development and validation of rotorcraft theory and for evaluating advanced rotor systems. It is equipped with a variable-incidence wing to load and unload the rotor, auxiliary thrust engines and drag brakes to cover a wide range of rotor propulsive force, and fly-by-wire controls to evaluate advanced flight-control systems. The RSRA can be flown as a

---

*U.S. Army Air Mobility R&D Laboratory.

single-rotor helicopter, a compound helicopter, or a fixed-wing aircraft. Additional details of the RSRA may be found in reference 1.

Because the aircraft is unique, four phases of wind-tunnel testing were conducted to determine and refine the aerodynamic characteristics of the RSRA. The Phase I test results indicated potential lateral- and longitudinal-stability problems with the rotors removed. (See ref. 2.) The aircraft was refined in Phase II and Phase III to improve the stability levels. (See refs. 2 and 3.) The Phase IV tests obtained force and moment data on the airframe, main rotor, empennage, and wing for the rotor off and the rotor on, and the results are reported herein.

SYMBOLS

The units used for the physical quantities defined in this paper are given in the International System of Units (SI) and parenthetically in U.S. Customary Units. Measurements and calculations were made in U.S. Customary Units. Conversion factors relating the two systems are presented in reference 4.

The longitudinal data on the airframe, wing, and tail are resolved in the stability-axis system and the lateral data in the body-axis system. Positive directions for the forces and moments are defined in figures 1(a), (b), and (c). All main-rotor data are resolved in the rotor-shaft-axis system. (See fig. 1(d).) The moment reference center for the airframe, wing, and tail was located 3.81 cm (1.5 in.) behind and 35.13 cm (13.83 in.) below the center of the rotor hub, which corresponds to the nominal aft center of gravity of the RSRA. (Note that model fuselage station 0 cm (0 in.) corresponds to full-scale fuselage station 91.4 cm (36.0 in.).) The moment reference center for the main-rotor data is the center of the rotor hub. Sign conventions used for the control angles for the rotor and the control surfaces are shown in figure 1(e).

a	airfoil section lift-curve slope, rad^{-1}
a_0	main-rotor coning angle, deg
a_{1s}	first-harmonic rotor longitudinal flapping angle, deg
A	area of main-rotor disk, πR^2, 7.791 m^2 (83.86 ft^2)
b	wing span, 2.29 m (90.0 in.)
b_R	number of blades, four

b_{1s}	first-harmonic rotor lateral flapping angle, deg
$\bar{c}$	wing mean aerodynamic chord, 0.423 m (16.67 in.)
c_R	rotor blade chord, 0.108 m (0.353 ft)
C_D	drag coefficient, $\frac{D}{q_\infty S}$
$C_{D,s}$	slipstream drag coefficient, $\frac{D}{q_s S}$
C_H/σ	rotor horizontal-force coefficient, $\frac{H_R}{\rho_\infty A V_T{}^2 \sigma}$
C_l	rolling-moment coefficient, $\frac{M_X}{q_\infty S b}$
$C_{l,s}$	slipstream rolling-moment coefficient, $\frac{M_X}{q_s S b}$
C_{l_β}	effective dihedral parameter, $\frac{dC_l}{d\beta}$, per deg
C_L	lift coefficient, $\frac{L}{q_\infty S}$
$C_{L,s}$	slipstream lift coefficient, $\frac{L}{q_s S}$
C_{L_α}	airframe lift-curve slope, $\frac{dC_L}{d\alpha}$, per deg
C_m	pitching-moment coefficient, $\frac{M_Y}{q_\infty S \bar{c}}$
$C_{m,s}$	slipstream pitching-moment coefficient, $\frac{M_Y}{q_s S \bar{c}}$
C_{m_α}	static longitudinal-stability parameter, $\frac{dC_m}{d\alpha}$, per deg
C_m/σ	rotor pitching-moment coefficient, $\frac{M_R}{\rho_\infty A V_T{}^2 R \sigma}$

C_n	yawing-moment coefficient, $\frac{M_Z}{q_\infty Sb}$
C_{n_β}	static directional-stability parameter, $\frac{dC_n}{d\beta}$, per deg
$C_{n,s}$	slipstream yawing-moment coefficient, $\frac{M_Z}{q_s Sb}$
C_Q/σ	rotor torque coefficient, $\frac{Q_R}{\rho_\infty A V_T{}^2 \sigma R}$
$C_{T,J}$	auxiliary jet engine thrust coefficient, $\frac{T_J}{q_\infty S}$
C_T/σ	main-rotor thrust coefficient, $\frac{T_R}{\rho_\infty A V_T{}^2 \sigma}$
C_Y	side-force coefficient, $\frac{F_Y}{q_\infty S}$
$C_{Y,s}$	slipstream side-force coefficient, $\frac{F_Y}{q_s S}$
C_Y/σ	rotor side-force coefficient, $\frac{F_{Y,R}}{\rho_\infty A V_T{}^2 \sigma}$
D	drag, N (lbf); rotor diameter, 3.149 m (10.33 ft)
F_Y	side force, N (lbf)
$F_{Y,R}$	rotor side force, N (lbf)
h	height of rotor hub above tunnel floor, m (ft)
h/D	ratio of rotor-hub height above tunnel floor to rotor diameter
H_R	rotor horizontal force, N (lbf)

i_t	horizontal-tail incidence, deg
i_w	wing incidence, deg
I	moment of inertia of rotor blade about flapping hinge, $kg\text{-}m^2$ ($slug\text{-}ft^2$)
L	lift, N (lbf)
M_R	rotor pitching moment, N-m (lbf-ft)
M_X	rolling moment, N-m (lbf-in.)
M_Y	pitching moment, N-m (lbf-in.)
M_Z	yawing moment, N-m (lbf-in.)
q_s	slipstream dynamic pressure, $q_\infty + \frac{T_R}{A}$, Pa (lbf/ft^2)
q_∞	free-stream dynamic pressure, Pa (lbf/ft^2)
Q_R	main-rotor torque, N-m (lbf-ft)
R	main-rotor radius, 1.575 m (5.167 ft)
S	wing area, 0.954 m^2 (10.27 ft^2)
T_J	total auxiliary engine thrust, N (lbf)
T_R	main-rotor thrust, N (lbf)
V_T	rotor tip speed, ΩR, m/sec (ft/sec)
V_∞	free-stream velocity, m/sec (ft/sec)
α	angle of attack, deg
β	angle of sideslip, deg
γ	blade Lock number, $\frac{\rho_\infty c_R a R^4}{I}$, 10.3

δ_f	flap deflection, deg
δ_3	rotor pitch-flap coupling angle, deg
ϵ	downwash at tail, deg
θ_c	main-rotor collective pitch angle measured at 0° lag and 0° flapping angles, deg
μ	rotor advance ratio, $\frac{V_\infty}{V_T}$
ρ_∞	free-stream density, kg/m^3 (slugs/ft^3)
σ	main-rotor solidity, $\frac{b_R c_R R}{A}$
ψ	main-rotor azimuth angle, deg
Ω	main-rotor rotational speed, rad/sec

Model components:

F_1	fuselage and ventral fin
F_2	fuselage and ventral fin with main-rotor pylon removed
H_C	compound horizontal tail
H_H	helicopter horizontal tail
J_1	flow-through nacelles
J_2	auxiliary thrust fans and nacelles
M_R	main rotor
V	vertical tail

W_x	variable wing/flap settings:
	W_1 $i_w = 0^{\circ}$, $\delta_f = 0^{\circ}$
	W_2 $i_w = 7.5^{\circ}$, $\delta_f = 0^{\circ}$
	W_4 $i_w = -9^{\circ}$, $\delta_f = 0^{\circ}$
	W_5 $i_w = 0^{\circ}$, $\delta_f = 30^{\circ}$
	W_6 $i_w = 7.5^{\circ}$, $\delta_f = 30^{\circ}$

Subscripts:

t	tail
u	uncorrected
w	wing

MODEL AND APPARATUS

The general rotor model system (GRMS) in the Langley V/STOL tunnel was used in this investigation (Phase IV). The external configuration was a 1/6-scale model of the RSRA. A detailed three-view sketch and an internal component layout of the model are presented in figures 2(a) and 2(b). The dimensions and areas of the model components may be found in table I.

The exterior is identical with the Phase III model described in reference 3 except for the main-rotor pylon and the compound tail. The main-rotor pylon was widened 2.54 cm (1.00 in.) to accommodate the main-rotor control system. The compound T-tail had the same planform, but with an NACA 0015 airfoil section instead of the flat plate used in Phase III. The lower-tail span was changed to 114.3 cm (45.0 in.). The various components of the model, such as the wings, auxiliary thrust engine nacelles, and the horizontal and vertical tails, were removable to simulate the RSRA in either the single-rotor helicopter mode or the compound helicopter mode. Transition grit was used on the wings, horizontal tail, vertical tail, and nose of the model.

The variable-incidence wing, which pivoted about the 3/4-root-chord location, could be set at incidence angles of -9°, 0°, and 7.5°. The partial-span, single-slotted flaps were deflectable to 30°. During these tests, in lieu of sealing the wing roots to the fuselage, large end plates were attached at the wing roots to allow the wing to be mounted on a six-component strain-gage balance. Having the wing mounted on this balance permitted direct measurement of wing loads. The load capacity of the wing balance and of the other load balances is given in table II.

The empennage was attached to the GRMS main structure with a strain-gage balance to measure the empennage loads directly. Loads on the empennage included loads on the tail cone from fuselage station 231.78 cm (91.25 in.) aft. (See fig. 2(c).) At that point, a 0.28-cm (0.11-in.) gap in the tail cone allowed clearance for balance deflections. The horizontal tails could be removed from the vertical tail and the vertical tail could be removed from the tail cone.

The vertical tail remained the same for both the helicopter and the compound helicopter. A T-tail (H_H), which had an area of 0.091 m^2 (0.98 ft^2), was used for the helicopter. Two tails (H_C) were used for the compound helicopter: a smaller T-tail, which had an area of 0.046 m^2 (0.48 ft^2), and a lower horizontal tail, which had an area of 0.228 m^2 (2.45 ft^2).

Two removable auxiliary thrust engine nacelles were mounted on the model. Each nacelle contained a removable fan used to simulate the jet thrust. These fans, nacelles, and engine pylon fairings were the same as those used in reference 3. The engine pylon fairings were the modified minimum fairings described in reference 3. (See fig. 2(d).)

Each fan had a stator and a rotor. A ring with turbine blades was attached to the rotor. Dry, high-pressure air directed onto the turbine blade tips drove the fan to produce thrust. Each nacelle had one static-pressure orifice and three total-pressure probes mounted in the fan exit of each engine. The three total-pressure probes were connected to a manifold. A pressure transducer was used to measure the difference between the total pressure and the static pressure to obtain an average reference dynamic pressure at the exit. This exit reference dynamic pressure was used to calibrate the engine thrust. During the investigation, the fans were removed from the nacelles for a "flow-through" mode and for a reference condition in engine thrust calibration.

The main rotor used in this investigation had four blades (with no twist) and an articulated hub. Rotor blade construction was an aluminum D-spar with balsa-filled, magnesium-skin trailing surfaces. One of the blades was instrumented with strain gages. Strain gages for in-plane and out-of-plane bending moments were located at 30, 48, 65, and 83 percent of the radius. Strain gages for torsional bending were located at 30 and 48 percent of the radius. The push rod for changing the blade pitch for the instrumented blade had a strain gage to measure control loads. Also, the instrumented blade flapping and lead-lag angles were measured at the blade root. The GRMS rotor diameter of 274.3 cm (108.0 in.) was increased with 20.3-cm (8.0-in.) root extenders. The rotor as tested had a solidity of 0.087, a diameter of 315 cm (124 in.), a root cutout of 33 percent, and a shaft angle of 0°. This is different from the RSRA rotor, which has five blades, 8° of twist, a solidity of 0.077, and a shaft angle of 2°.

The rotor hub was fully articulated. Pitch-horn geometry was variable to allow for changes in pitch-flap coupling angle δ_3. Cyclic pitch and collective pitch on the blades were controlled with a swash plate driven by remotely controlled actuators. The flapping hinge offset was 7.62 cm (3.0 in.). The main-rotor hub was located at water line 127 cm (50 in.), which is 1.27 cm (0.5 in.) above the scale location for the RSRA.

The rotor was driven by twin 67-kW (90-hp) electric motors driving a common transmission. These variable-speed electric motors were water cooled through an umbilical from an external water source. The transmission was cooled and lubricated by oil pumped into the model through the umbilical. The entire system – rotor, transmission, and motor – was mounted on a six-component strain-gage balance within the model to measure the rotor forces and moments.

A photograph of the model in the Langley V/STOL tunnel is shown in figure 3. The model was mounted on a strain-gage balance attached to a special model sting. This sting model support system allows high angles of attack and sideslip to be obtained and keeps the model near the center of the test section for pitch, roll, and yaw excursions. Height excursions are obtained by moving the sting vertically. High-pressure air is piped into the model from an air plenum mounted directly below the total balance. This plenum is fed by an air line running through the center of the sting. A reverse double coil in this air line minimizes pressure effects and mechanical tare effects of the air line crossing the total balance.

Static and dynamic data were recorded during the test. The static data consisted of averaged values taken from the four strain-gage balances, air pressures, rotor speeds and control positions, engine exit pressures, and wind-tunnel test conditions. The dynamic data consisted of blade bending and torsional stresses, blade flapping and lagging motion, dynamic balance loads, and model vibrations.

TEST CONDITIONS AND CORRECTIONS

This investigation was conducted in the Langley V/STOL tunnel, which is a closed-return, atmospheric tunnel. The tunnel test section, which measures 4.42 m (14.50 ft) by 6.63 m (21.75 ft), can be operated in three modes: (1) with a closed test section; (2) with a slotted test section; and (3) with an open test section with walls and ceiling removed. Tunnel free-stream dynamic pressure was varied from 0 Pa (0 lbf/ft^2)

to 2777 Pa (58 lbf/ft^2). Except where noted, all tests at forward speeds were performed in the closed test section with the model close to the center line of the tunnel. This position corresponds to $h/D = 0.92$.

The auxiliary engine thrust was calibrated statically, that is, at zero wind speed. For the static calibration, the engine thrust measured on the airframe balance was calibrated against the difference between the dynamic pressure measured at the fan exit and the free-stream dynamic pressure. The engine thrusts were balanced for zero yawing moment at maximum thrust at static conditions. Basically, this static calibration procedure was used in reference 3 and was also used in this report for direct comparison of the results from the two tests.

Testing of the model was carried out in two phases: rotor off and rotor on. For the rotor-off testing, pitch- and yaw-angle variations were made to establish a baseline for rotor effects and to allow a comparison with reference 3. These rotor-off tests were made in the closed test section with the model in the center line of the test section. The basic fuselage was tested with several combinations of the tail, wing, and jets to determine the aerodynamic contribution of each component. Four wing/flap settings were used for the compound helicopter: i_w/δ_f of $0^\circ/0^\circ$, $0^\circ/30^\circ$, $7.5^\circ/0^\circ$, and $7.5^\circ/30^\circ$. The horizontal-tail incidence was set at 0° for all rotor-off testing, except where noted. The auxiliary jet engine thrust coefficient was set at zero, trim, and alternate thrust levels (above or below trim thrust). For zero thrust, the dynamic pressure at the jet exit was set equal to the free-stream dynamic pressure at 0° angle of attack. At trim thrust, the thrust level was set for zero model drag $(C_D = 0)$ at 0° angle of attack. For all cases, the fan rotational speed for the desired thrust level was held constant throughout each run.

For the rotor-on testing, variations of pitch, yaw, and main-rotor collective pitch angles were made about estimated trim conditions. The main-rotor controls were fixed for the pitch- and yaw-angle variations; the controls were varied to maintain a tip-path-plane angle for the runs in which collective pitch angle was varied. The trim conditions for 1g level flight were obtained from an analytical simulation program. Both the single-rotor helicopter and the compound helicopter were tested. The T-tail for the compound tail H_C and the helicopter tail H_H was set at 0° incidence. The lower horizontal tail of the compound tail H_C was set to 3° when it was installed on the model. For the compound helicopter, only the $0^\circ/0^\circ$ and $7.5^\circ/30^\circ$ wing/flap settings were tested. Each wing/flap setting was tested at two values of the ratio of wing lift to total lift L_w/L. These two values of the ratio are referred to as high wing lift and low wing lift.

Main-rotor testing was conducted with the nominal rotor speed of 1290 rpm for a calculated tip speed of 213 m/sec (700 ft/sec). During the first part of the rotor-on testing, the main rotor had a pitch-flap coupling angle δ_3 of -27.76°, which was later changed to -2.0° to simulate more closely the stability characteristics of the RSRA five-blade rotor with $\delta_3 = 0^{\circ}$.

Several corrections were made in the data reduction scheme to compensate for certain identifiable mechanical and aerodynamic interferences. Correction factors were obtained for (1) the effect of the air line crossing the airframe balance; (2) the effect of the model support system; (3) the effect of the proximity of the sting to the model; (4) and the effects of the wind-tunnel walls. The effect of the air line was determined by loading the balance statically with the air line attached and the air line off. The effect of the model support system was determined by rotating the joints of the sting in such a way as to maintain a constant model attitude so that variations of model loads could be attributed to tunnel-flow alterations caused by joint position. The effect of the proximity of the sting was estimated from unpublished data from Phase III tests. In these tests, a large tube was attached to the strut model support system in the same position as the front horizontal portion of the sting mount of Phase IV. The methods described in reference 5 were used to account for the wall effects.

PRESENTATION OF RESULTS

The results of the wind-tunnel investigation have been presented in coefficient form. The rotor forces and moments are resolved in the shaft-axis system. The wing, tail, and airframe forces and moments are resolved in the body- and stability-axis systems. Care should be used when comparing the rotor data with the data from the wing, tail, and airframe, because a different moment reference center was used for the rotor data. The rotor-off data are presented in figures 4 to 39; the rotor-on data, in figures 40 to 64. Specifically, the results are presented as follows:

	Figure for –			
	Airframe	Wing	Tail	Rotor
Rotor off:				
Longitudinal aerodynamic characteristics:				
Comparison of Phase IV with Phase III	4 to 8			
Effect of empennage components	9		17	
Effect of i_w and δ_f	10	15	18	
Effect of auxiliary thrust engine nacelles . . .	11		19	
Effect of i_t	12		20	
Effect of $C_{T,J}$	13	16	21	
Effect of $C_{T,J}$ on Cm_{α}	14			

DISCUSSION OF RESULTS

ROTOR OFF

Longitudinal Aerodynamic Characteristics

Comparison of Phase IV and Phase III.- There were several differences in the external contours of the models used in Phase IV and Phase III. (See the section "Model and Apparatus.") Also, the results from Phase III suggest that the data contain some interference effects arising from the model strut support. Five configurations were retested in Phase IV to evaluate the differences between these two phases: the fuselage and vertical tail with (1) the wing; (2) the horizontal tail; (3) the wing and horizontal tail; (4) the wing and jets; and (5) the wing, horizontal tail, and jets. The results for these configurations are presented in figures 4 to 8. The data for Phase III are presented in figure 5(b) for the 118.5-cm (46.67-in.) span lower horizontal tail and in figure 6 for the 127.0-cm (50.0-in.) span lower horizontal tail. The data presented in figure 8 for Phase III are the average of the data for the 118.5-cm (46.67-in.) span tail and the 110.1-cm (43.33-in.) span tail to obtain data approximating a 114.3-cm (45.0-in.) span tail.

In general, the longitudinal aerodynamic data from Phase III and Phase IV for the fuselage and vertical tail with either the wing or the horizontal tail are in reasonable agreement. (See figs. 4, 5, and 7.) The differences that do appear may be caused by some of the changes in the model, by the interferences from the model support system, or by small differences in the positions defined as 0° angle of attack or 0° wing incidence.

With the wing and the tail on, the differences in lift and pitching-moment coefficients are larger. (See figs. 6 and 8.) As the wing incidence or flap deflection increases, the differences in lift and pitching-moment coefficients increase and the static longitudinal stability $C_{m_{\alpha}}$ decreases near 0° angle of attack. A limited amount of data was obtained for an increased separation between the sting and tail. These data indicate that the sting interference on the tail moderately increases with increasing wing lift. Part of the stability degradation and part of the difference in lift and pitching moment may be attributable to sting aerodynamic interference.

The difference in lift and pitching moment for the configuration with the wing and tail on may also be due to a difference in the tail angle of attack. This could be caused by a difference in either tail incidence (that is, error in tail-incidence setting) or downwash at the tail between Phase III and Phase IV. Data from Phase III for several different values of tail span and tail incidence were used to predict the downwash at the tail for 0° wing incidence, 0° flap deflection, and a 114.3-cm (45.0-in.) tail span. These results were compared with those computed for Phase IV from figure 12. The downwash at the tail was about 1.7° less for Phase IV than for Phase III. This downwash change accounts for a 0.03 change in lift coefficient and a -0.11 change in pitching-moment coefficient with the wing and the tail installed. This is approximately the difference found between the two tests when both the wing and tail are installed.

Further studies are needed to determine which model support (Phase III or Phase IV) caused the least interference at the tail. However, the results from this investigation are still meaningful if the interference is relatively constant for the model support system used in this investigation.

Airframe loads.- The model was tested with the rotor removed to determine the baseline aerodynamic characteristics of the airframe. The various components of the model were tested on the fuselage to determine the aerodynamic contribution of each component and the mutual interference effects between the components. The fuselage was tested with and without the empennage for the wings off and on, and the results are presented in figure 9. The addition of the vertical tail to the fuselage has a negligible effect on the lift-curve slope or the static longitudinal stability. (See fig. 9(a).) The addition of either the compound tail or the helicopter tail provided static longitudinal stability. This configuration, which represents the helicopter without the rotor, had static longitudinal stability. These results approach those for a tail-alone configuration and represent the maximum each tail can contribute to the longitudinal stability.

The addition of the compound horizontal tail to the fuselage with the wing adds a positive increment in pitching moment at 0° angle of attack. (See figs. 9(b) and 9(c).) This nose-up pitching-moment change is caused by the wing downwash at the tail. The addition of the wing reduces the longitudinal static stability because the wing increases $d\epsilon/d\alpha$ and reduces the dynamic pressure at the tail. The stability reduction is larger for the wing/flap setting of $7.5^\circ/30^\circ$ than for $0^\circ/0^\circ$.

The fuselage was tested with five wing/flap settings (combinations of wing incidence and flap deflection): $-9^\circ/0^\circ$, $0^\circ/0^\circ$, $7.5^\circ/0^\circ$, $0^\circ/30^\circ$, and $7.5^\circ/30^\circ$, or model component designations W_4, W_1, W_2, W_5, and W_6, respectively. These results are presented in figure 10 for the wing and (1) the fuselage; (2) the fuselage and compound tail; and (3) the fuselage, auxiliary thrust jets, and compound tail. The addition of the wing to the fuselage alone provides a negative increment to the static stability (that is, increased stability) because the wing center of pressure is slightly aft of the moment reference center. (See fig. 10(a).) The lift-curve slope C_{L_α} was not dependent on the wing incidence and increased slightly with flap deflection for the conditions tested. The maximum lift coefficient was larger for 0° wing incidence than for 7.5° wing incidence. This is attributed to a better lift carryover across the fuselage and to increased fuselage lift.

The effect of wing incidence and flap deflection on the configuration with the compound tail installed is presented in figure 10(b). Increasing the wing incidence or deflecting the flaps increases the downwash and decreases the dynamic pressure at the tail. The increased downwash results in an incremental increase in pitching moment. Also, increasing the wing incidence decreases the static longitudinal stability. In general, increasing the wing lift by increasing the wing incidence or flap deflection decreases the stability. The decrease is larger with the auxiliary thrust engines installed. (See figs. 10(c) and 10(d).)

The effect of the engine nacelles is shown in figure 11. The wing incidence was set at 0°, the flaps were retracted, and the compound tail was set at 0°. The addition of flow-through nacelles decreased the static longitudinal stability and increased the lift-curve slope. The effects of the nacelles with the fans $\left(\text{with } C_{T,J} \approx 0\right)$ are similar to those for the flow-through nacelles.

The effect of horizontal-tail incidence on the longitudinal aerodynamic characteristics of various configurations is presented in figure 12. When tail-off data were unavailable, the tail-off pitching moment was computed by removing the pitching moment measured on the tail balance from the airframe pitching moment. The results are presented in figure 12(a) for the helicopter tail and in figures 12(b) and 12(c) for the compound tail. For the compound tail, only the incidence of the lower tail was changed; the T-tail was fixed at 0^{o} incidence. Before comparing these results with those of reference 3, a correction should be made for the difference in tail spans.

The effect of thrust level on the longitudinal aerodynamic characteristics of configuration $F_1W_xVH_CJ_2$ is presented in figure 13 for wing incidence angles of 0^{o} and 7.5^{o} with the flaps retracted and deflected. The compound tail was set at 0^{o} incidence. This configuration, which represents the compound helicopter without the rotor, had static longitudinal stability for the wing incidence angles tested. In general, increasing the thrust coefficient increases C_{L_α} slightly and decreases C_{m_α} at negative angles of attack. The change in C_{L_α} comes from the component of thrust in the lift direction; the change in longitudinal stability comes from the increase in $d\epsilon/d\alpha$ with thrust. The effect of thrust coefficient on the static longitudinal stability of the compound helicopter is summarized in figure 14.

Wing loads.- The wing balance measured the wing forces and moments directly. To make comparisons between the wing and airframe data easier, the wing data are nondimensionalized by the same factors as the airframe data, and the moment data are resolved about the same moment reference center. The effect of wing incidence on the wing longitudinal aerodynamic characteristics is presented in figure 15 for the auxiliary thrust nacelles on and off. Without the nacelles (fig. 15(a)), deflecting the flaps 30^{o} increases the wing lift coefficient and makes the wing pitching-moment coefficient more negative. The drag of the wing at a given lift is independent of wing incidence.

With the nacelles on and the jets at $C_{T,J} \approx 0$, the results are slightly different because of the interference of the nacelles (fig. 15(b)). The lift-curve slopes are the same for all wing/flap settings, as are the pitching-moment slopes. Deflecting the flaps 30^{o} produces the same changes in pitching moment and lift as previously mentioned. The drag at a given lift with the flaps retracted decreases slightly with wing incidence. The interference arises because, as the wing pivots about the 3/4-chord line, the upper surface comes closer to the nacelles.

The effect of the auxiliary engine thrust on the wing aerodynamic characteristics is presented in figure 16 for several wing/flap settings. In general, the addition of thrust increases the lift slightly except near stall, makes the pitching moment slightly more negative, and reduces the wing drag. The effects increase with increasing wing incidence or flap deflection.

Tail loads.- The tail balance measured the empennage forces and moments directly. As was done for the wing, the tail data are nondimensionalized by the same factors as the airframe data, and the moments are resolved about the same moment reference center. The aerodynamic characteristics of the vertical tail, the helicopter tail, and the compound tail on the fuselage alone are presented in figure 17. The tail lift and the tail contribution to the static longitudinal stability (difference between tail-on and tail-off stability) agree with the results from figure 9(a). Adding the wing to the fuselage and tail increases the downwash at the tail, reduces the dynamic pressure at the tail, and reduces the tail contribution to stability. (See fig. 18.) The tail contribution to stability increases with angle of attack for 7.5° wing incidence at trim thrust. (See fig. 18(c).)

The addition of the auxiliary thrust nacelles does not change the downwash significantly although it does reduce the stability contribution of the tail. (See fig. 19.) This reduction is smaller than the total stability reduction found in figure 11. Therefore, the destabilizing effect of the nacelles is due to both the direct effect of the nacelles acting like a lifting surface in front of the center of gravity and an induced effect at the tail. The differences between the effect of the flow-through nacelles and the nacelles with the fans at zero thrust $\left(C_{T,J} \approx 0\right)$ are small. The effect of increasing the thrust coefficient is presented in figure 21. The results show the same trends but they do not show the stability reduction at small angles of attack that was found for the complete configuration. The tail provides more stability at angles of attack near or above stall as thrust is increased; this is especially notable in figure 21(d) for $i_w = 7.5^{\circ}$ and $\delta_f = 30^{\circ}$.

Lateral Aerodynamic Characteristics

Comparison of Phase IV and Phase III.- As was previously described, there were several differences in the external contour of the models used in Phase IV and in Phase III. The only lateral aerodynamic data obtained in Phase III were for the compound helicopter with the 127-cm (50.0-in.) span lower horizontal tail. These results are presented with the results for the 114.3-cm (45.0-in.) span horizontal tail from Phase IV in figure 22. It was expected that the increased tail span from Phase III would have little effect on the yawing-moment or the side-force coefficients and would make the effective dihedral parameter C_{l_β} more negative by about 0.00002/deg. In general, the side-force coefficients are in good agreement for the two phases. The slopes of the rolling-moment and yawing-moment coefficients are in agreement, although the magnitudes sometimes differ. These differences may be caused by small errors in setting the rudder deflection or the incidence of the two wing panels.

Airframe loads.- Various components of the model were tested on the fuselage to determine the aerodynamic contribution of each. The effective dihedral parameter C_{l_β} and the static directional-stability parameter C_{n_β} were evaluated from $\beta = -5^{\circ}$ to $\beta = 5^{\circ}$ for several configurations. Adding the vertical tail to the fuselage (fig. 23) increases the positive effective dihedral $\left(C_{l_\beta}\text{ becomes more negative}\right)$ and the static directional stability $\left(C_{n_\beta}\text{ becomes more positive}\right)$. Figure 24 presents the effect of adding the helicopter tail H_H and adding the compound tail H_C. Adding the helicopter tail increases the positive effective dihedral and static directional stability, but adding the compound tail reduces the positive effective dihedral and increases the static directional stability.

The effect of wing incidence and flap deflection on the lateral aerodynamic characteristics of the model without the empennage is presented in figure 25. As was discussed in reference 3, the 7° geometric dihedral was counteracted by the position of the wing on the bottom of the fuselage. The effective dihedral parameter varied from 0 for the $-9^{\circ}/0^{\circ}$ wing/flap setting to slightly positive for the $7.5^{\circ}/30^{\circ}$ wing/flap setting. The effect of wing incidence and flap deflection on the lateral aerodynamic characteristics of the fuselage with the horizontal and vertical tails is presented in figure 26. The data for the wing-fuselage configurations presented in figure 25 generally displayed negative effective dihedral, whereas the data for the wing-fuselage-tail configurations presented in figure 26 displayed positive effective dihedral. The static directional stability increased with increasing wing incidence because the wing wake drew the free-stream flow down on the vertical tail and thus increased its effectiveness.

The engine nacelles and pylon fairings were added to the previous configuration and the results are presented in figure 27. Both the flow-through nacelles and the nacelles with the fans were tested. No significant differences are apparent between the configuration with and the configuration without the nacelles and pylons.

Angle of attack affects the lateral aerodynamic characteristics because the portion of the vertical tail that is in the wake of the main-rotor pylon changes. The effect of angle of attack is presented in figure 28 for several model configurations. For the configurations without the engine nacelles and pylon fairings (figs. 28(a) to 28(d)), the effective dihedral became less positive as angle of attack increased; the opposite occurred when the engine nacelles and pylon fairings were on (figs. 28(e) to 28(h)). For the tail-on configurations, the static directional stability decreased with angle of attack regardless of whether the nacelles and pylons were installed on the model.

The effect of auxiliary engine thrust coefficient is presented in figure 29 for several wing/flap settings and angles of attack. Increasing the auxiliary engine thrust coefficient made the effective dihedral less positive and reduced the static directional stability.

Wing loads.- The effect of wing incidence on the lateral aerodynamic characteristics of the wing for the configuration with the nacelles removed is presented in figure 30. These results indicate that at 0° angle of attack, the wing is producing a stabilizing increment to the directional stability and a negative effective dihedral. The results for the configuration with the nacelles installed, presented in figure 31 $\left(C_{T,J} \approx 0\right)$, show the same effect. It should be noted that the scale used for $C_{l,w}$ in figures 30 to 33 is enlarged compared with that in figures 24 to 29; as a result, the effects of apparent differences in wing incidence and flap deflection angle are magnified. The effect of increasing angle of attack, shown in figure 32, is similar to the effect of wing incidence in that the level of negative effective dihedral is reduced as the wing lift is increased (by increased wing incidence, flap deflection, or angle of attack). In some cases, corresponding to high lift coefficients, the wing is providing positive effective dihedral. The effect of auxiliary engine thrust is presented in figure 33. Except for 7.5° wing incidence with the flaps deflected 30°, increasing the thrust does not affect the wing side-force or yawing-moment coefficient, but it does decrease the effective dihedral of the wing.

Tail loads.- The effect of the vertical tail on the tail lateral aerodynamic characteristics is presented in figure 34. For the vertical tail off (F_1), loads on the ventral fin and the tail cone provide a negative effective dihedral and positive directional stability. The effect of the horizontal tail is presented in figure 35. The end-plate effect of the helicopter T-tail improved the contribution of the vertical tail to the effective dihedral, but it had little effect on the tail contribution to the directional stability. The double end-plate effect of the compound tail reduced the positive contribution of the vertical tail to the effective dihedral, but it improved the contribution to the directional stability.

The effect of wing incidence and flap deflection is presented in figure 36. Increasing either the wing incidence or the flap deflection improved the tail contribution to both the effective dihedral and the directional stability. The wing wake probably drew the flow down onto the vertical tail, where the flow had been blocked by the main rotor pylon. Adding the engine nacelles and pylons (fig. 37) slightly reduced the tail contribution to the effective dihedral; there was no effect on the directional stability.

The effect of angle of attack is presented in figure 38. In general, increasing the angle of attack reduced the tail contribution to both the effective dihedral and the directional stability. This is the opposite effect that the wing had. Increasing the angle of attack increases the portion of the tail that is in the wake of the main rotor pylon. The effect of auxiliary engine thrust is presented in figure 39. In general, increasing the thrust coefficient reduced the tail contribution to both the effective dihedral and the directional stability. The effect is smaller for 0° wing incidence than for 7.5° wing incidence.

ROTOR ON

Determination of Rotor-Wake Effects

Research on jet VTOL configurations has indicated that the jet diameter, jet thrust, and jet deflection angle are of primary importance when determining jet-wake-induced interference. If it is assumed that this also applies to rotor-wake-induced interference, the primary rotor-wake effects can be determined. The rotor system used in this investigation was not a scaled version of the first rotor system to be tested on the RSRA. The rotor diameter was 1/6 scale, but as previously noted, the number of blades, the twist, and the solidity were different. The rotor was operated at scaled thrust coefficients and a tip-path plane simulating trimmed, level flight. The rotor data for each configuration, measured directly by the rotor balance, are presented so that the direct rotor forces may be removed from the airframe data. The rotor-wake effect is the difference between the rotor-on data with the direct thrust effects removed and the rotor-off data.

Longitudinal Aerodynamic Characteristics

Rotor loads.- Rotor thrust recovery in ground effect is an important factor in determining hover performance. The compound helicopter was tested at several values of ground height (ground proximity) in hover and the results are presented in figure 40. For a given collective pitch or a given power (torque), reducing the ground height increases the thrust.

The effect of forward speed (advance ratio) on the rotor aerodynamic characteristics is presented in figure 41 for $\delta_3 = -27.6^\circ$ and in figure 42 for $\delta_3 = -2.0^\circ$. Generally, the rotor force coefficients C_T/σ, C_H/σ, and C_Y/σ increase linearly with the blade collective pitch. The tip-path-plane angle of attack $(\alpha + a_{1s})$ was held constant for each collective variation. However the tip-path-plane angle of attack could change for each collective pitch variation. For a constant positive tip-path-plane angle of attack, the rotor thrust increases with increasing advance ratio for a given collective pitch setting. Similarly, the rotor torque decreases with increasing advance ratio for a given thrust level. (See fig. 41(c).) The differences in the slopes of C_T/σ as a function of θ_c for comparable conditions in figures 41 and 42 are due to the difference in δ_3. If the approximate correction factor from reference 6 of $\dfrac{1}{1 + \dfrac{\tan(\delta_3)\gamma}{8}}$ is used, the data for the two values of δ_3 are in good agreement.

The variation of the rotor data with the airframe angle of attack for a range of forward speeds is presented in figures 43 and 44 for $\delta_3 = -27.6^\circ$ and -2.0°. Generally, the thrust coefficient increased, and the horizontal-force and torque coefficients decreased with angle of attack. The pitching-moment variation with angle of attack was generally unstable. The pitch instability increased with increasing advance ratio. Changing the pitch-flap coupling angle δ_3 from -27.6° to -2.0° further destabilized the rotor in pitch.

Airframe loads.- The model was tested with the main rotor to evaluate the aerodynamic characteristics of the complete airframe. In hover, the download on the fuselage from the rotor wake is an important factor in determining the hover performance. The effect of ground proximity h/D on the download on the airframe, wing, and tail is presented in figure 45. Reducing h/D reduces the download. ($\text{For no download, } L/T_R = 1.0$). Only a very small part of the download is due to the tail; a larger part is due to the wing, and a larger part, yet, is due to the fuselage and jet engine.

The interference from the wind-tunnel walls can be significant in tests at low forward speeds and high rotor thrusts. Methods have been developed for correcting the results with or without the walls to free-air conditions. To shed more light on the interference effects, the model was tested in three test-section configurations: closed, slotted, and open (floor in place). The results for an advance ratio of 0.07 are presented in figure 46. The uncorrected data are presented in figure 46(a). The slopes and magnitudes of C_L and C_D against θ_c differ. Correcting the data for the closed and open test sections improves the agreement in C_L, but there are still discrepancies in C_D. (See fig. 46(b).) The data for the slotted test section were not corrected. The difference in C_D after it has been corrected for all effects is due to the difference in angle of attack. The corrected results, adjusted to the same angle of attack, are presented in figure 46(c). The slopes are similar, although there is an incremental difference in drag between the data for the open and the closed test sections. The difference in flapping angle a_{1s} can account for the drag difference.

At low forward speeds, the main-rotor effects dominate, so that conventional aerodynamic coefficients based on free-stream dynamic pressure may be misleading. (Note the very large lift coefficients in fig. 46.) Therefore, the coefficients for the airframe data are based on the slipstream dynamic pressure. The effect of forward speed on the longitudinal aerodynamic characteristics of the model with the main rotor is presented in figures 47 and 48 for several model configurations. Increasing the forward speed reduces the lift and drag coefficients because of the large increase in dynamic pressure in the denominator of the coefficient. No such generalization is possible for the pitching-moment coefficients. The helicopter configuration with the helicopter tail is longitudinally unstable. (See fig. 47(a).) The instability decreases with increasing forward speed. The lift-curve slope is not strongly dependent on forward speed. Substituting the compound tail for the helicopter tail provides static stability. (See fig. 47(b).) Increasing the forward speed increases the level of stability because of increased free-stream dynamic pressure and decreased rotor-wake effects. The compound helicopter (with both the wing and the auxiliary thrust jets) is unstable for the $0^\circ/0^\circ$ and $7.5^\circ/30^\circ$ wing/flap settings. (See figs. 47(c) to 47(f).) The variation of the stability is small as the forward speed increases. The results for the compound helicopter with $\delta_3 = -2.0^\circ$ are similar to those just discussed. (See fig. 48.)

The variation of the longitudinal aerodynamic characteristics with rotor collective pitch angle is presented in figures 49 and 50 for several model configurations for $\delta_3 = -27.6^\circ$ and -2.0°. As before, increasing the forward speed reduces the lift and drag coefficients. For $\delta_3 = -27.6^\circ$, increasing the collective pitch increases the lift and, except at low forward speeds, makes the pitching moment more positive. The change in lift with collective pitch decreases with increasing forward speed. For $\delta_3 = -2.0^\circ$, the trends are similar except for the drag, which increases with increasing collective pitch.

Wing loads.- The rotor wake will induce a change in the wing aerodynamic characteristics. Because these induced effects are small and the direct rotor forces are not included, conventional aerodynamic coefficients are still meaningful. Therefore, free-stream dynamic pressure is used in computing the coefficients to simplify comparisons with the rotor-off data.

The effect of forward speed on the wing longitudinal aerodynamic characteristics for the model with the main rotor is presented in figures 51 and 52. The primary effect of the rotor wake is to decrease the effective angle of attack of the wing. The effect is largest at low forward speeds. The variation of the wing longitudinal aerodynamic characteristics with rotor collective pitch angle is presented in figures 53 and 54. Increasing the collective pitch decreases the lift, increases the drag, and makes the pitching moment less negative.

Tail loads.- The tail data are presented as conventional aerodynamic coefficients based on free-stream dynamic pressure and wing reference area for the same reasons stated for the wing. The effect of forward speed on the tail longitudinal aerodynamic characteristics is presented in figures 55 and 56. The lower-horizontal-tail incidence was set at 3°. As forward speed or angle of attack increases, the download on the tail decreases and the pitching moment decreases. The variation of the tail longitudinal aerodynamic characteristics with main-rotor collective pitch angle is presented in figures 57 and 58. Increasing the collective pitch increases the download on the tail except for $\mu \approx 0.09$ in figure 57(a). The effect is largest at low forward speeds with the compound tail. (See figs. 57(b) and 57(c).) The download is smallest when the wing lift is high.

Lateral Aerodynamic Characteristics

Airframe loads.- The lateral aerodynamic data for the airframe are presented in coefficient form based on the slipstream dynamic pressure. The effect of forward speed on the airframe lateral aerodynamic characteristics is presented in figures 59 and 60. The rolling-moment and side-force coefficients do not pass through zero at 0° sideslip because the rotor was not exactly trimmed; the yawing-moment coefficient does not pass through zero at 0° sideslip because there was no antitorque device to cancel the main-rotor torque. All configurations tested showed positive effective dihedral and static directional stability. The values are not directly comparable with those obtained with the rotor off because of the differences in the dynamic-pressure basis for the coefficients.

Wing loads.- The lateral aerodynamic data for the wing are presented in coefficient form based on the free-stream dynamic pressure as were the longitudinal aerodynamic data for the wing. The effect of forward speed on the wing lateral aerodynamic characteristics is presented in figures 61 and 62. Because the wing is below and behind the moment reference center, the wing produces a stabilizing contribution to the static directional stability and a destabilizing contribution to the effective dihedral.

Tail loads.- As was done for the tail longitudinal aerodynamic data, the tail lateral aerodynamic data are presented in coefficient form based on the free-stream dynamic pressure and the wing reference area. The effect of forward speed on the tail lateral aerodynamic characteristics is presented in figures 63 and 64. The tail produces a stable contribution to the effective dihedral and the static directional stability.

SUMMARY OF RESULTS

The results from the wind-tunnel tests of a 1/6-scale model of the rotor systems research aircraft with and without the main rotor can be summarized as follows:

1. With the rotors removed, both the helicopter and the compound helicopter had static longitudinal stability. The stability for the compound helicopter decreased as the wing incidence or auxiliary engine thrust increased.

2. Both the helicopter and the compound helicopter had stable effective dihedral and static directional stability with the rotors removed. For the compound helicopter, the static directional stability decreased with increasing angle of attack or thrust coefficient and the positive effective dihedral increased with increasing angle of attack and decreased with increasing thrust coefficient.

3. With the rotor system tested, the helicopter and the compound helicopter were longitudinally unstable. For the helicopter configuration, the instability decreased as forward speed increased; for the compound helicopter, the instability did not change significantly with forward speed.

4. With the rotor system tested, the helicopter and the compound helicopter exhibited static directional stability and positive effective dihedral.

Langley Research Center
National Aeronautics and Space Administration
Hampton, VA 23665
March 28, 1977

REFERENCES

1. Linden, A. W.; and Hellyar, M. W.: The Rotor Systems Research Aircraft – A Flying Wind Tunnel. AIAA Paper No. 74-1277, Oct. 1974.
2. Flemming, R.; and Ruddell, A.: RSRA Sixth Scale Wind Tunnel Test – Final Report. Doc. No. SER-72011 (Contract NAS1-13000), Sikorsky Aircraft Div., United Aircraft Corp., Dec. 4, 1974. (Available as NASA CR-144964.)
3. Mineck, Raymond E.; Freeman, Carl E.; and Hassell, James L., Jr.: Aerodynamic Characteristics of a 1/6-Scale Model of the Rotor Systems Research Aircraft With the Rotors Removed. NASA TN D-8198, 1976.
4. Mechtly, E. A.: The International System of Units – Physical Constants and Conversion Factors (Second Revision). NASA SP-7012, 1973.
5. Heyson, Harry H.: Use of Superposition in Digital Computers To Obtain Wind-Tunnel Interference Factors for Arbitrary Configurations, With Particular Reference to V/STOL Models. NASA TR R-302, 1969.
6. Seckel, Edward: Stability and Control of Airplanes and Helicopters. Academic Press, Inc., c.1964.

TABLE I.- MODEL DATA

Fuselage:	
Length, m (ft)	3.057 (10.03)
Frontal area, m^2 (ft^2)	0.172 (1.85)
Wing:	
Airfoil section	NACA 63_2415
Area, m^2 (ft^2)	0.954 (10.27)
Span, m (in.)	2.29 (90.0)
Mean aerodynamic chord, m (in.)	0.423 (16.67)
Aspect ratio	5.52
Taper ratio	0.66
Sweep of 25-percent-chord line, deg	3.0
Dihedral, deg	7.0
Flaps (each):	
Area, m^2 (ft^2)	0.074 (0.80)
Span, percent of wing semispan	49.0
Chord, percent of local wing chord	33.0
Aileron:	
Area, m^2 (ft^2)	0.047 (0.50)
Span, percent of wing semispan	34.0
Chord, percent of local wing chord	34.0
Vertical stabilizer:	
Airfoil section	NACA 0015
Area, m^2 (ft^2)	0.294 (3.164)
Span, m (ft)	0.813 (2.67)
Aspect ratio	2.25
Root chord, m (ft)	0.476 (1.56)
Rudder, percent of local chord	37.0
Helicopter T-tail:	
Airfoil section	NACA 0015
Area, m^2 (ft^2)	0.091 (0.98)
Span, m (ft)	0.674 (2.21)
Aspect ratio	5.15
Root chord, m (ft)	0.183 (0.599)
Taper ratio	0.487

TABLE I.- Concluded

Compound T-tail:	
Airfoil section	NACA 0015
Area, m^2 (ft^2)	0.046 (0.48)
Span, m (ft)	0.44 (1.43)
Aspect ratio	4.29
Root chord, m (ft)	0.128 (0.42)
Taper ratio	0.60
Lower horizontal tail:	
Airfoil section	NACA 0015
Area, m^2 (ft^2)	0.228 (2.45)
Span, cm (in.)	114.3 (45.0)
Aspect ratio	5.75
Root chord, m (ft)	0.198 (0.65)
Taper ratio	1.00
Ratio of elevator chord to tail chord	0.30
Main rotor:	
Number of blades	4
Airfoil section	NACA 0012
Radius, m (ft)	1.575 (5.167)
Blade chord, m (ft)	0.108 (0.353)
Twist, deg	0
Solidity	0.087
Disk area, m^2 (ft^2)	7.791 (83.86)
Hinge offset, m (ft)	0.076 (0.25)
Pitch-flap coupling angle, deg	-27.6 or -2.0
Blade Lock number	10.3

TABLE II.- STRAIN-GAGE BALANCE CAPACITIES

[Accuracies are nominally ±0.5 percent of maximum load]

Balance	Maximum load measured by balance for –					
	Normal force, N (lbf)	Axial force, N (lbf)	Side force, N (lbf)	Pitching moment, N-m (lbf-in.)	Rolling moment, N-m (lbf-in.)	Yawing moment, N-m (lbf-in.)
Airframe	13 344 (3000)	2224 (500)	8006 (1800)	1130 (10 000)	847 (7500)	508 (4500)
Rotor	4448 (1000)	2224 (500)	1334 (300)	1243 (11 000)	488 (4318)	895 (7920)
Tail	4448 (1000)	2224 (500)	2224 (500)	452 (4000)	339 (3000)	339 (3000)
Wing	8006 (1800)	2224 (500)	4448 (1000)	791 (7000)	452 (4000)	339 (3000)

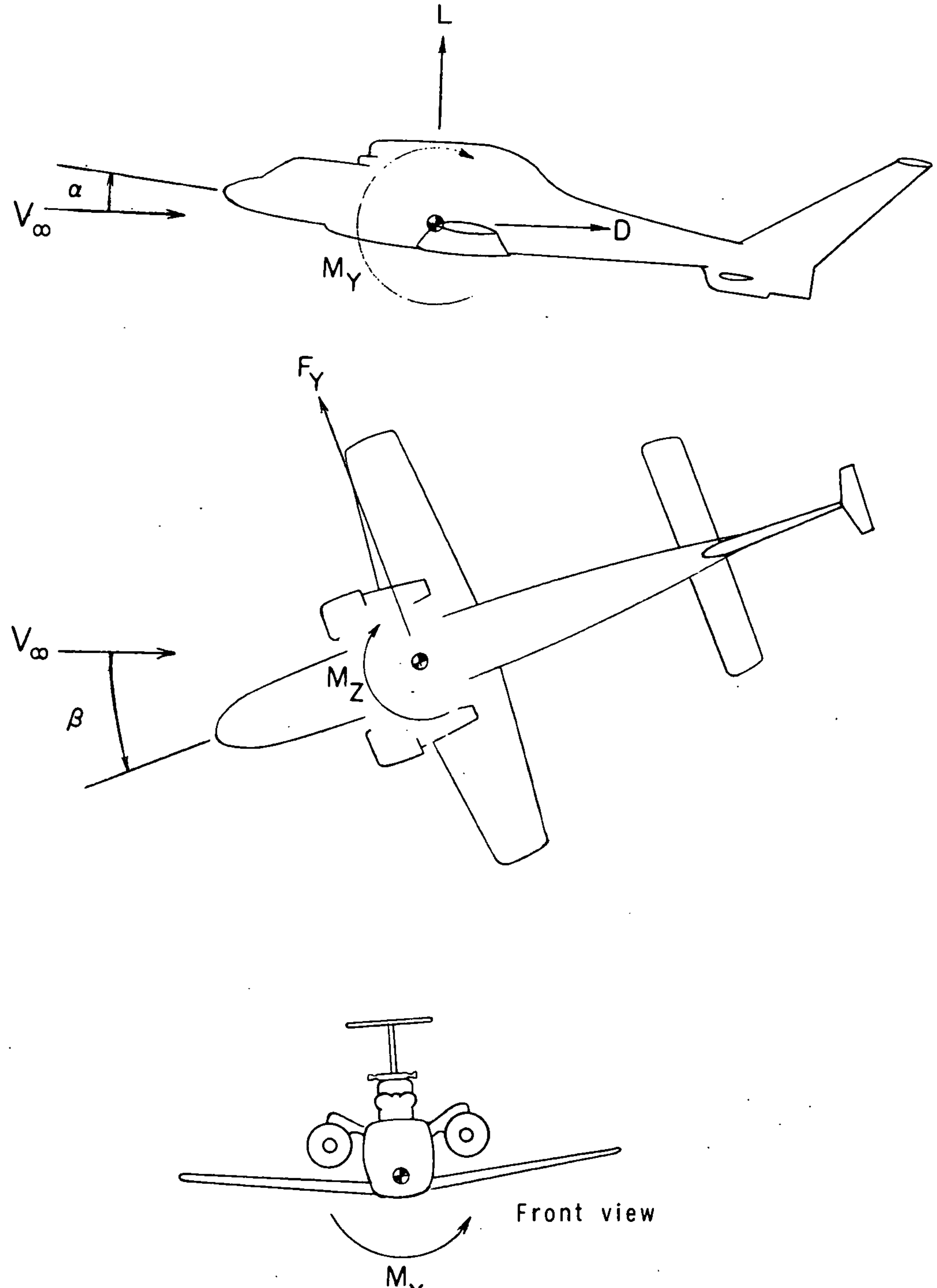

(a) Airplane.

Figure 1.- Sign convention for moments, forces, and angles. Positive directions are indicated by arrows.

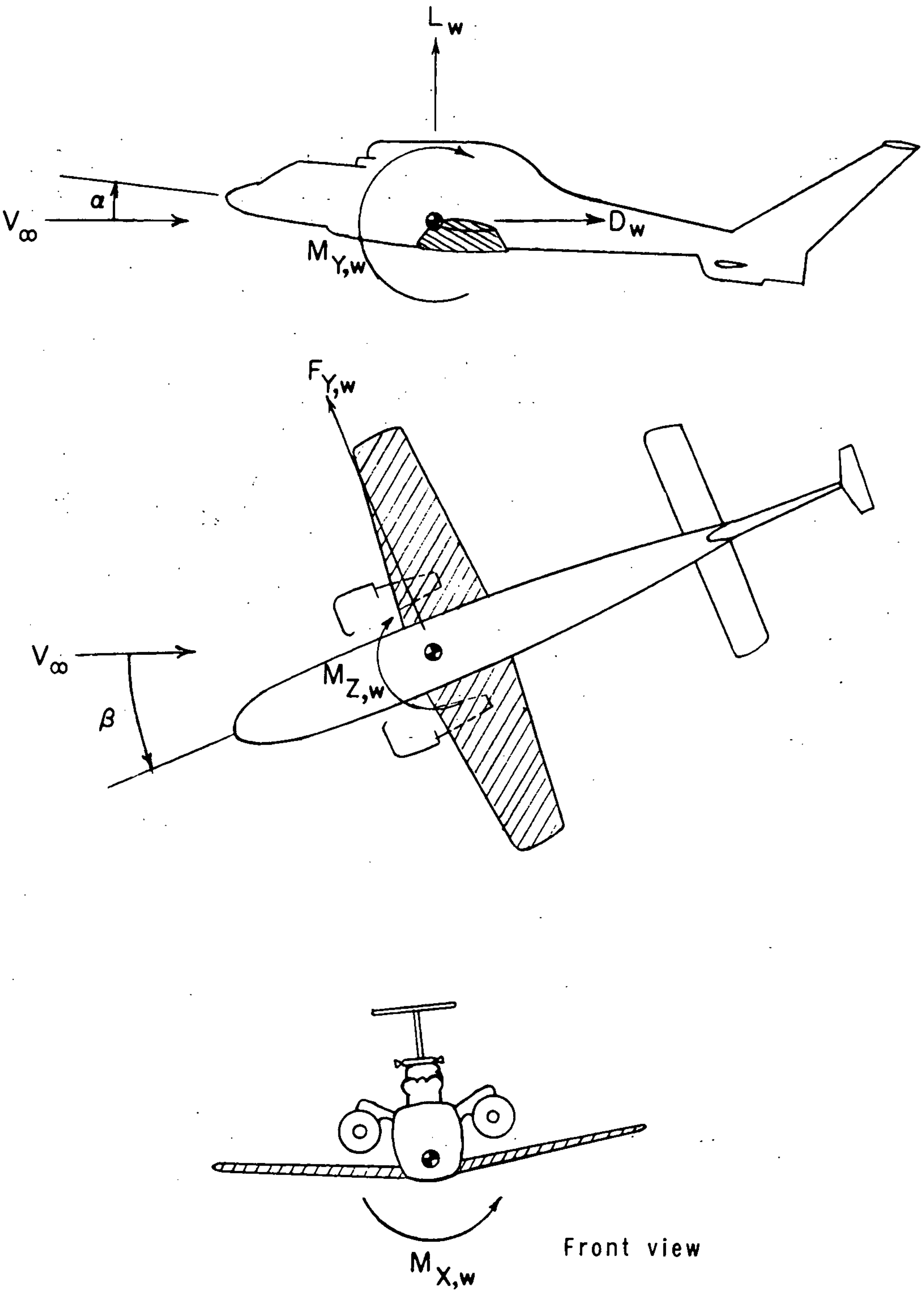

(b) Wing (hatched area).

Figure 1.- Continued.

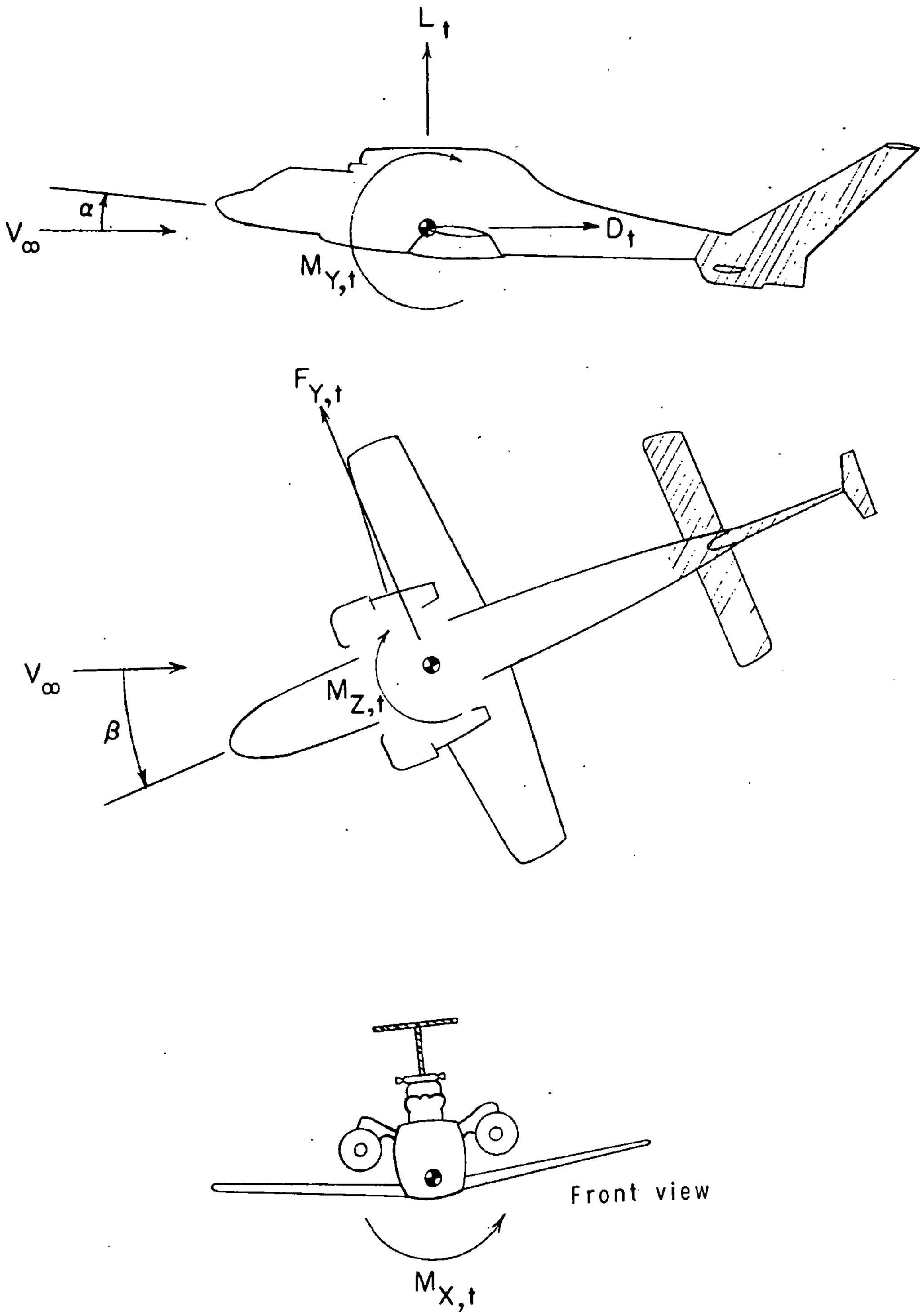

(c) Tail (hatched area).

Figure 1.- Continued.

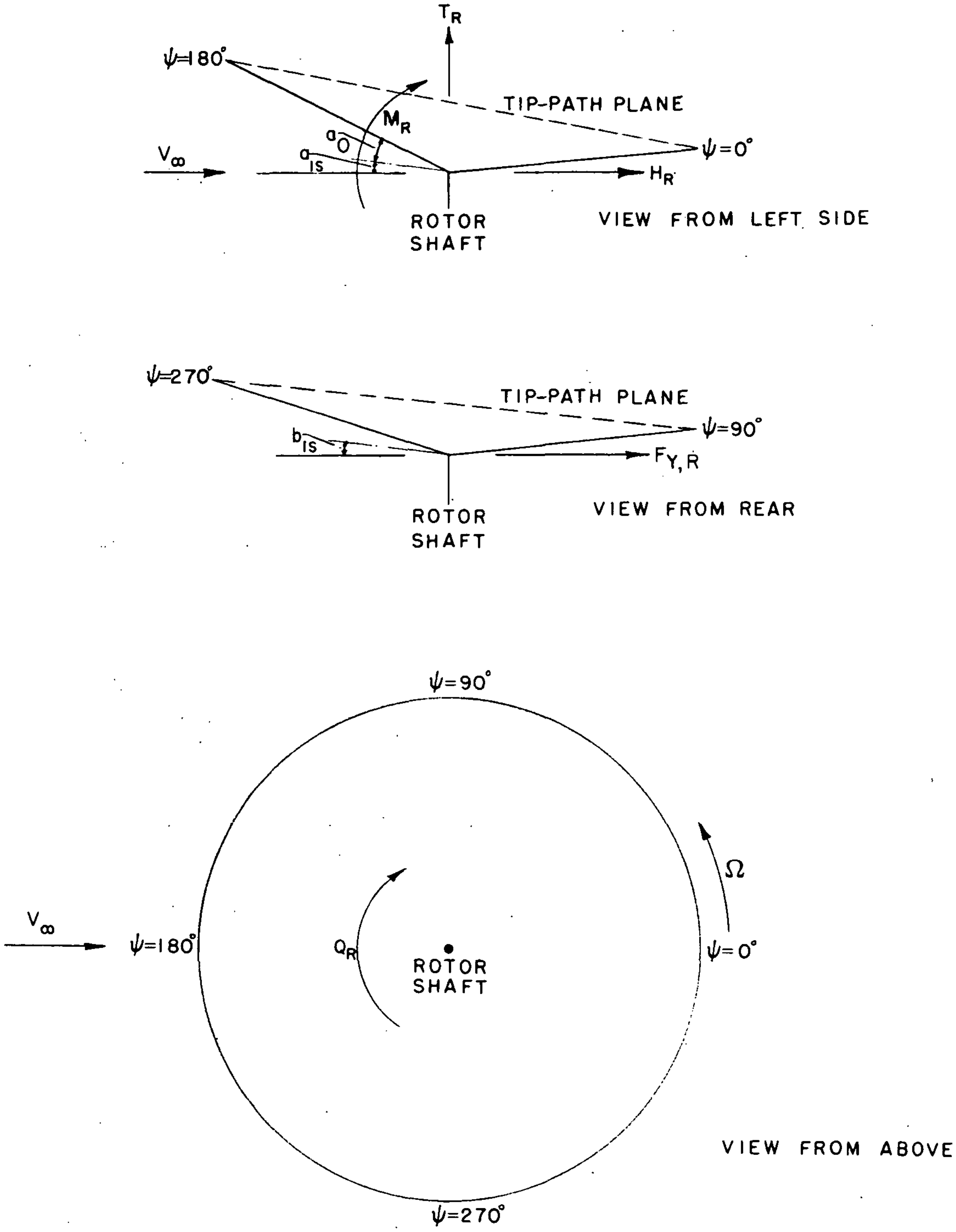

(d) Rotor.

Figure 1.- Continued.

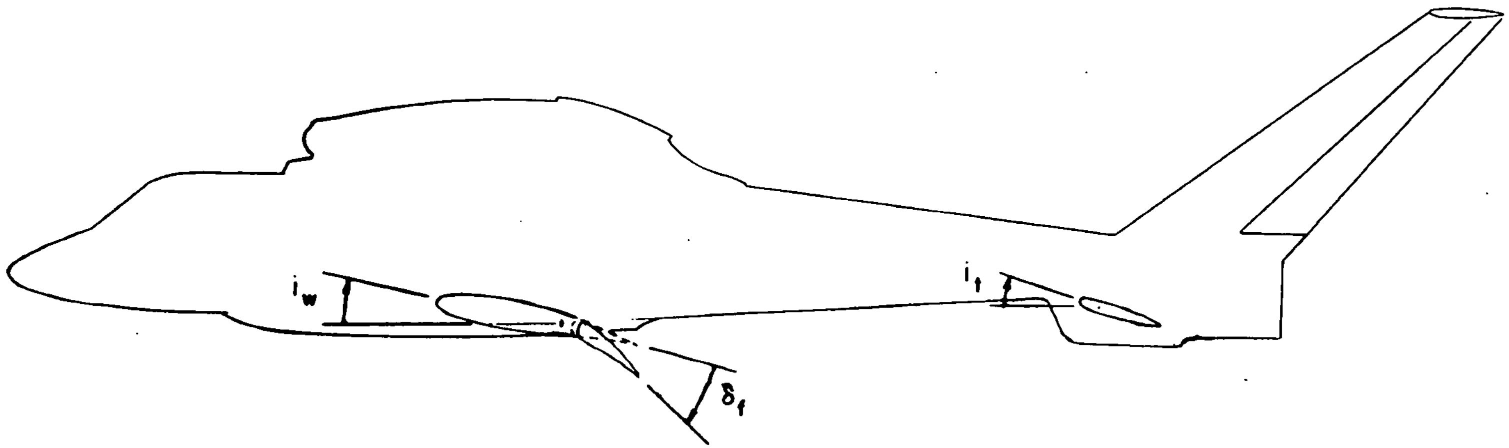

(e) Aerodynamic surfaces.

Figure 1.- Concluded.

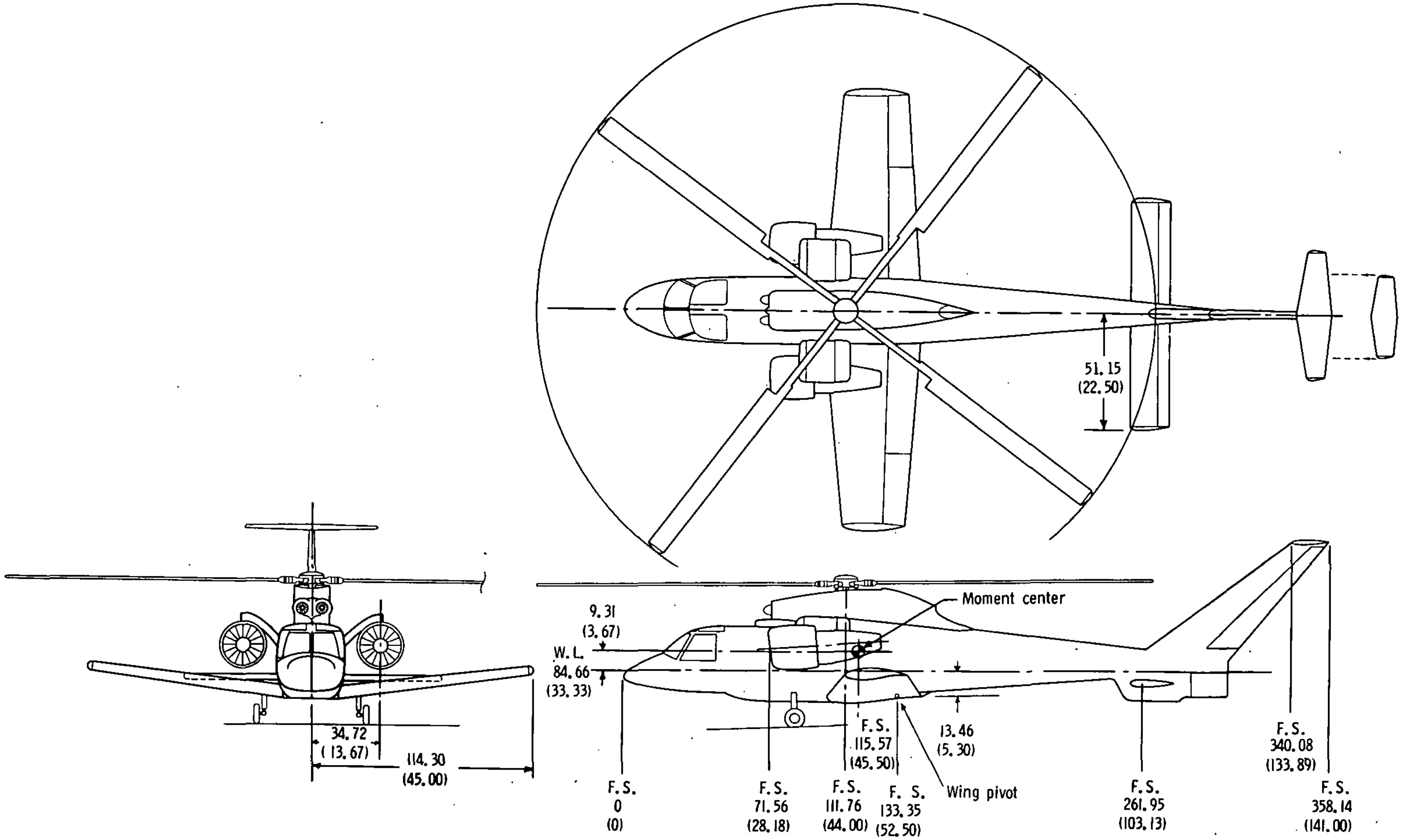

(a) Three-view sketch. (See table I for further details.)

Figure 2.- **Details** of model. All dimensions are in cm (in.) unless specified otherwise. (F.S., fuselage station; W.L., water line.)

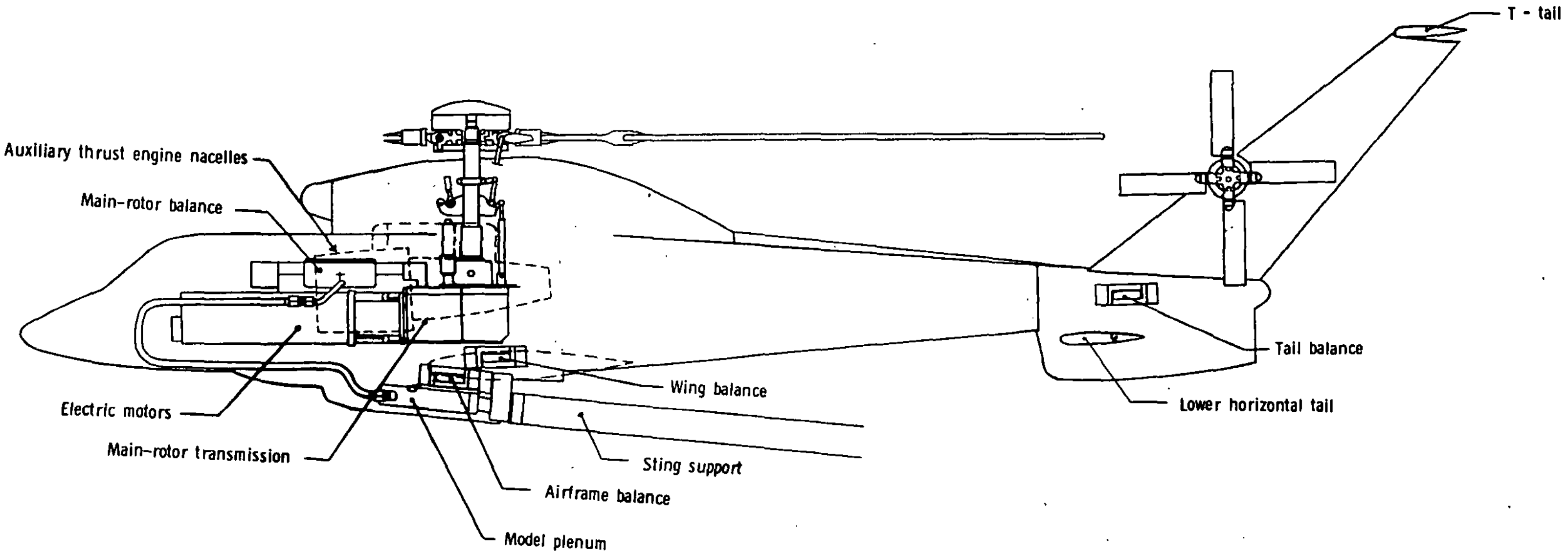

(b) Internal component layout.

Figure 2.- Continued.

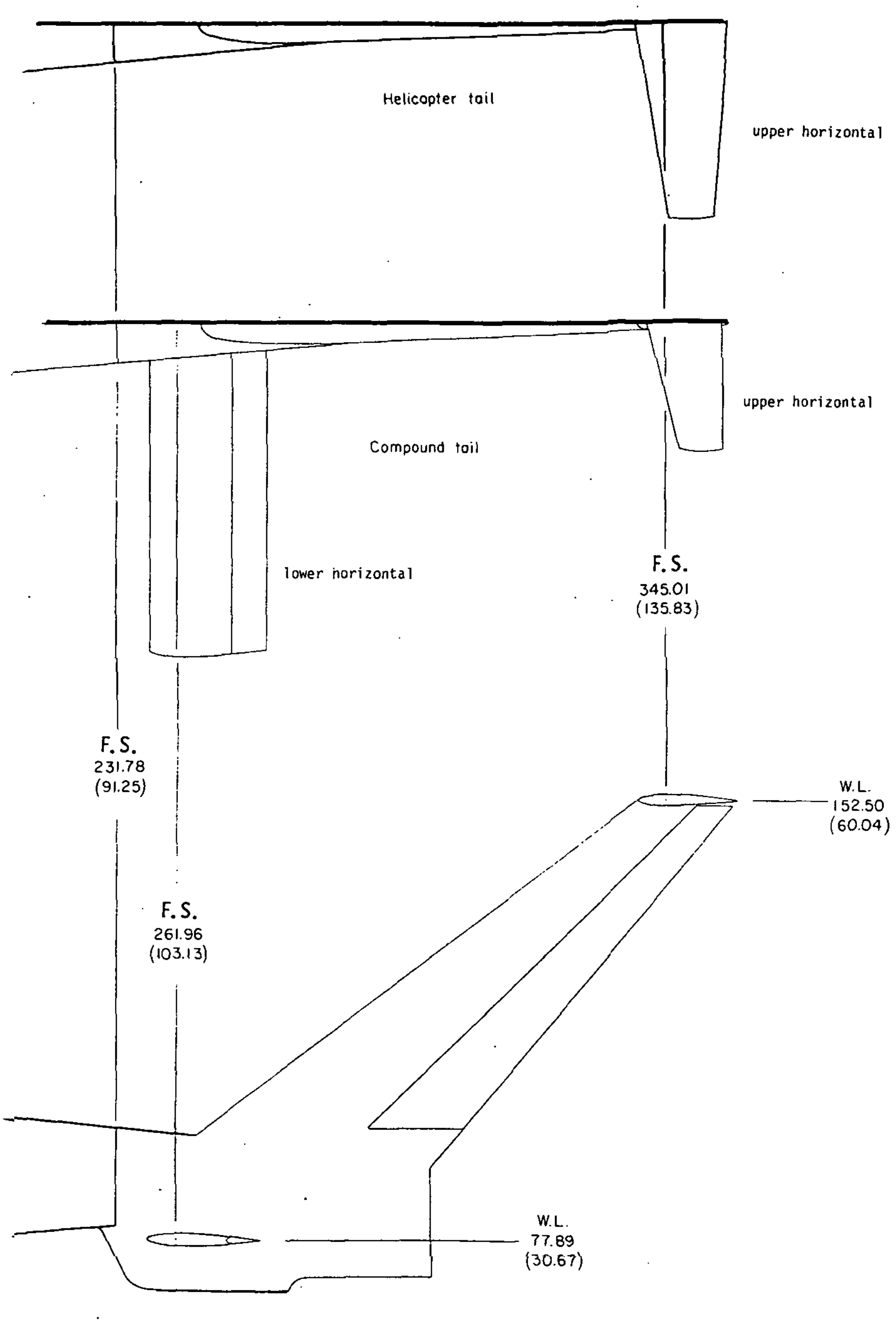

(c) Helicopter tail H_H and compound tail H_C.

Figure 2.- Continued.

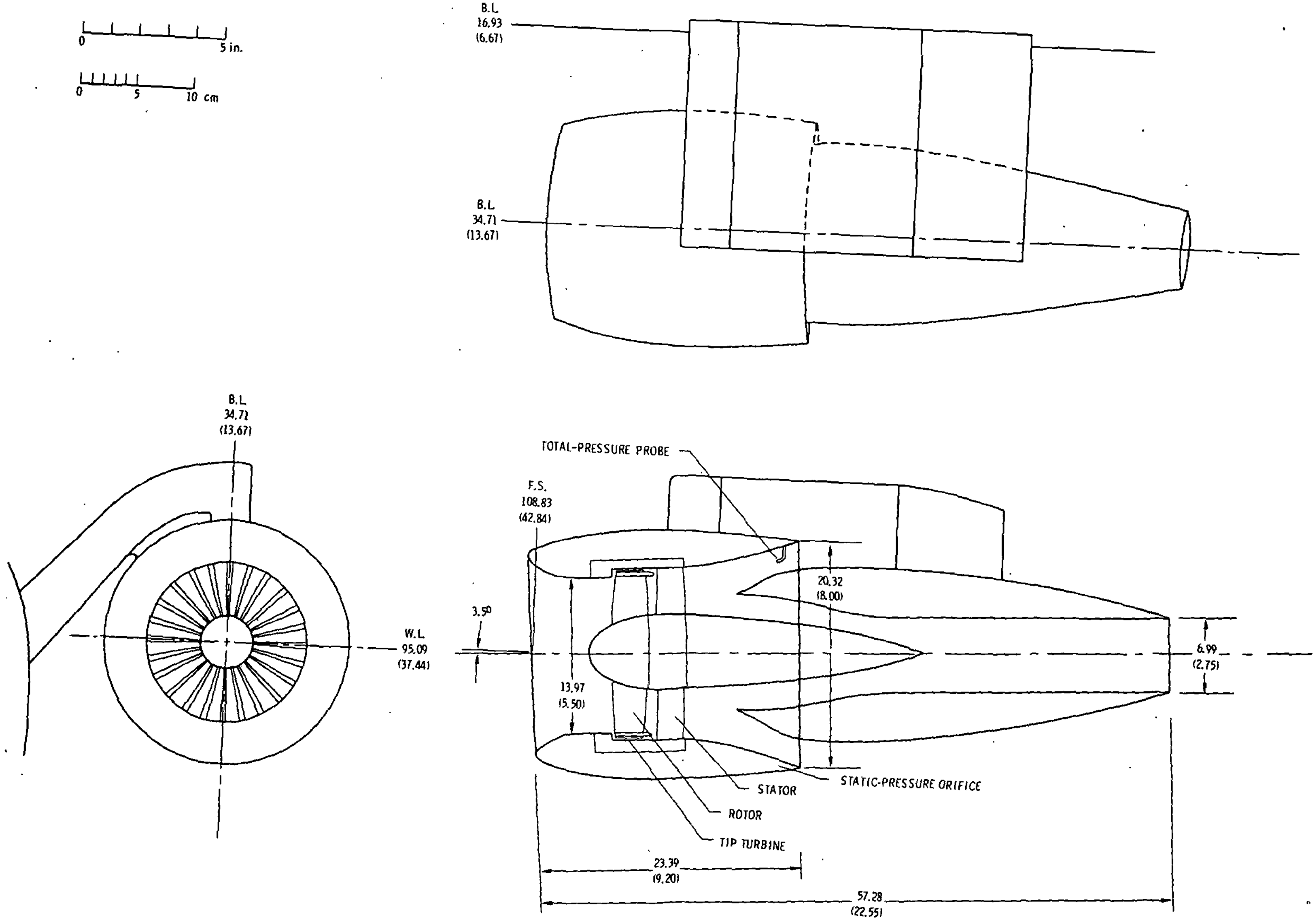

(d) Auxiliary thrust engine simulators. (B.L., buttock line.)

Figure 2.- Concluded.

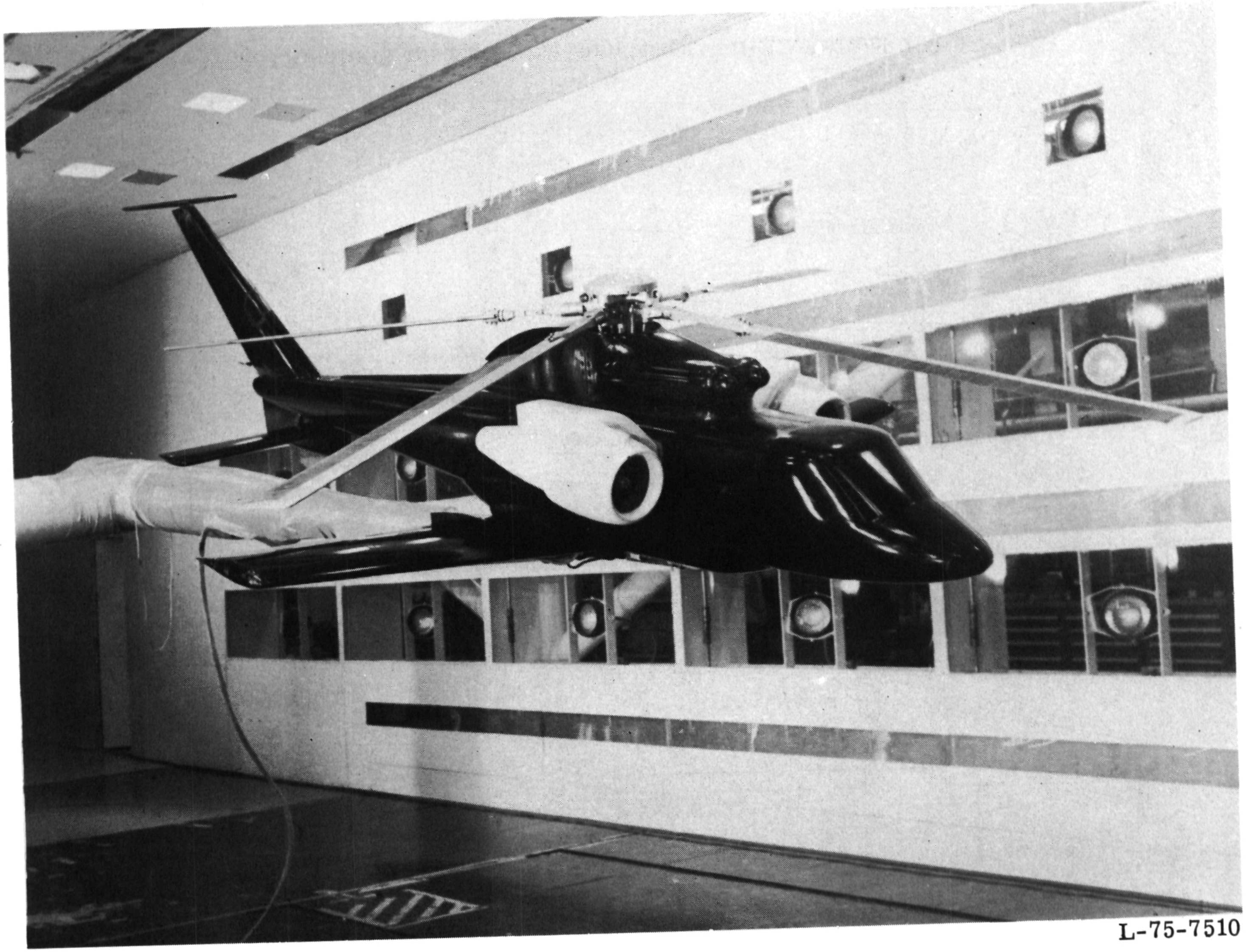

L-75-7510

Figure 3.- Model in Langley V/STOL tunnel.

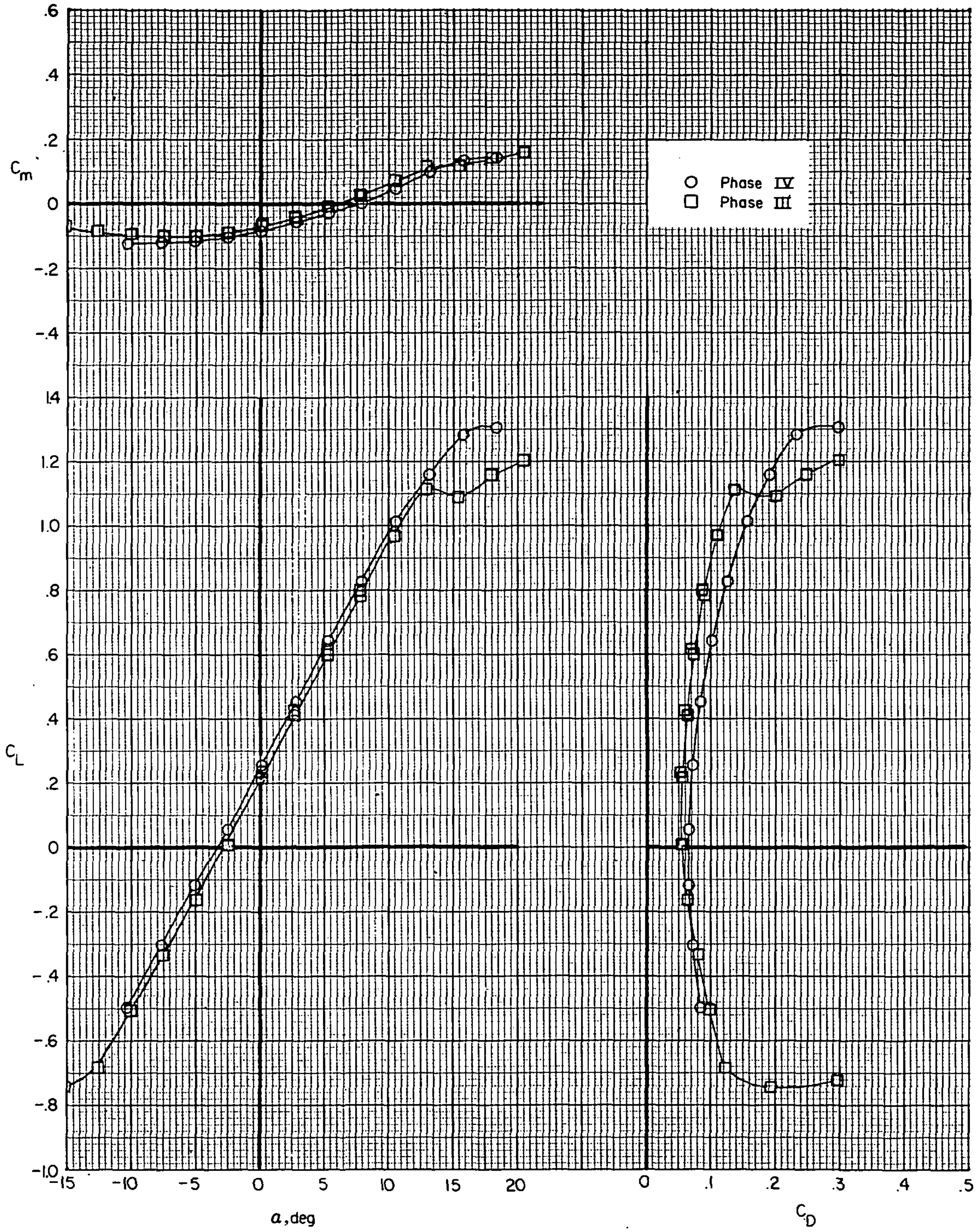

(a) $i_w = 0^\circ$; $\delta_f = 0^\circ$.

Figure 4.- Comparison of results from Phase IV and Phase III for fuselage, vertical tail, and wing (F_1W_xV).

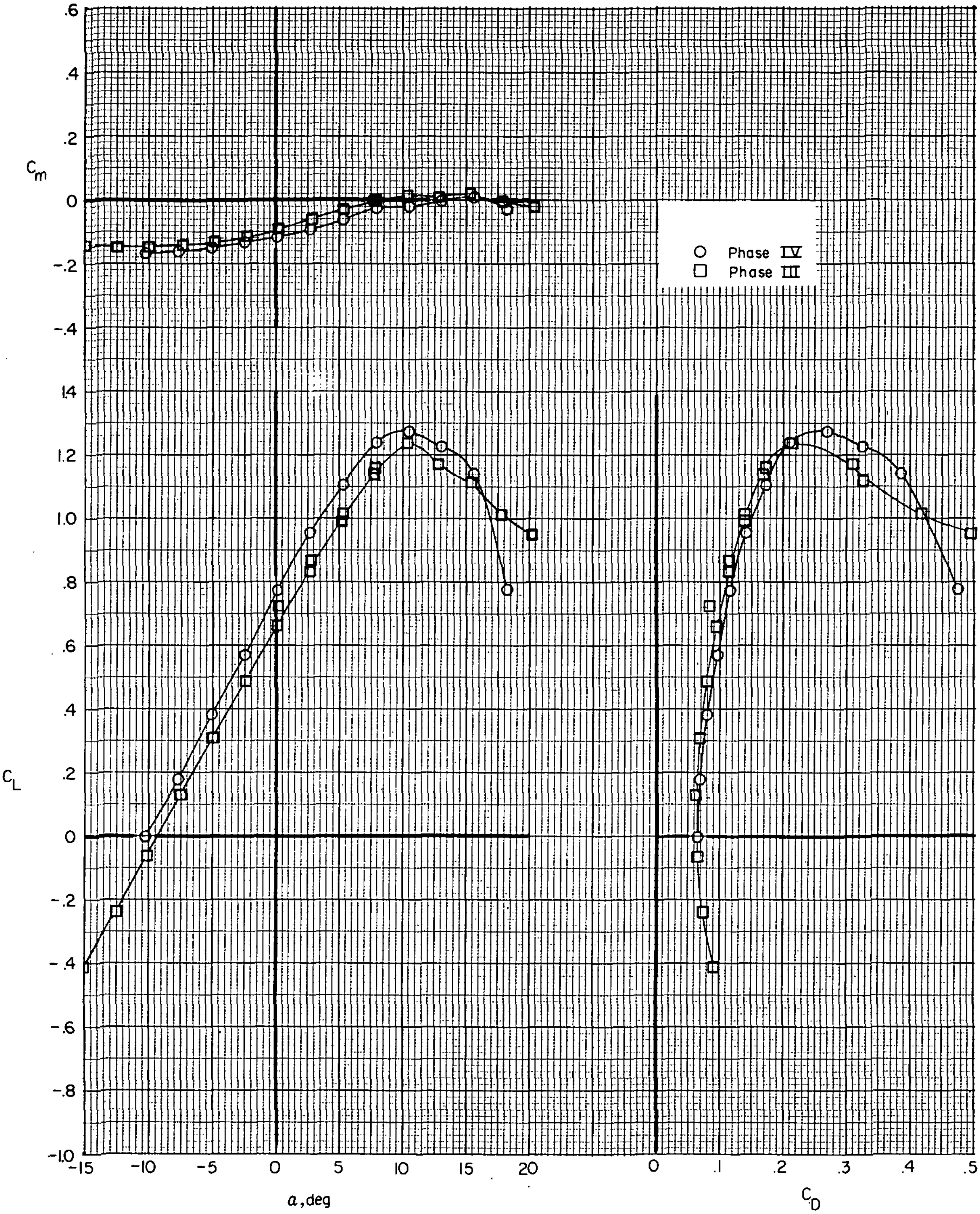

(b) $i_w = 7.5^\circ$; $\delta_f = 0^\circ$.

Figure 4.- Concluded.

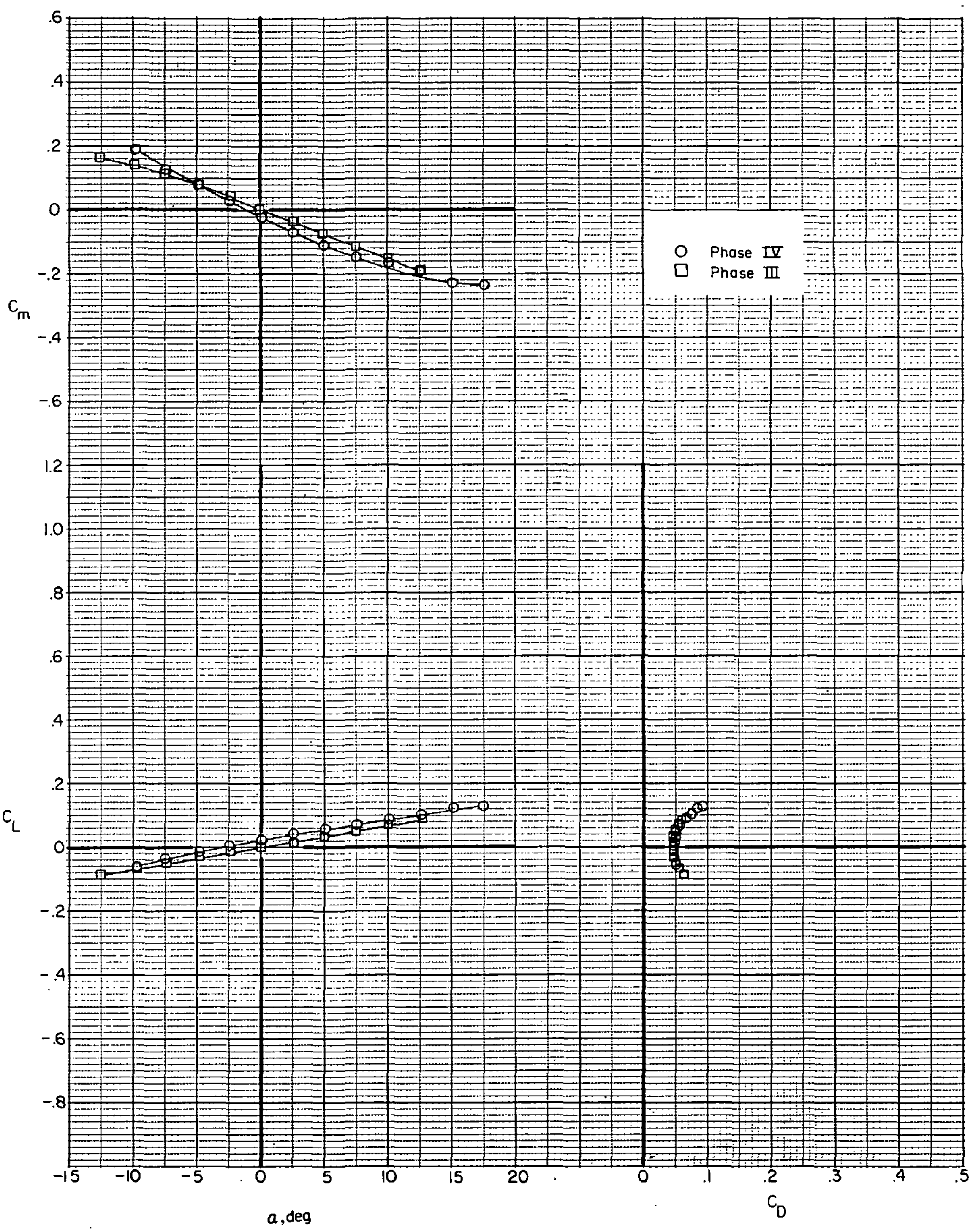

(a) Helicopter tail (F_1VH_H). (Phase III data for shortened vertical tail.)

Figure 5.- Comparison of results from Phase IV and Phase III for fuselage, vertical tail, and horizontal tail.

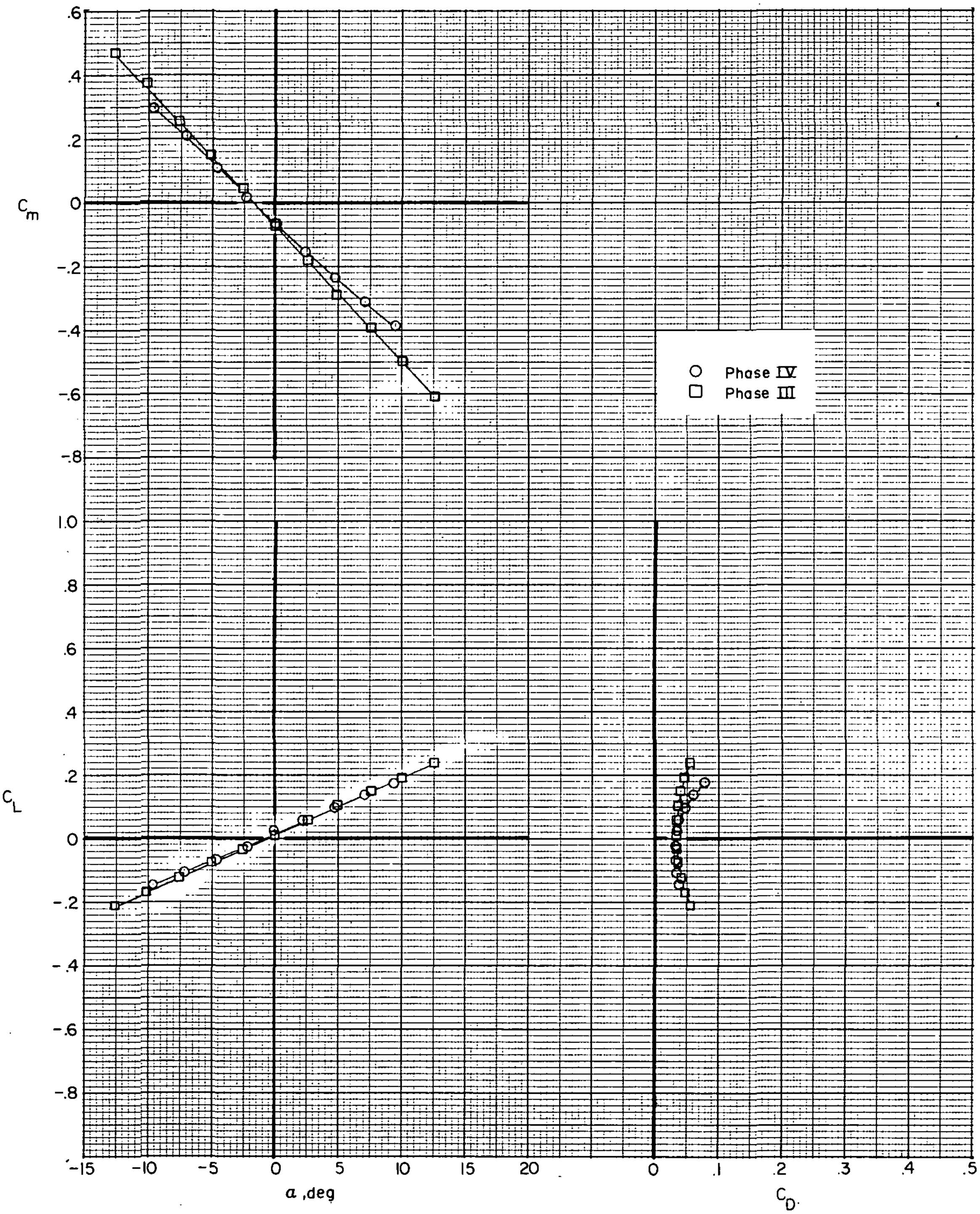

(b) Lower tail of compound tail; main-rotor pylon removed (F_2VH_C). (Phase III data for 118.5-cm (46.67-in.) span horizontal tail.)

Figure 5.- Concluded.

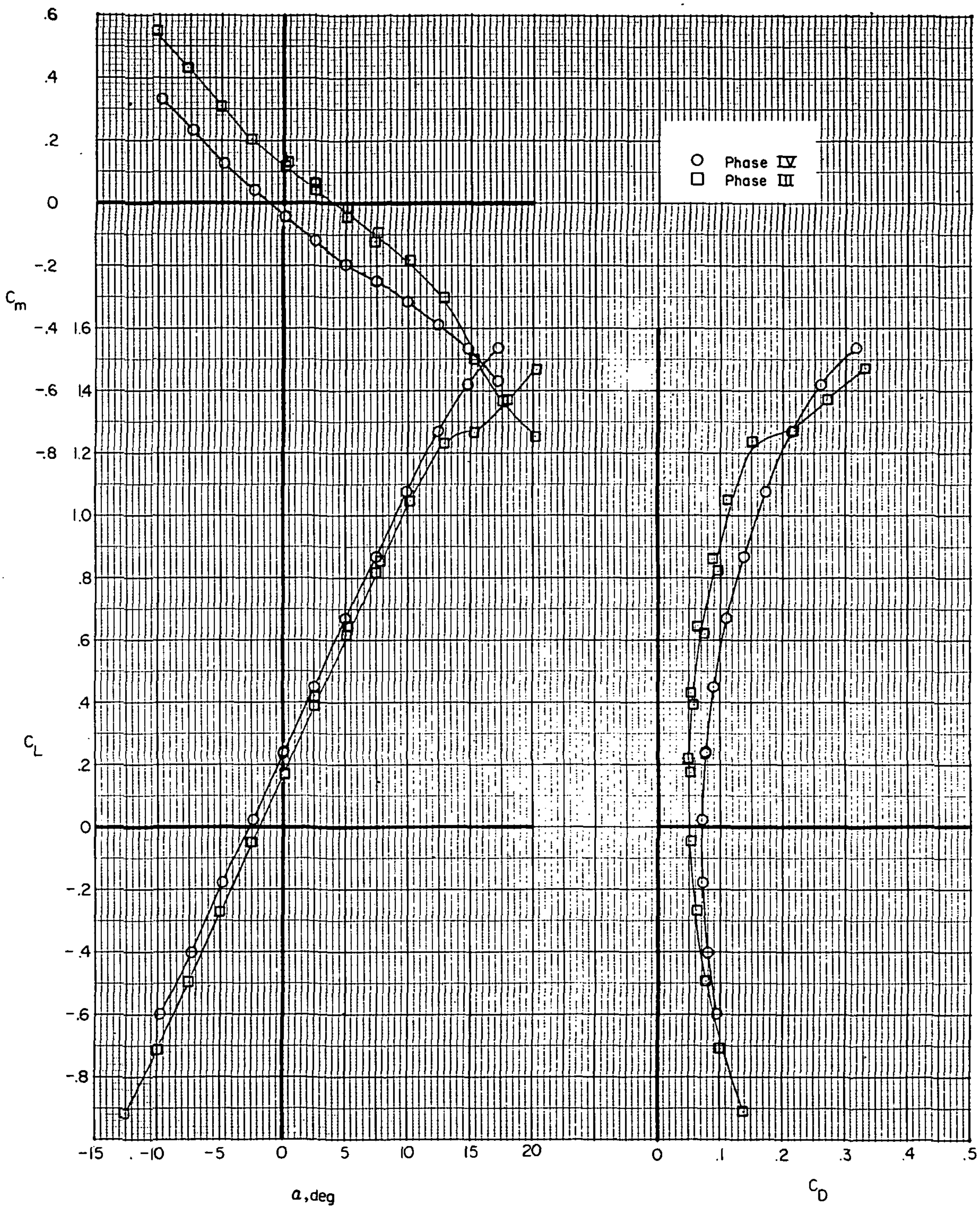

Figure 6.- Comparison of results from Phase IV and Phase III for fuselage, wing, vertical tail, and compound horizontal tails ($F_1 W_1 VH_C$). (Phase III data for 127.0-cm (50.0-in.) span horizontal tail.)

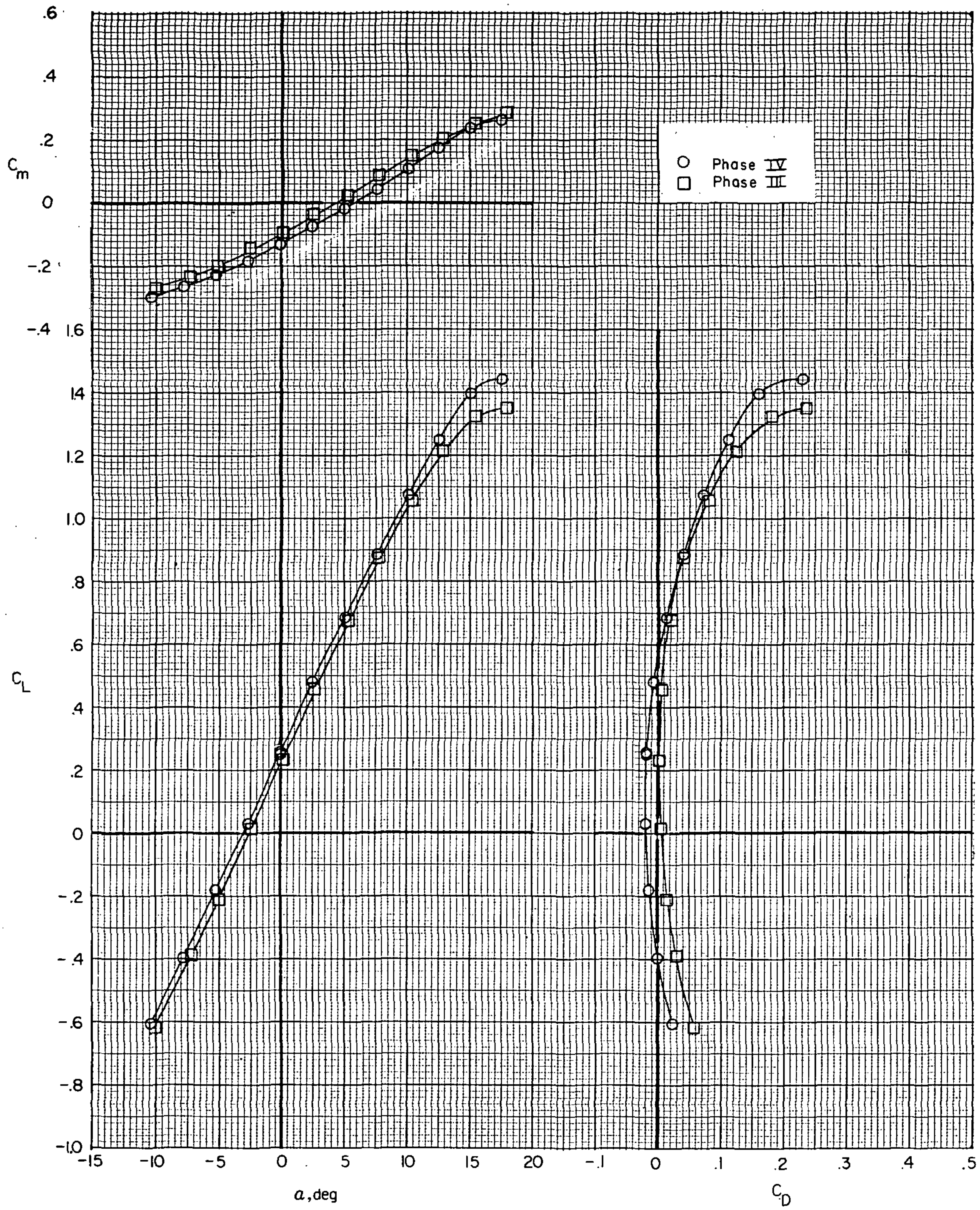

(a) $i_w = 0^\circ$; $\delta_f = 0^\circ$.

Figure 7.- Comparison of results from Phase IV and Phase III for fuselage, wing, vertical tail, and auxiliary thrust jets ($F_1W_xVJ_2$). Jets at trim thrust.

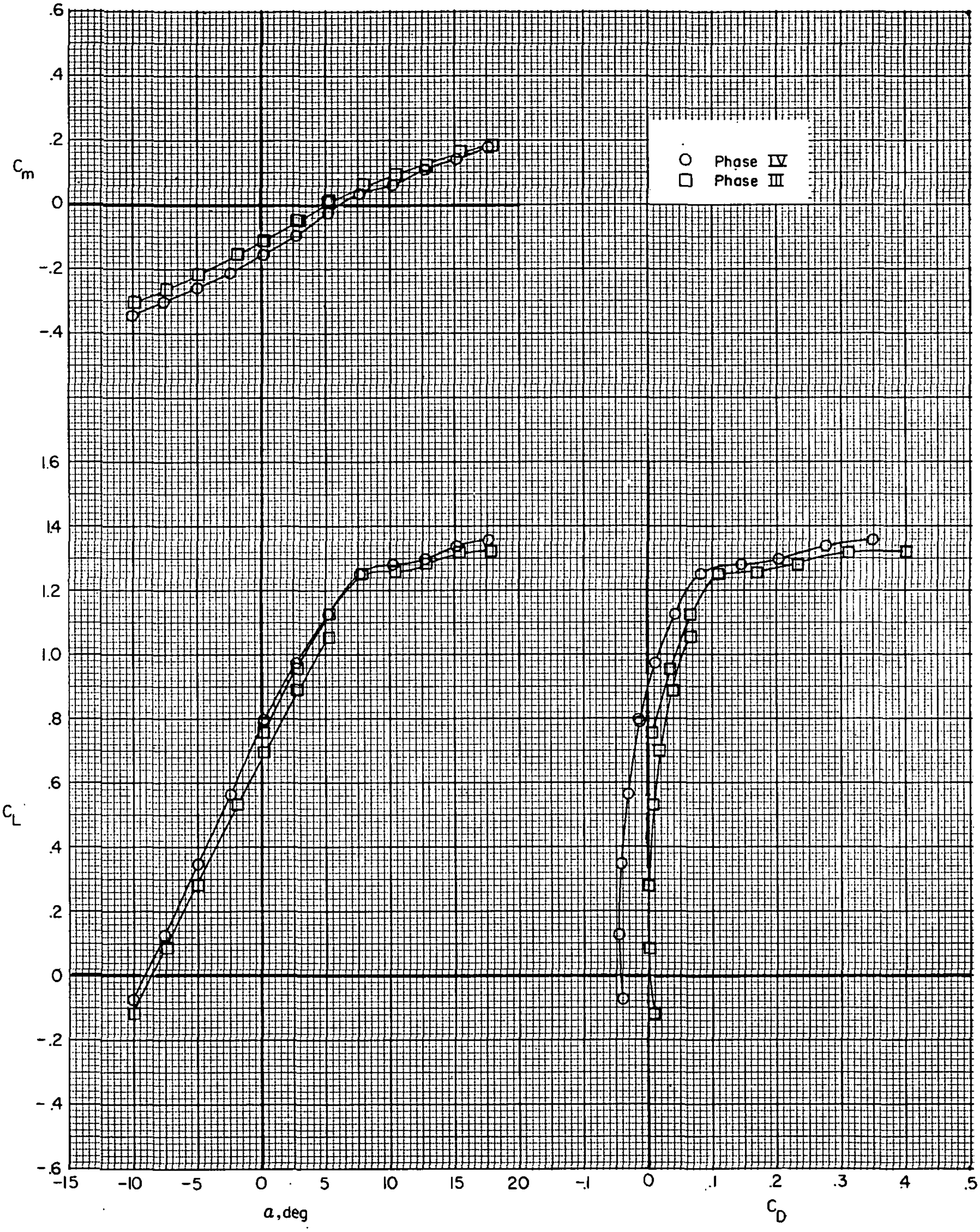

(b) $i_w = 7.5^\circ$; $\delta_f = 0^\circ$.

Figure 7.- Concluded.

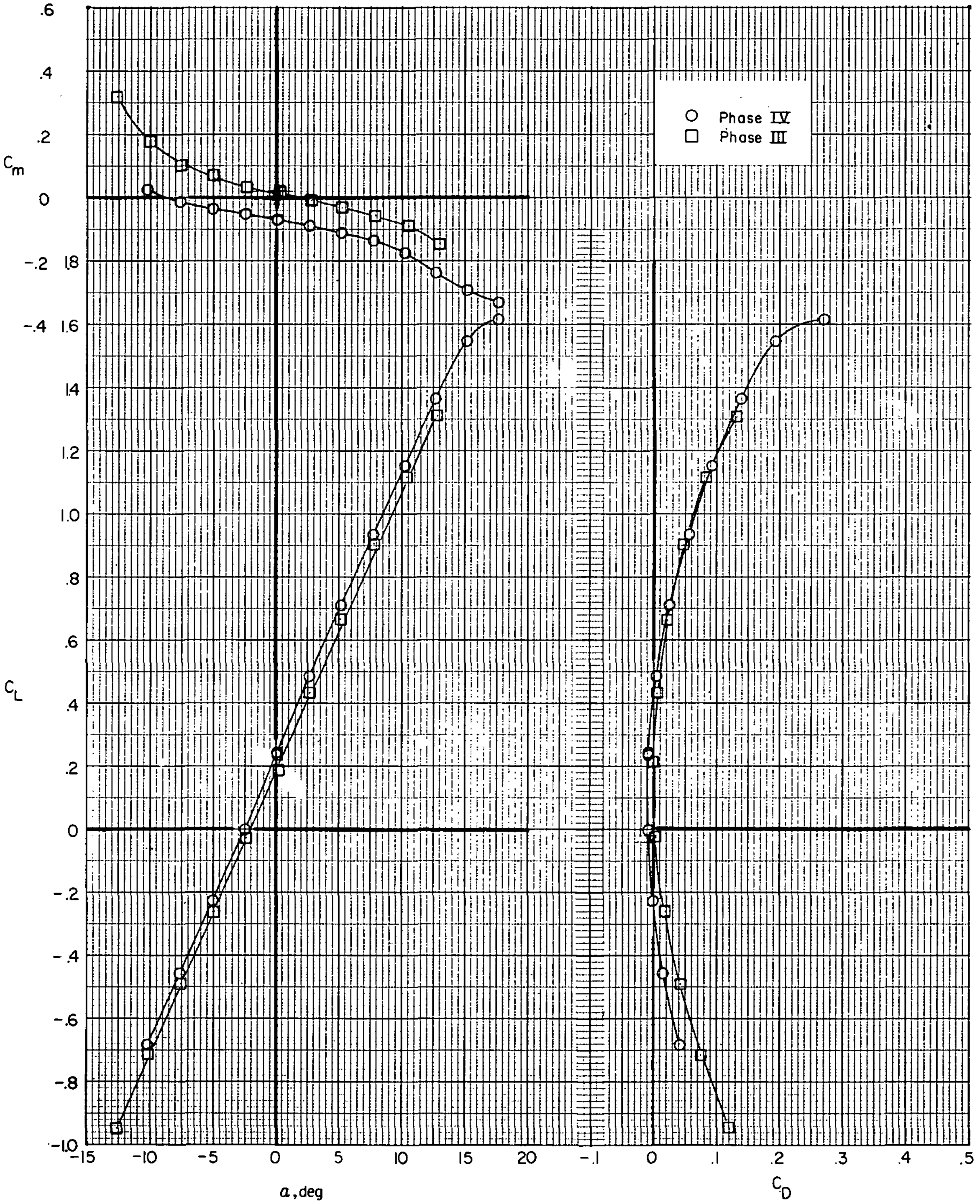

(a) $i_w = 0^\circ$; $\delta_f = 0^\circ$.

Figure 8.- Comparison of results from Phase IV and Phase III for fuselage, wing, vertical tail, compound horizontal tail, and auxiliary thrust jets ($F_2W_XVH_CJ_2$). Jets at trim thrust. (Phase III data are average of data for the 118.5-cm (46.67-in.) span tail and the 110.1-cm (43.33-in.) span tail.)

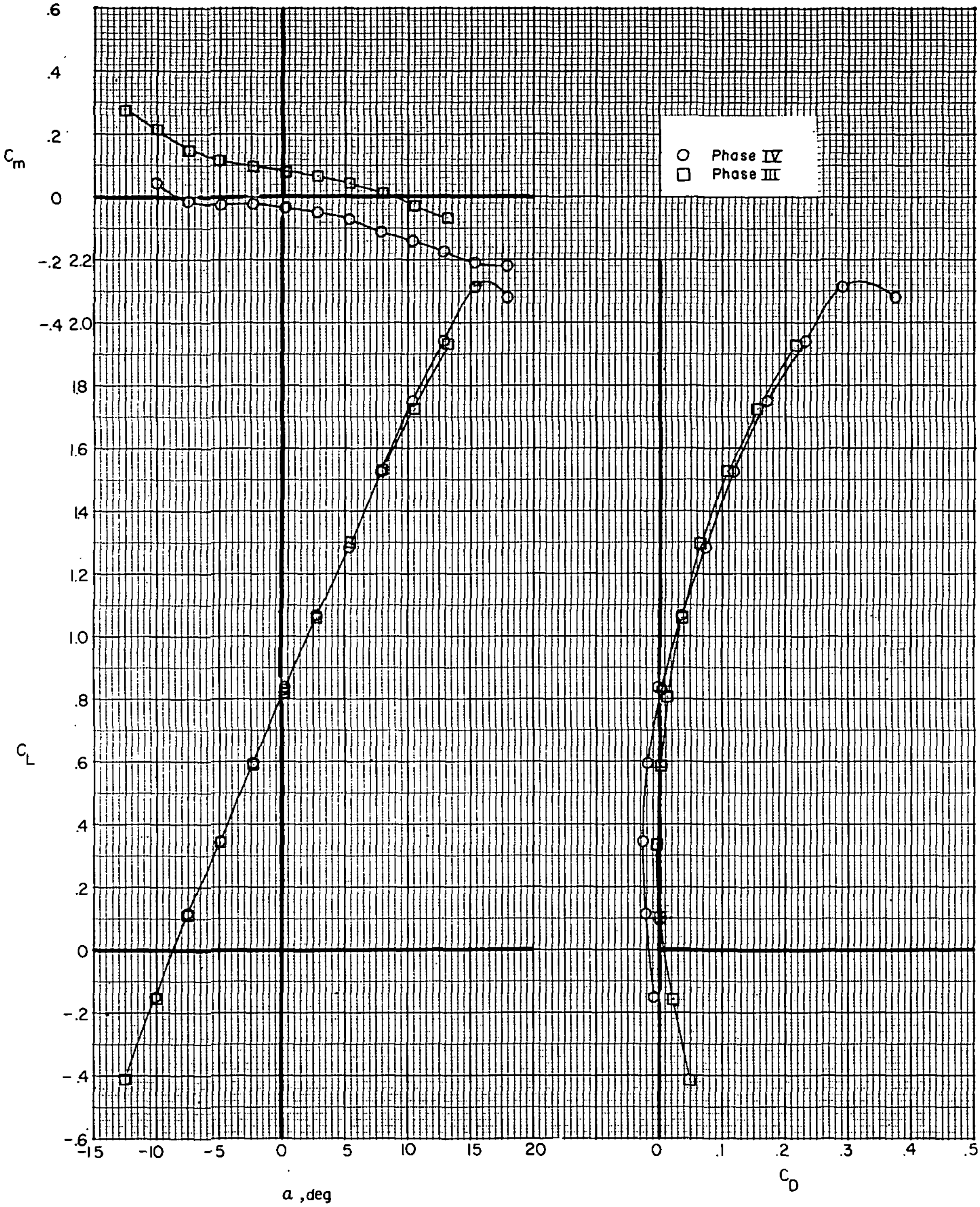

(b) $i_w = 0^{\circ}$; $\delta_f = 30^{\circ}$.

Figure 8. - Continued.

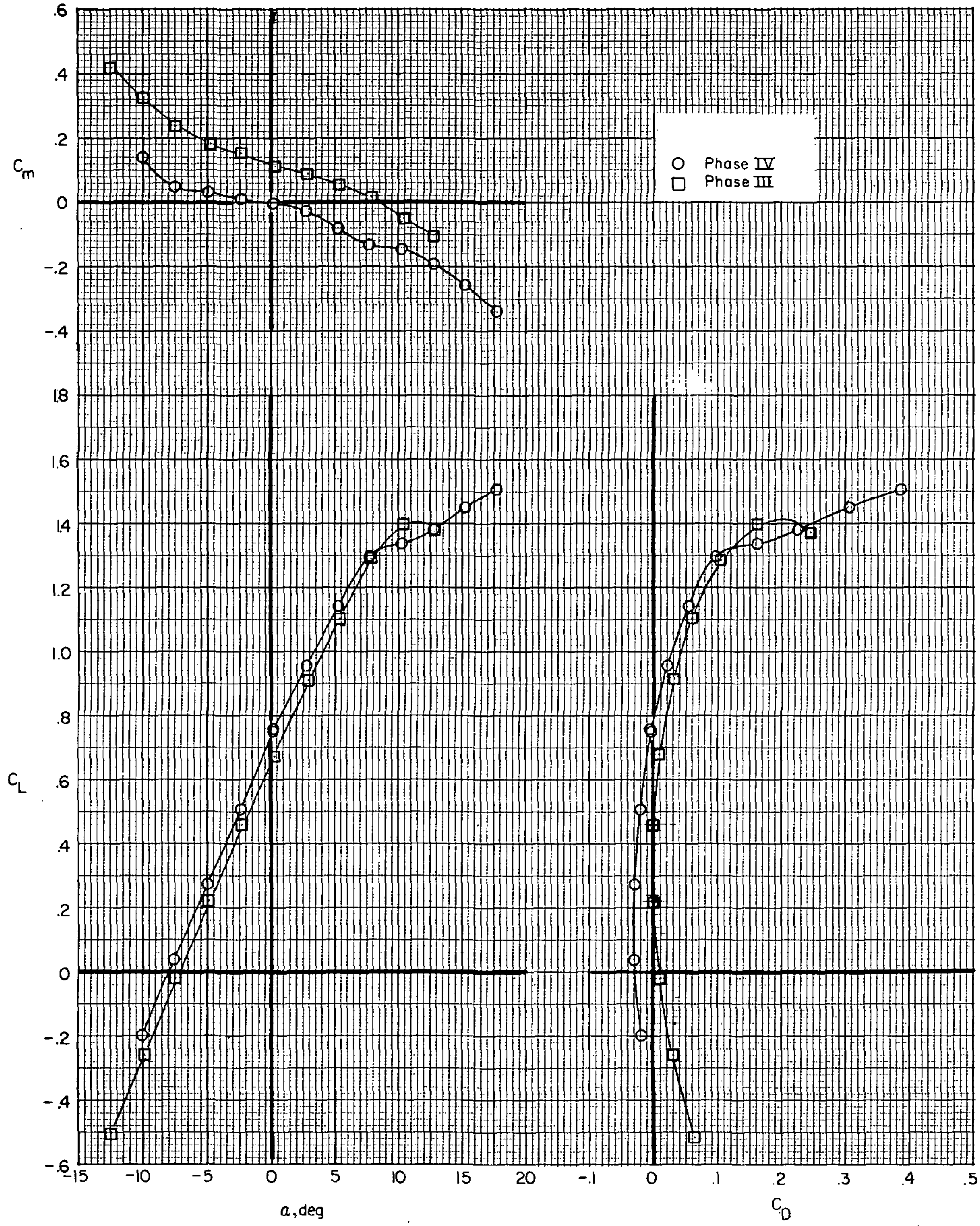

(c) $i_w = 7.5^{\circ}$; $\delta_f = 0^{\circ}$.

Figure 8.- Continued.

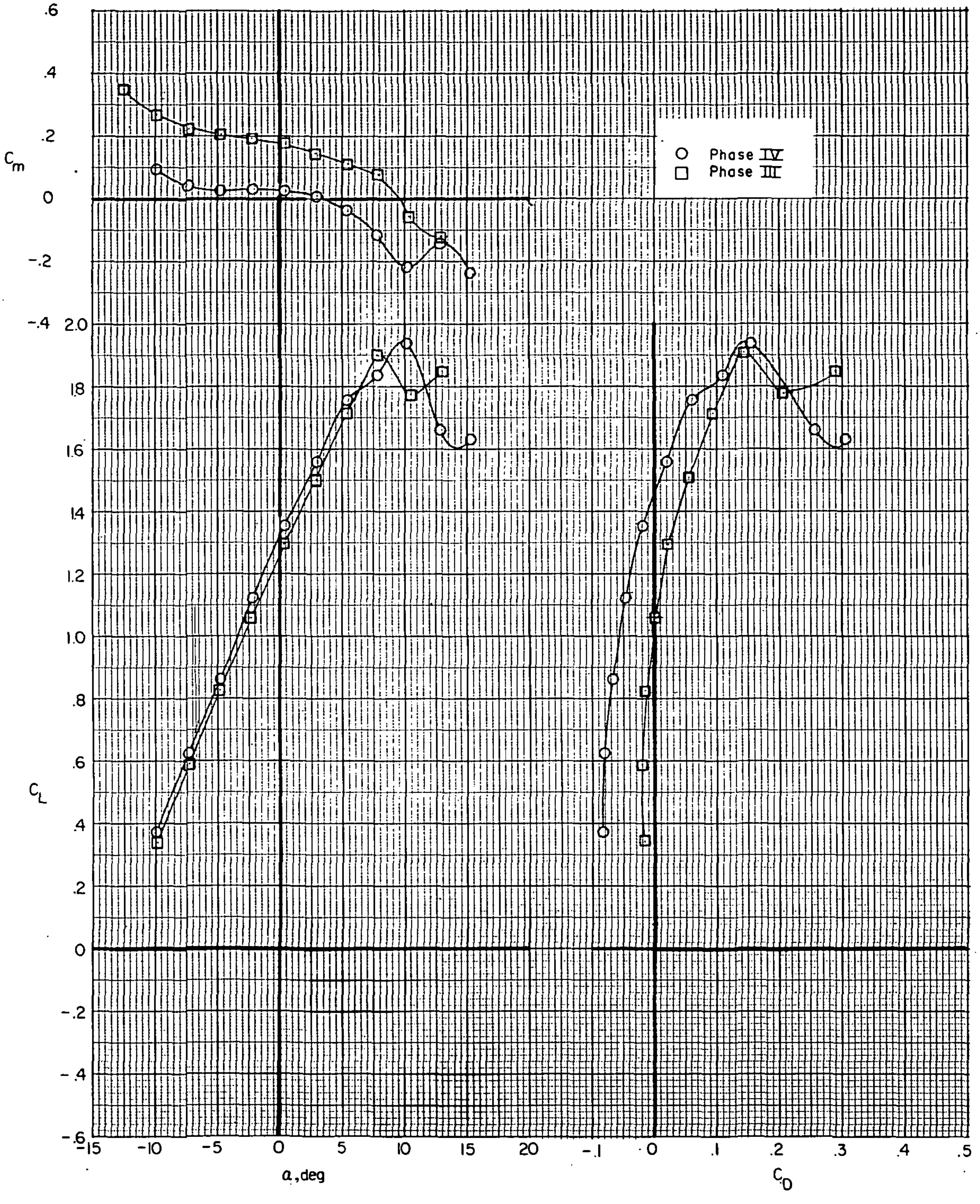

(d) $i_w = 7.5^\circ$; $\delta_f = 30^\circ$.

Figure 8.- Concluded.

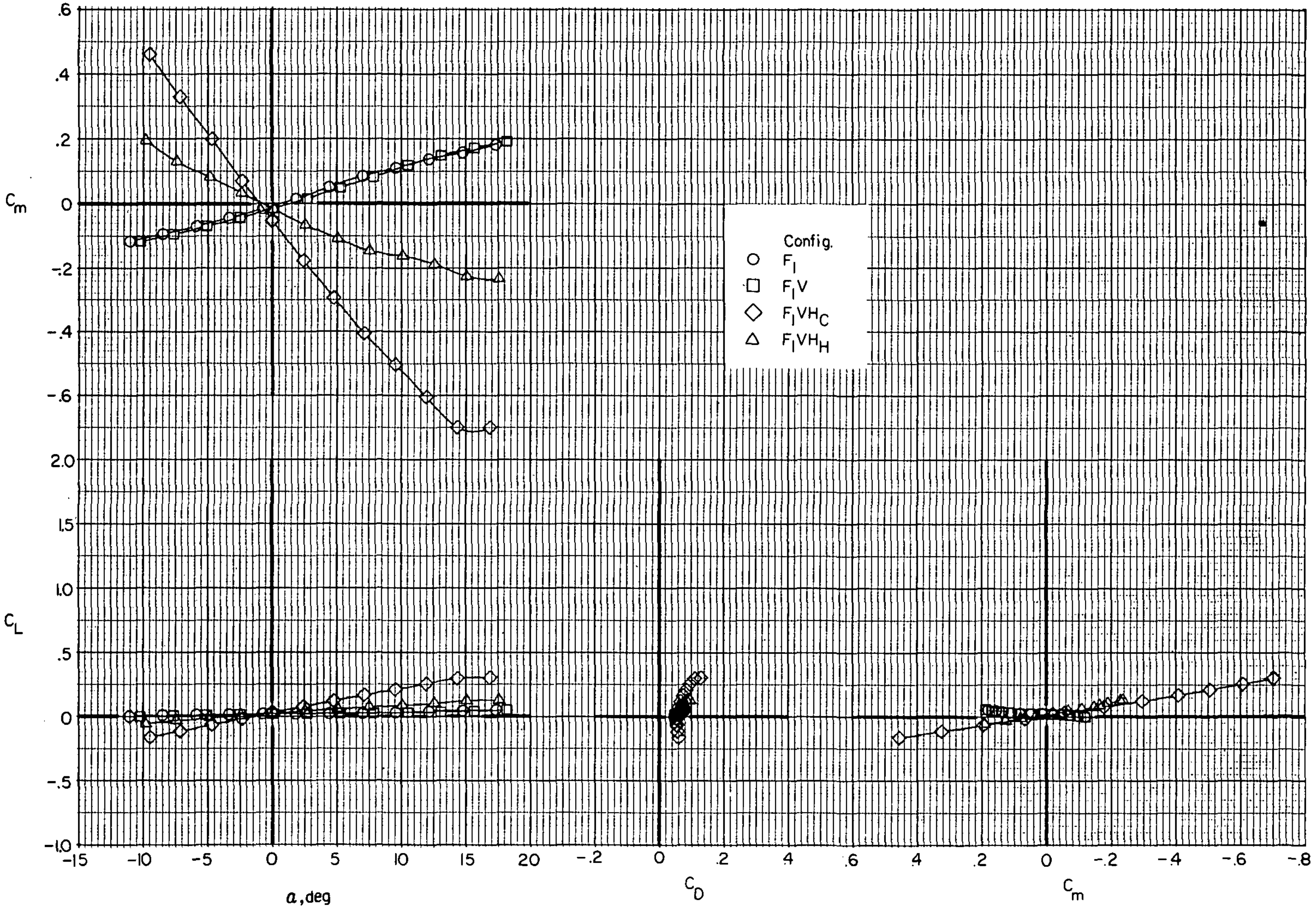

(a) Wing and jets removed.

Figure 9.- Effect of empennage components on airframe longitudinal aerodynamics. $i_t = 0^o$.

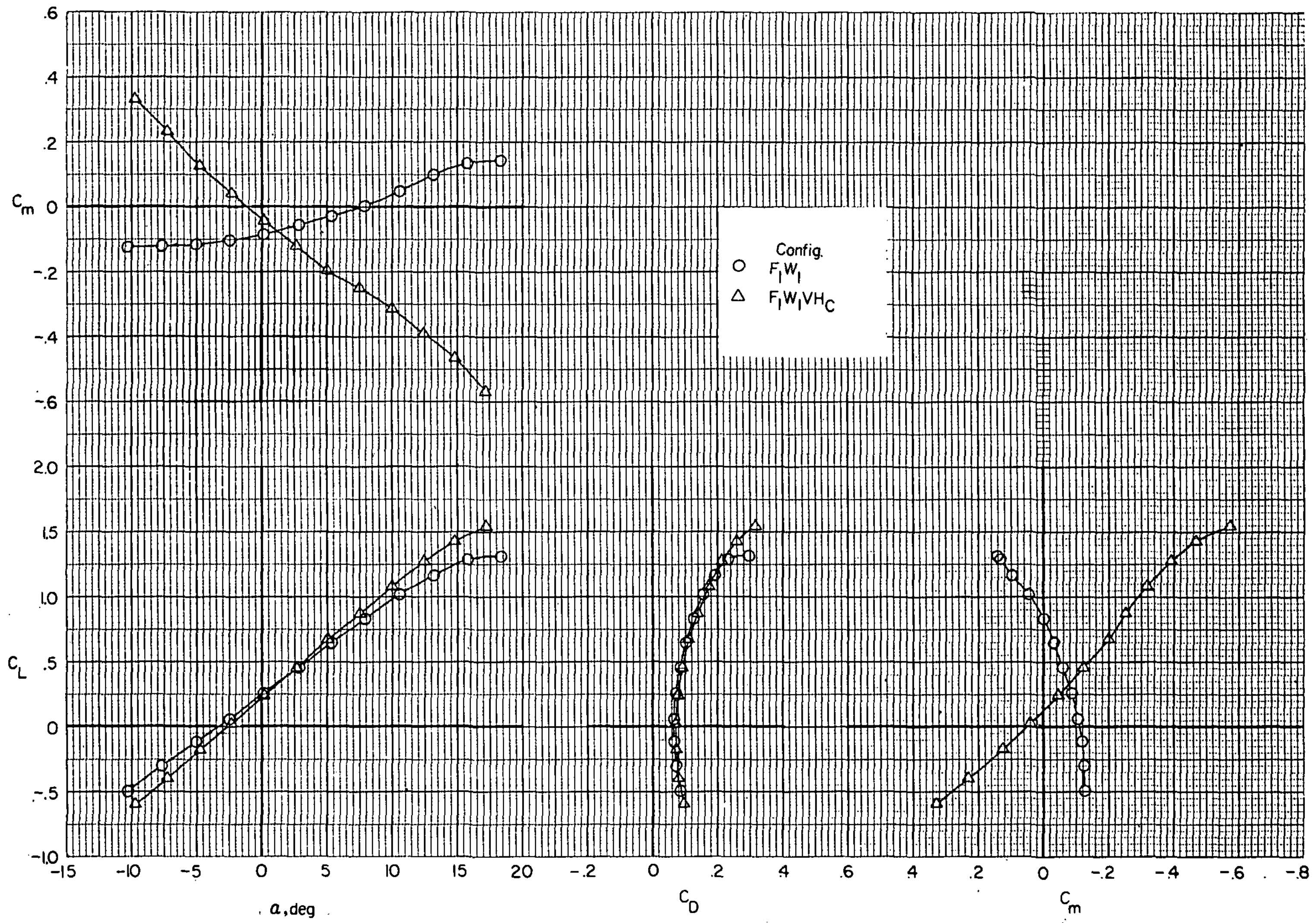

(b) $i_W = 0^o$; $\delta_f = 0^o$; jets removed.

Figure 9.- Continued.

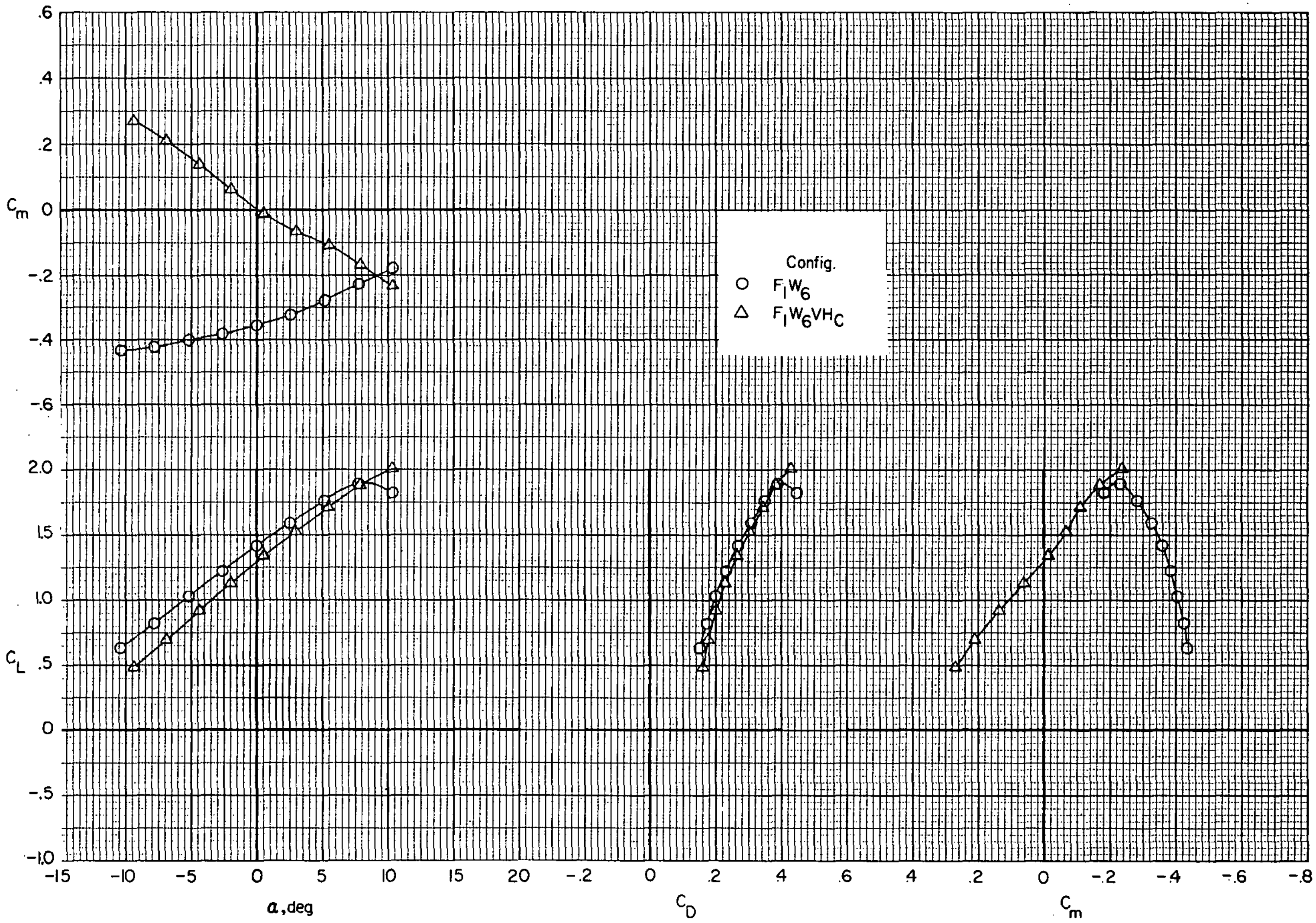

(c) $i_w = 7.5^\circ$; $\delta_f = 30^\circ$; jets removed.

Figure 9.- Concluded.

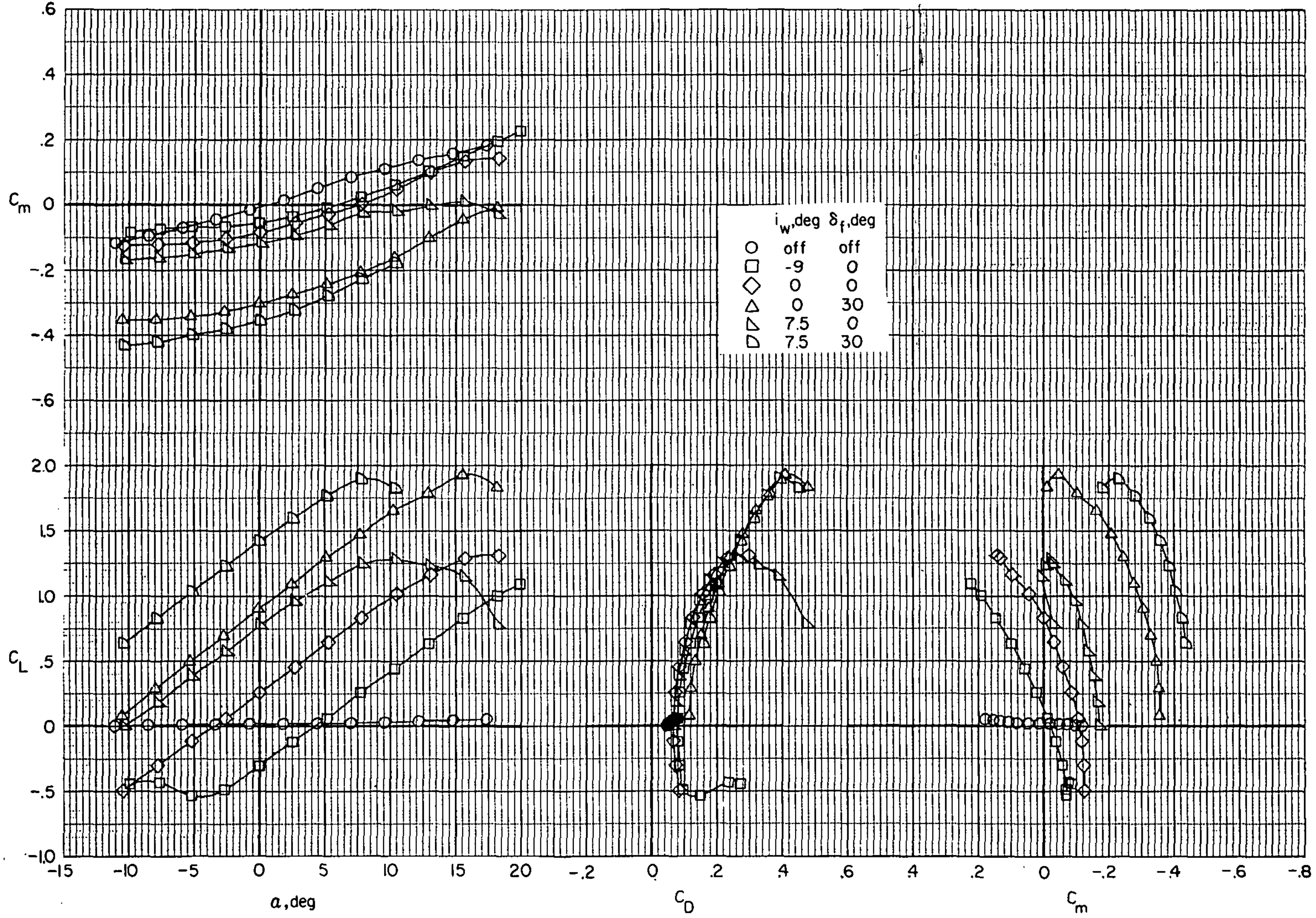

(a) Empennage and jets removed (F_1W_x).

Figure 10.- Effect of wing incidence and flap deflection on airframe longitudinal aerodynamics. $i_t = 0^o$.

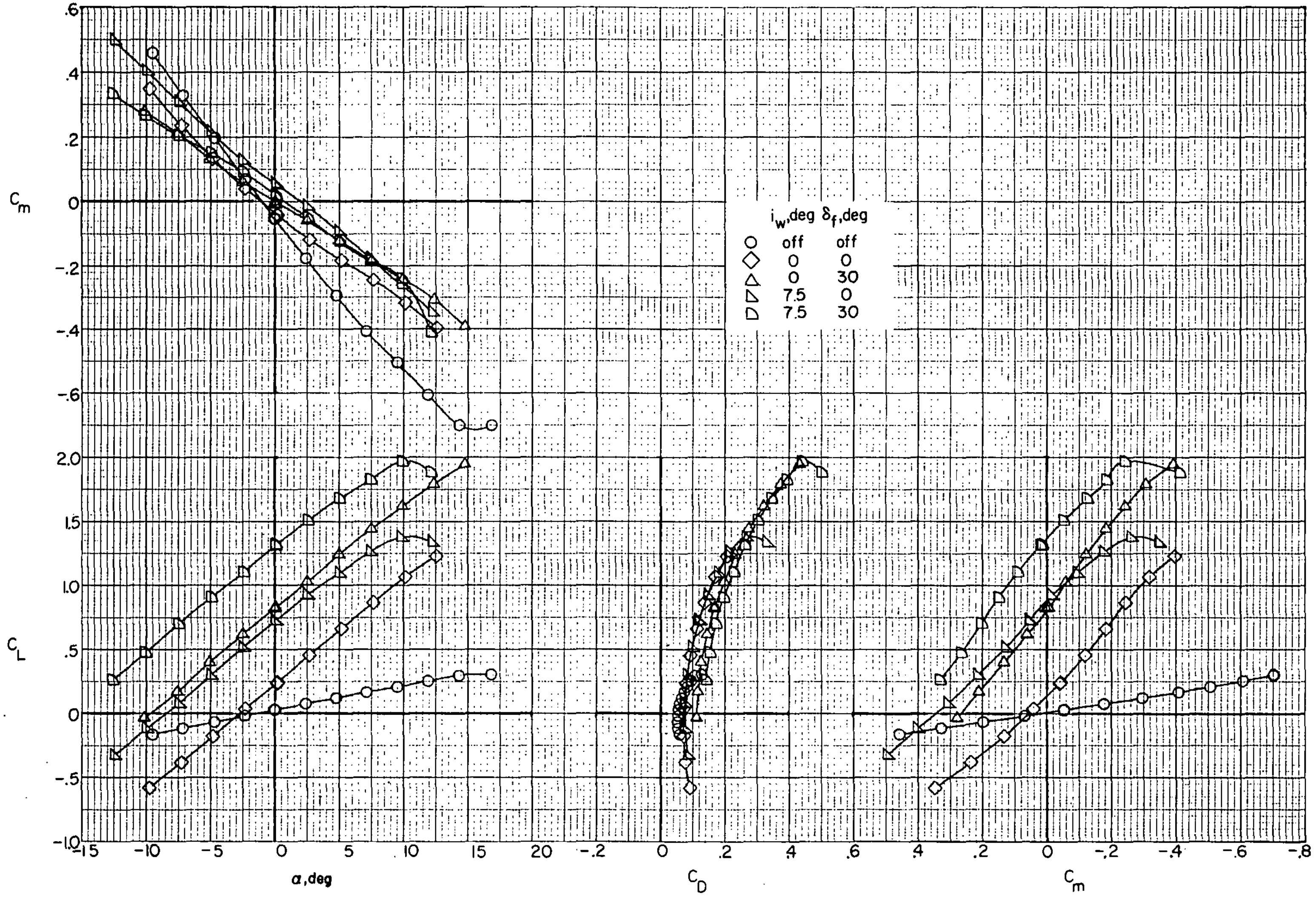

(b) Empennage on and jets removed ($F_1W_xVH_C$).

Figure 10.- Continued.

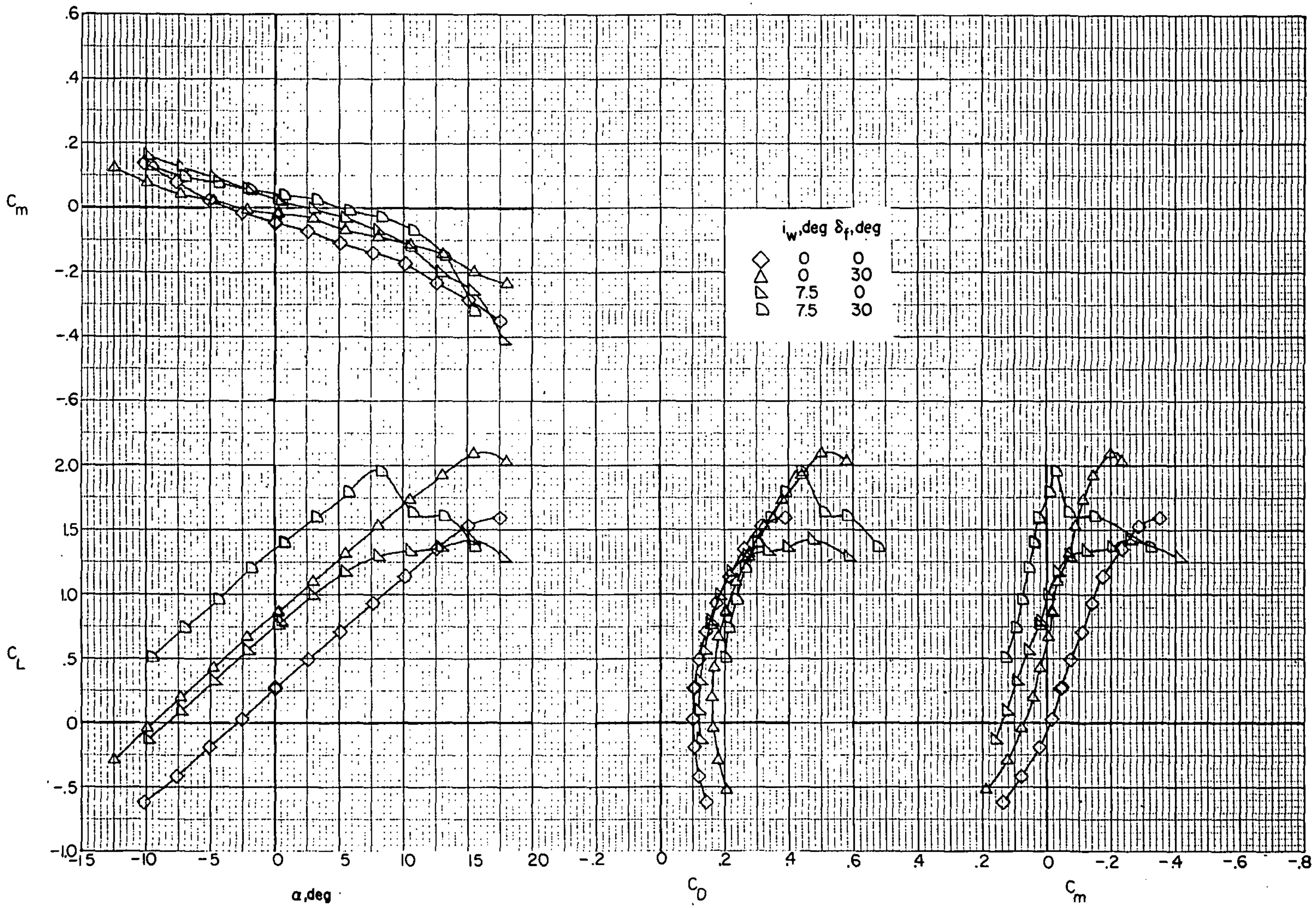

(c) Empennage and jets on $(F_1W_xVH_CJ_2)$. $C_{T,J} \approx 0$.

Figure 10.- Continued.

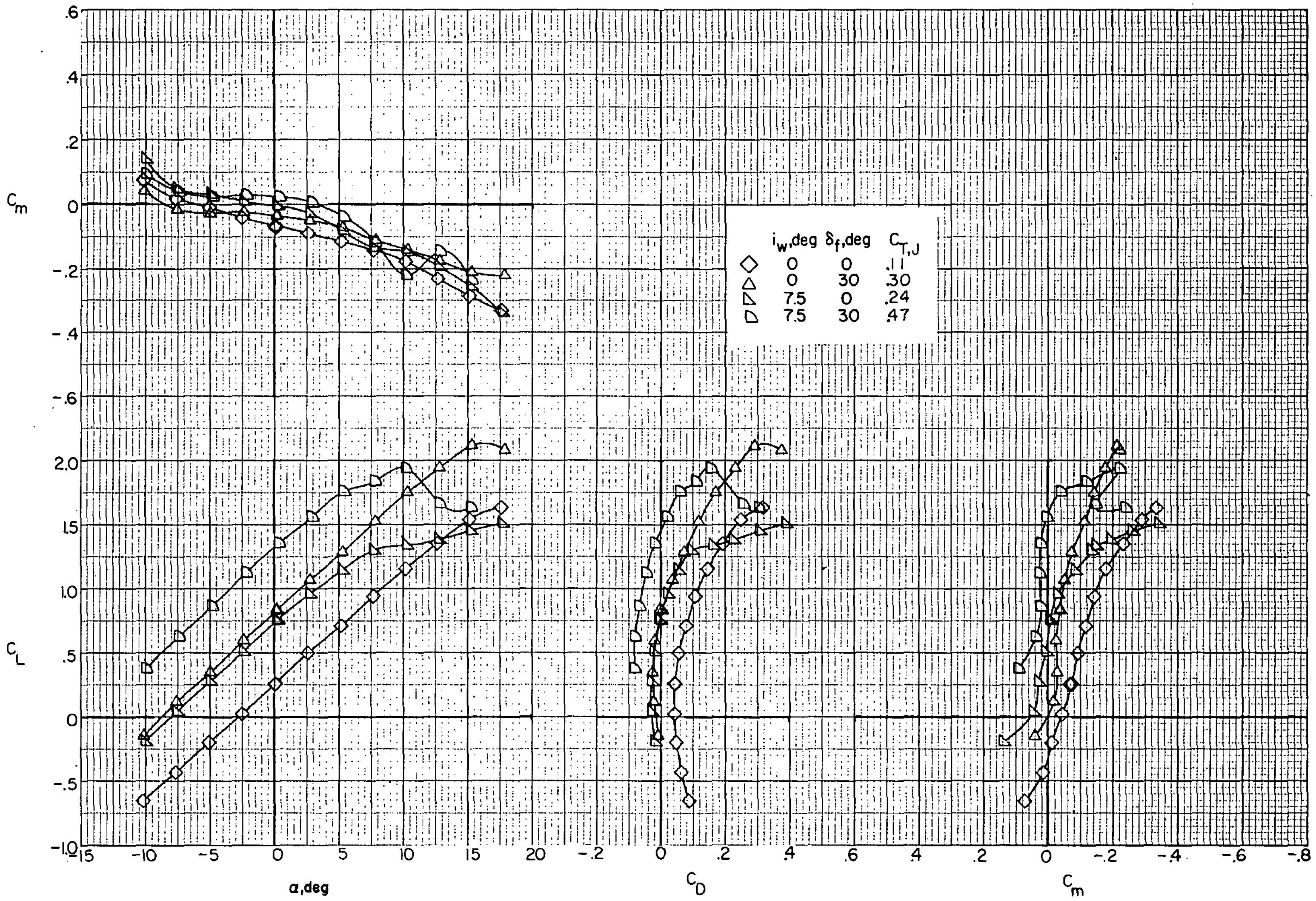

(d) Empennage and jets on $(F_1W_xVH_CJ_2)$. Trim thrust.

Figure 10.- Concluded.

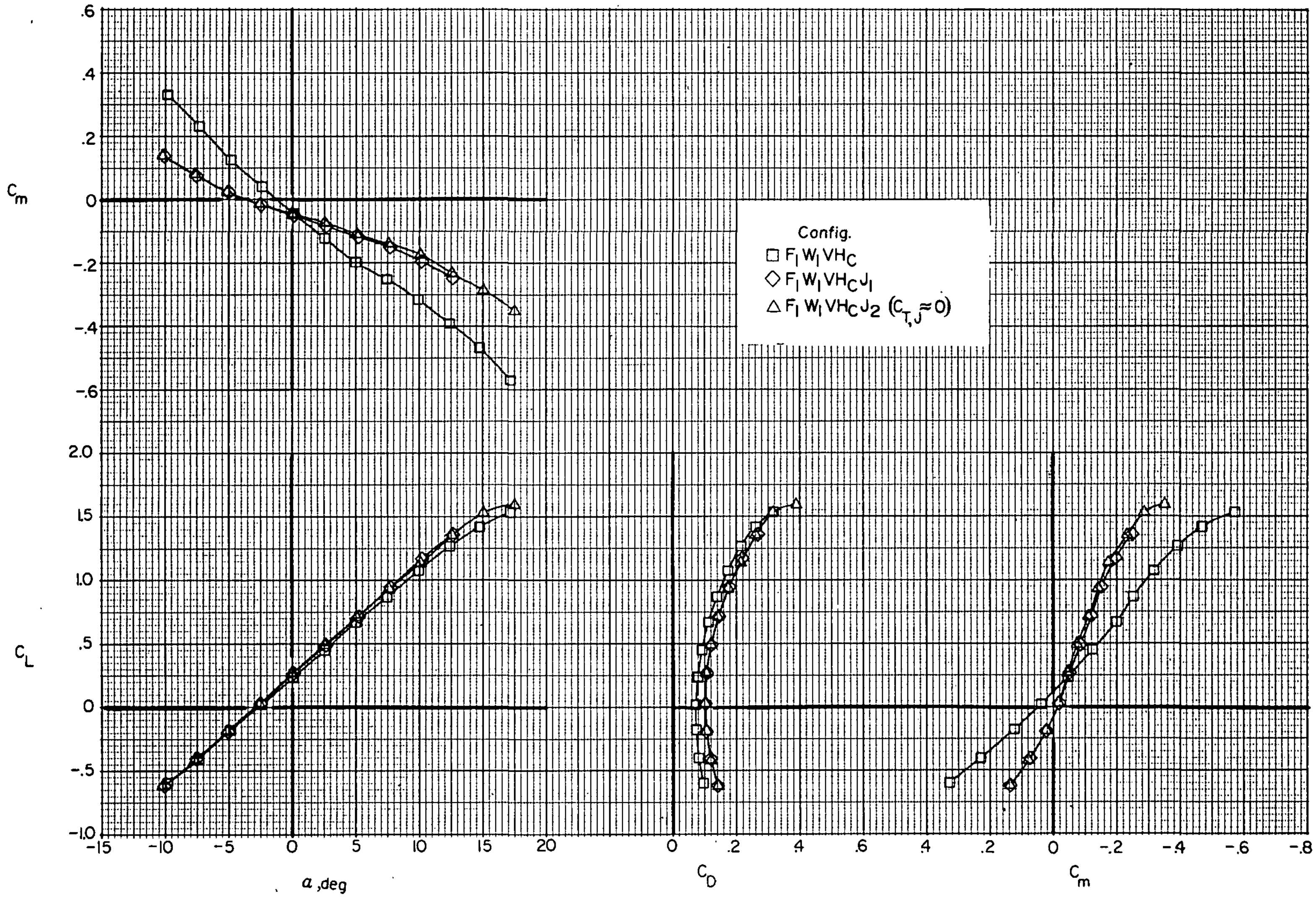

Figure 11.- Effect of auxiliary thrust engine nacelles on airframe longitudinal aerodynamics.

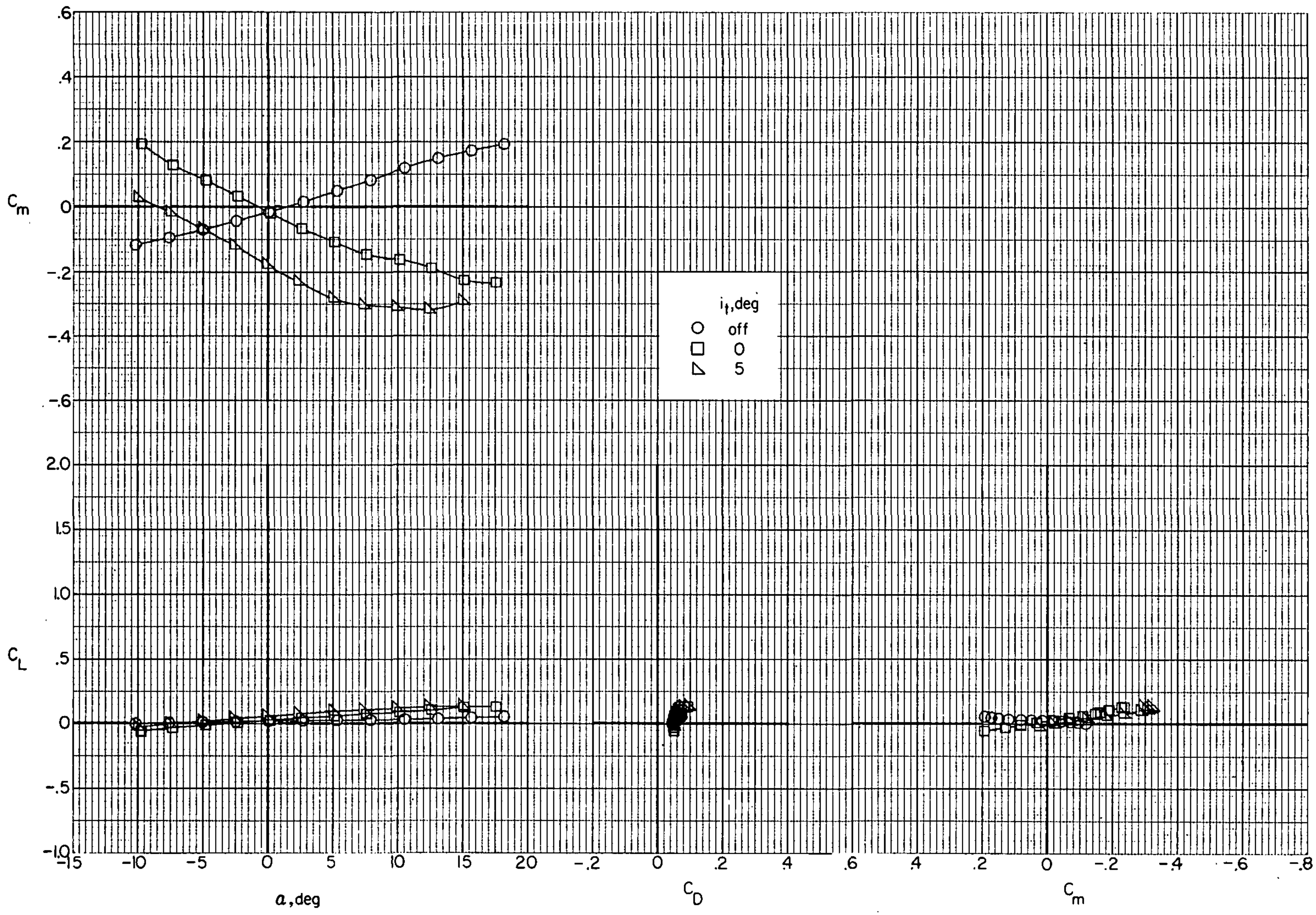

(a) Helicopter tail ($F_1 VH_H$).

Figure 12. - Effect of horizontal-tail incidence on airframe longitudinal aerodynamics.

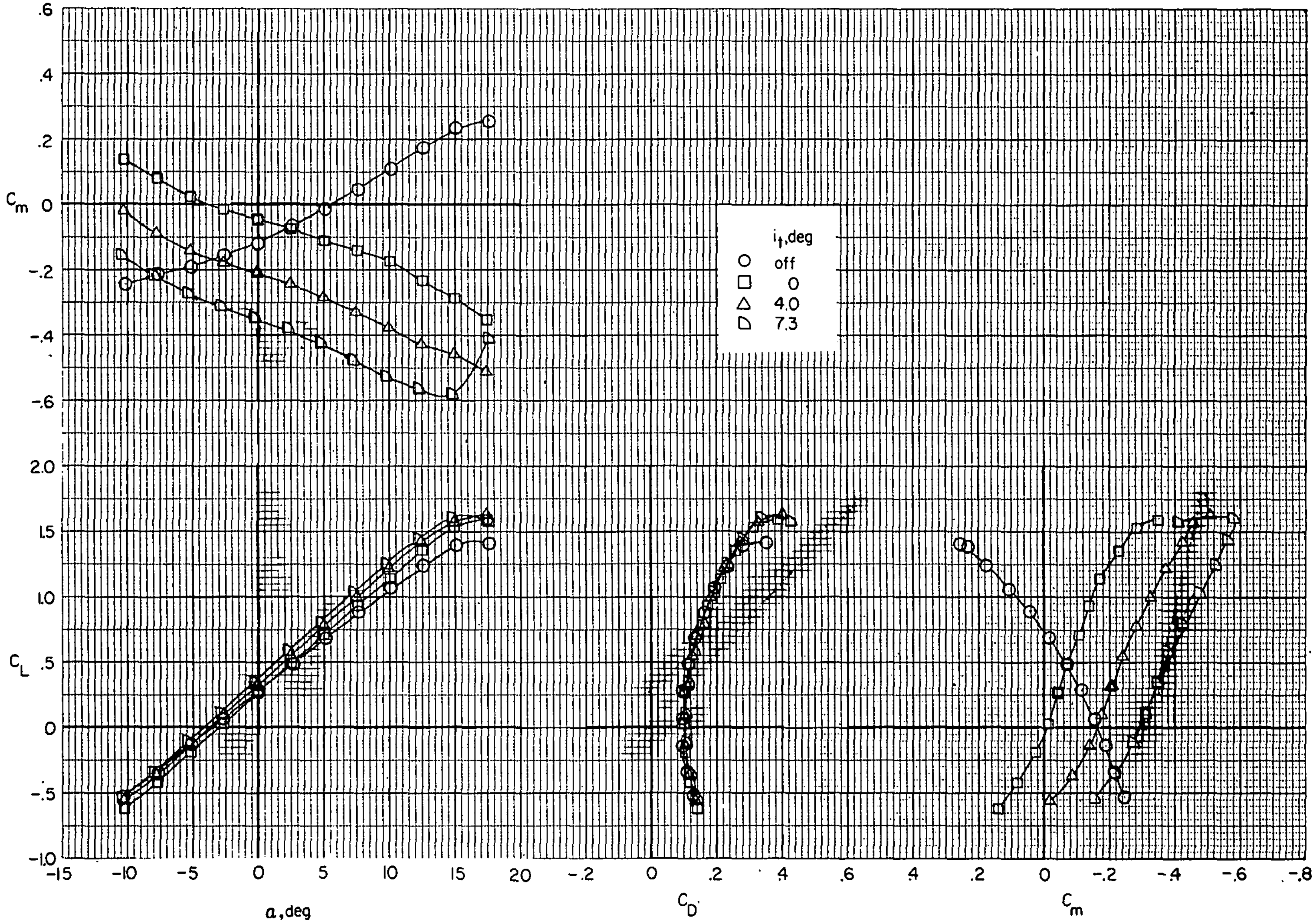

(b) Compound tail ($F_1 W_1 VH_C J_2$). $C_{T,J} \approx 0$.

Figure 12. - Continued.

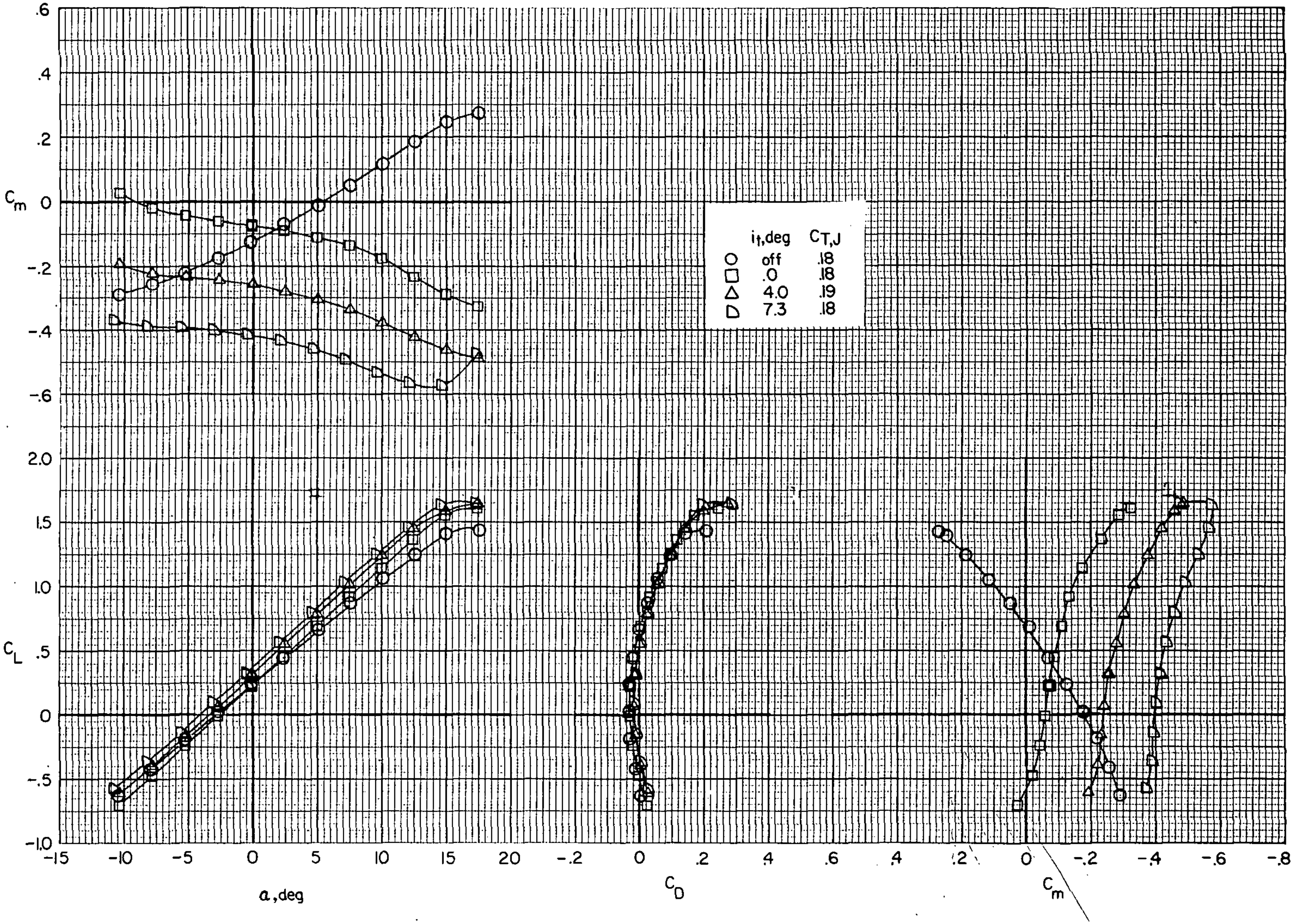

(c) Compound tail ($F_1W_1VH_CJ_2$). Trim thrust.

Figure 12.- Concluded.

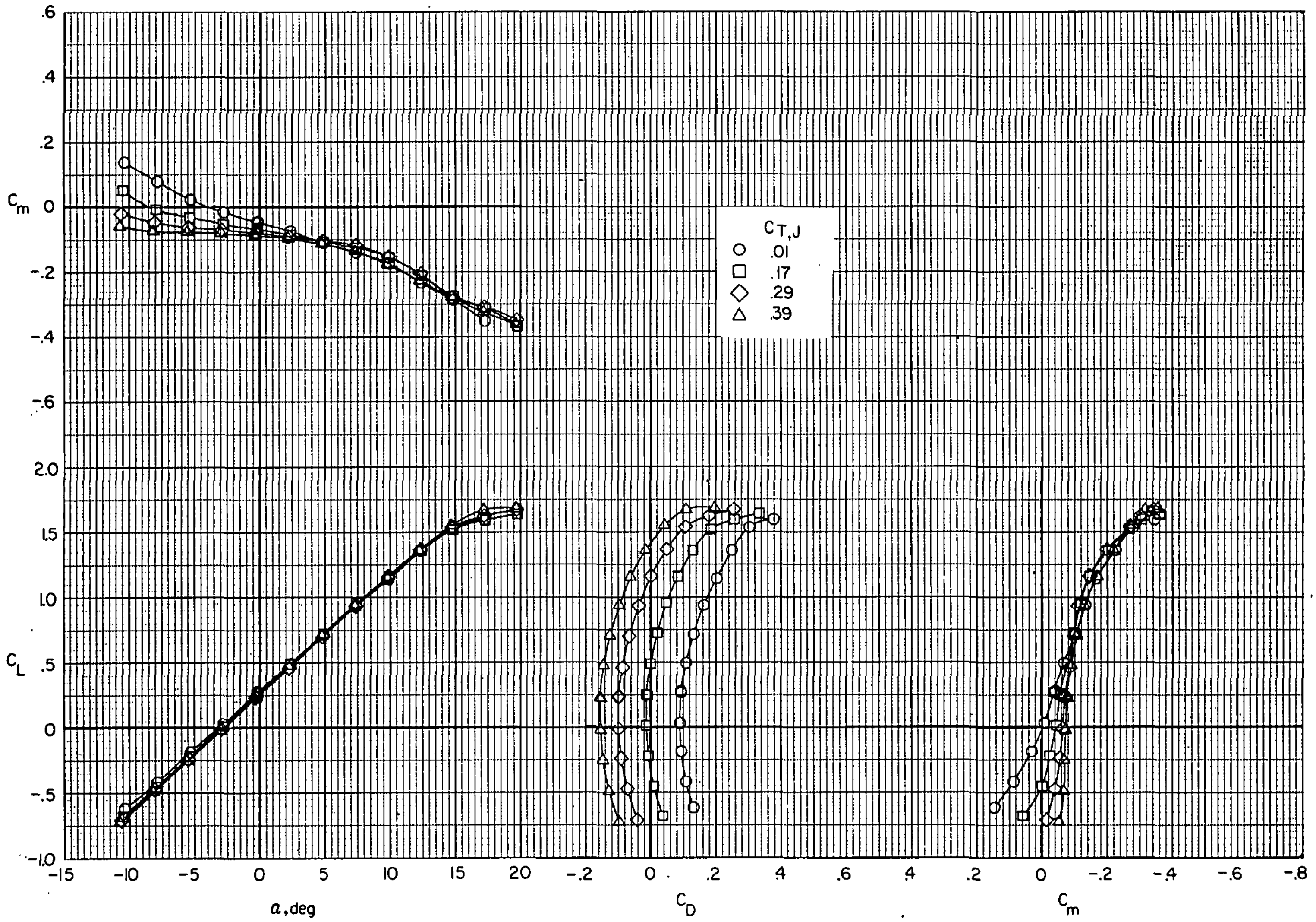

(a) $i_w = 0^o$; $\delta_f = 0^o$.

Figure 13.- Effect of auxiliary thrust coefficient on longitudinal aerodynamics of configuration $F_1W_xVH_CJ_2$. $i_t = 0^o$.

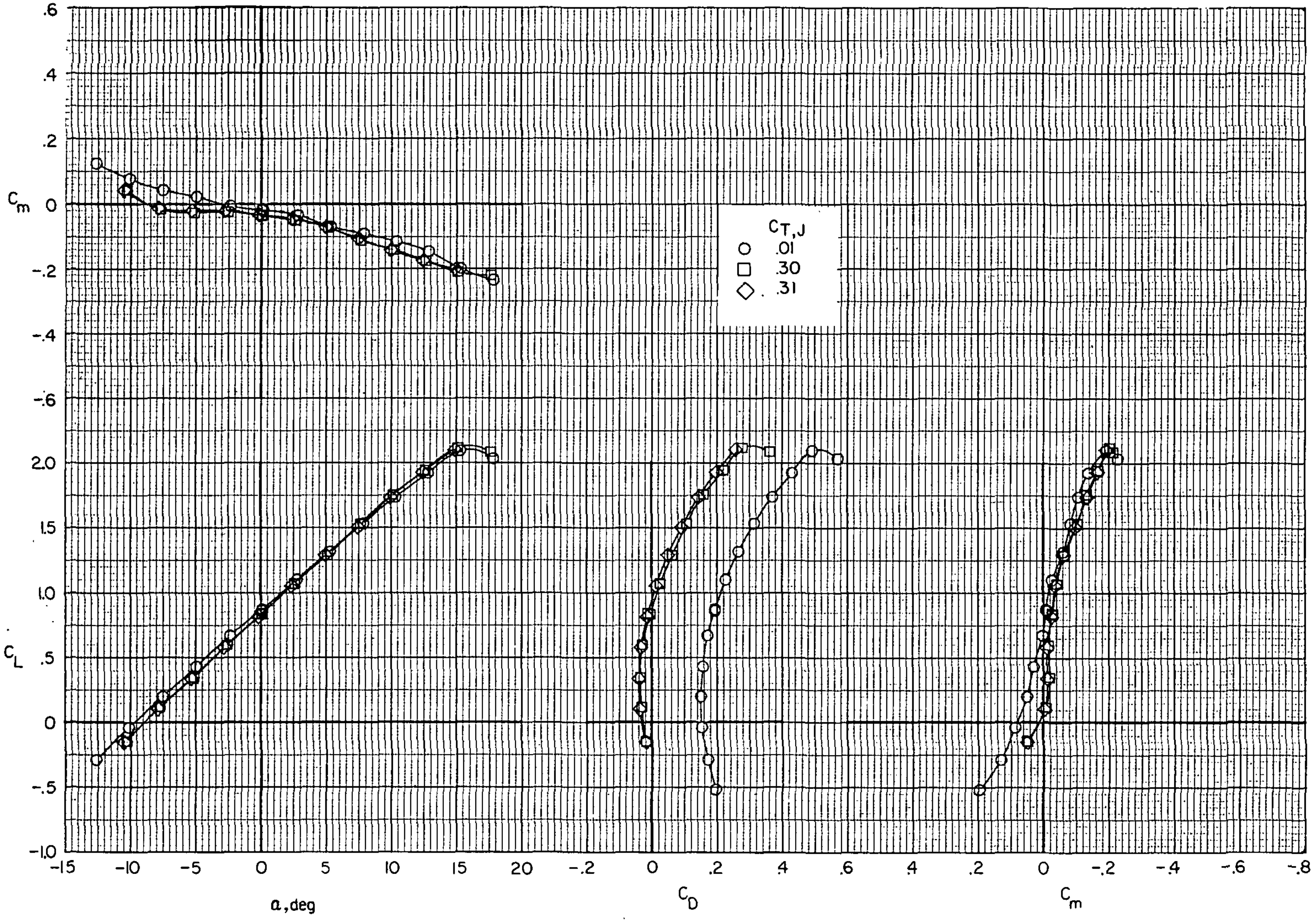

(b) $i_w = 0^o$; $\delta_f = 30^o$.

Figure 13.- Continued.

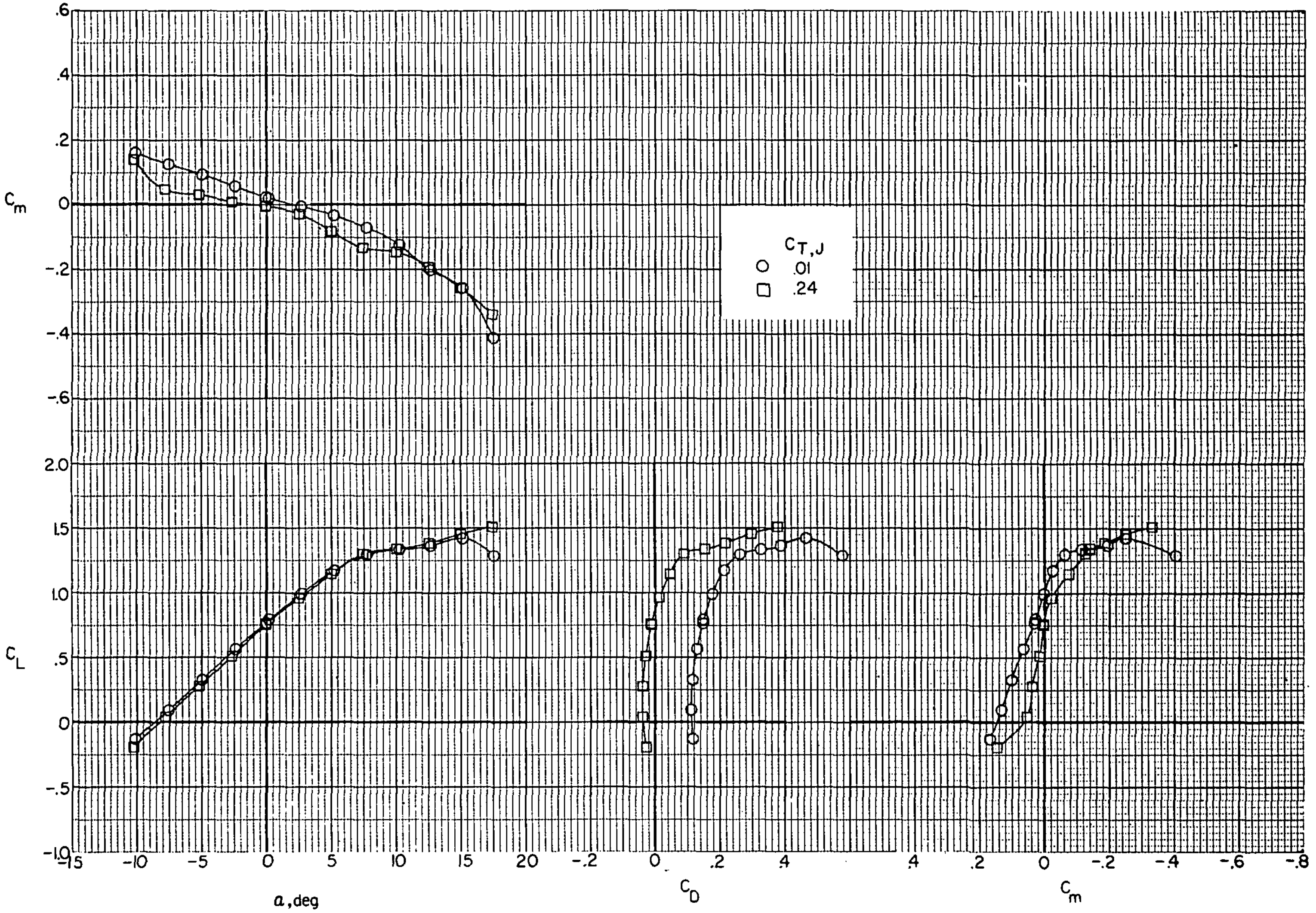

(c) $i_w = 7.5^\circ$; $\delta_f = 0^\circ$.

Figure 13. - Continued.

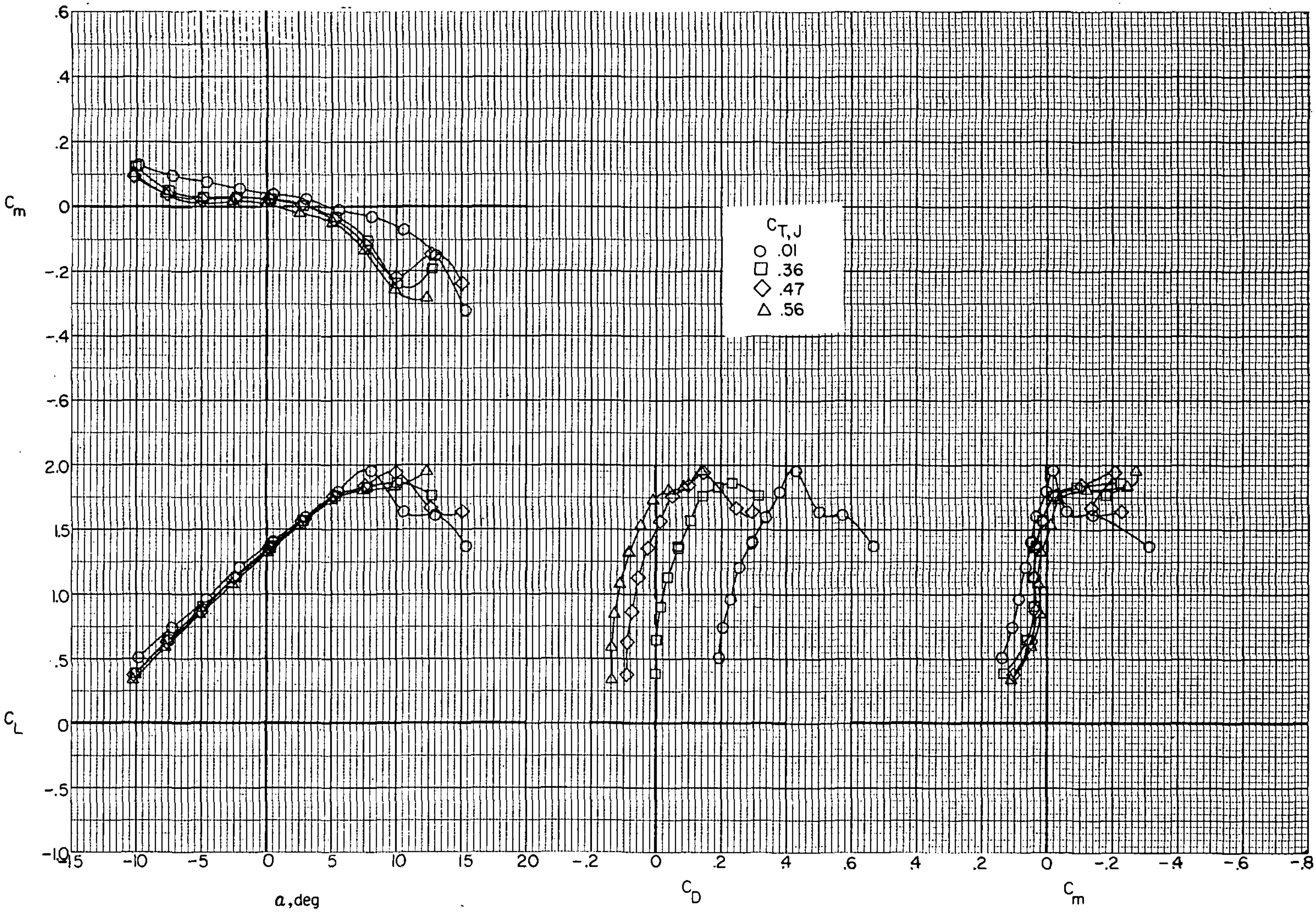

(d) $i_w = 7.5^\circ$; $\delta_f = 30^\circ$.

Figure 13.- Concluded.

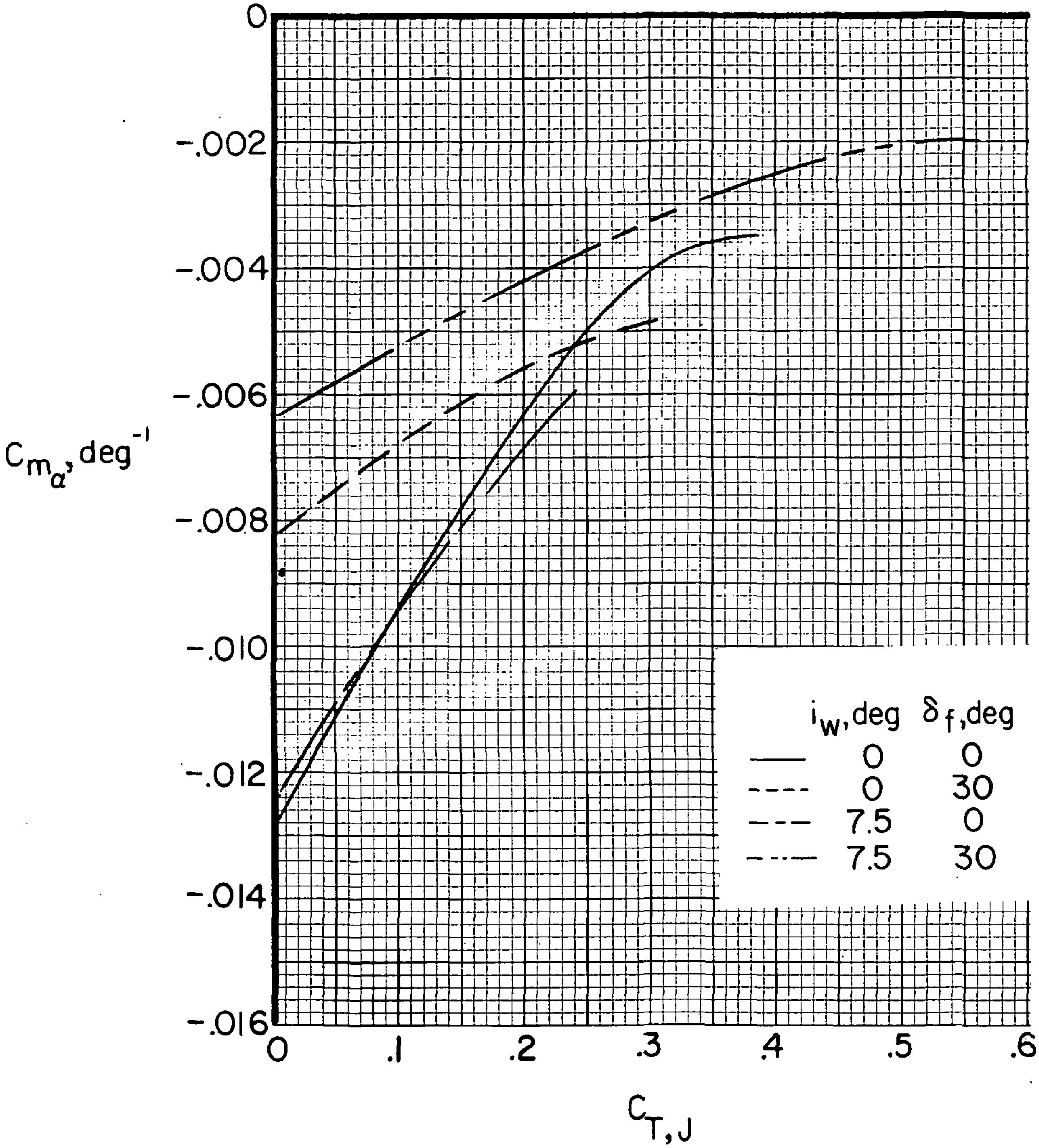

Figure 14.- Effect of auxiliary engine thrust on airframe static longitudinal stability of $F_1W_xVH_CJ_2$.

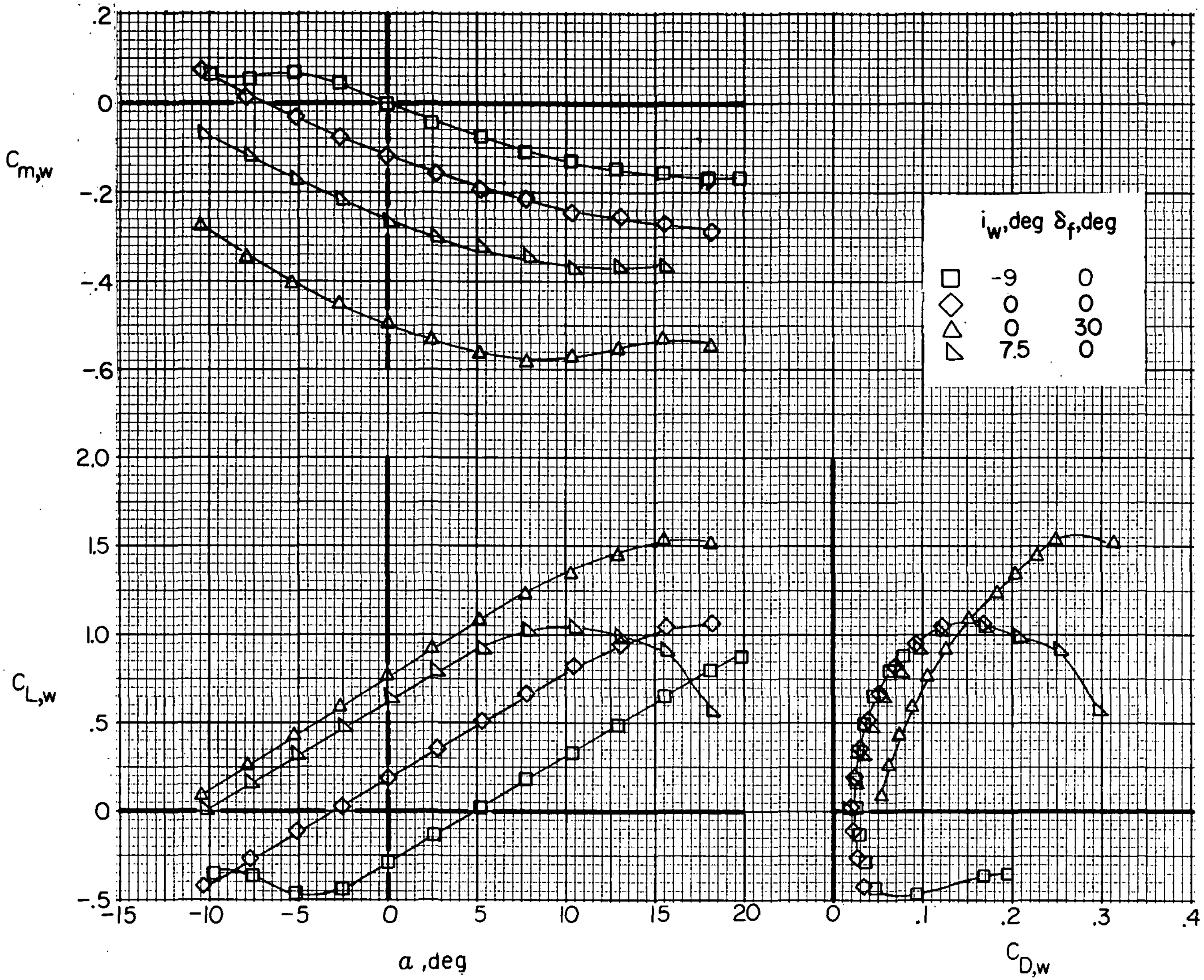

(a) Jets removed (F_1W_x).

Figure 15.- Effect of wing incidence and flap deflection on wing longitudinal aerodynamics.

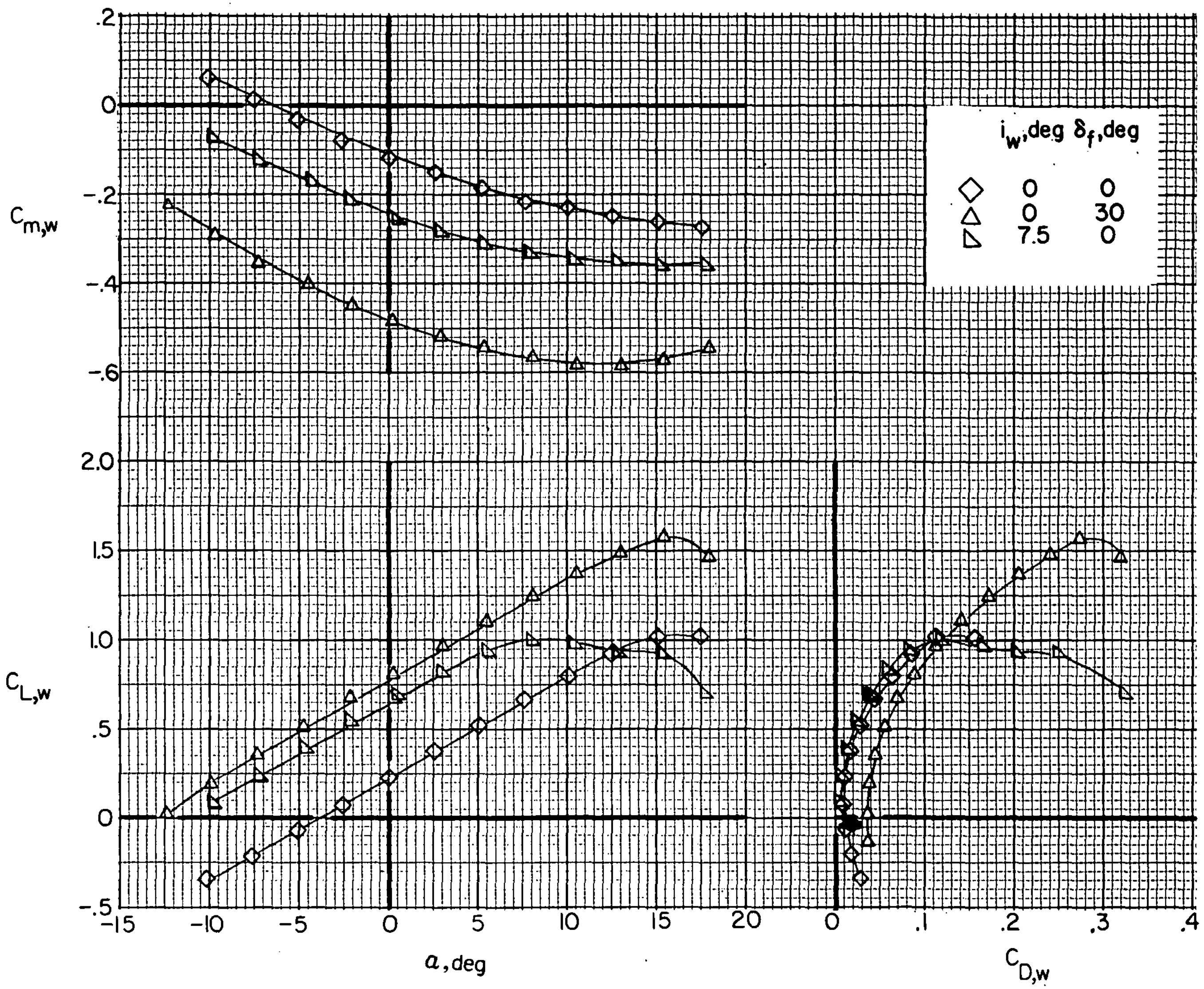

(b) Jets on ($F_1W_xVH_CJ_2$). $C_{T,J} \approx 0$.

Figure 15.- Concluded.

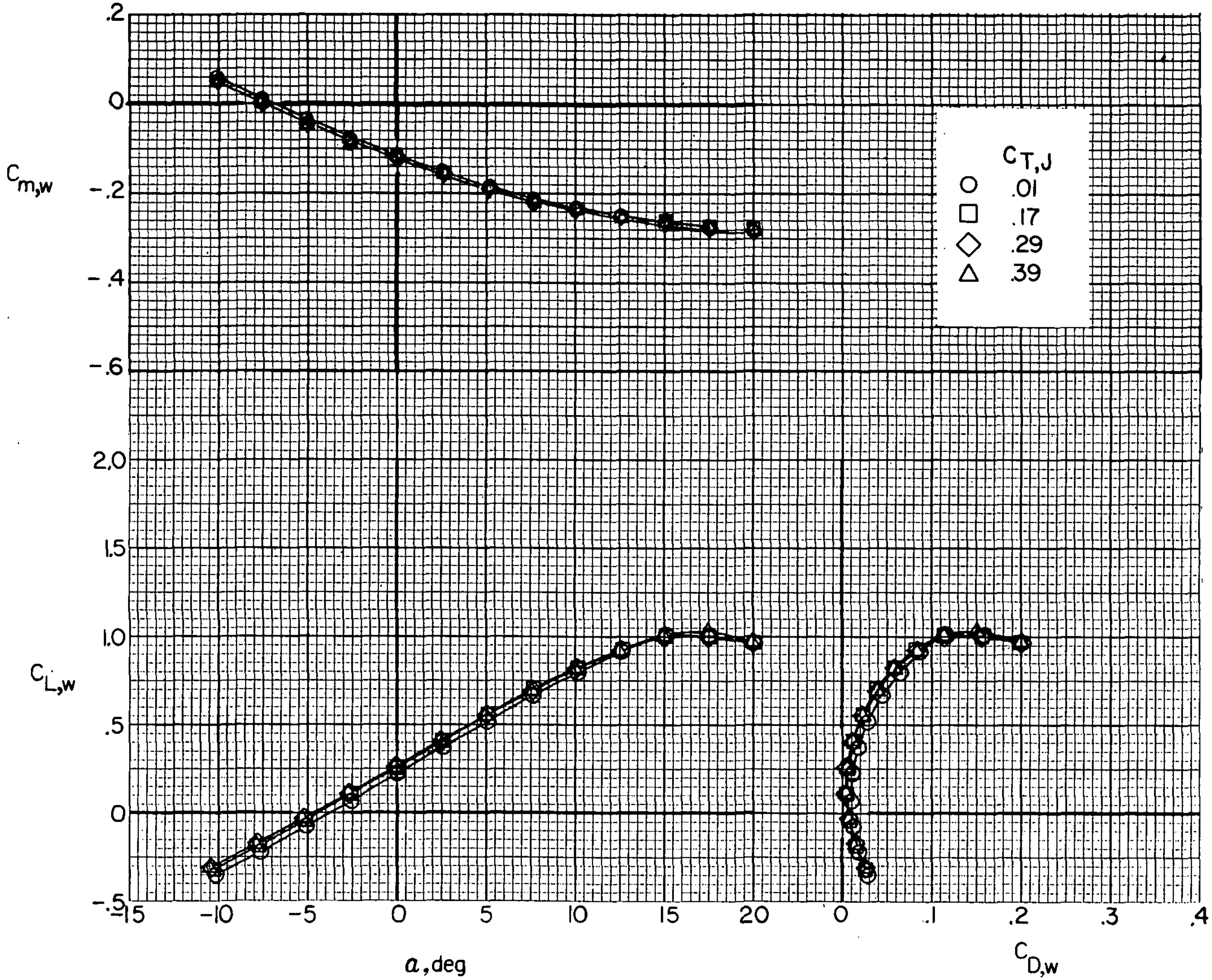

(a) $i_w = 0^{\circ}$; $\delta_f = 0^{\circ}$.

Figure 16.- Effect of auxiliary engine thrust on wing longitudinal aerodynamics.

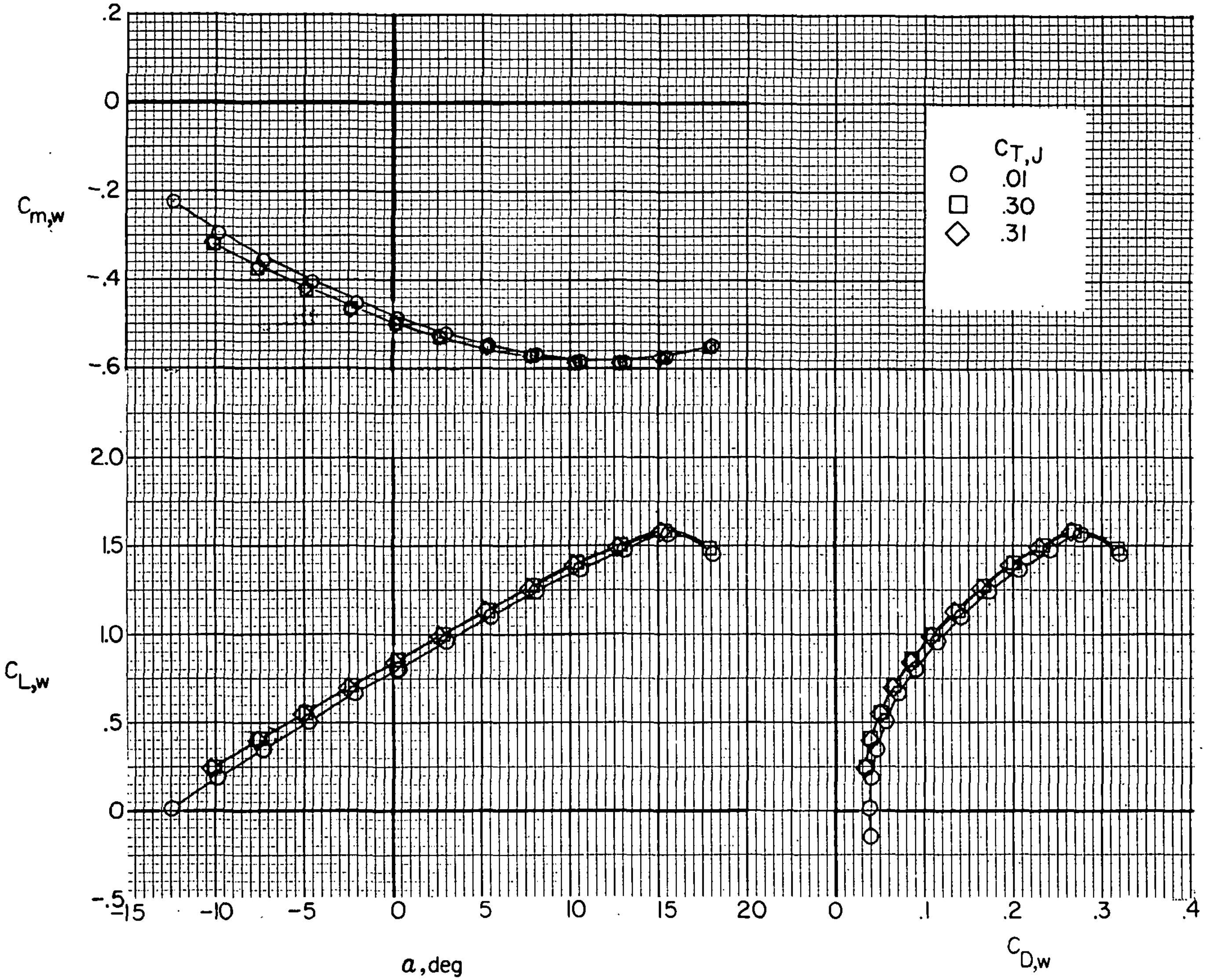

(b) $i_w = 0^o$; $\delta_f = 30^o$.

Figure 16.- Continued.

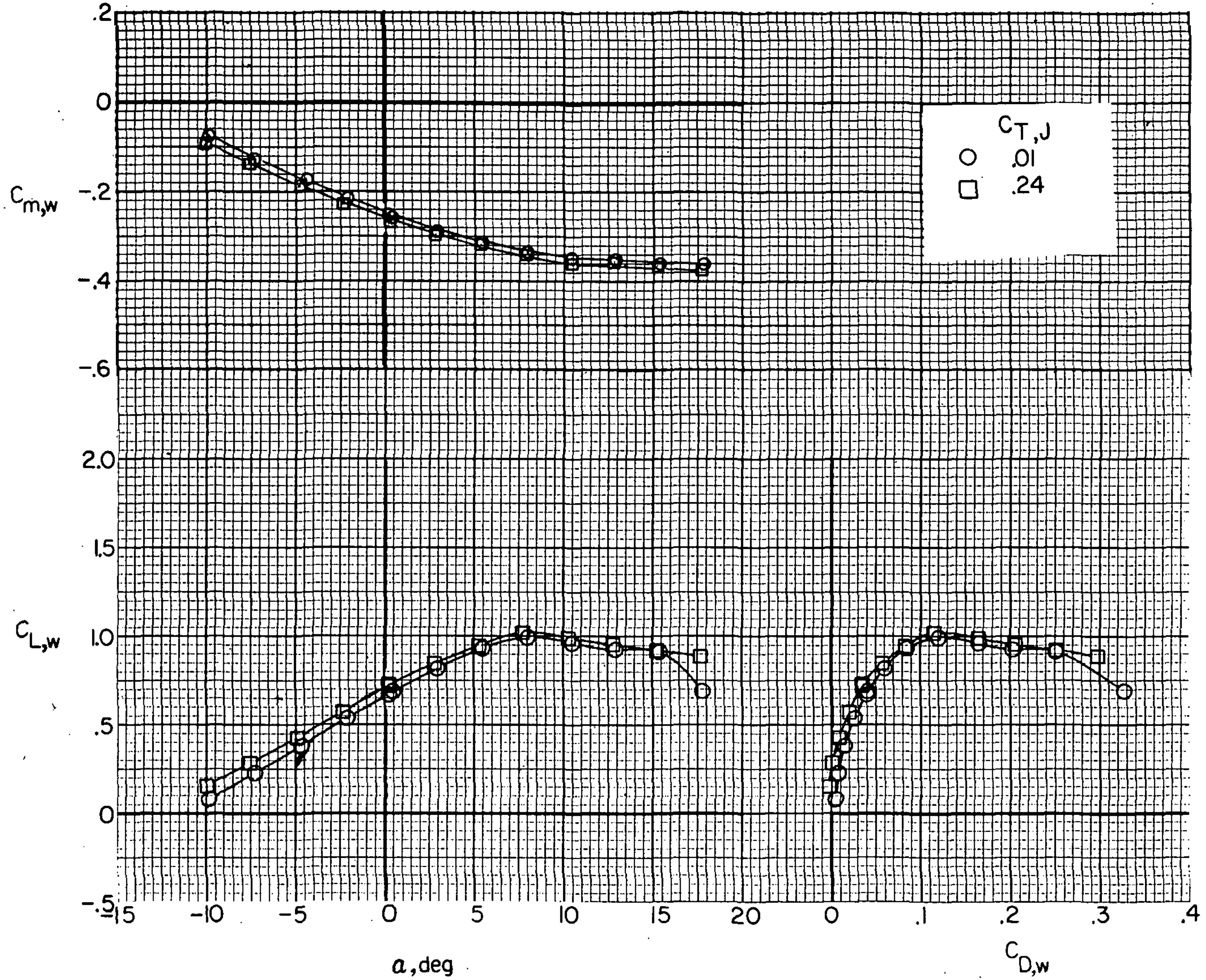

(c) $i_W = 7.5^{\circ}$; $\delta_f = 0^{\circ}$.

Figure 16.- Continued.

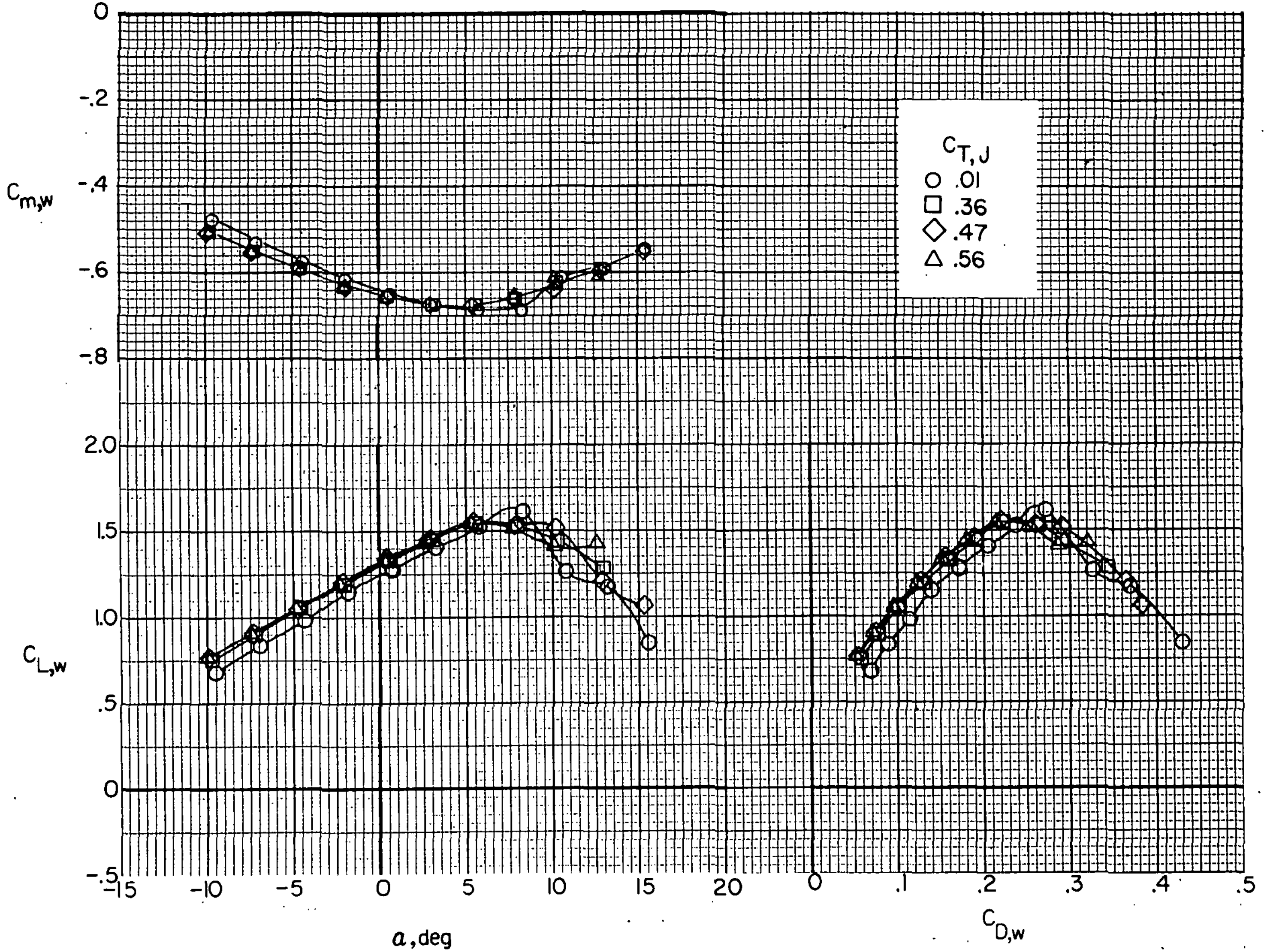

(d) $i_w = 7.5^o$; $\delta_f = 30^o$.

Figure 16.- Concluded.

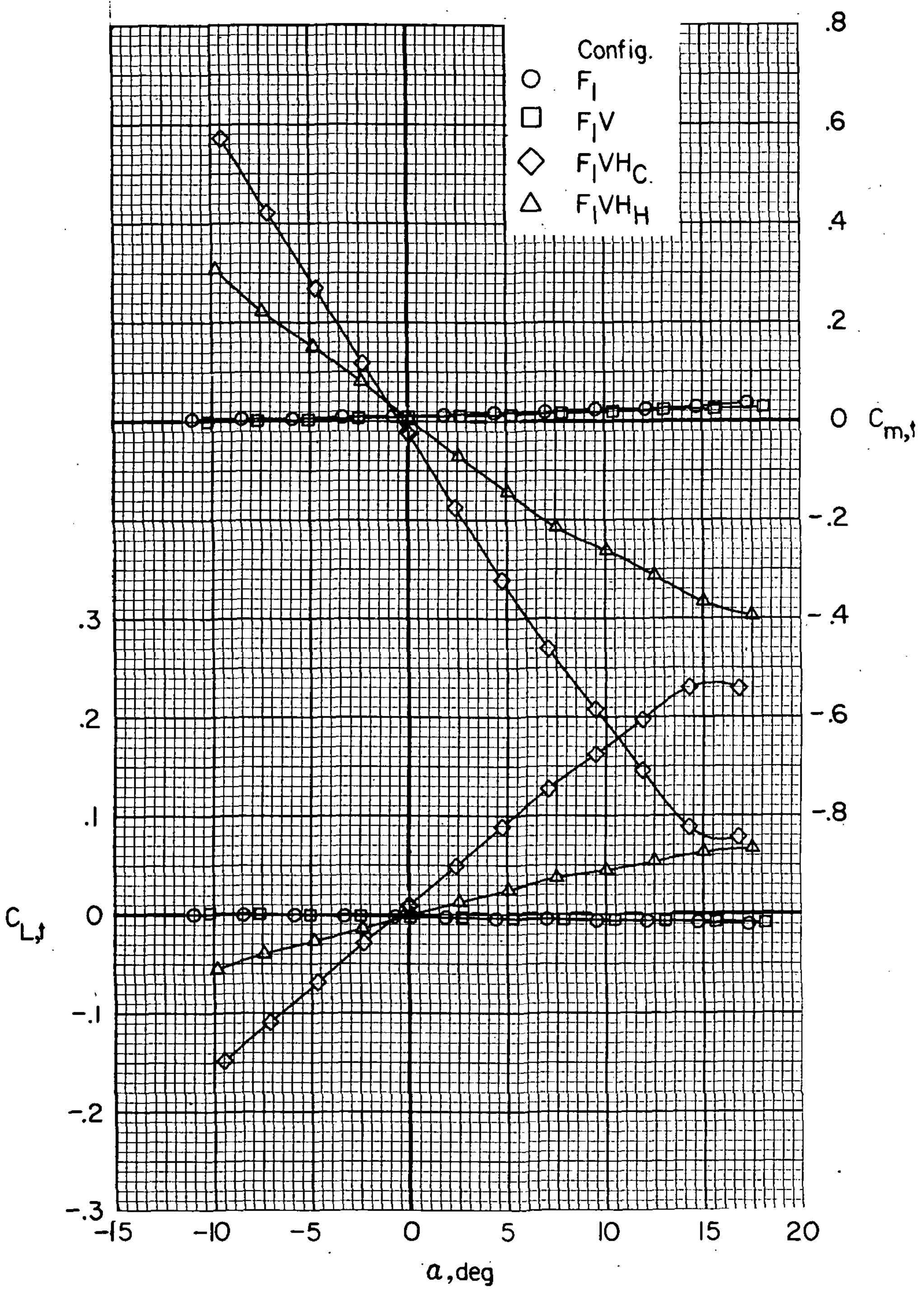

Figure 17.- Effect of empennage components on tail longitudinal aerodynamics with wing and jets removed. $i_t = 0^{\circ}$.

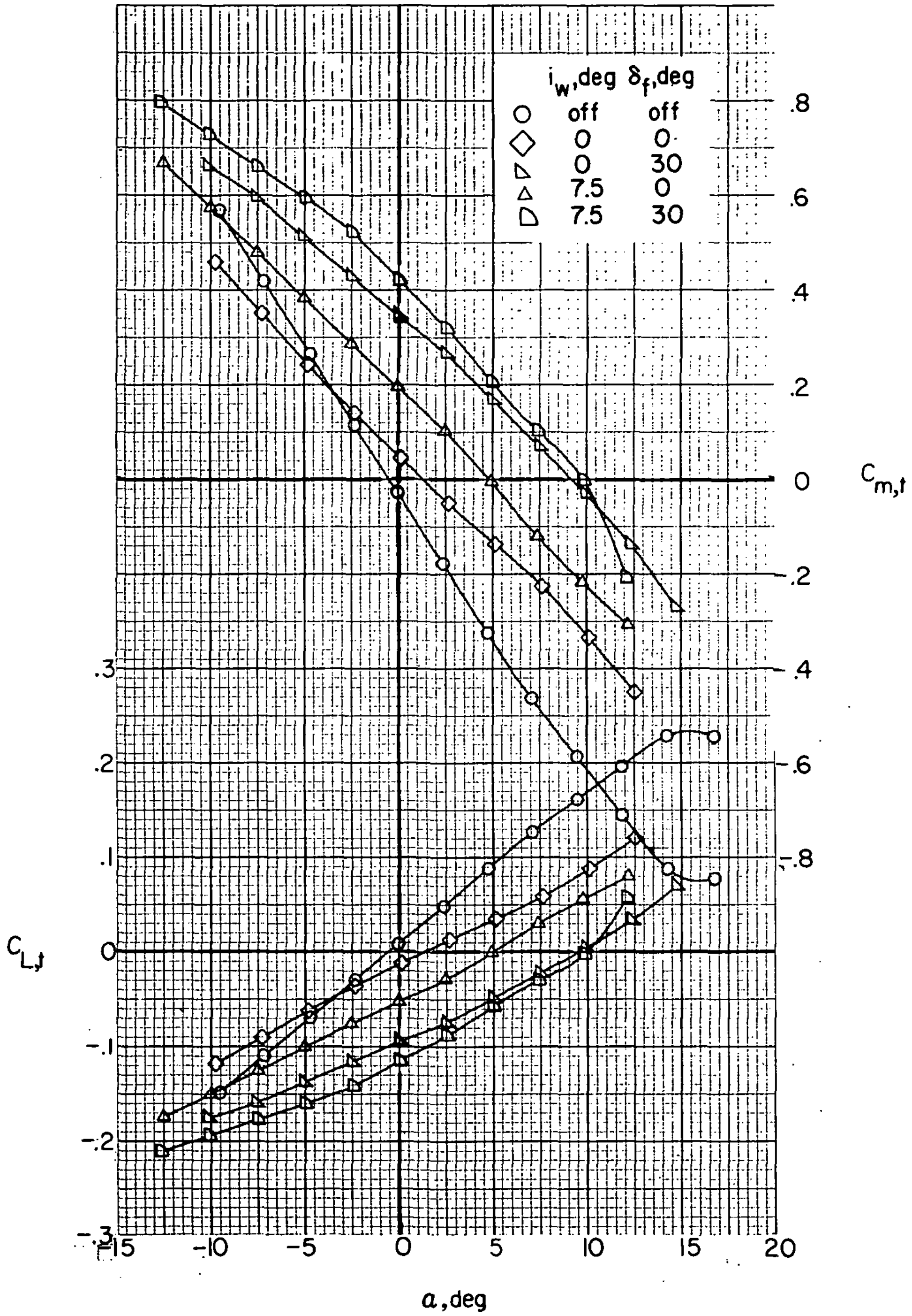

(a) Jets removed.

Figure 18.- Effect of wing incidence and flap deflection on tail longitudinal aerodynamics. $i_t = 0^o$.

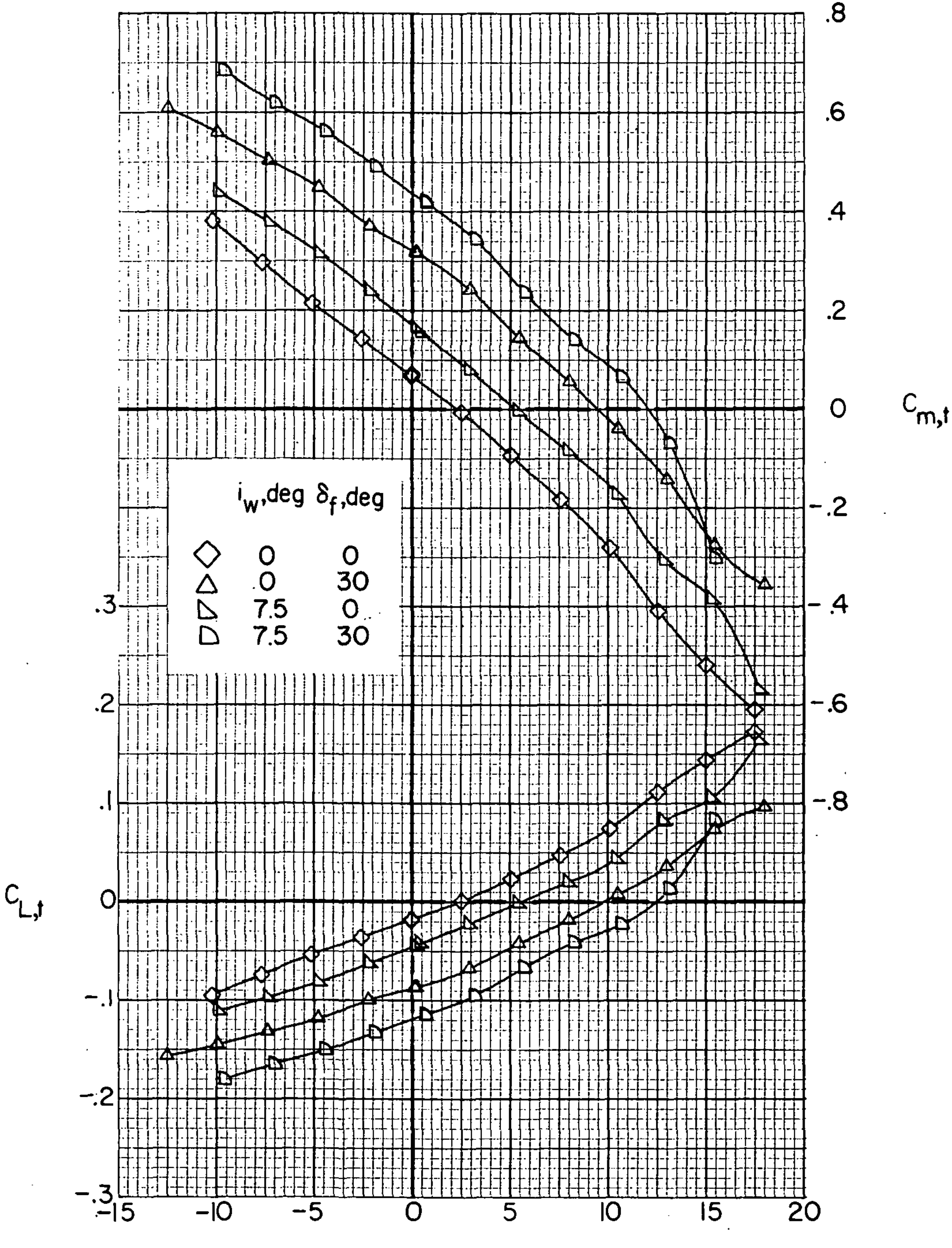

(b) Jets on; $C_{T,J} \approx 0$.

Figure 18.- Continued.

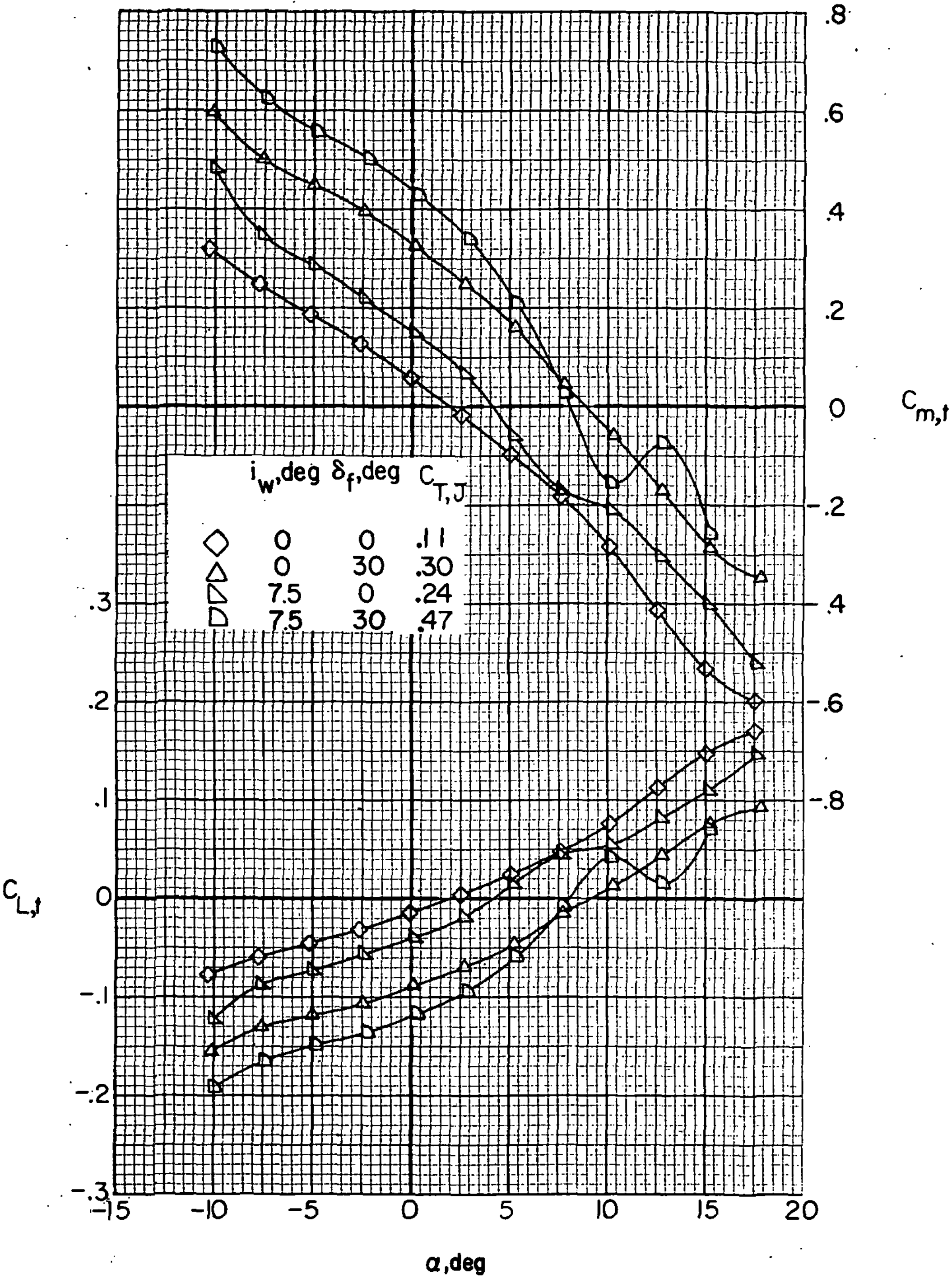

(c) Jets on; trim thrust.

Figure 18.- Concluded.

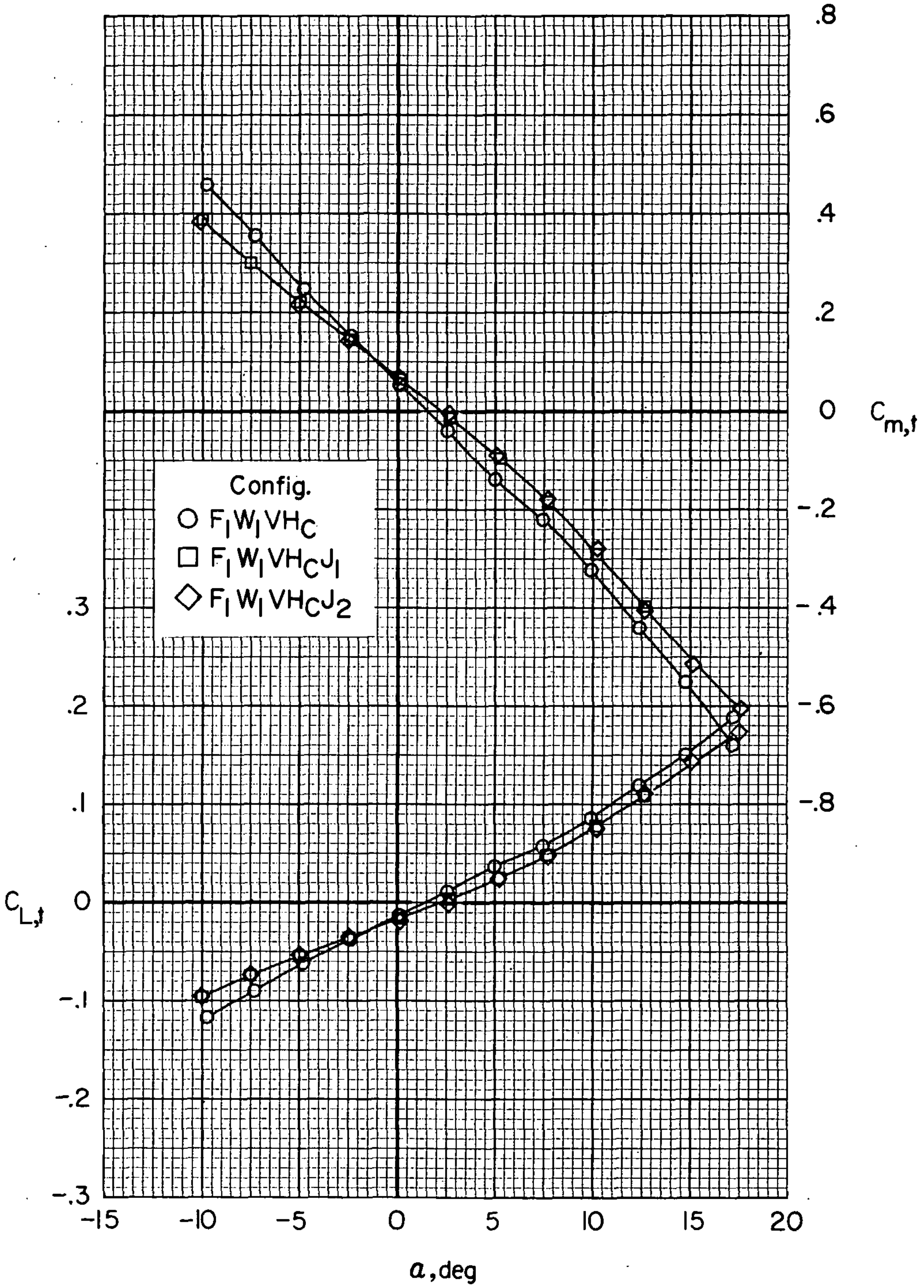

Figure 19.- Effect of auxiliary thrust engine nacelles on tail longitudinal aerodynamics. $i_w = 0^o$; $\delta_f = 0^o$; $i_t = 0^o$; $C_{T,J} \approx 0$.

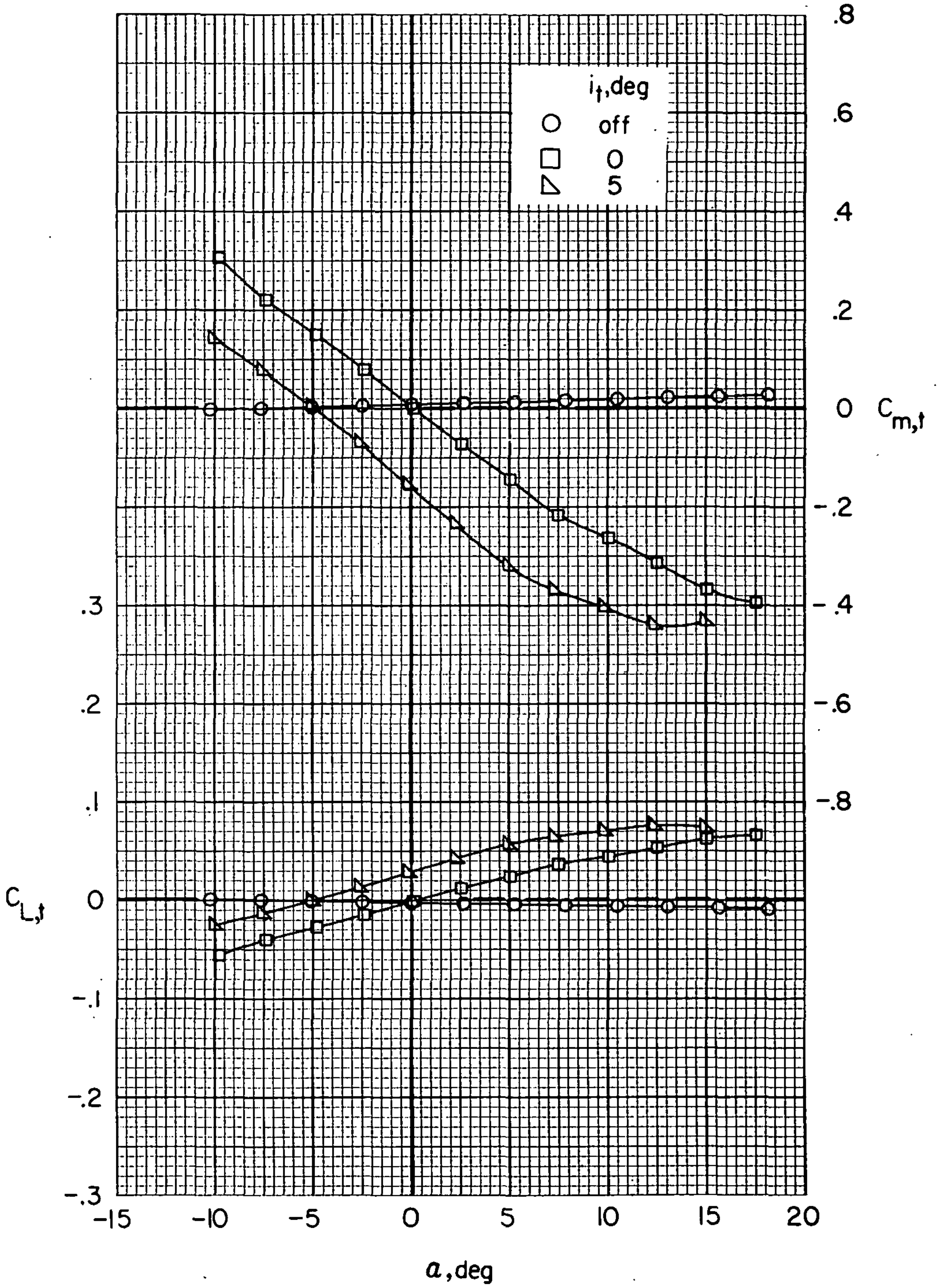

(a) Helicopter tail (F_1VH_H).

Figure 20.- Effect of horizontal-tail incidence on tail longitudinal aerodynamics.

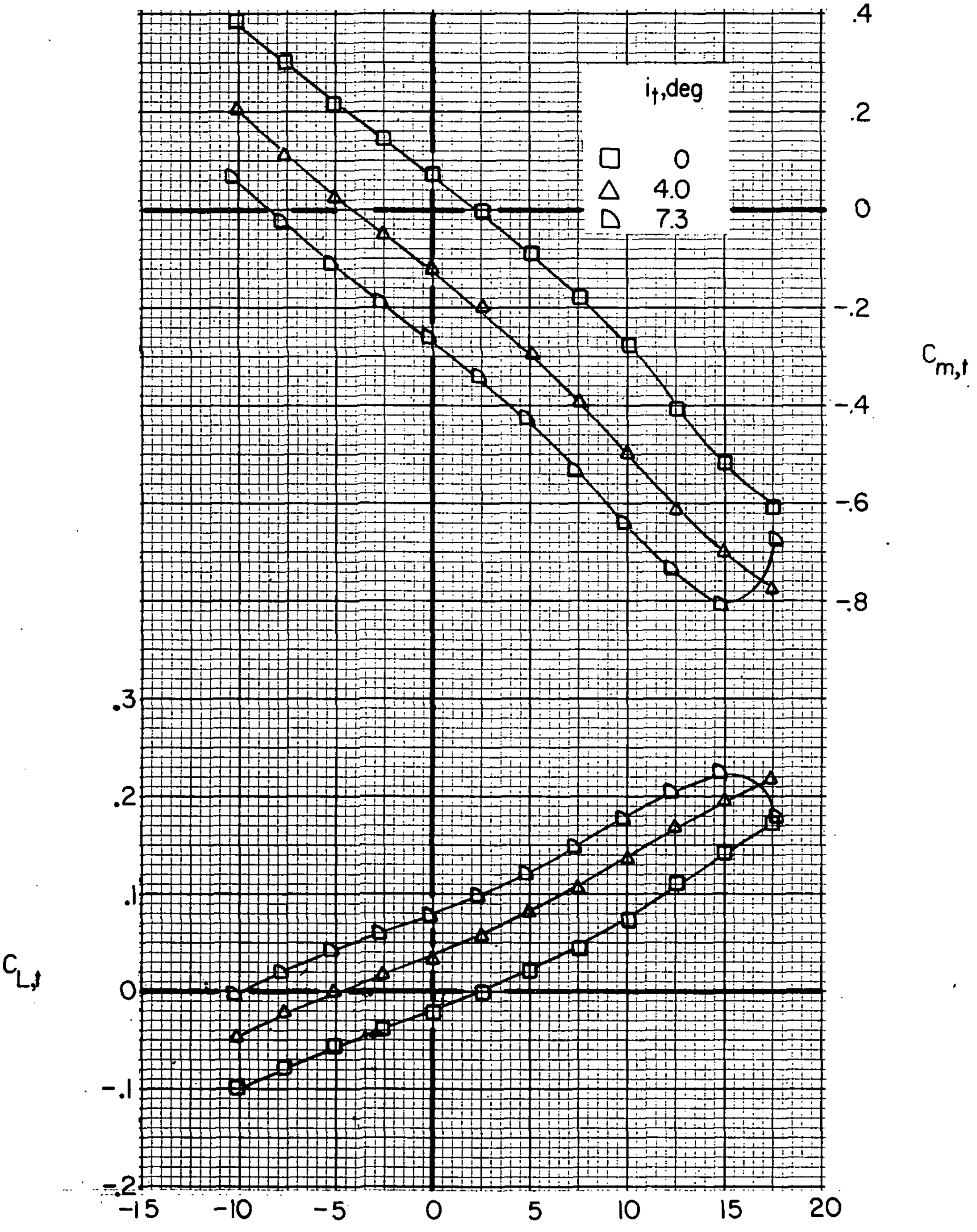

(b) Compound tail ($F_1W_1VH_CJ_2$). $C_{T,J} \approx 0$.

Figure 20.- Continued.

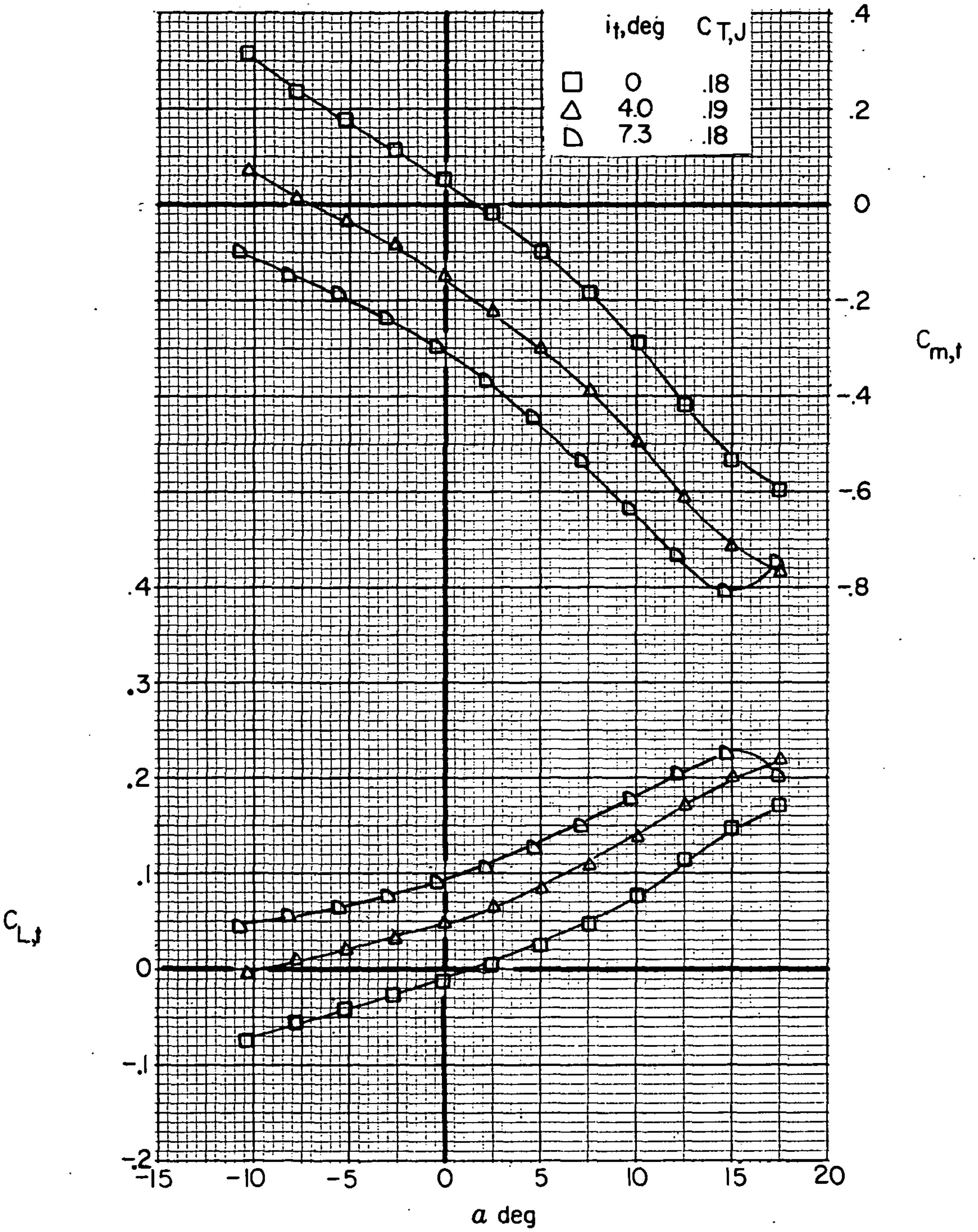

(c) Compound tail ($F_1W_1VH_CJ_2$). Trim thrust.

Figure 20.- Concluded.

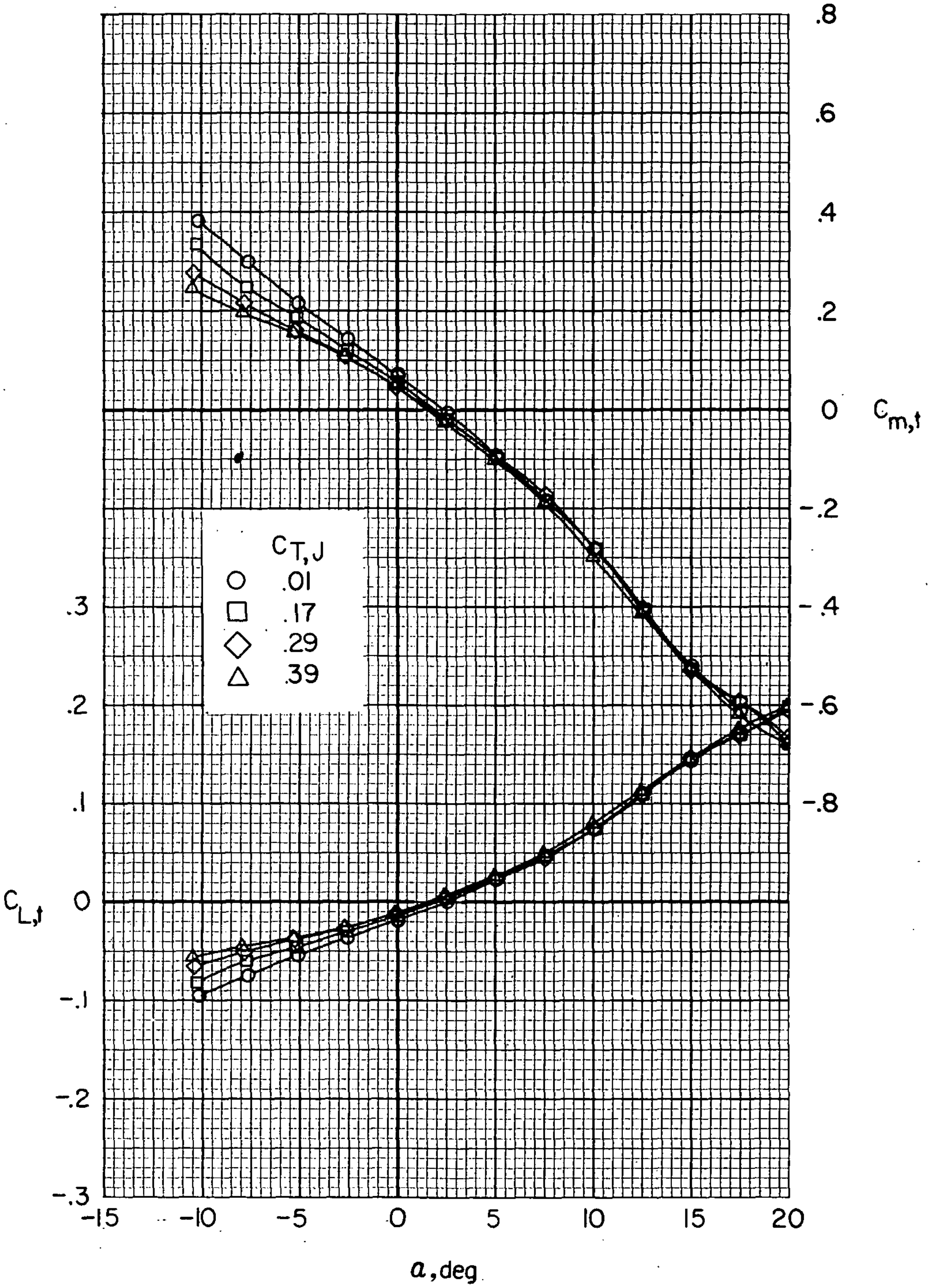

(a) $i_w = 0^{\circ}$; $\delta_f = 0^{\circ}$.

Figure 21. - Effect of auxiliary engine thrust coefficient on tail longitudinal aerodynamics. $i_t = 0^{\circ}$; $F_1W_xVH_CJ_2$.

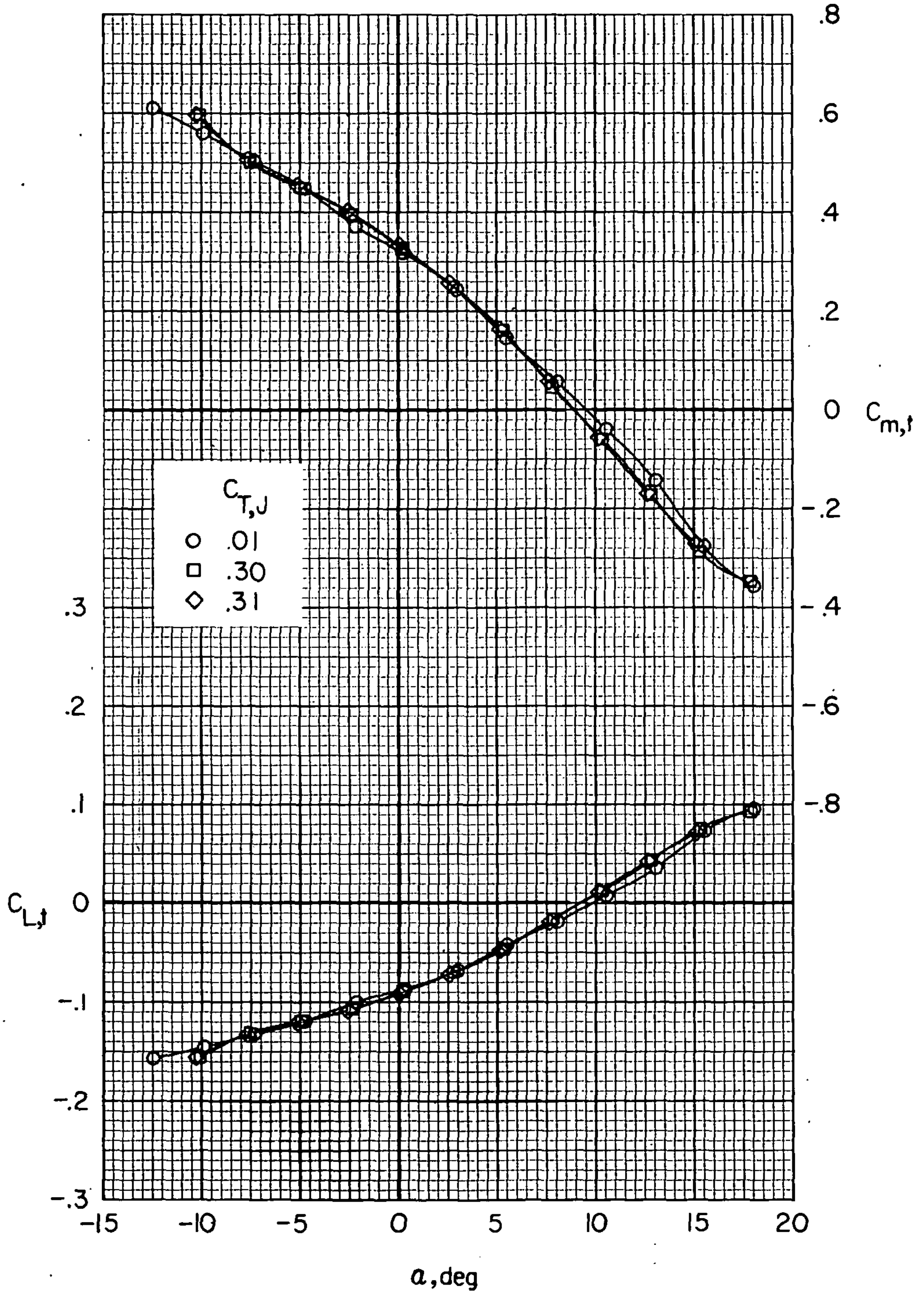

(b) $i_w = 0^{\circ}$; $\delta_f = 30^{\circ}$.

Figure 21.- Continued.

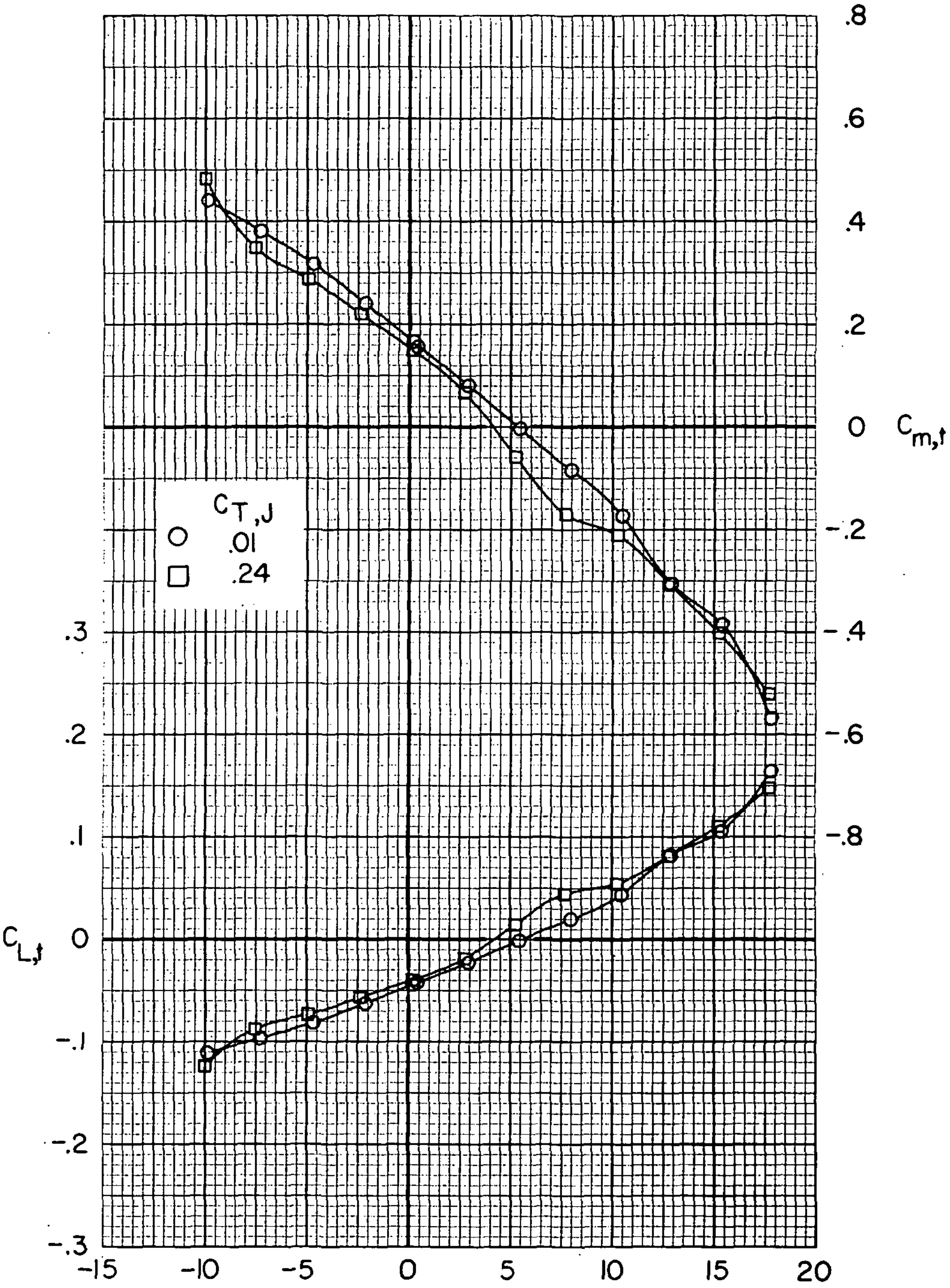

(c) $i_w = 7.5^{\circ}$; $\delta_f = 0^{\circ}$.

Figure 21.- Continued.

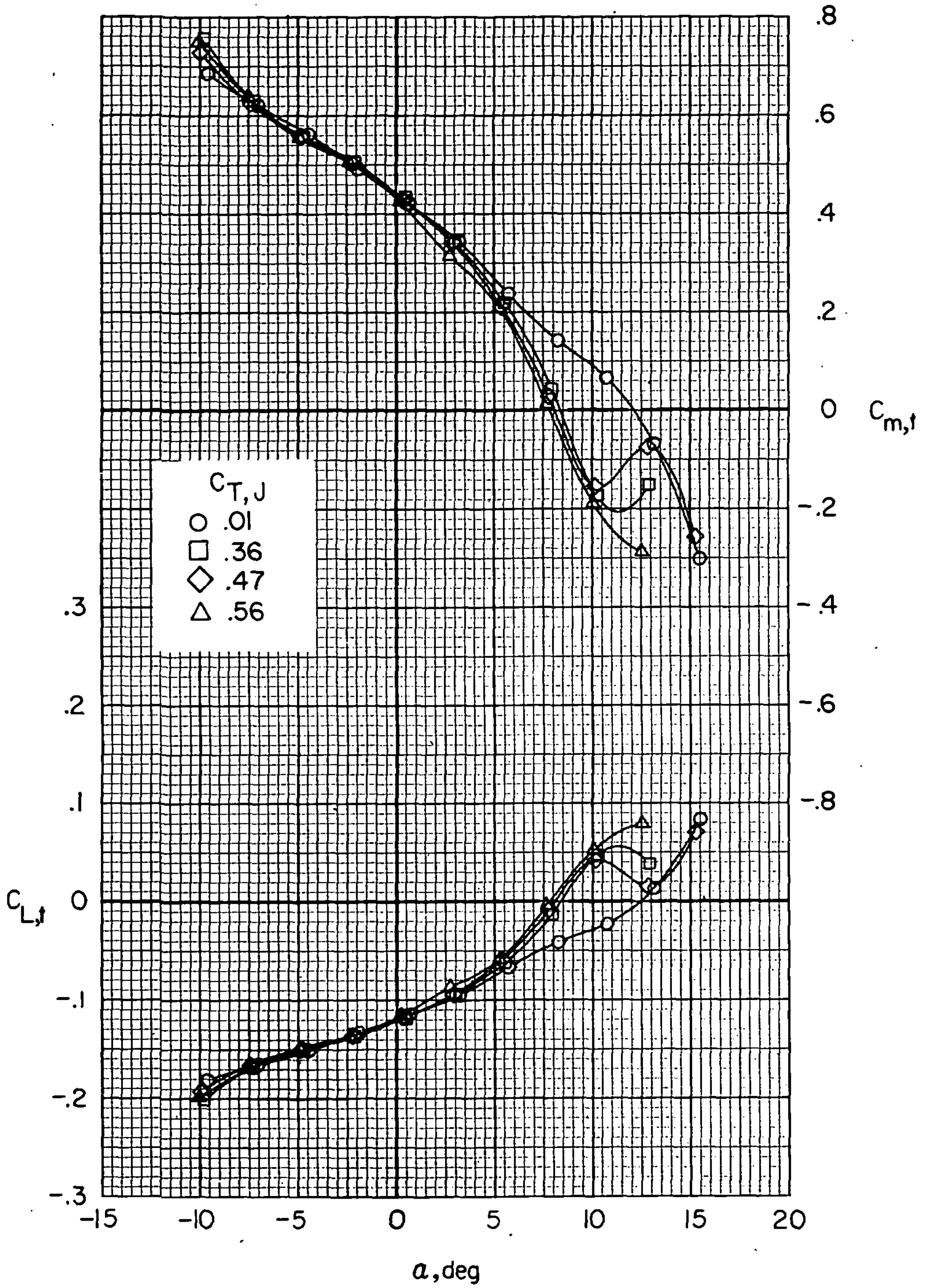

(d) $i_w = 7.5^{\circ}$; $\delta_f = 30^{\circ}$.

Figure 21.- Concluded.

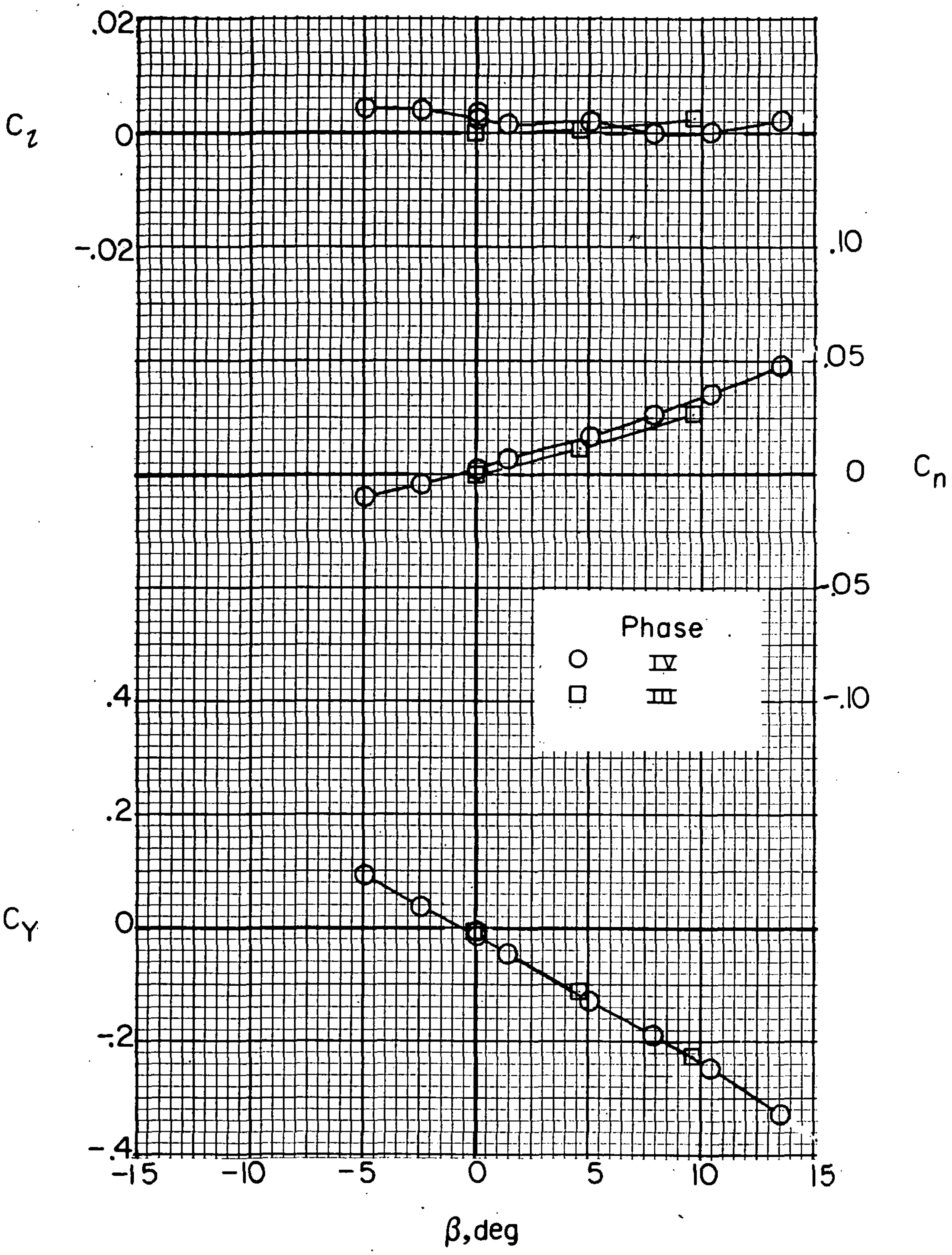

(a) $i_w = 0^\circ$; $\delta_f = 0^\circ$; $C_{T,J} \approx 0$; $\alpha = 0^\circ$.

Figure 22.- Comparison of lateral aerodynamics from Phase IV and Phase III. $F_1W_xVH_CJ_2$; $i_t = 0^\circ$.

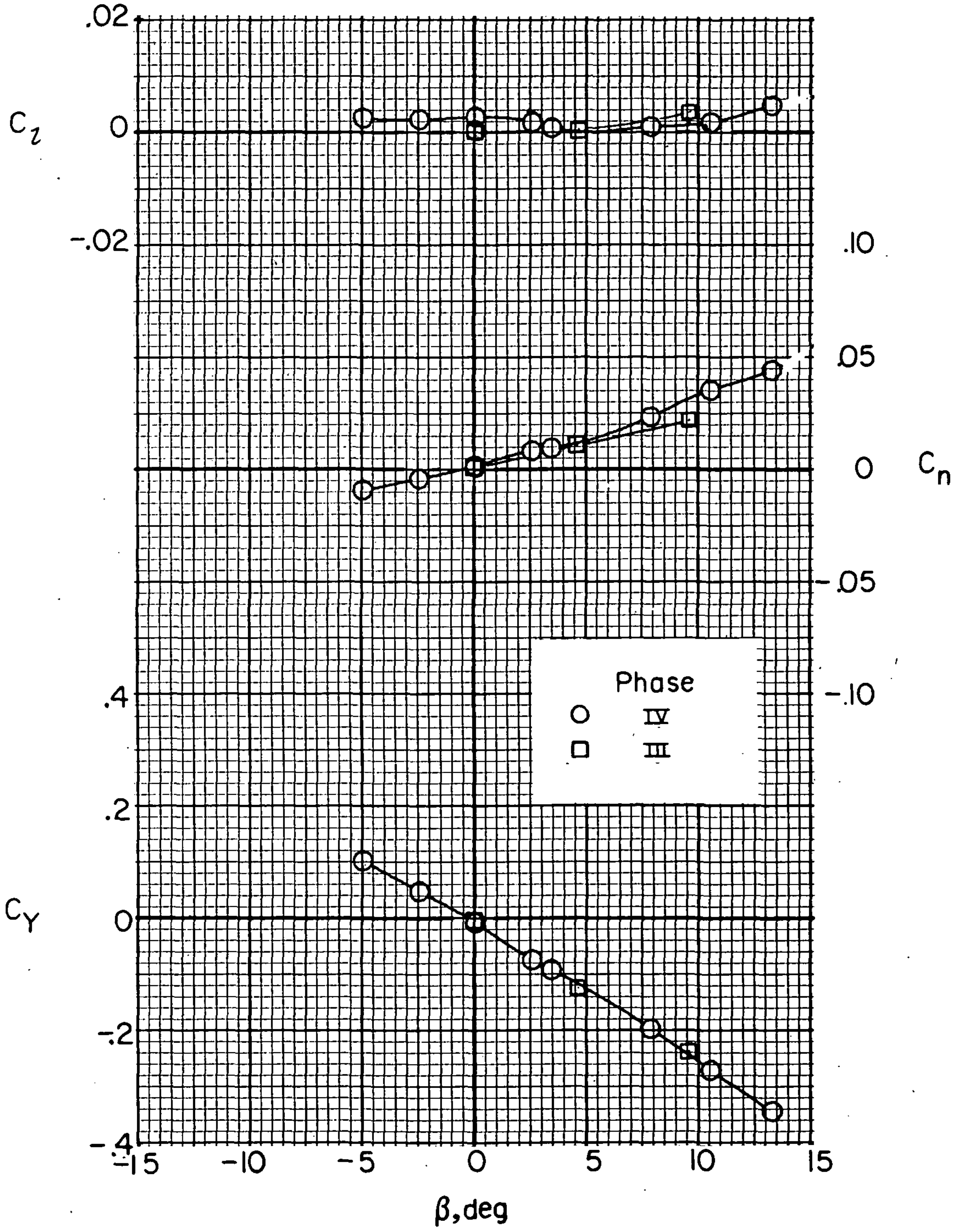

(b) $i_w = 0^o$; $\delta_f = 0^o$; $C_{T,J} = 0.11$; $\alpha = 0^o$.

Figure 22.- Continued.

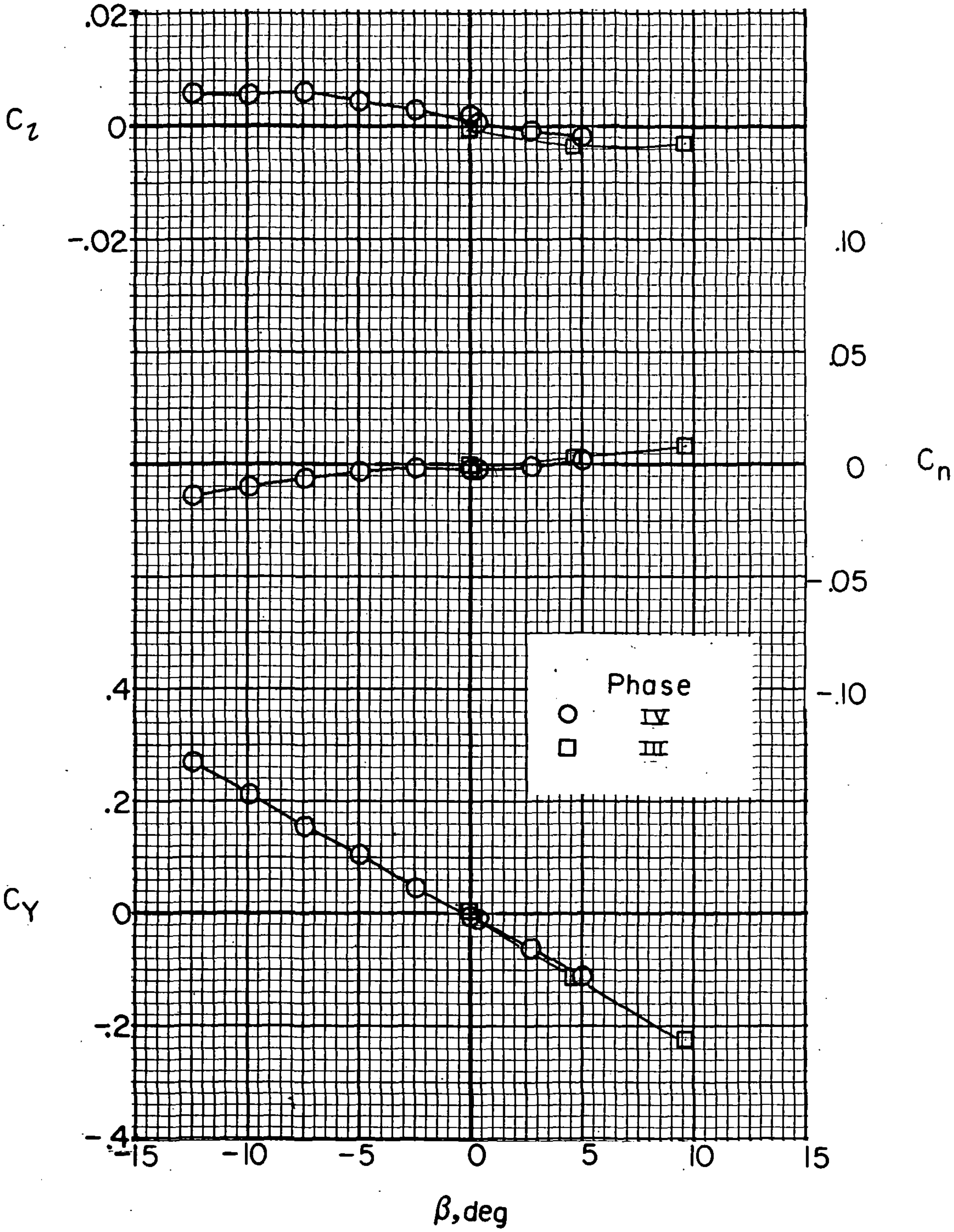

(c) $i_w = 0^\circ$; $\delta_f = 0^\circ$; $C_{T,J} \approx 0$; $\alpha = 10^\circ$.

Figure 22. - Continued.

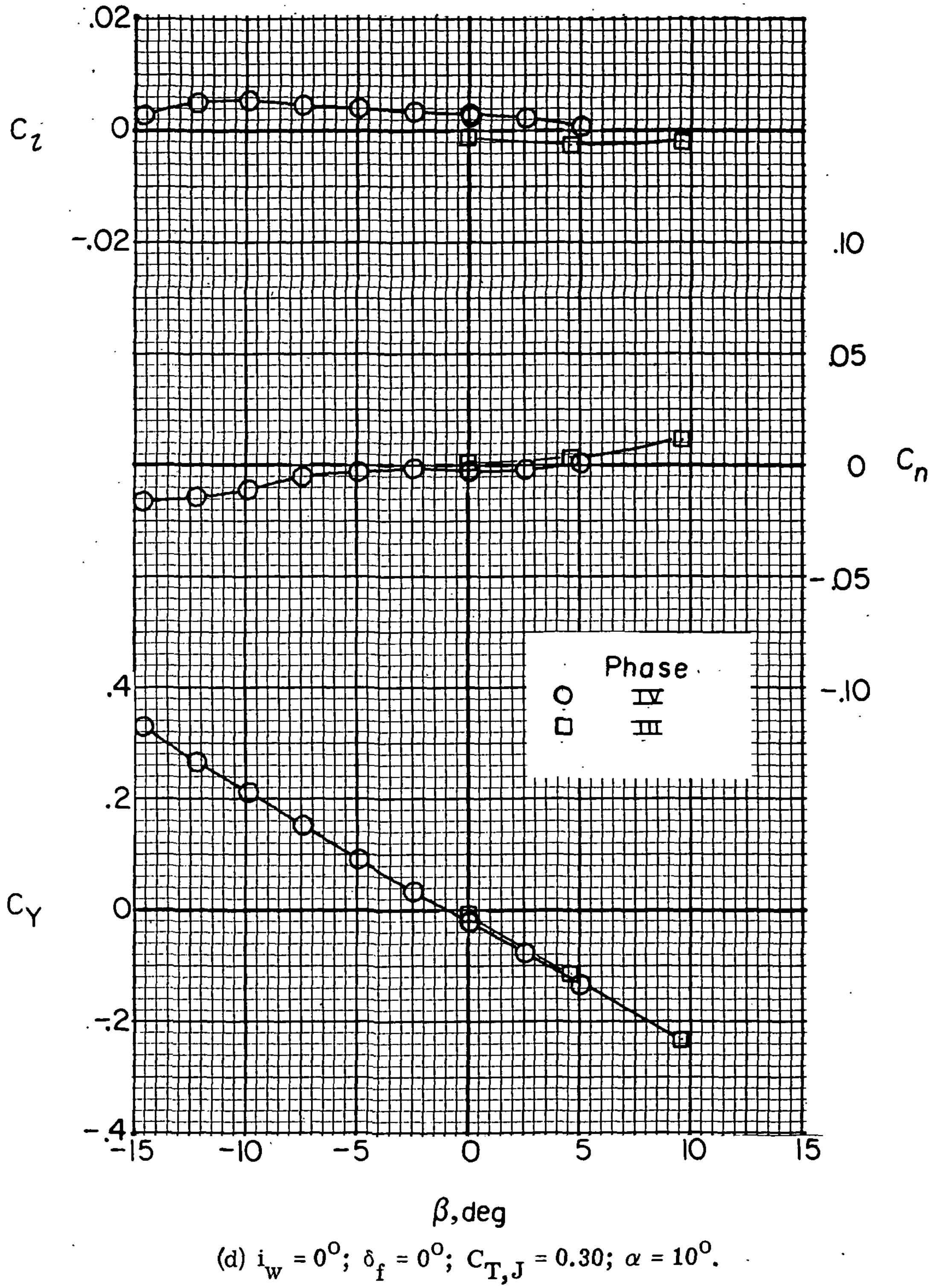

(d) $i_w = 0^{\circ}$; $\delta_f = 0^{\circ}$; $C_{T,J} = 0.30$; $\alpha = 10^{\circ}$.

Figure 22.- Continued.

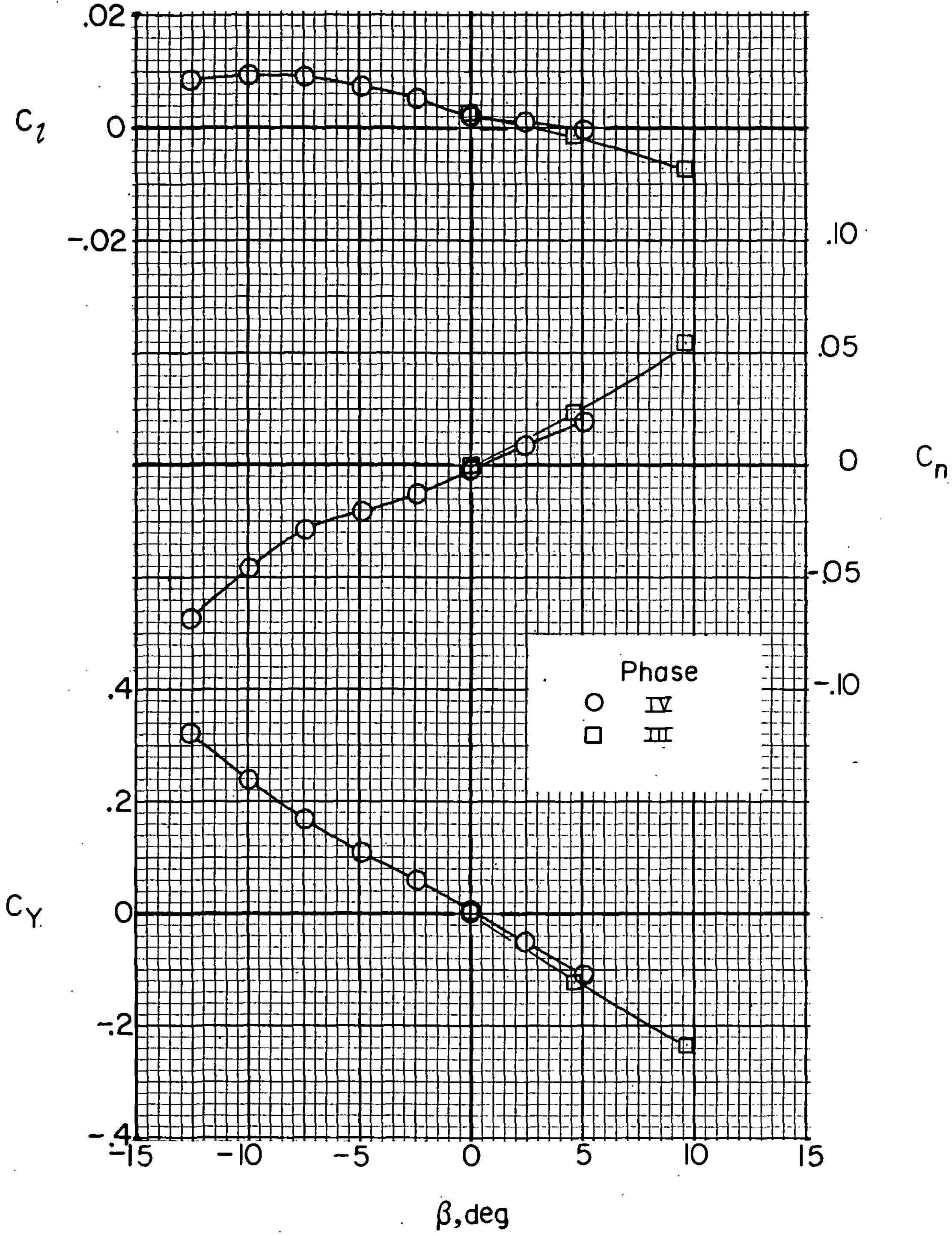

(e) $i_w = 0^\circ$; $\delta_f = 30^\circ$; $C_{T,J} \approx 0$; $\alpha = 0^\circ$.

Figure 22.- Continued.

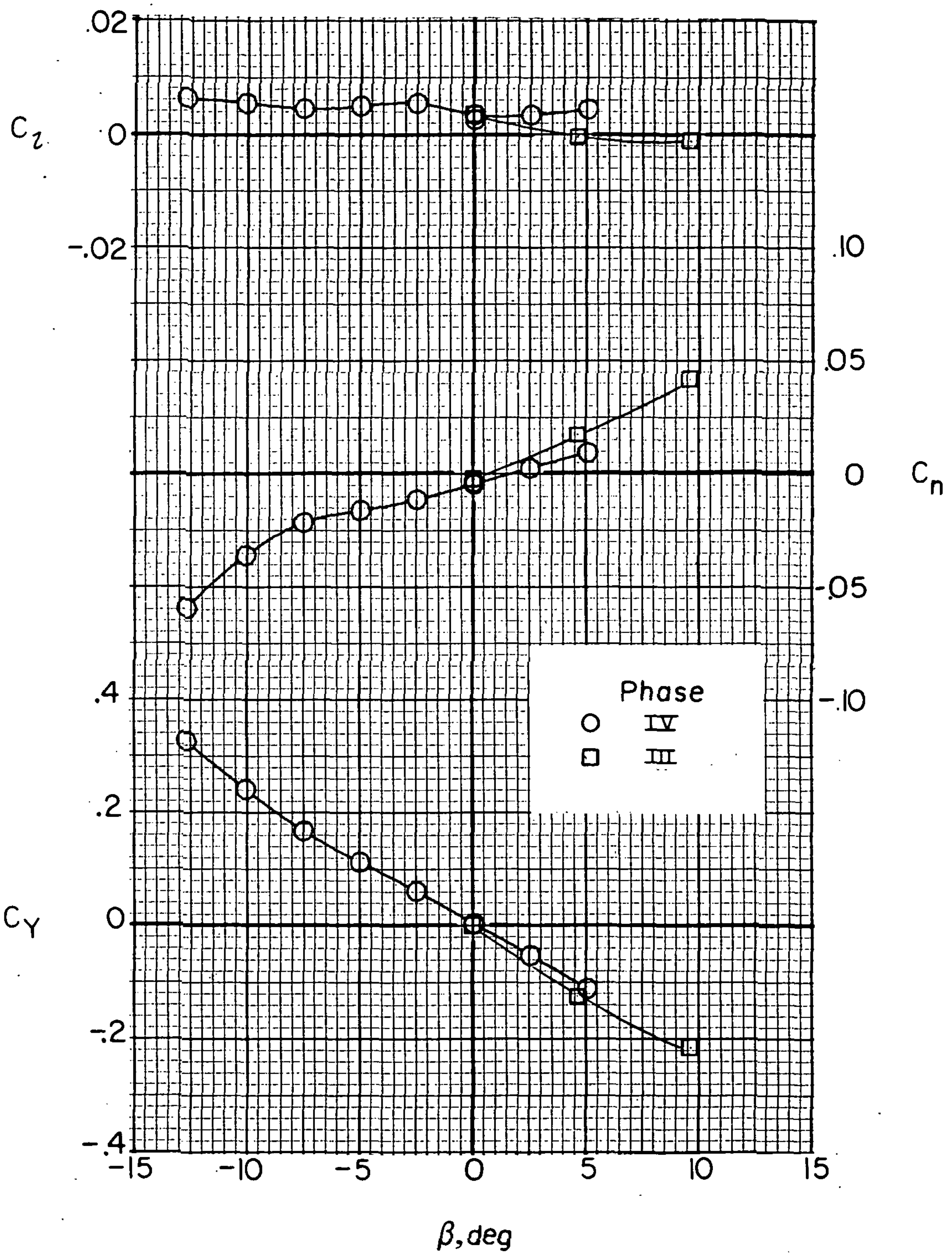

(f) $i_w = 0^o$; $\delta_f = 30^o$; $C_{T,J} = 0.29$; $\alpha = 0^o$.

Figure 22.- Continued.

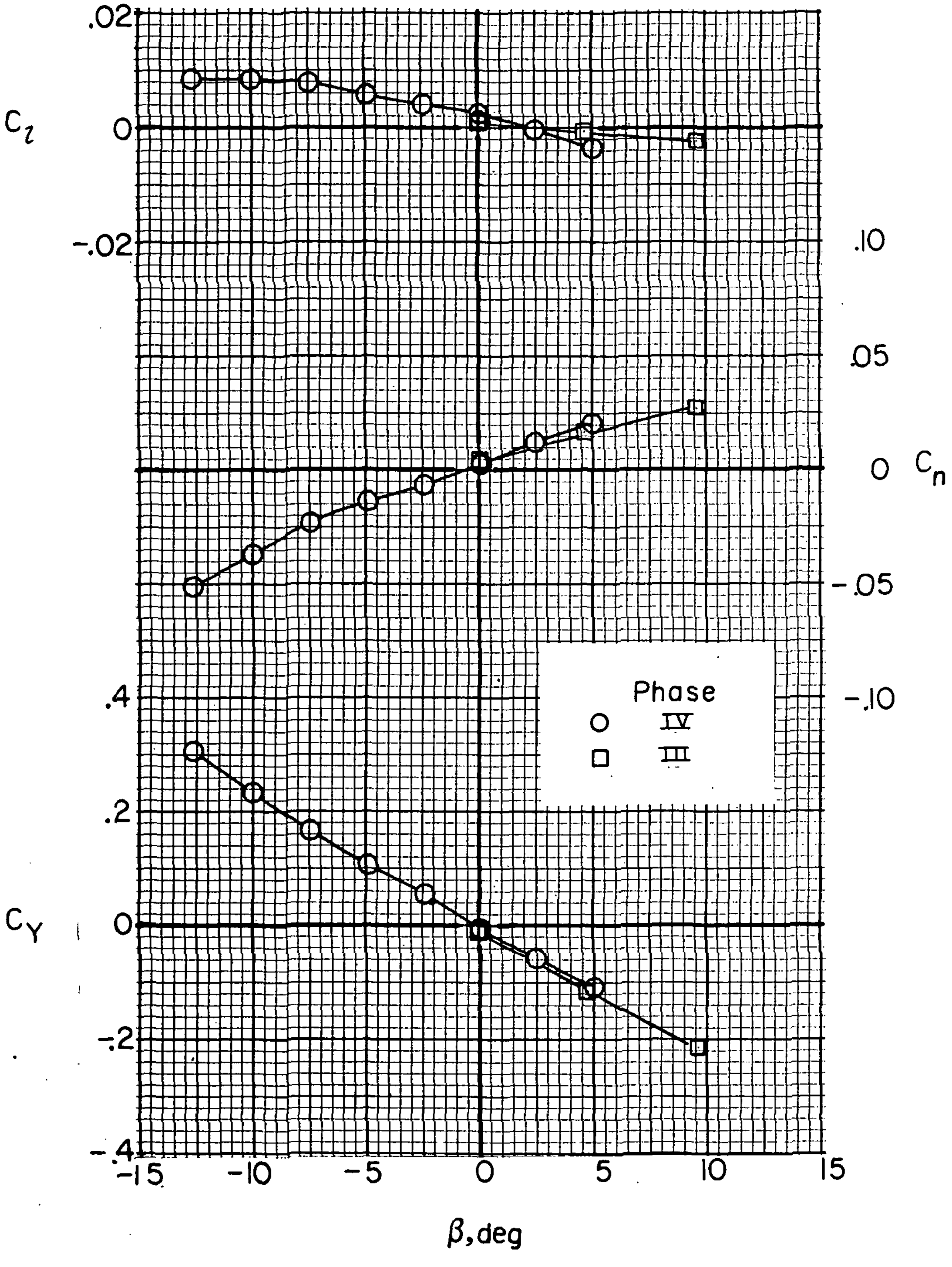

(g) $i_w = 7.5^{\circ}$; $\delta_f = 0^{\circ}$; $C_{T,J} \approx 0$; $\alpha = 0^{\circ}$.

Figure 22.- Continued.

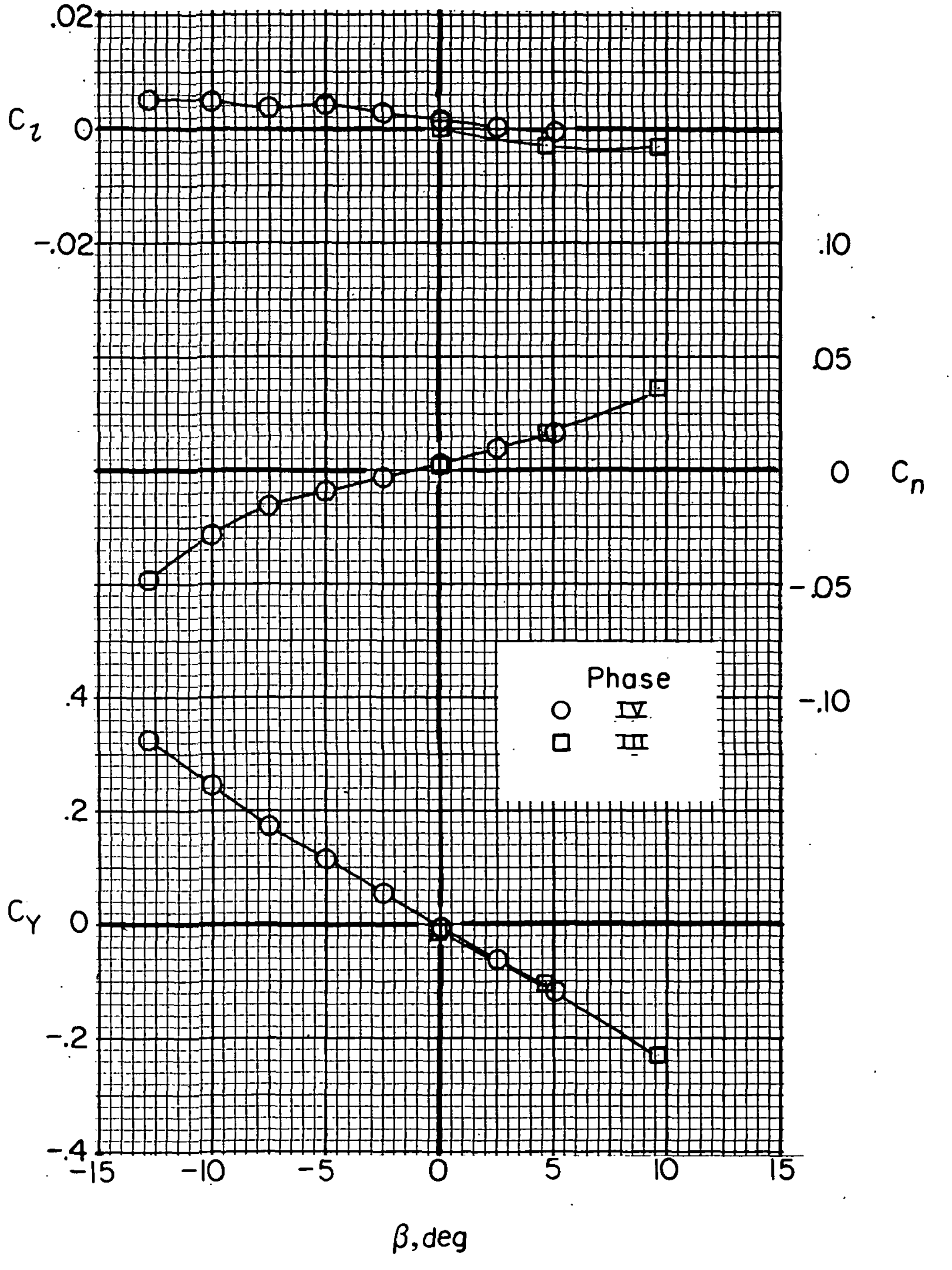

(h) $i_w = 7.5^\circ$; $\delta_f = 0^\circ$; $C_{T,J} = 0.23$; $\alpha = 0^\circ$.

Figure 22.- Continued.

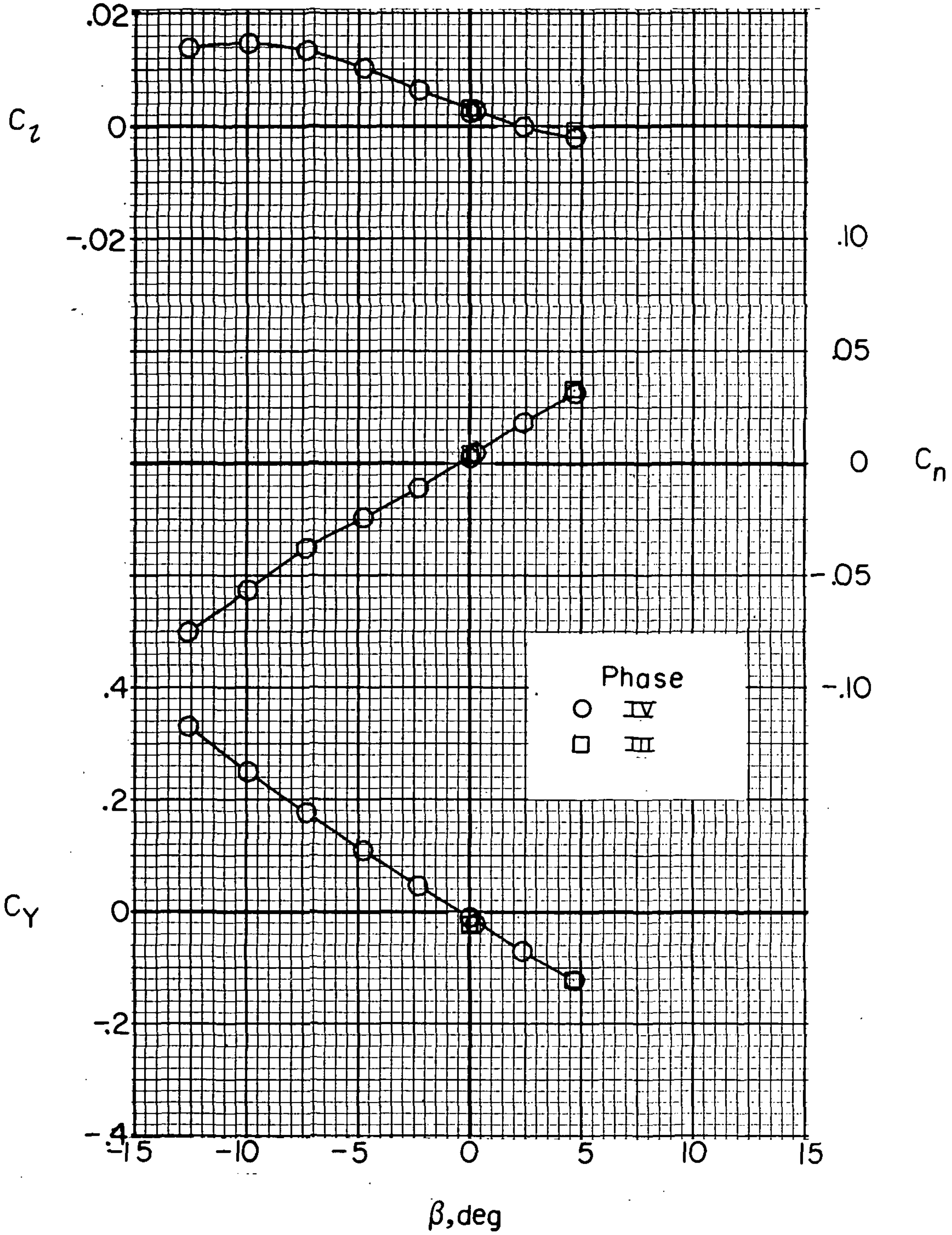

(i) $i_w = 7.5^\circ$; $\delta_f = 30^\circ$; $C_{T,J} \approx 0$; $\alpha = 0^\circ$.

Figure 22.- Continued.

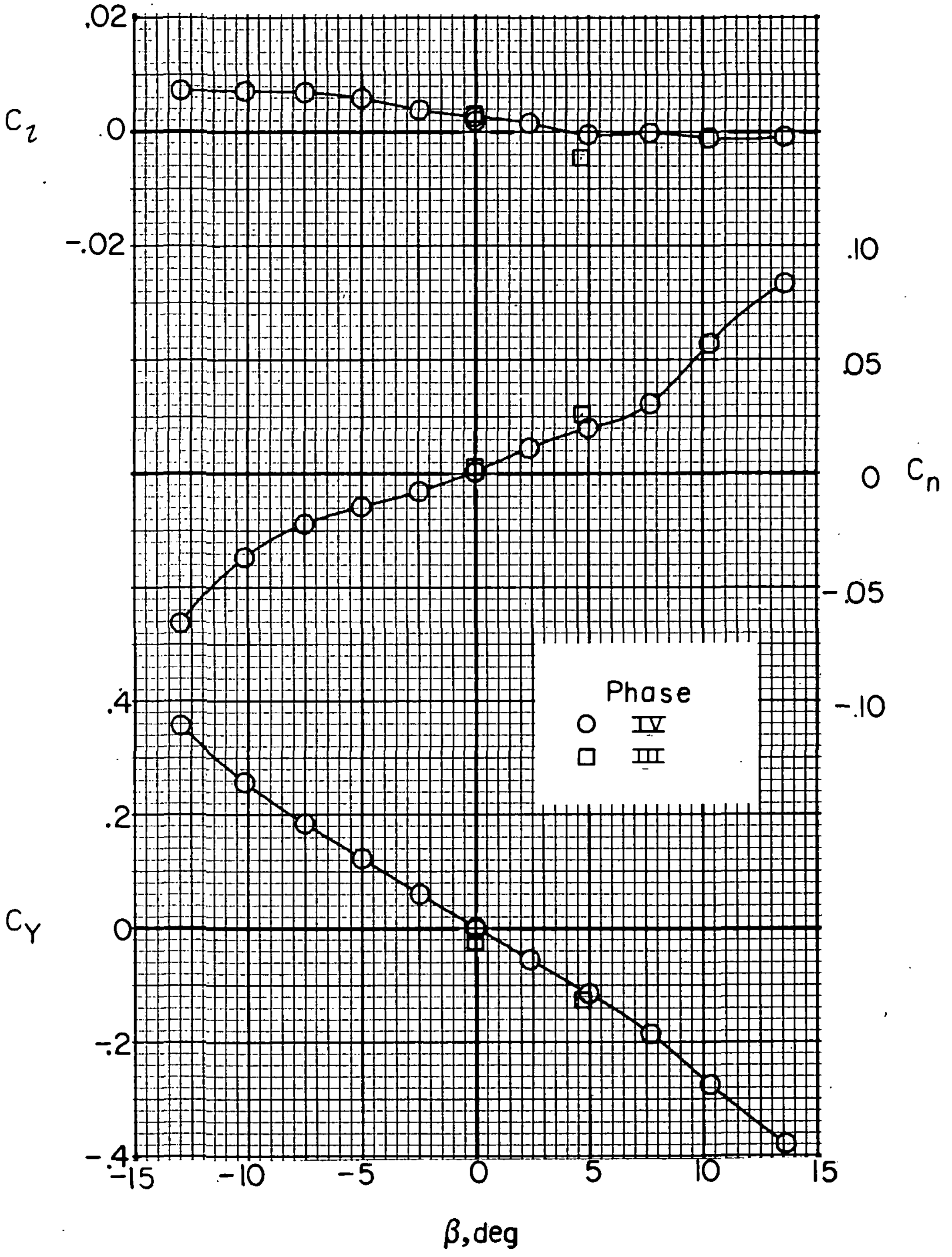

(j) $i_w = 7.5^\circ$; $\delta_f = 30^\circ$; $C_{T,J} = 0.43$; $\alpha = 0^\circ$.

Figure 22.- Concluded.

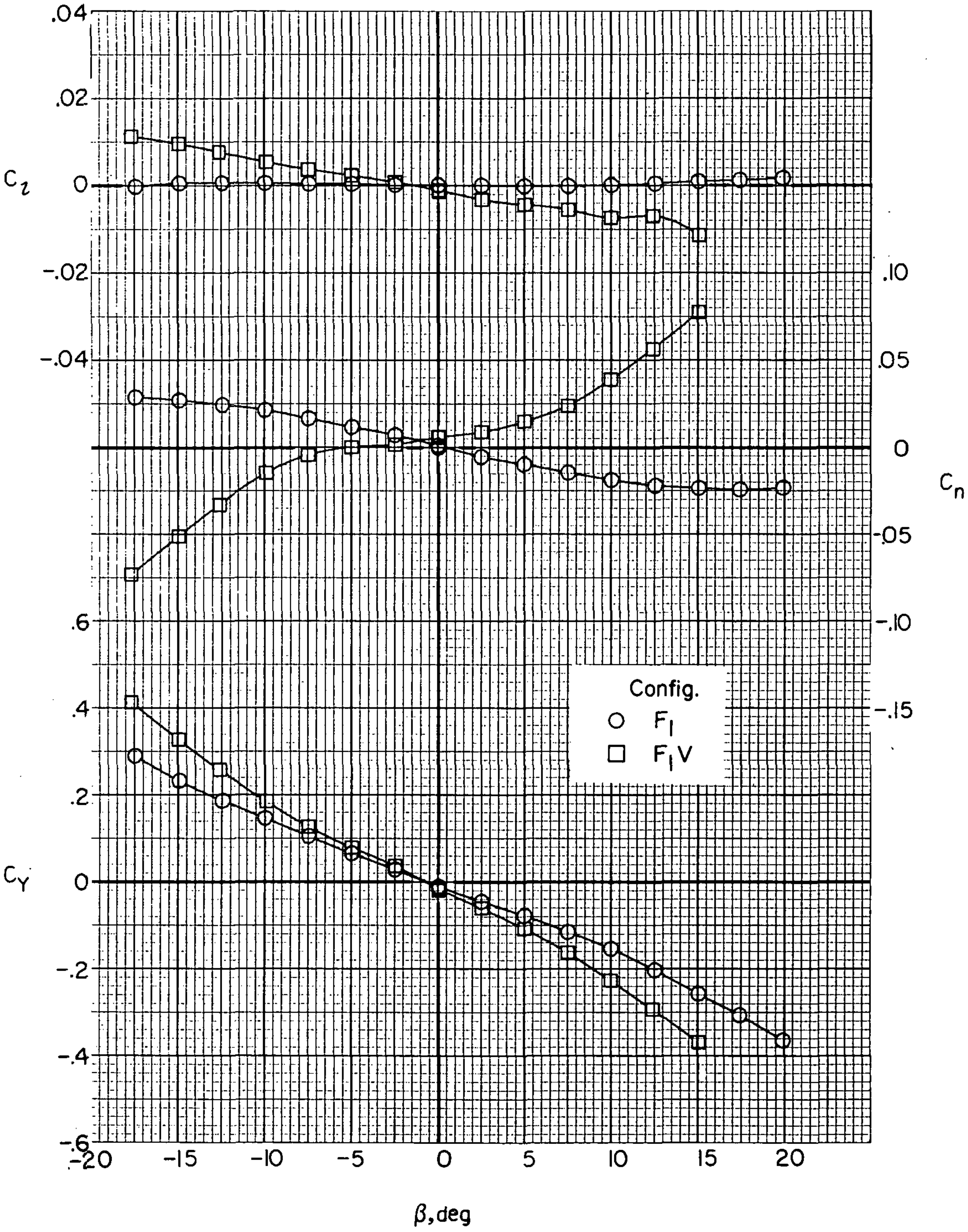

Figure 23.- Effect of vertical tail on airframe lateral aerodynamics. $\alpha = 0^o$.

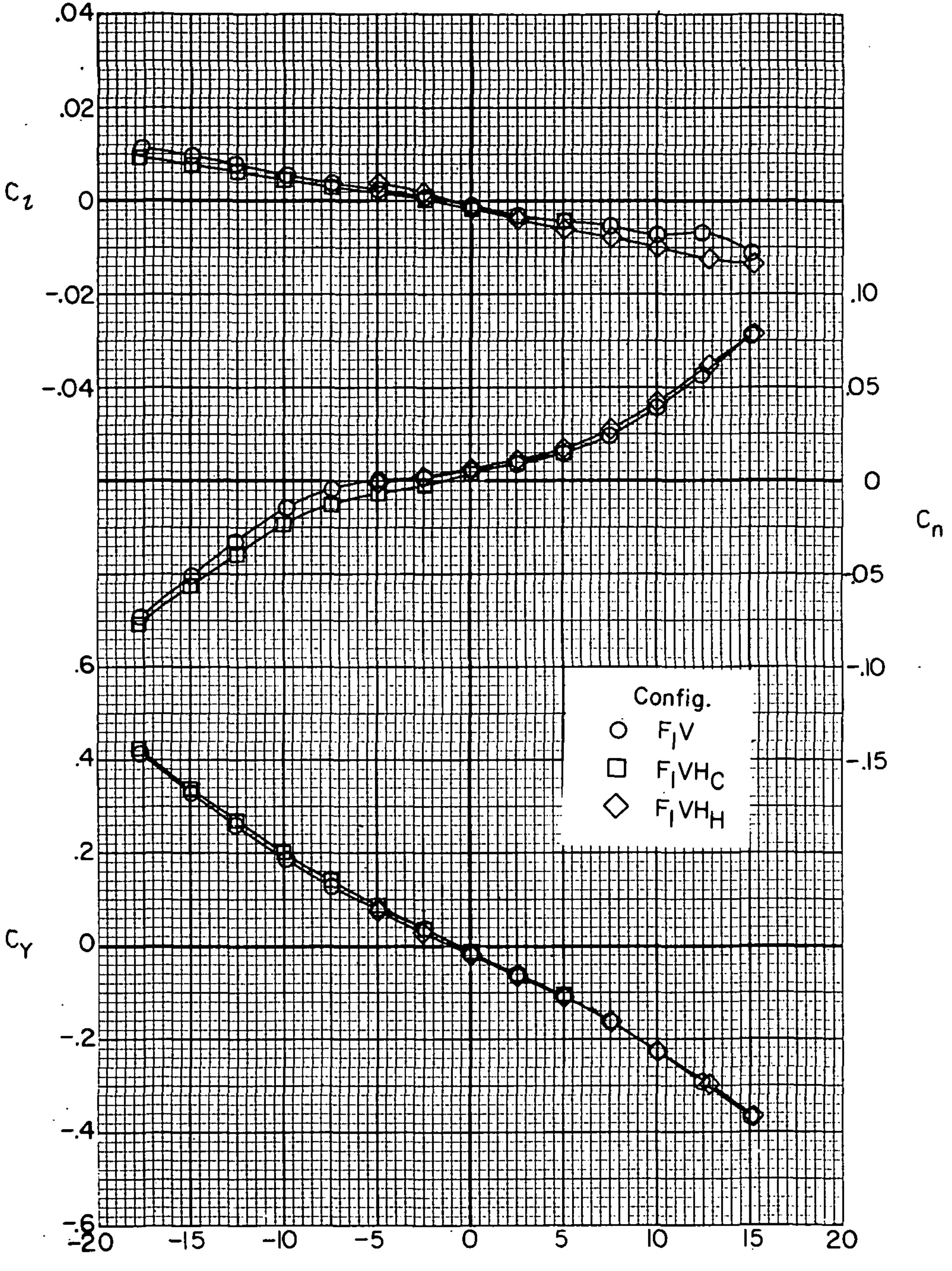

Figure 24.- Effect of horizontal tail on airframe lateral aerodynamics.
$\alpha = 0^o$; $i_t = 0^o$.

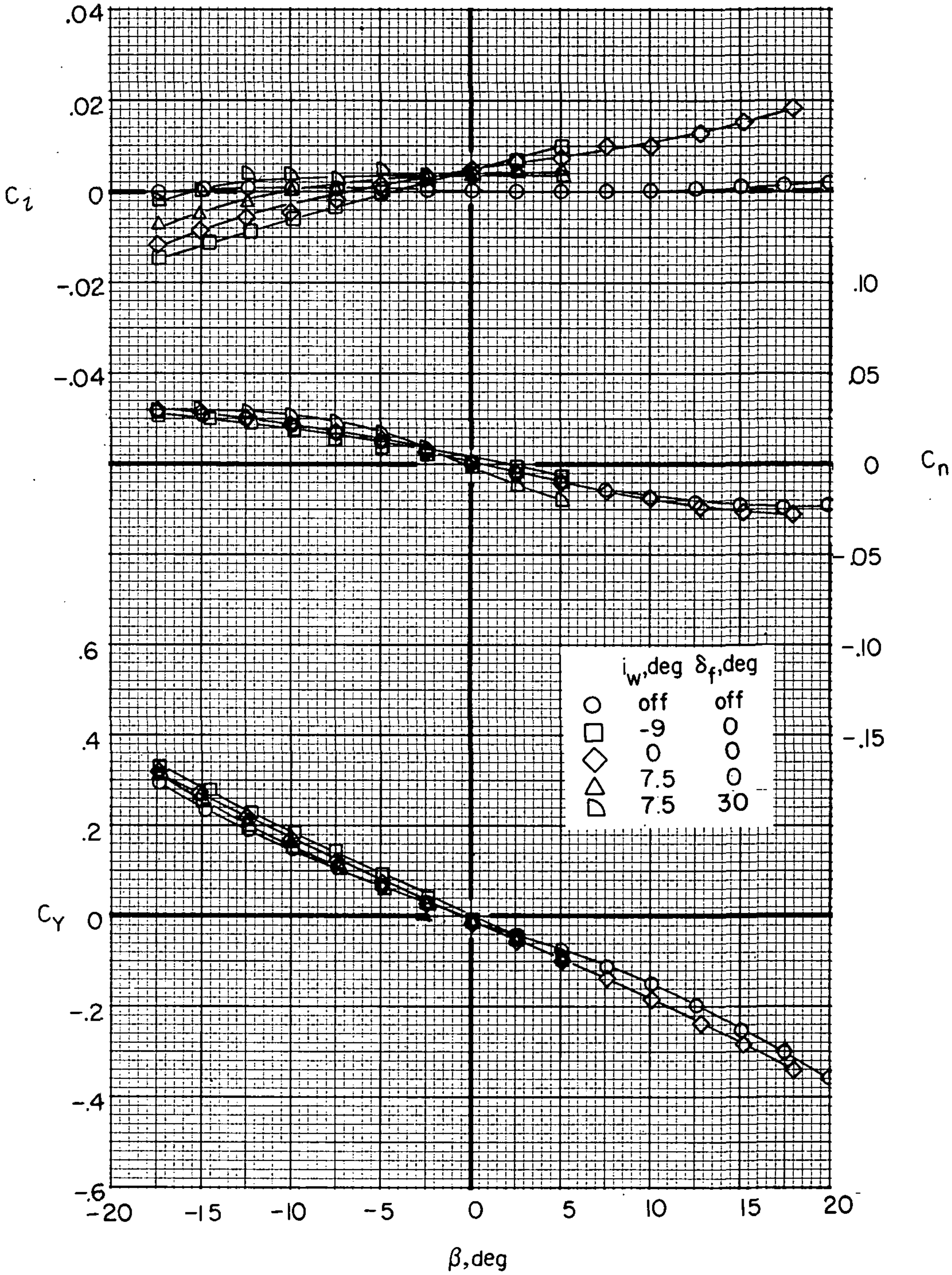

Figure 25.- Effect of wing incidence and flap deflection on airframe lateral aerodynamics with tail off. F_1W_x; $\alpha = 0^o$.

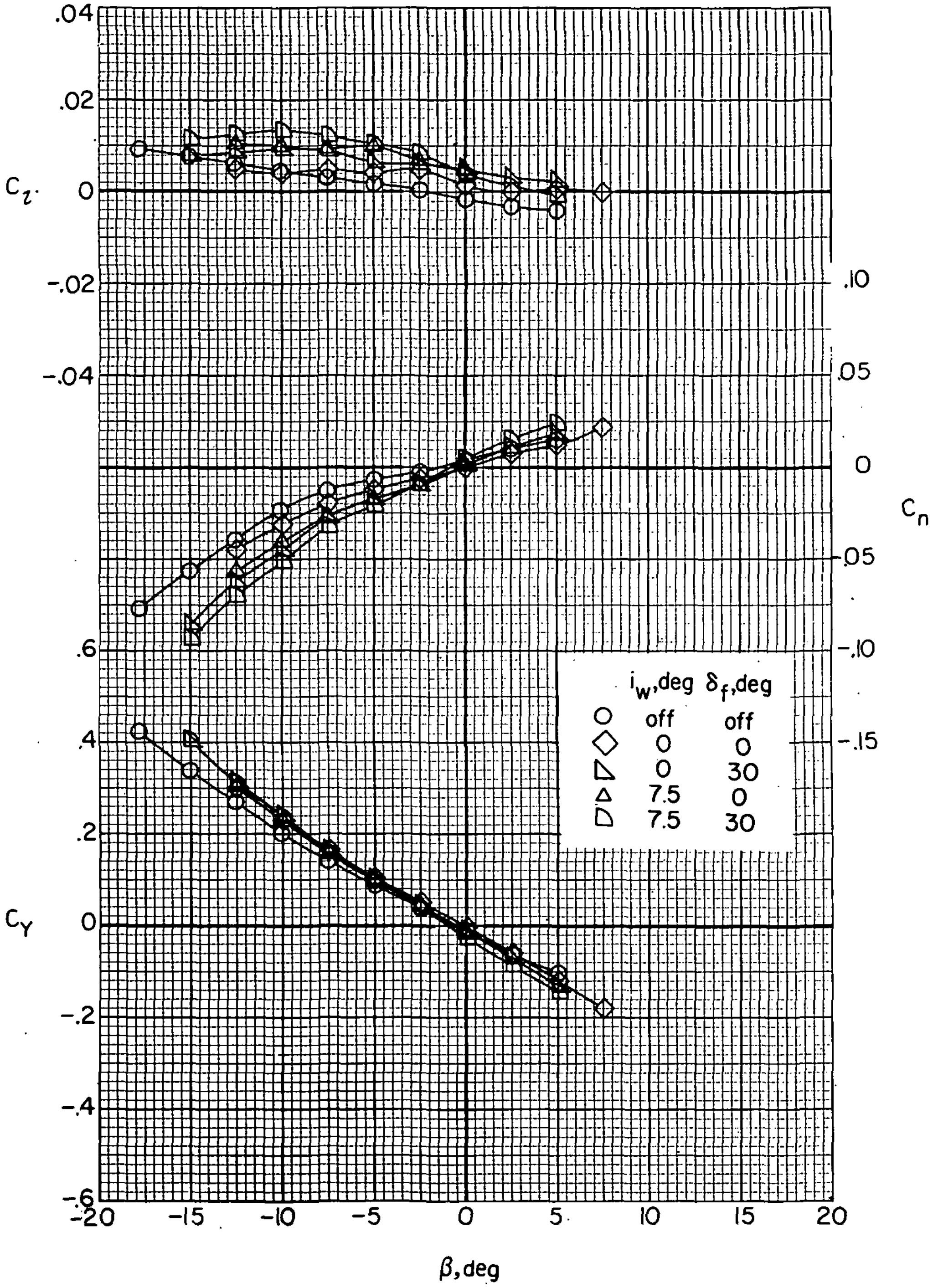

Figure 26.- Effect of wing incidence and flap deflection on airframe lateral aerodynamics with tail on. $\alpha = 0^{\circ}$; $i_t = 0^{\circ}$; $F_1W_XVH_C$.

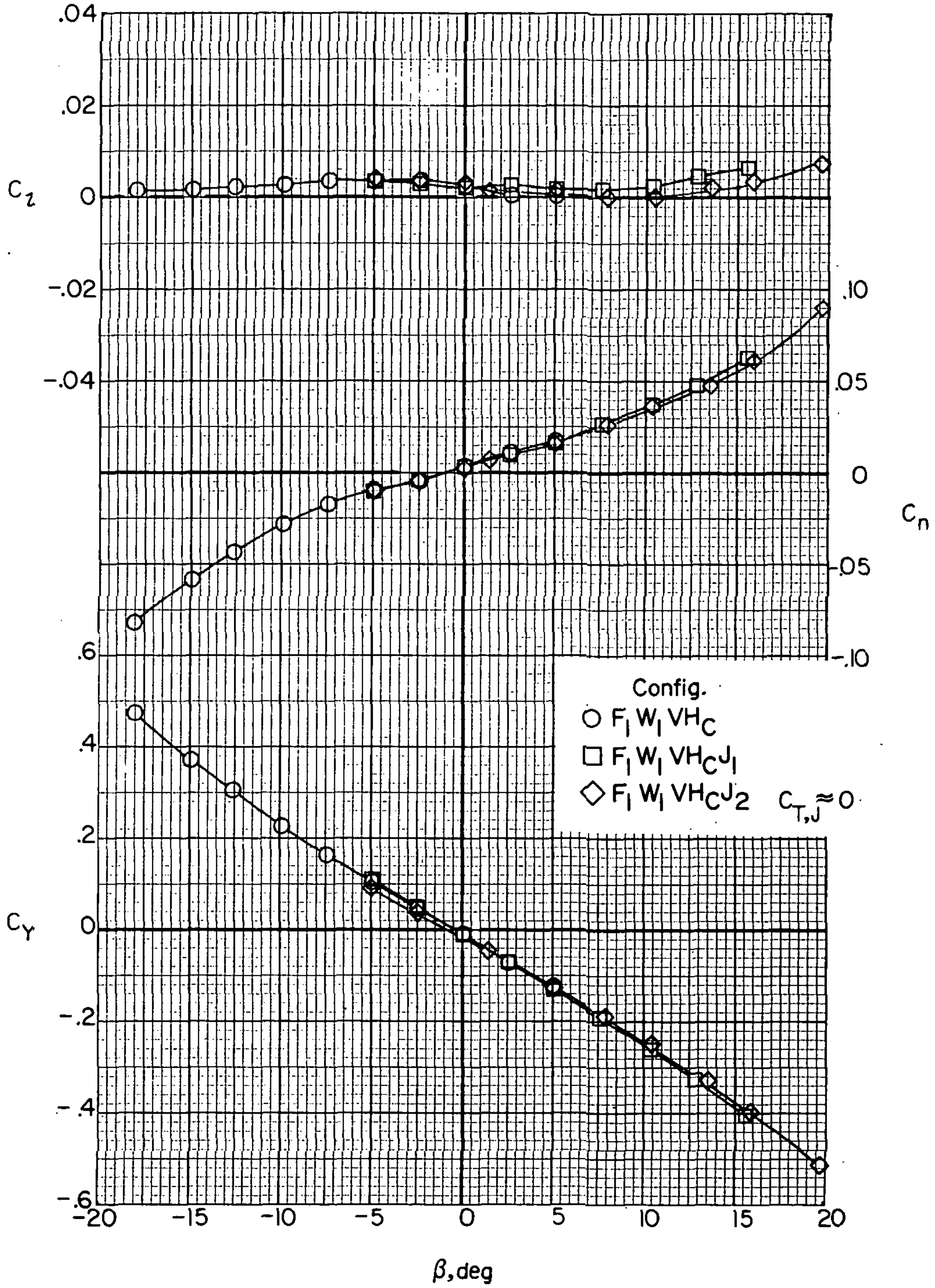

Figure 27.- Effect of engine nacelles on airframe lateral aerodynamics. $i_t = 0^{\circ}$; $\alpha = 0^{\circ}$.

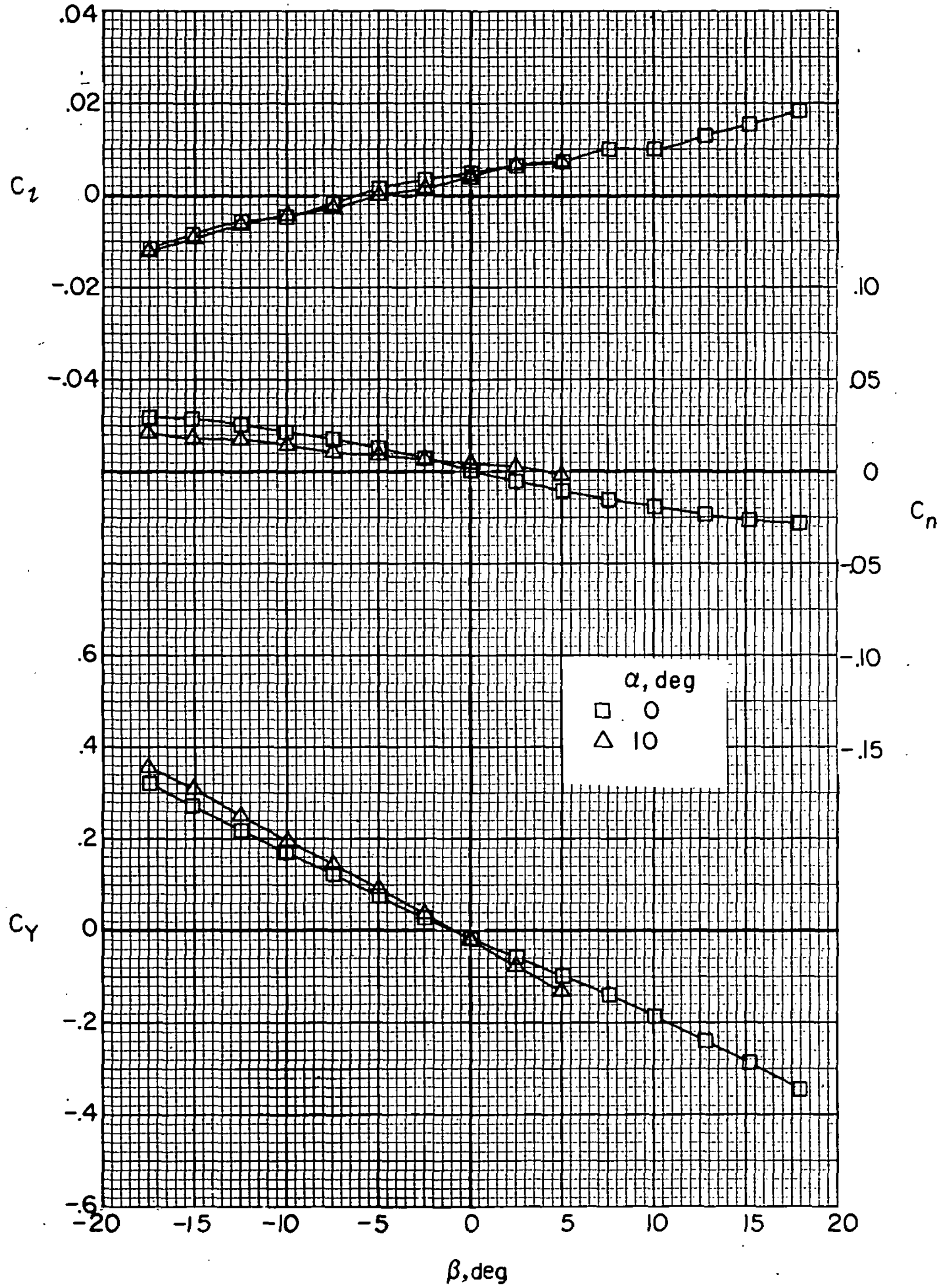

(a) Jets off; tail off; $i_w = 0^o$; $\delta_f = 0^o$; F_1W_1.

Figure 28.- Effect of angle of attack on airframe lateral aerodynamics.

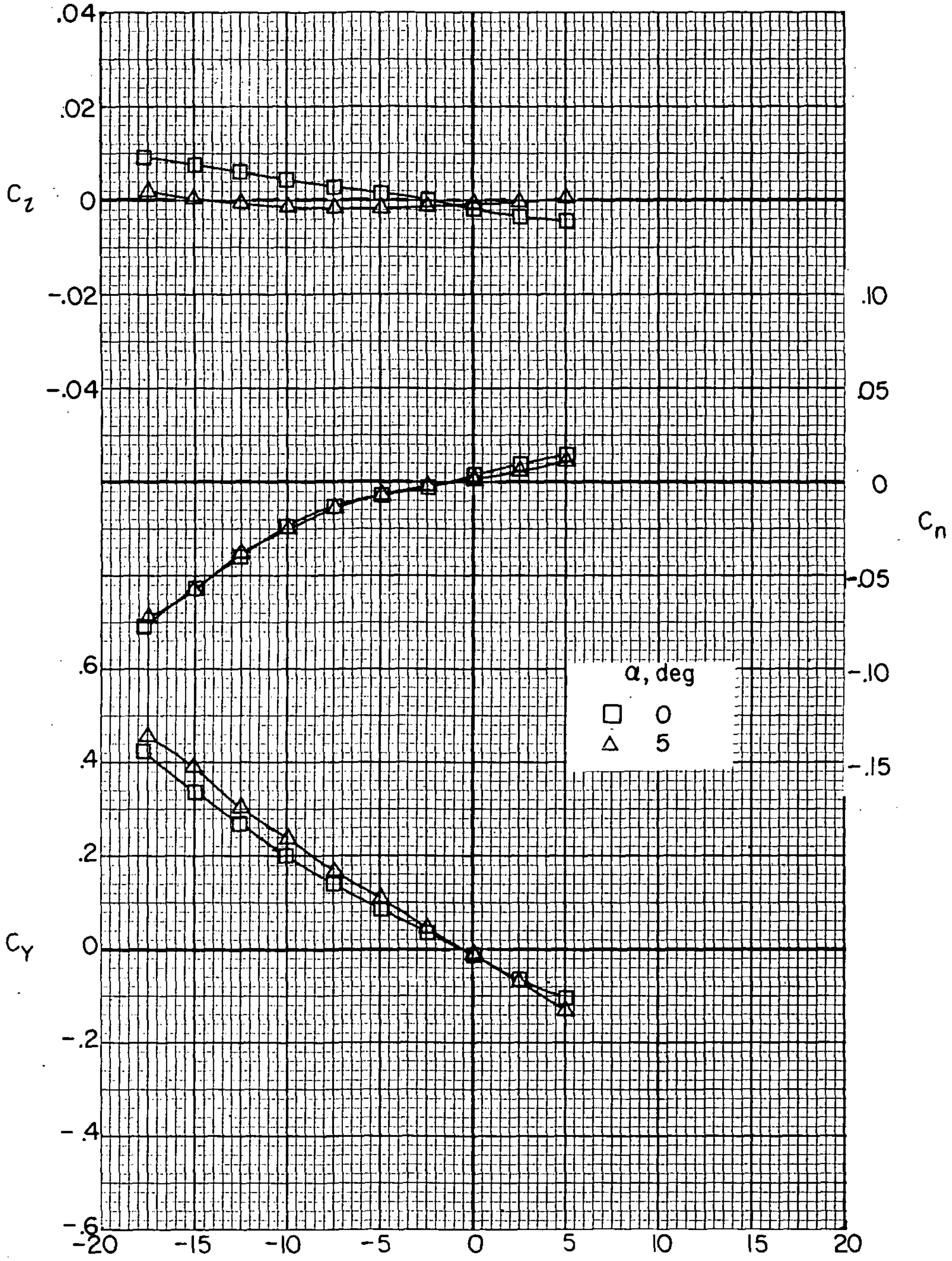

(b) Wing off; jets off; helicopter tail; F_1VH_H.

Figure 28.- Continued.

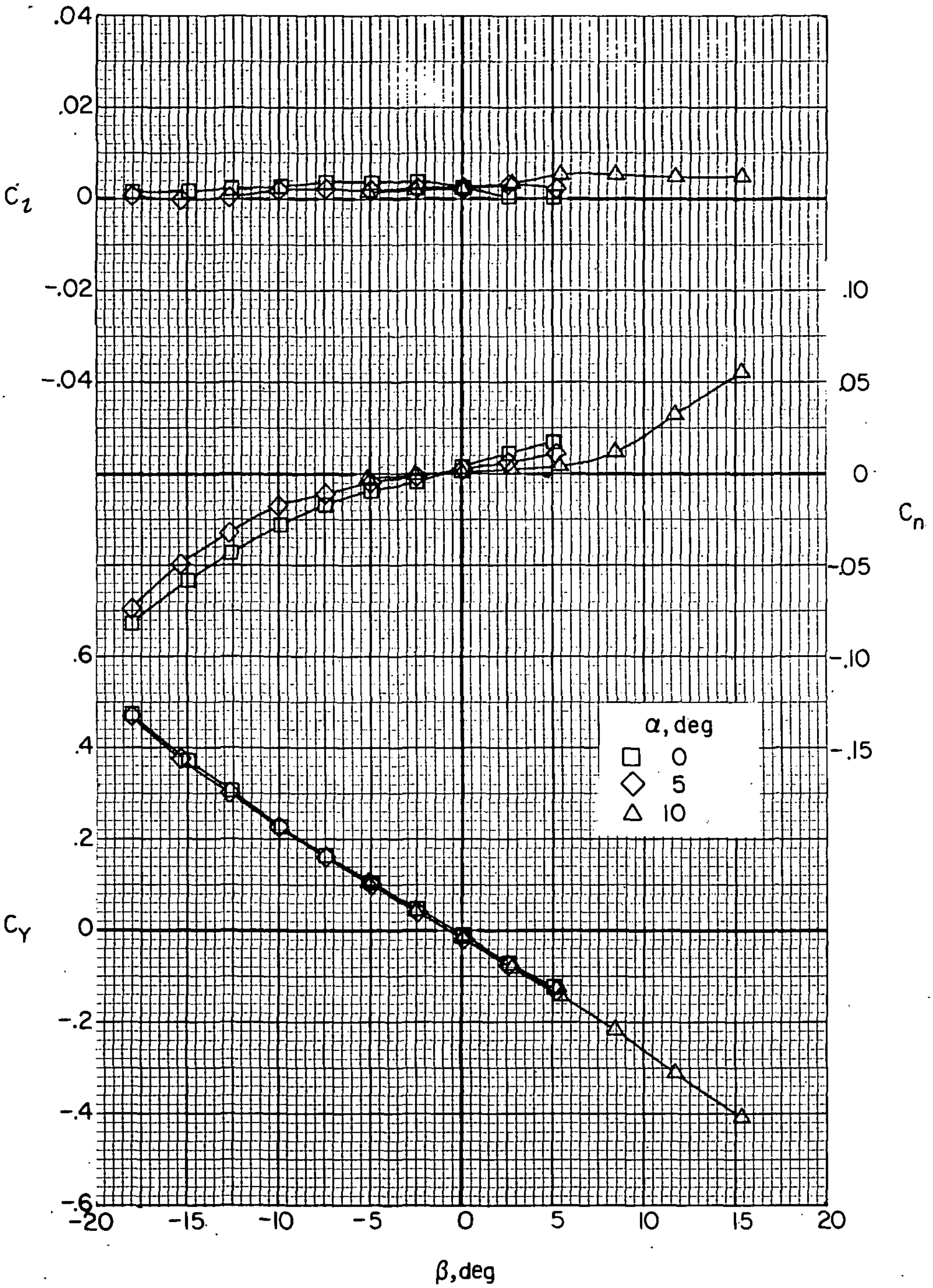

(c) Jets off; $i_w = 0^\circ$; $\delta_f = 0^\circ$; $F_1W_1VH_C$.

Figure 28.- Continued.

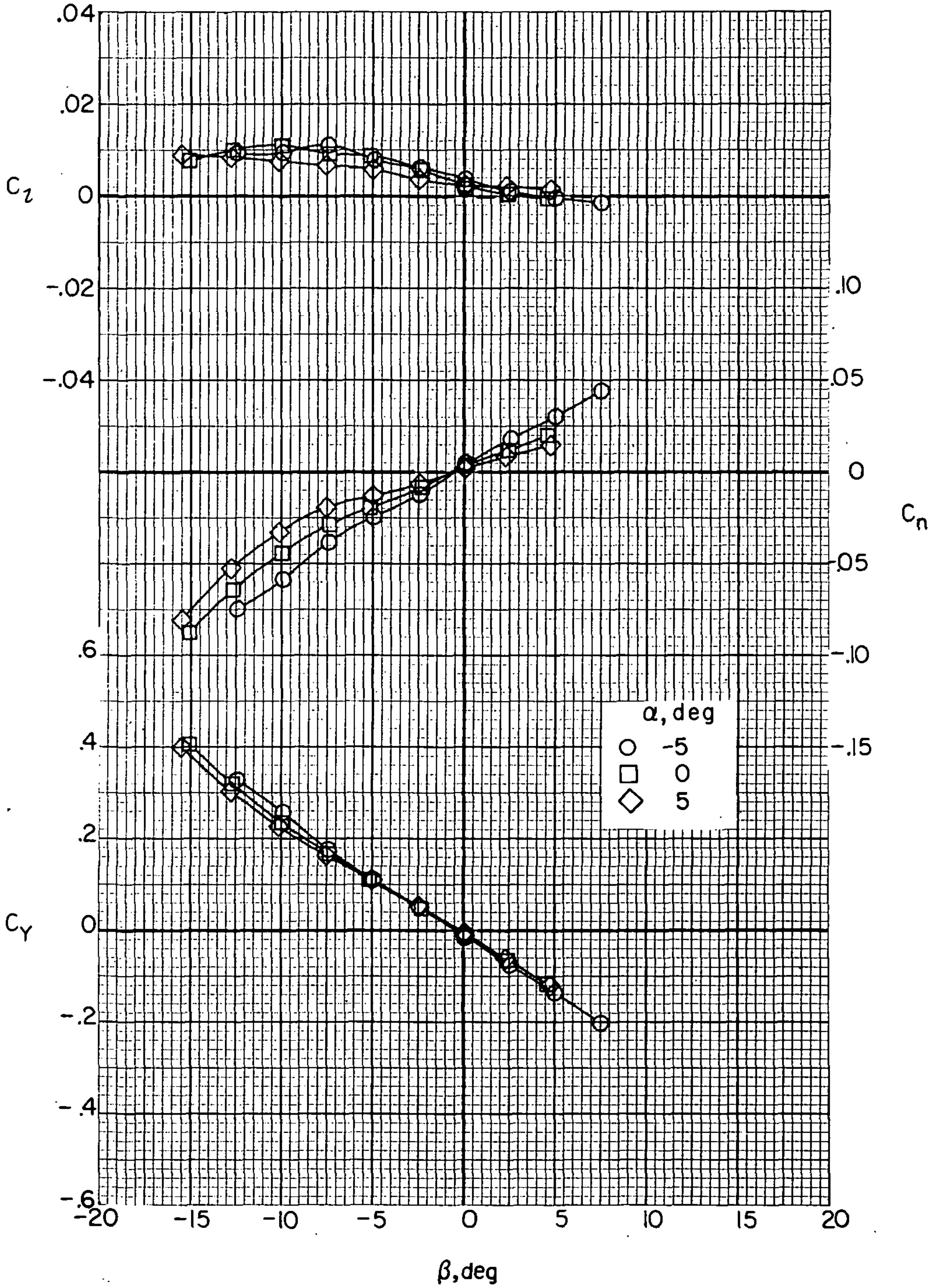

(d) Jets off; $i_w = 7.5^\circ$; $\delta_f = 30^\circ$; $F_1W_6VH_C$.

Figure 28. - Continued.

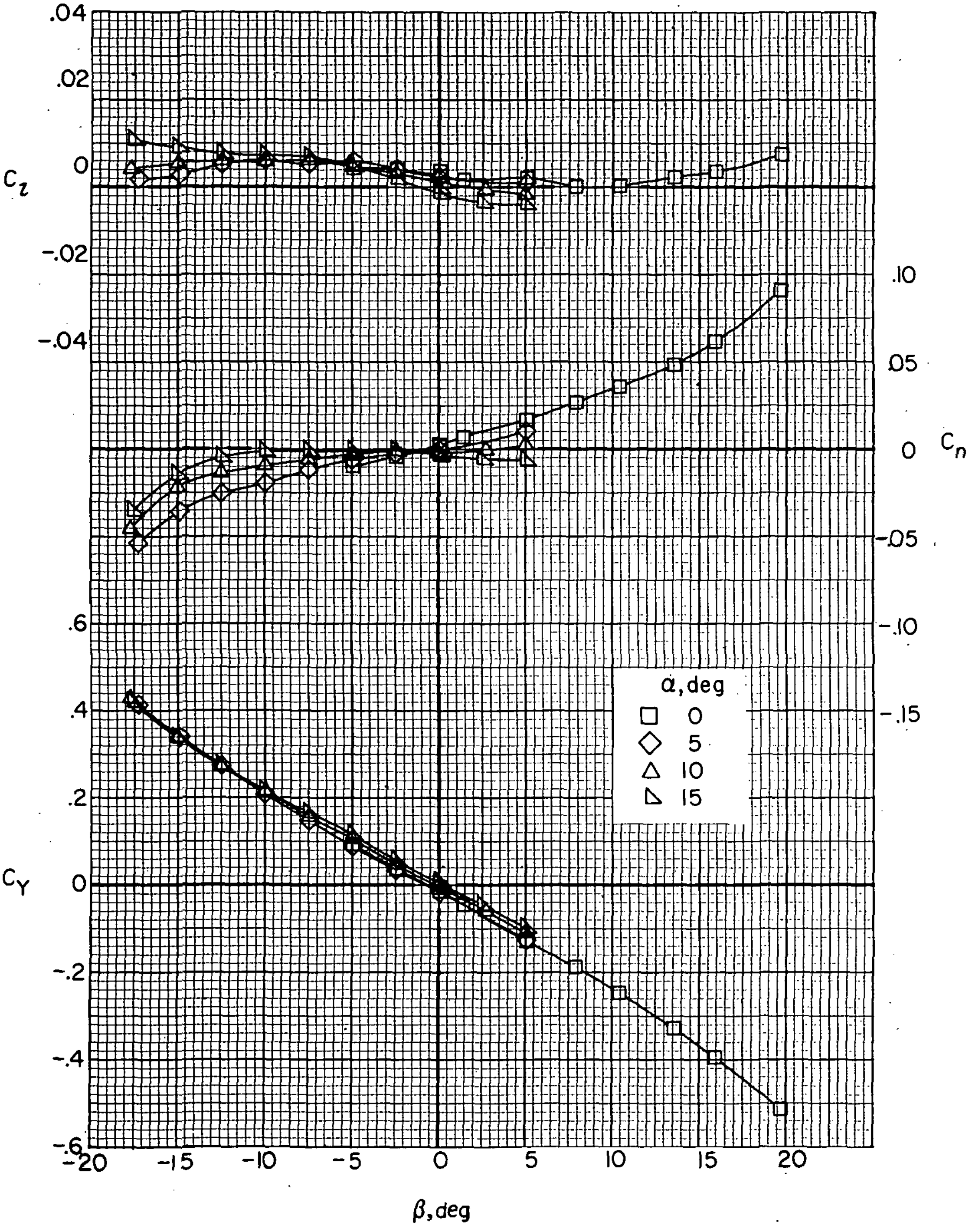

(e) Jets on; $C_{T,J} \approx 0$; $i_w = 0^\circ$; $\delta_f = 0^\circ$; $F_1W_1VH_CJ_2$.

Figure 28.- Continued.

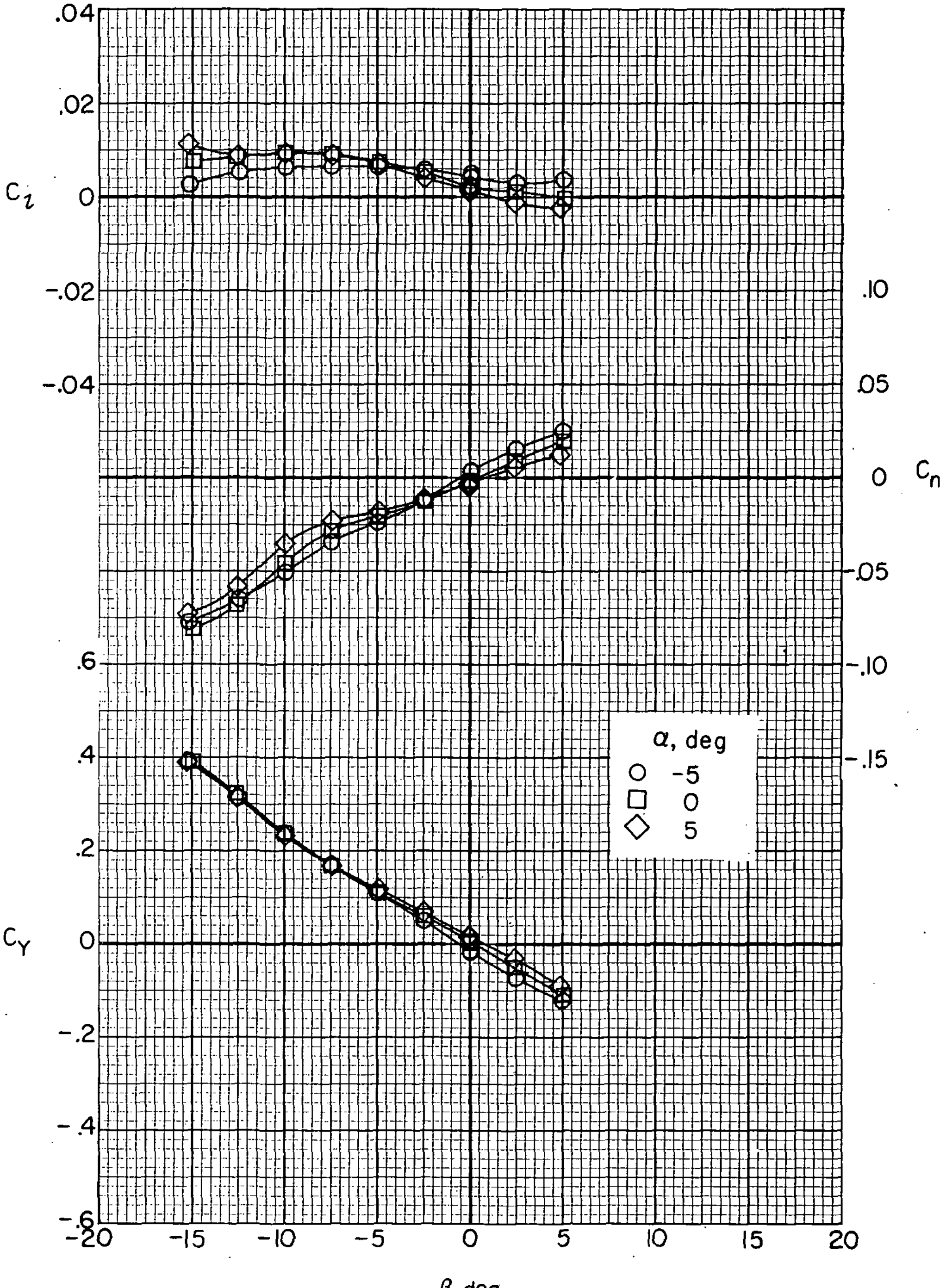

(f) Jets on; $C_{T,J} \approx 0$; $i_w = 0^\circ$; $\delta_f = 30^\circ$; $F_1W_5VH_CJ_2$.

Figure 28.- Continued.

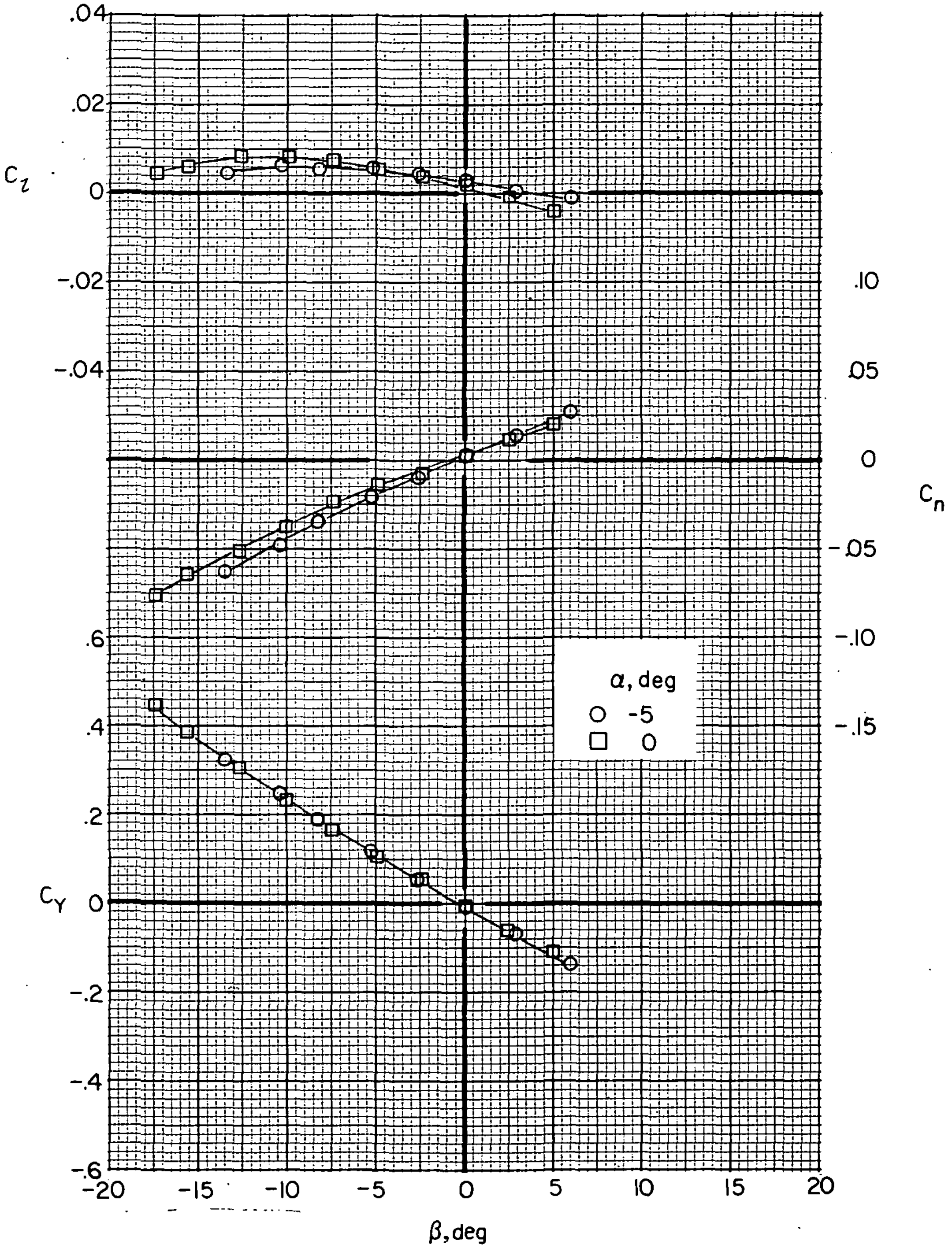

(g) Jets on; $C_{T,J} \approx 0$; $i_w = 7.5^\circ$; $\delta_f = 0^\circ$; $F_1W_2VH_CJ_2$.

Figure 28. - Continued.

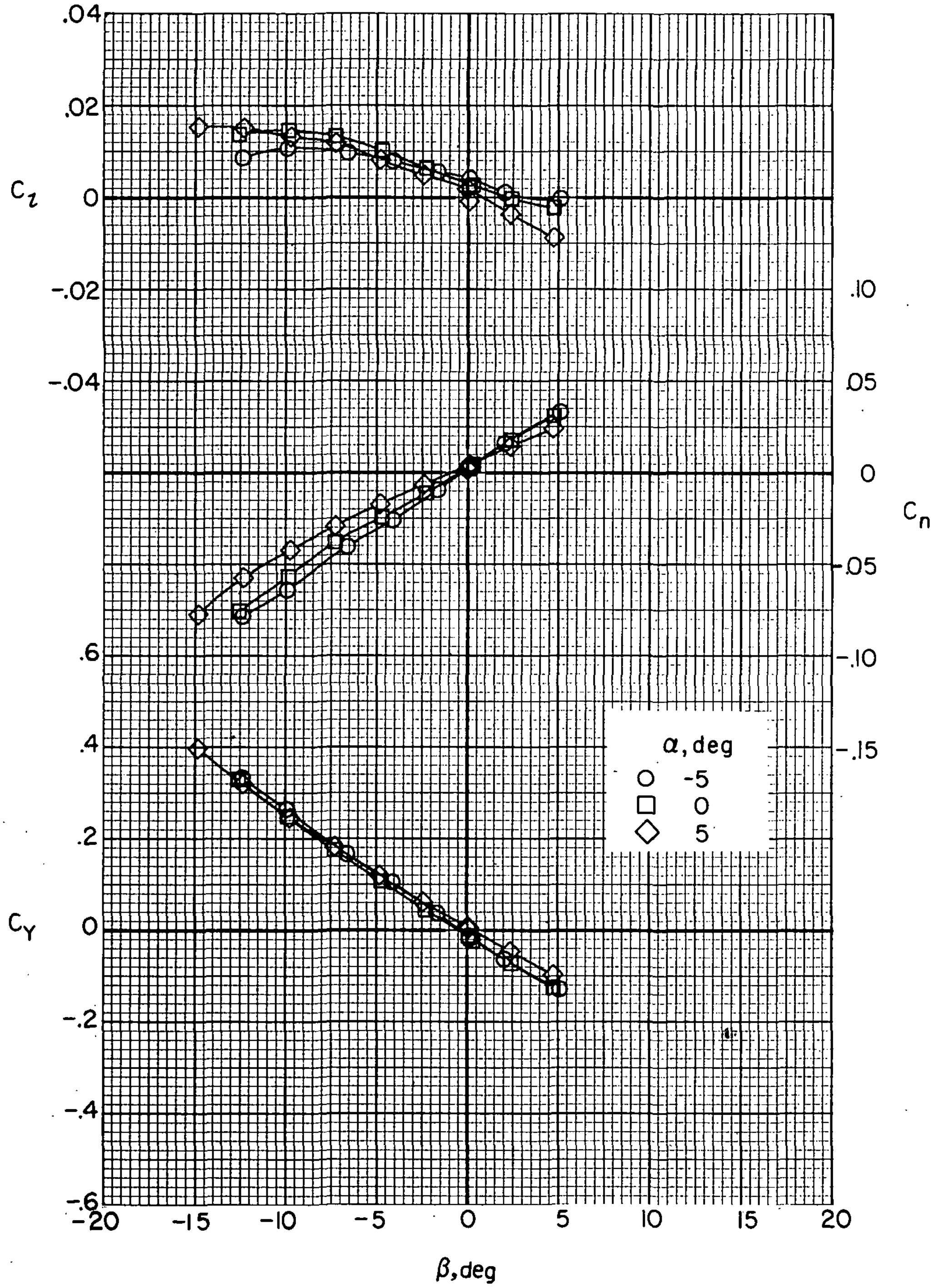

(h) Jets on; $C_{T,J} = 0.1$; $i_w = 7.5^\circ$; $\delta_f = 30^\circ$; $F_1W_6VH_CJ_2$.

Figure 28.- Concluded.

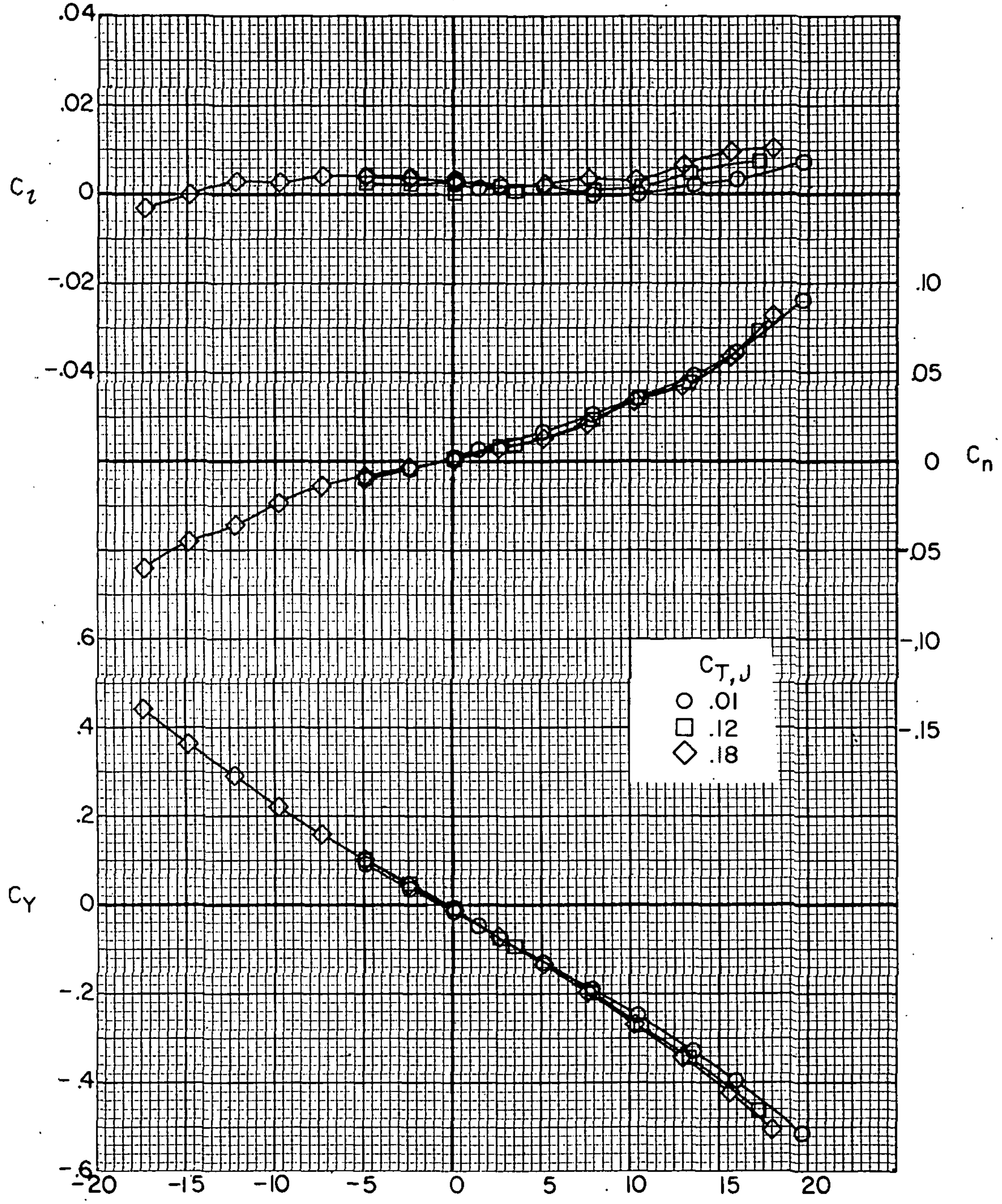

(a) $i_w = 0^\circ$; $\delta_f = 0^\circ$; $\alpha = 0^\circ$; $F_1W_1VH_CJ_2$.

Figure 29.- Effect of auxiliary engine thrust coefficient on airframe lateral aerodynamics. $i_t = 0^\circ$.

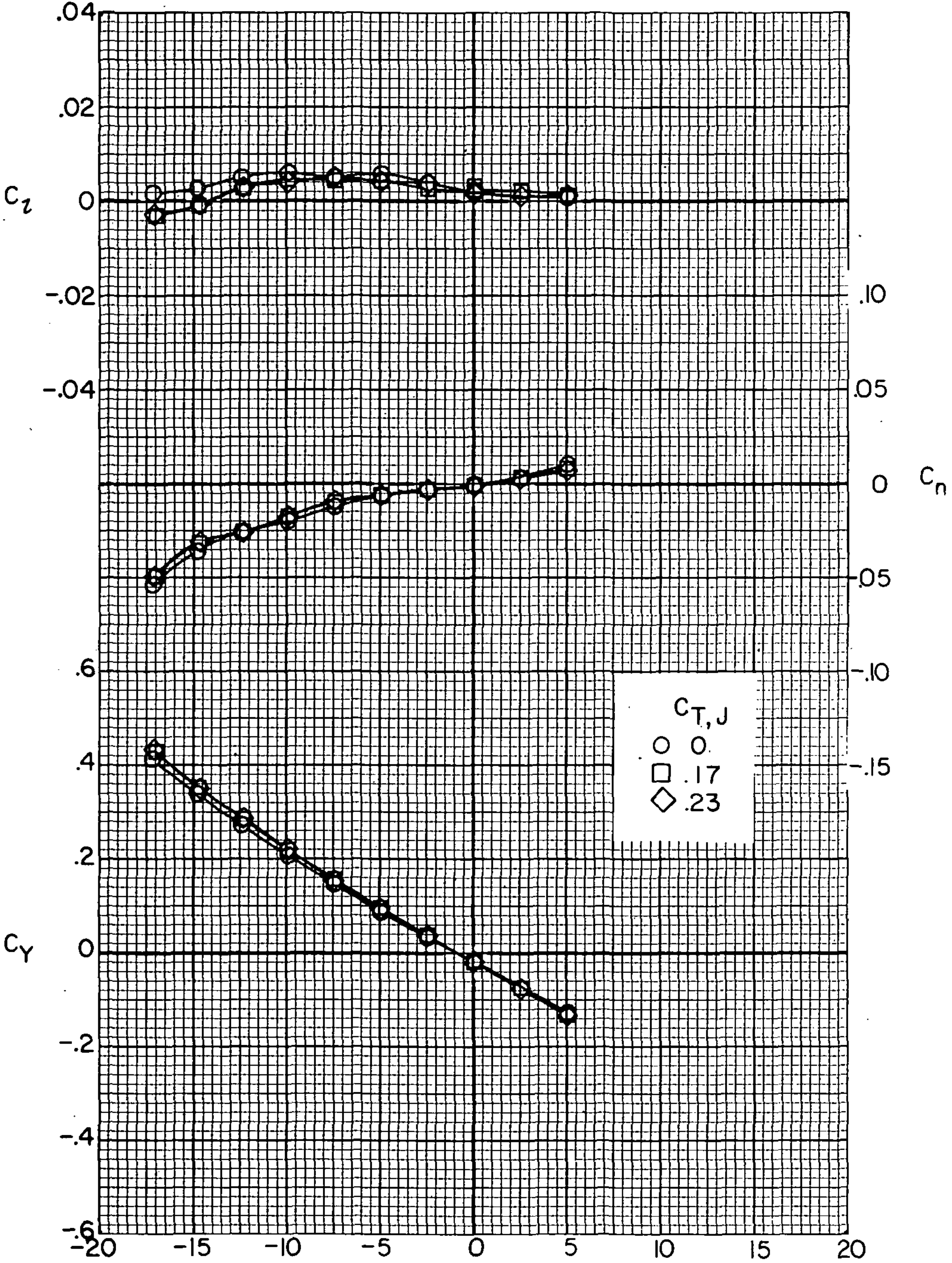

(b) $i_w = 0^\circ$; $\delta_f = 0^\circ$; $\alpha = 5^\circ$; $F_1W_1VH_CJ_2$.

Figure 29.- Continued.

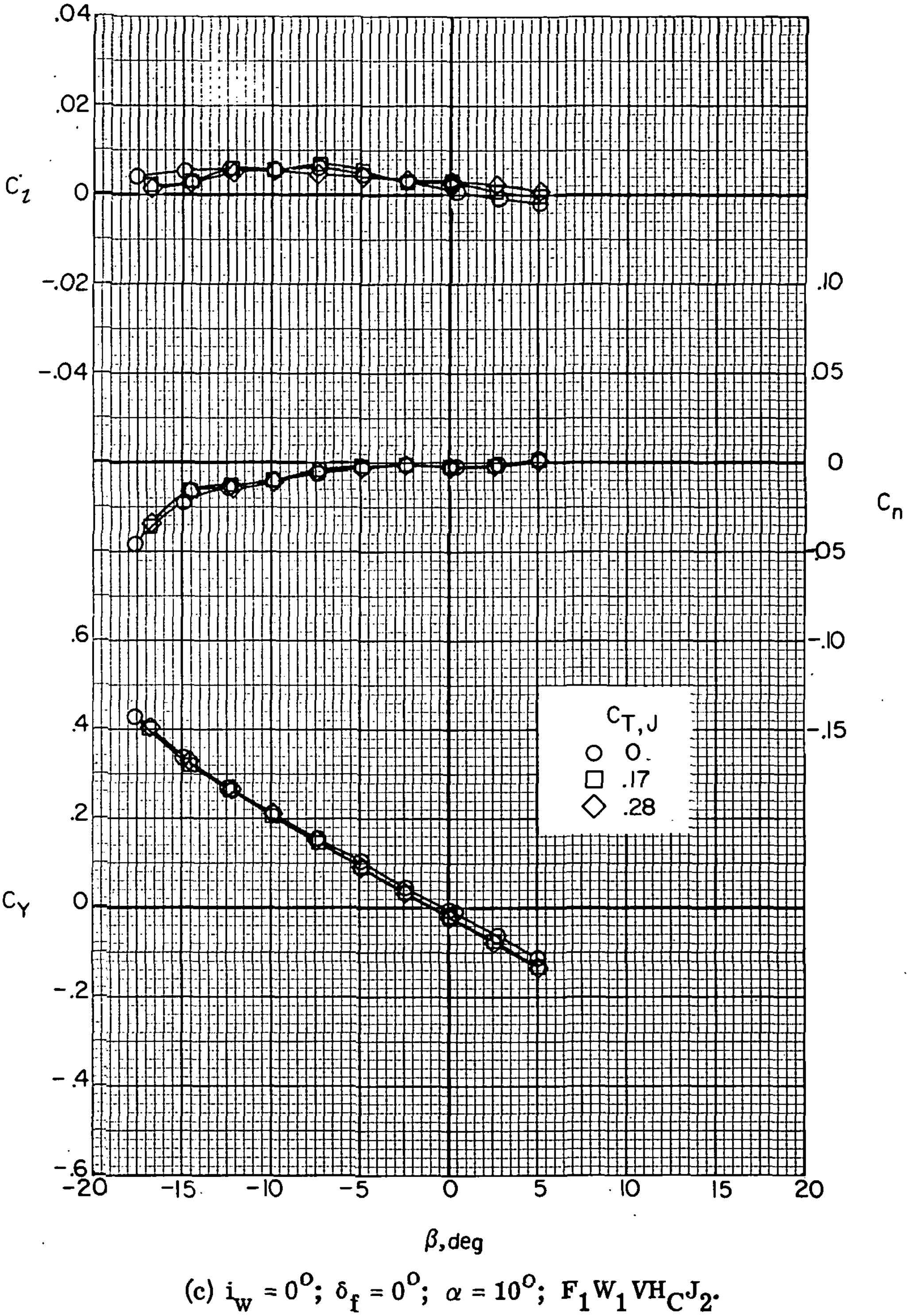

(c) $i_w = 0^o$; $\delta_f = 0^o$; $\alpha = 10^o$; $F_1W_1VH_CJ_2$.

Figure 29.- Continued.

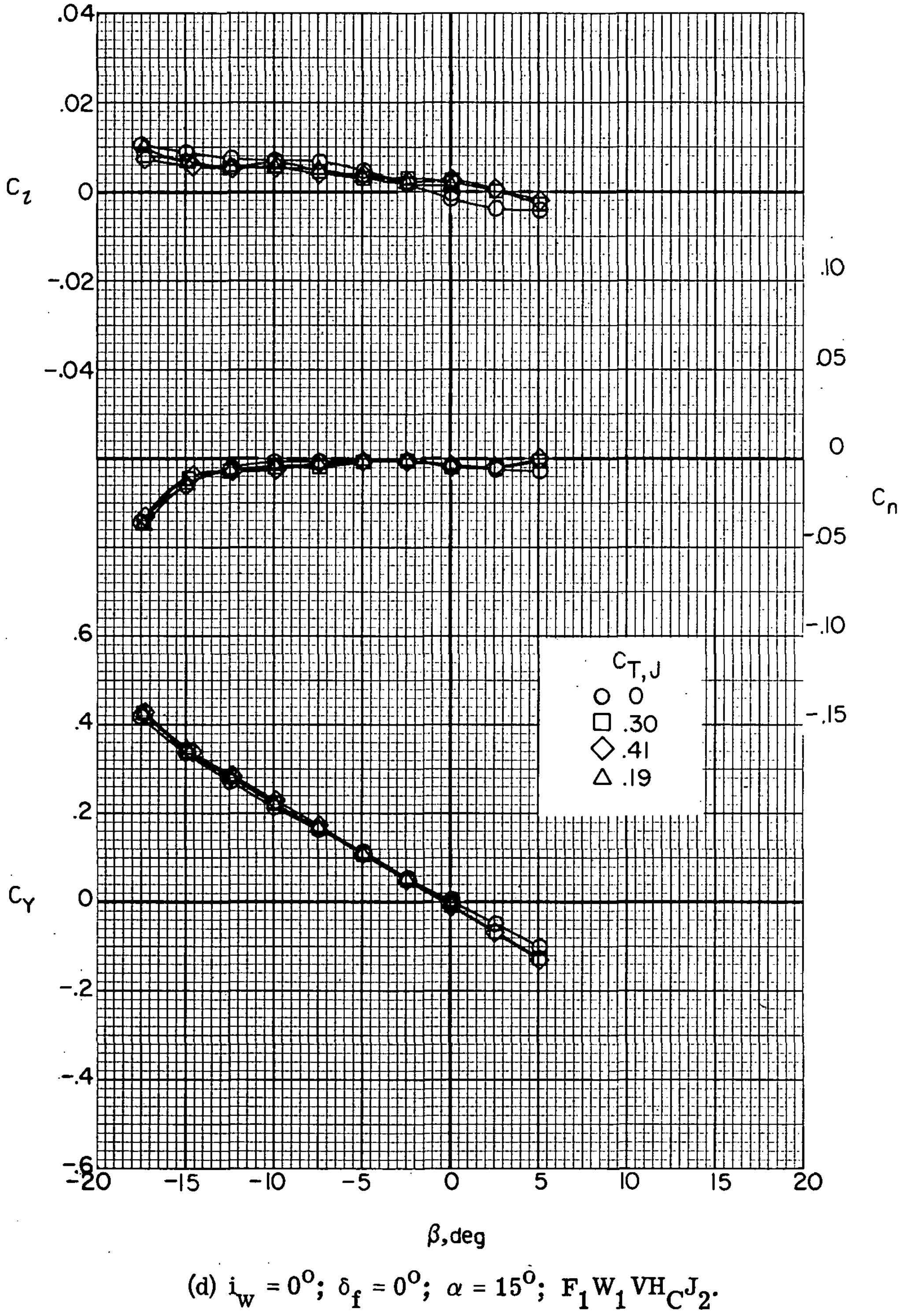

(d) $i_w = 0^\circ$; $\delta_f = 0^\circ$; $\alpha = 15^\circ$; $F_1W_1VH_CJ_2$.

Figure 29.- Continued.

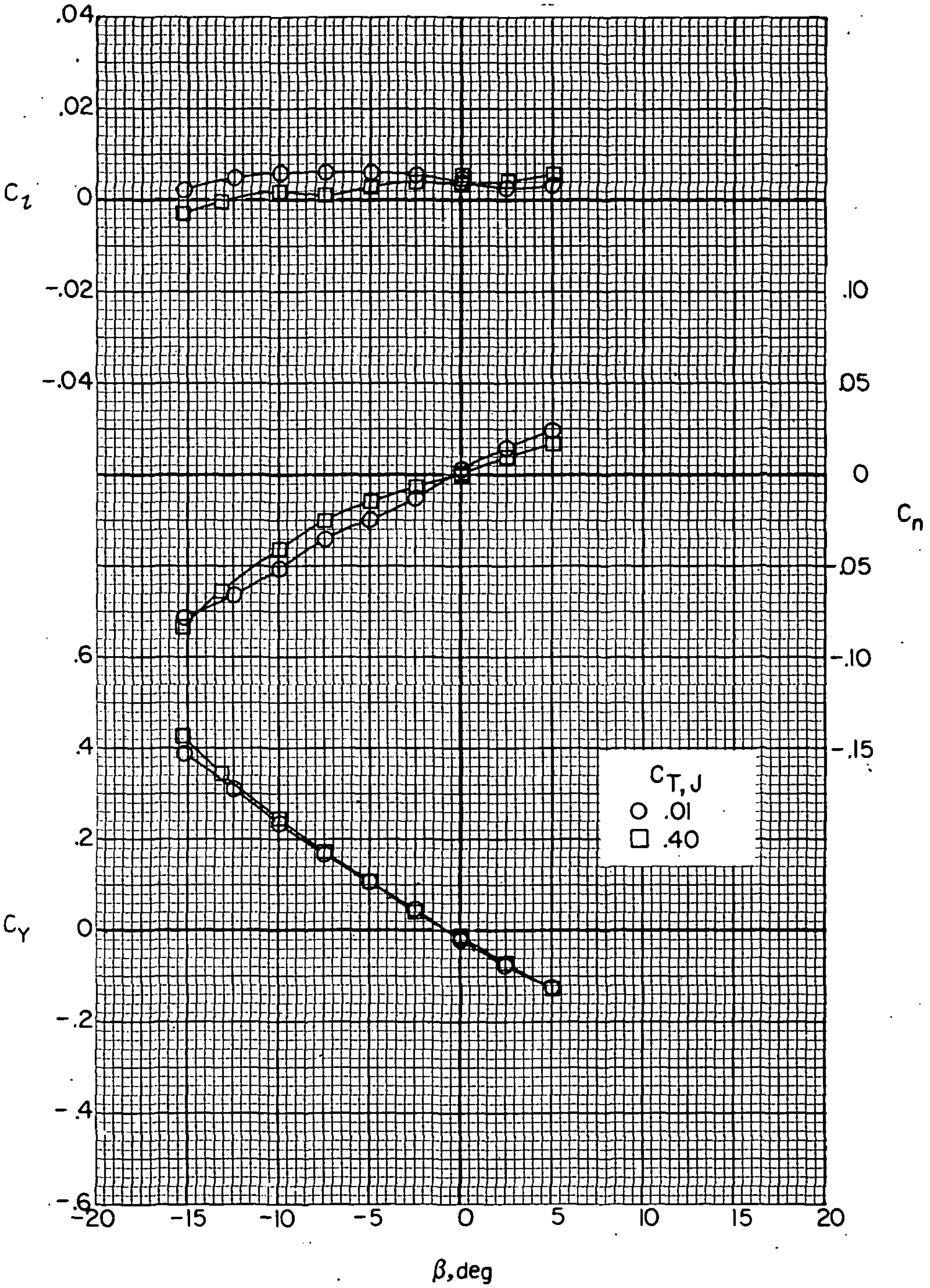

(e) $i_w = 0^\circ$; $\delta_f = 30^\circ$; $\alpha = -5^\circ$; $F_1W_5VH_CJ_2$.

Figure 29.- Continued.

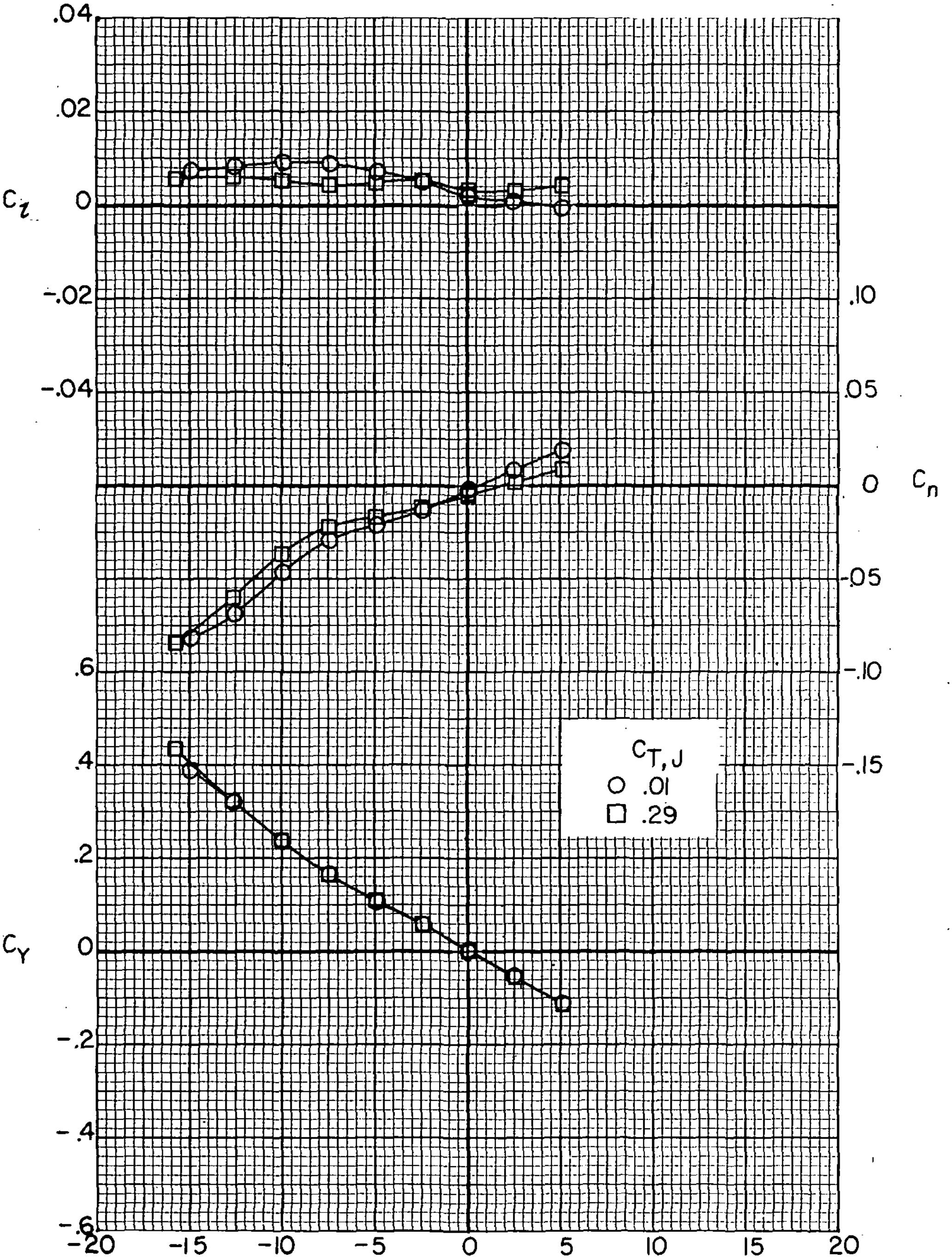

(f) $i_w = 0^\circ$; $\delta_f = 30^\circ$; $\alpha = 0^\circ$; $F_1W_5VH_CJ_2$.

Figure 29.- Continued.

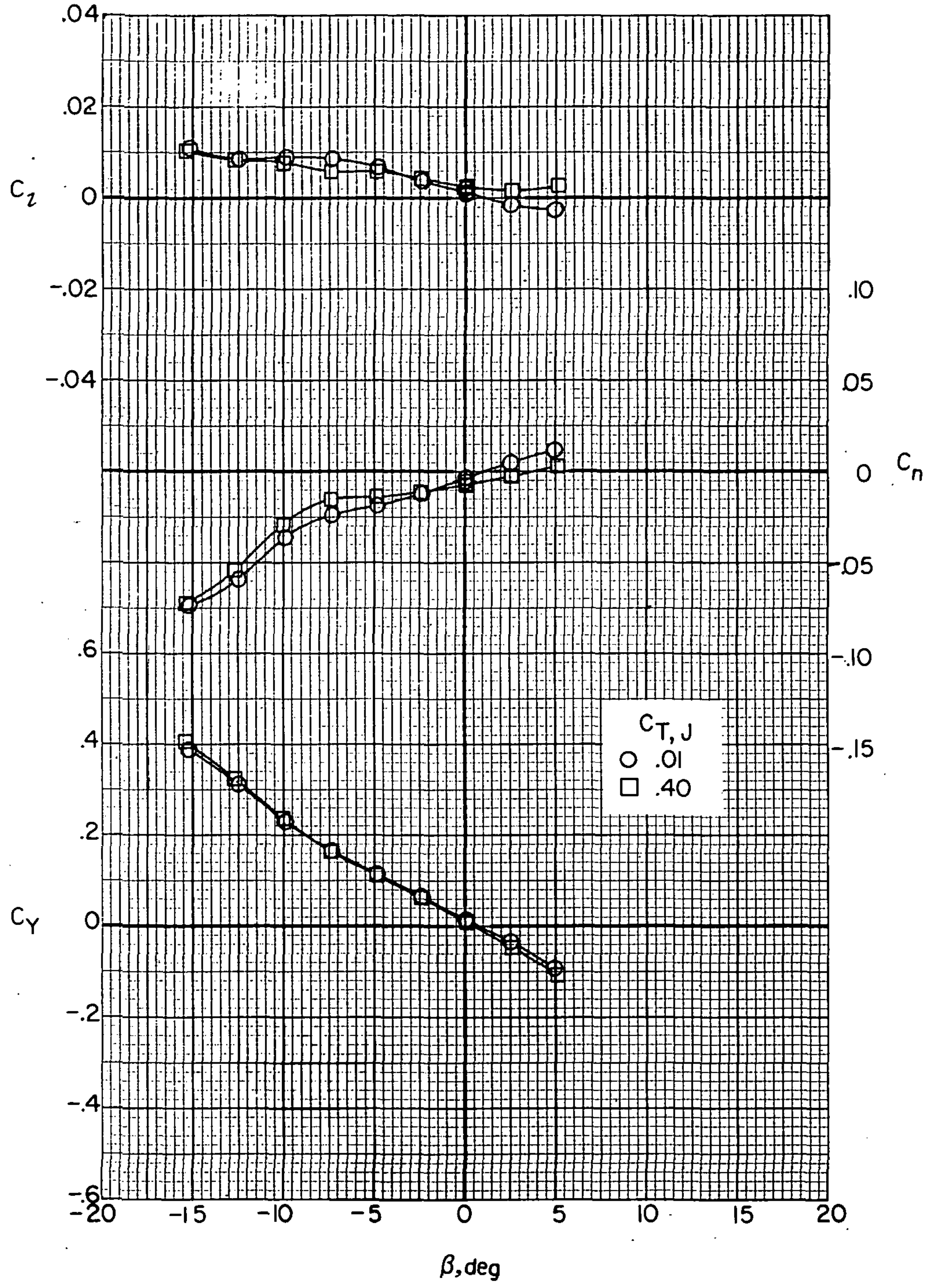

(g) $i_w = 0^\circ$; $\delta_f = 30^\circ$; $\alpha = 5^\circ$; $F_1W_5VH_CJ_2$.

Figure 29.- Continued.

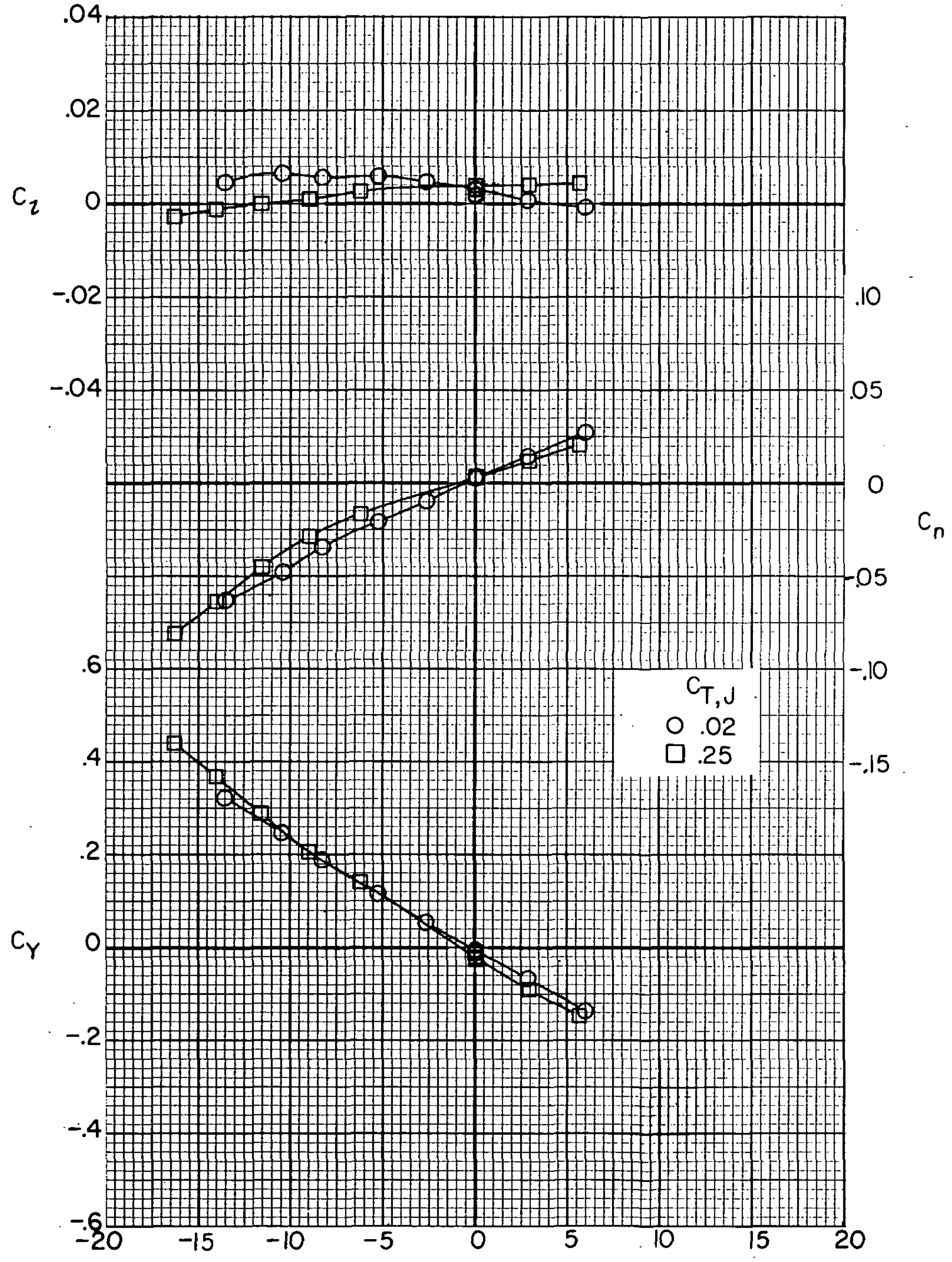

(h) $i_w = 7.5^\circ$; $\delta_f = 0^\circ$; $\alpha = -5^\circ$; $F_1W_2VH_CJ_2$.

Figure 29. - Continued.

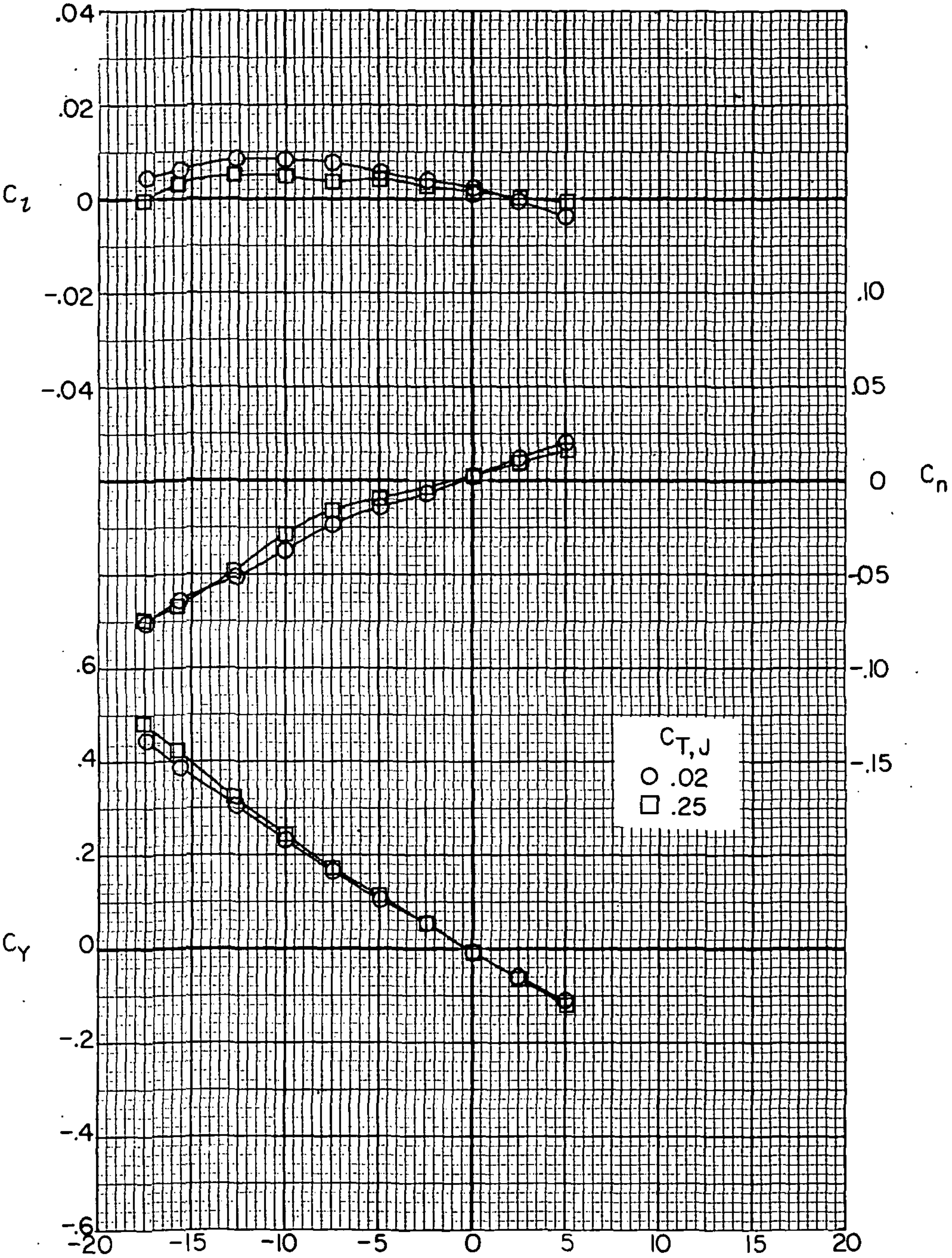

(i) $i_w = 7.5^{\circ}$; $\delta_f = 0^{\circ}$; $\alpha = 0^{\circ}$; $F_1W_2VH_CJ_2$.

Figure 29. - Continued.

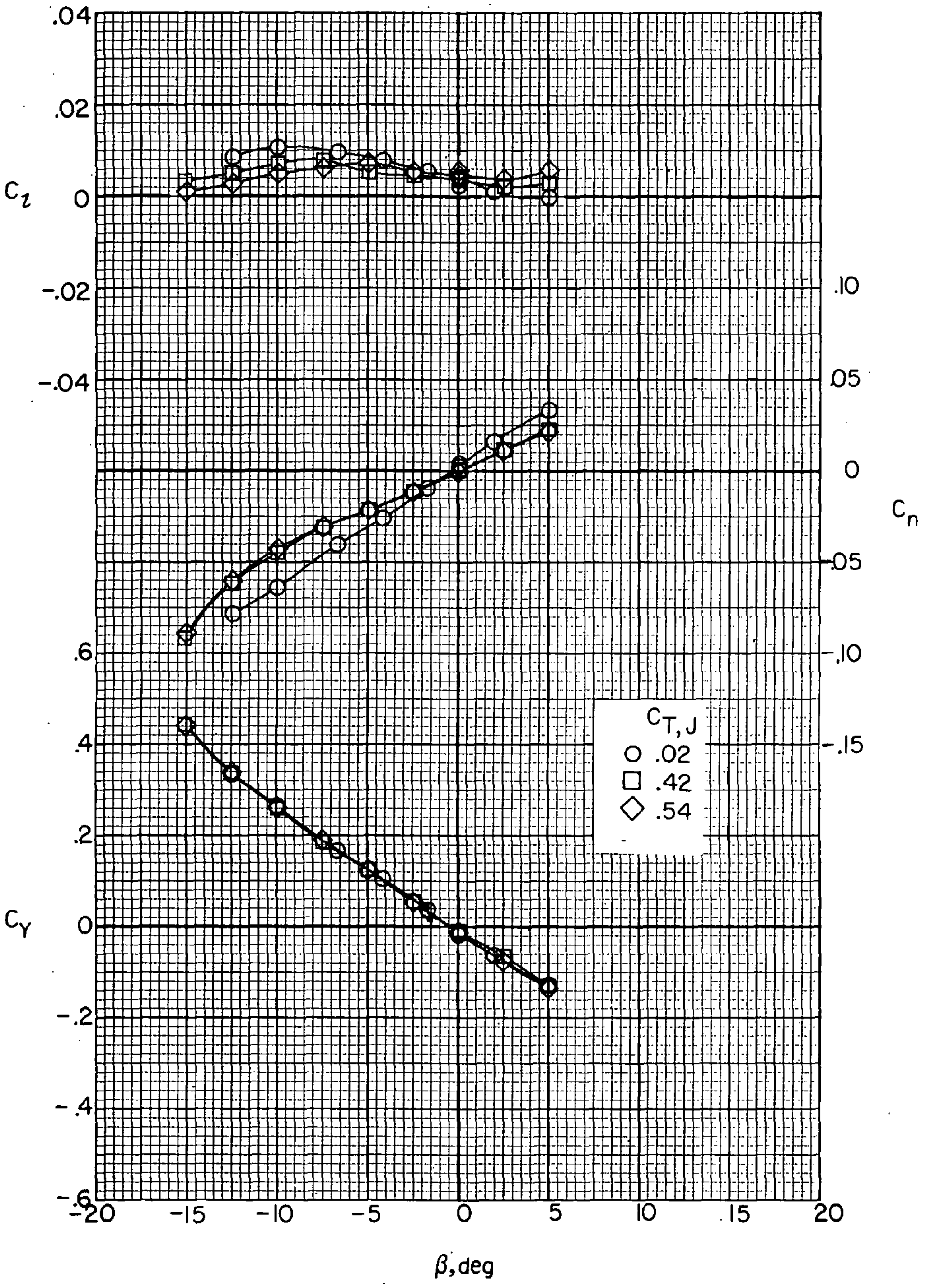

(j) $i_w = 7.5^\circ$; $\delta_f = 30^\circ$; $\alpha = -5^\circ$; $F_1W_6VH_CJ_2$.

Figure 29.- Continued.

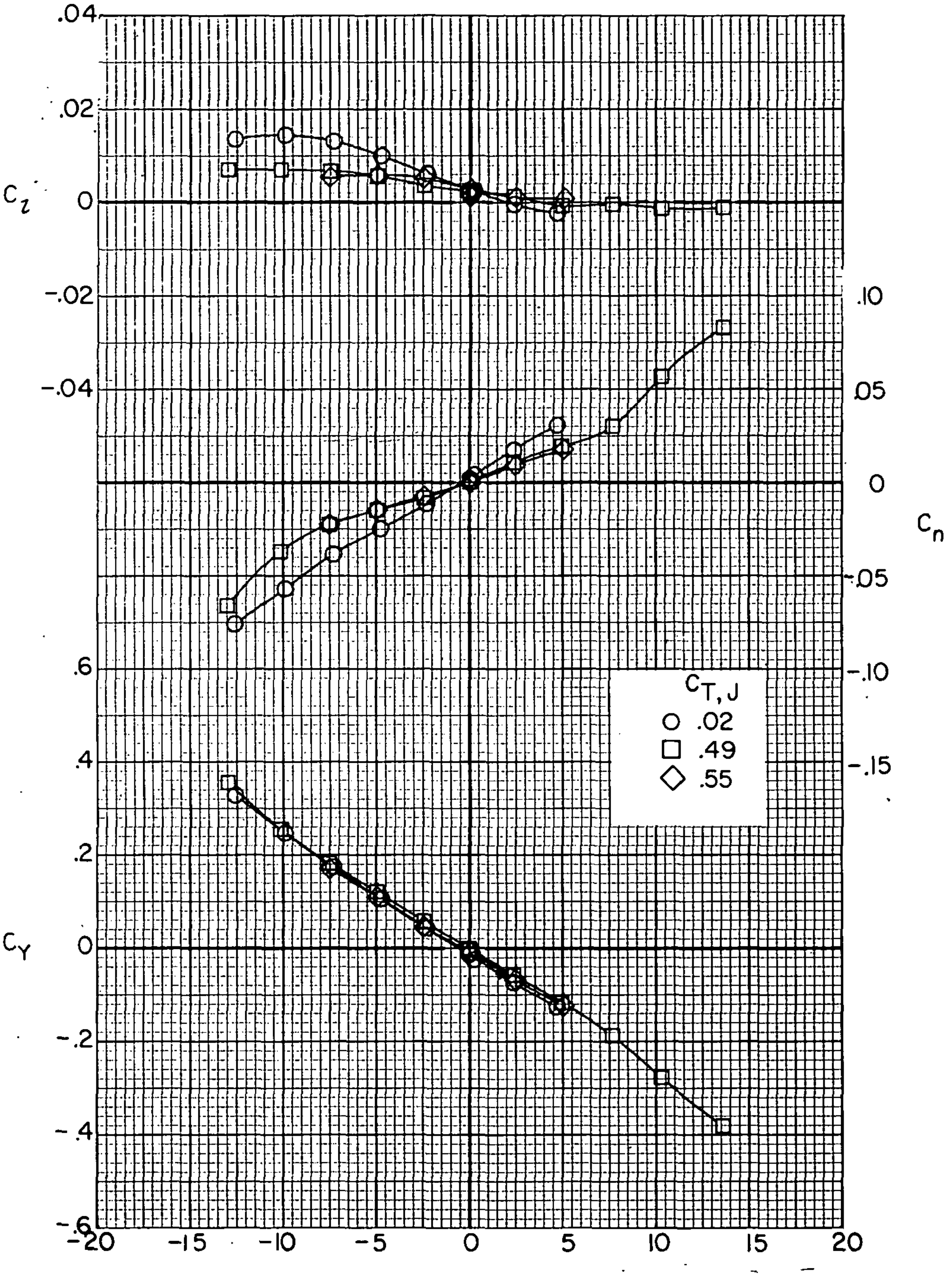

(k) $i_w = 7.5^\circ$; $\delta_f = 30^\circ$; $\alpha = 0^\circ$; $F_1W_6VH_CJ_2$.

Figure 29.- Continued.

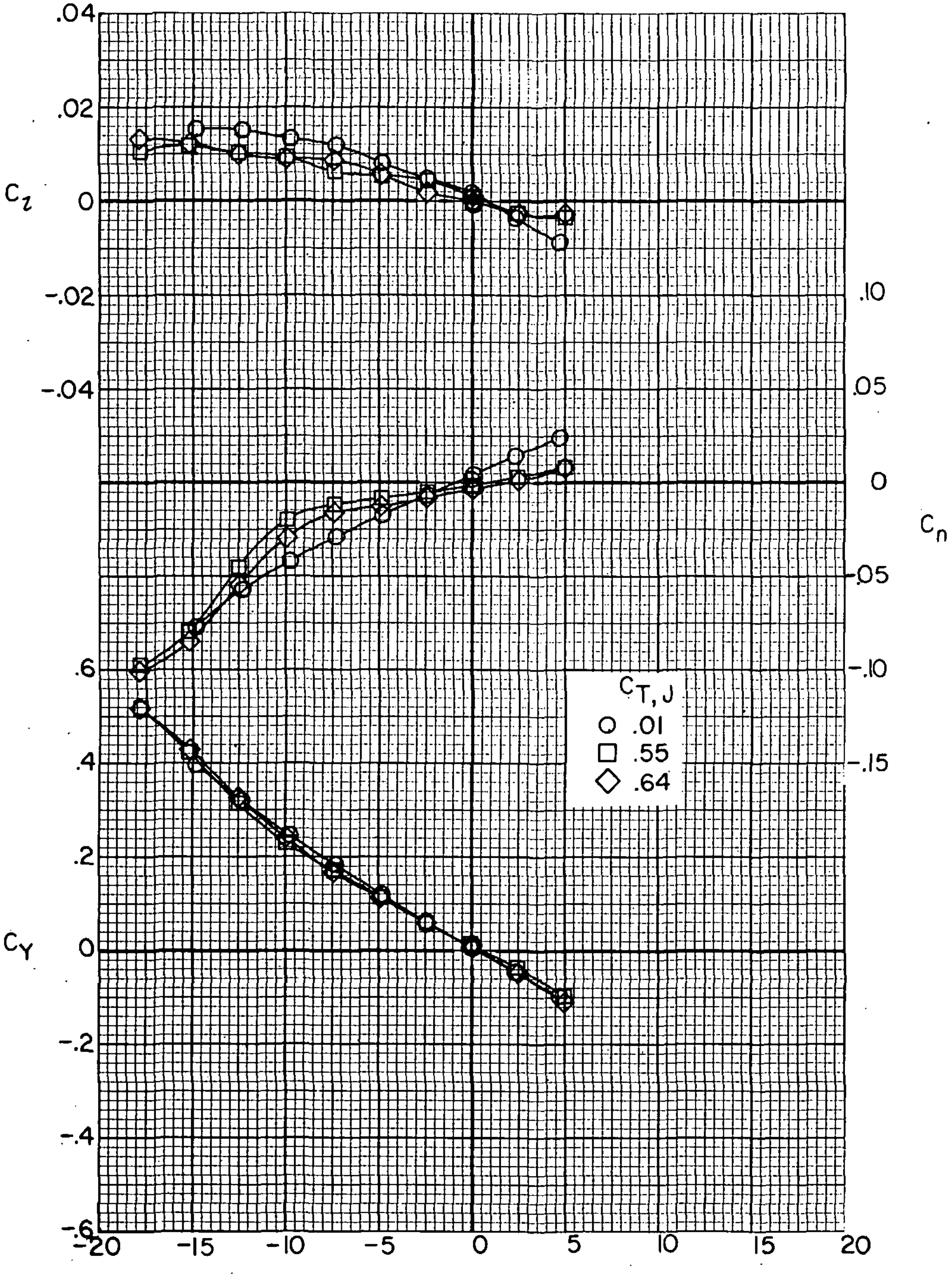

(l) $i_w = 7.5^{\circ}$; $\delta_f = 30^{\circ}$; $\alpha = 5^{\circ}$; $F_1W_6VH_CJ_2$.

Figure 29.- Concluded.

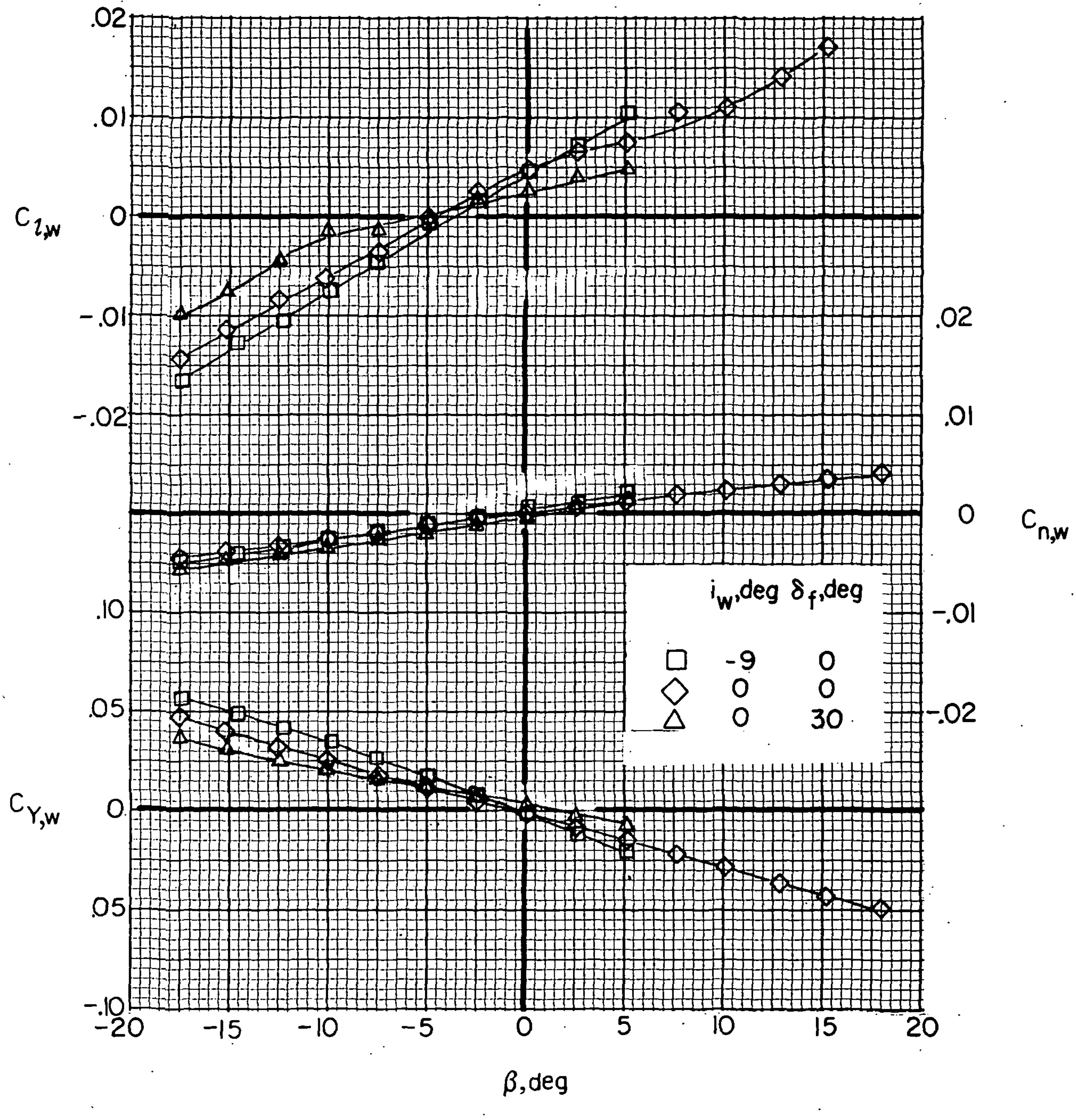

Figure 30.- Effect of wing incidence and flap deflection on wing lateral aerodynamics with jets and tails removed (F_1W_x). $\alpha = 0^o$.

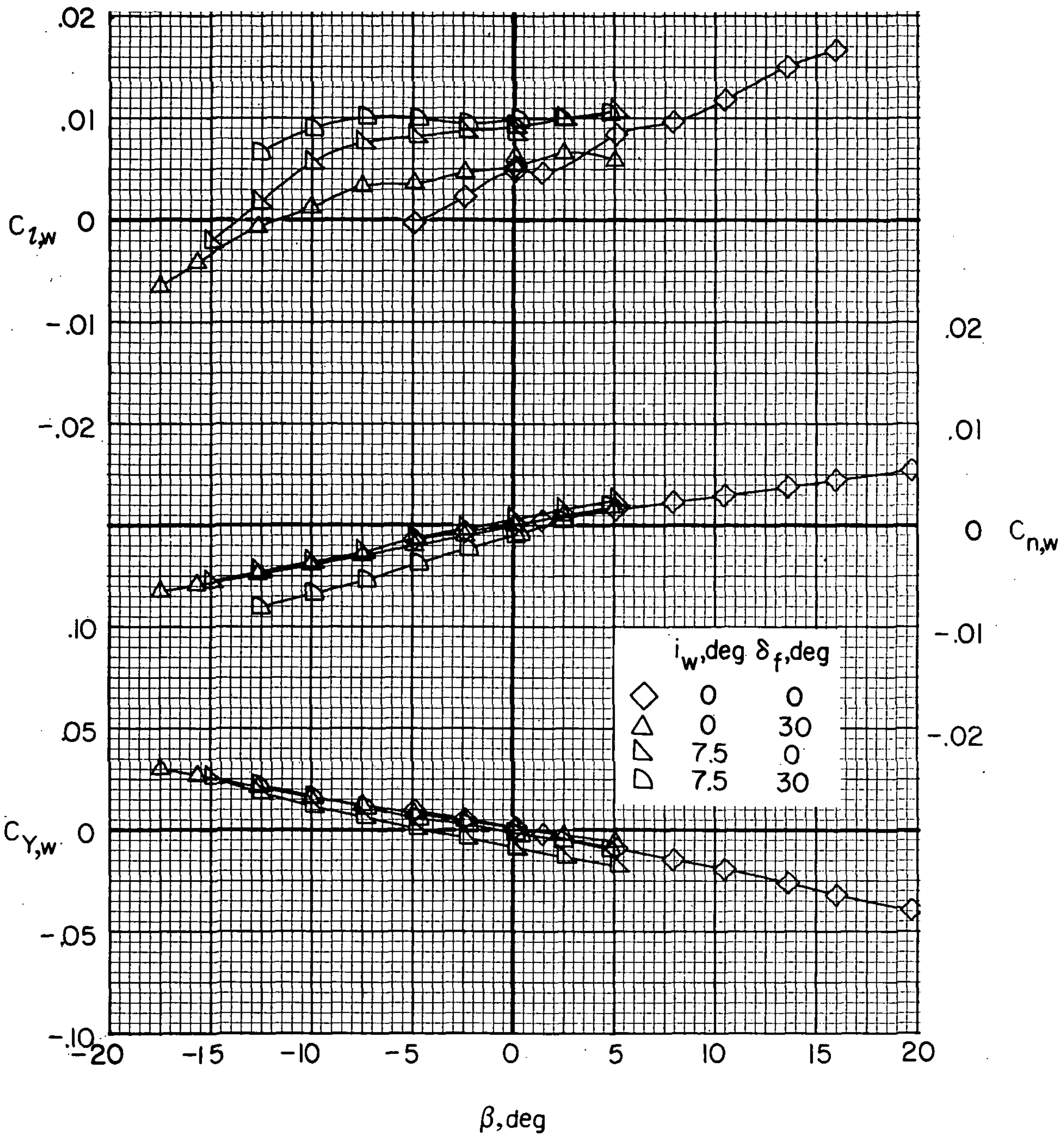

Figure 31.- Effect of wing incidence and flap deflection on wing lateral aerodynamics with jets on ($F_1W_xVH_CJ_2$). $C_{T,J} \approx 0$; $\alpha = 0^o$.

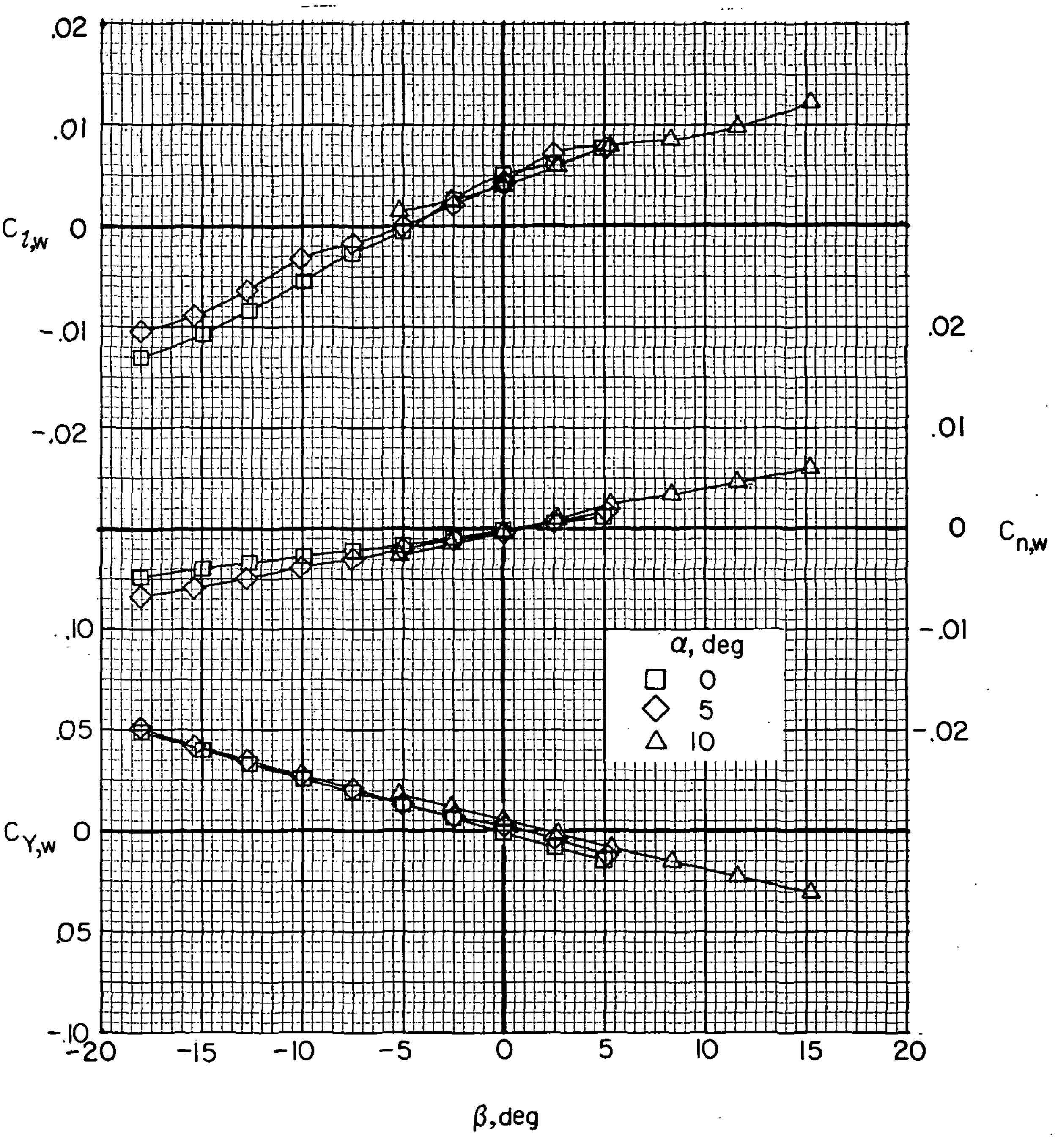

(a) Jets removed; $i_w = 0^o$; $\delta_f = 0^o$; $F_1W_1VH_C$.

Figure 32.- Effect of angle of attack on wing lateral aerodynamics.

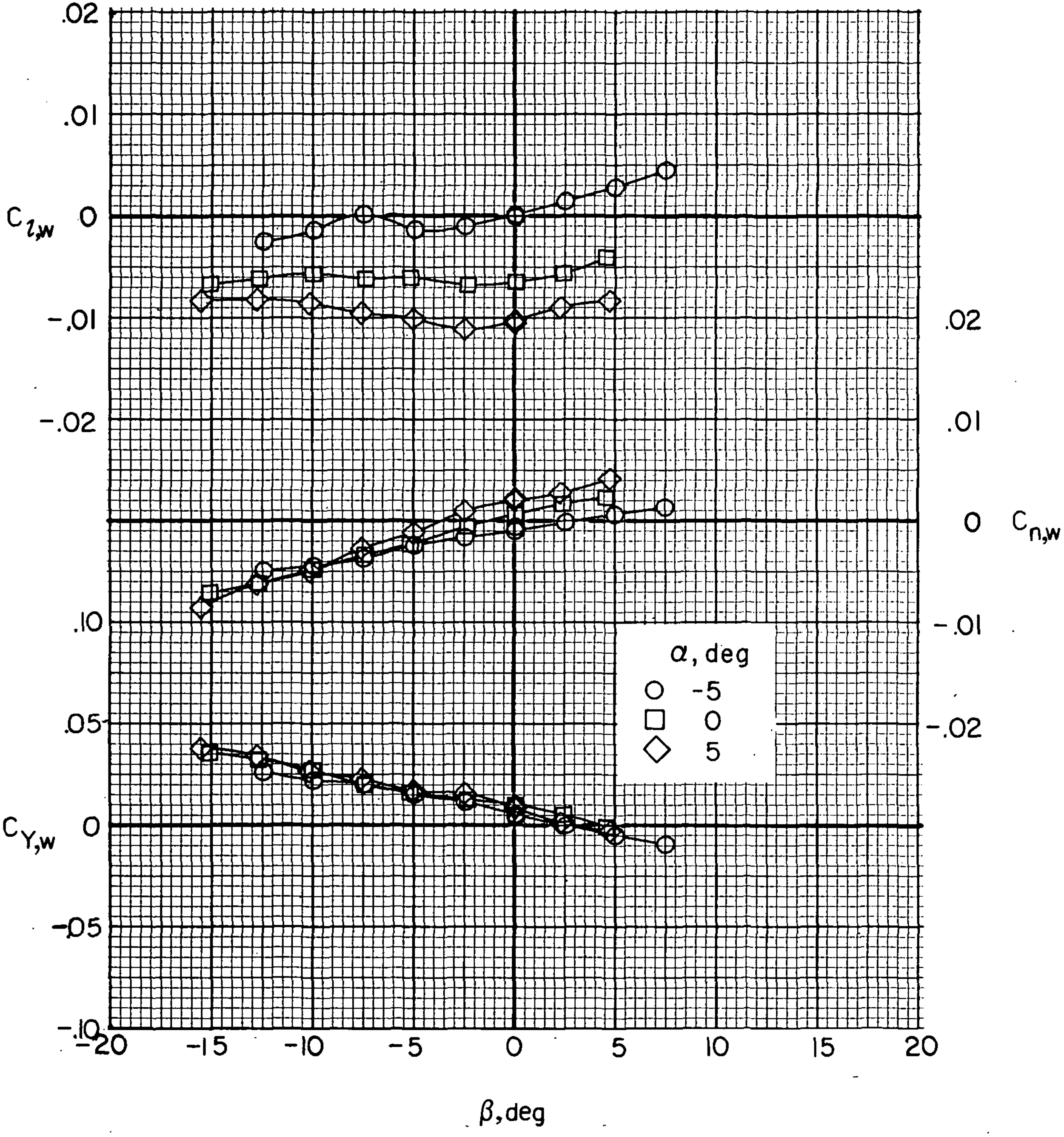

(b) Jets removed; $i_w = 7.5^{\circ}$; $\delta_f = 30^{\circ}$; $F_1W_6VH_C$.

Figure 32.- Continued.

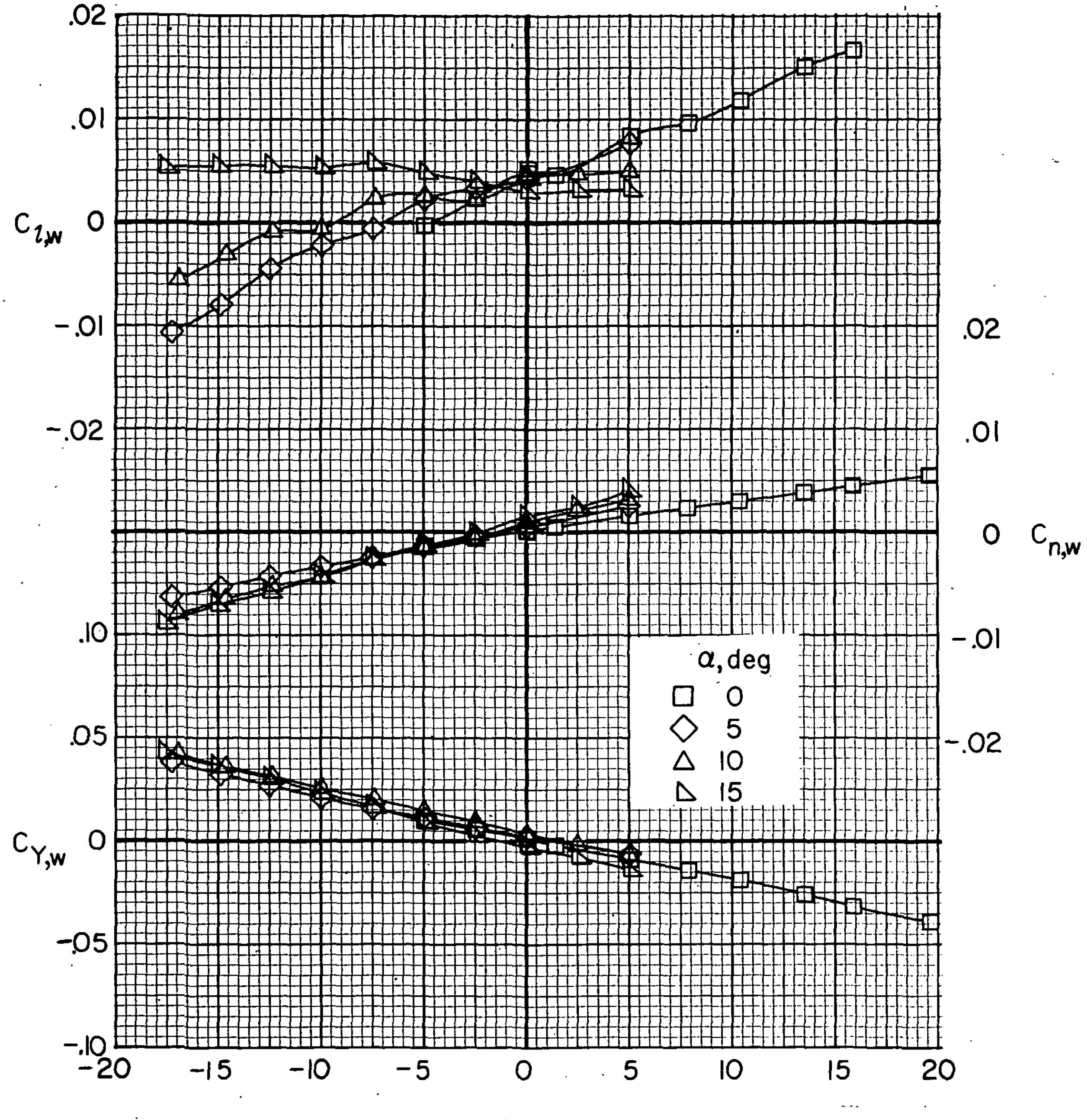

(c) Jets on; $C_{T,J} \approx 0$; $i_w = 0^\circ$; $\delta_f = 0^\circ$; $F_1W_1VH_CJ_2$.

Figure 32.- Continued.

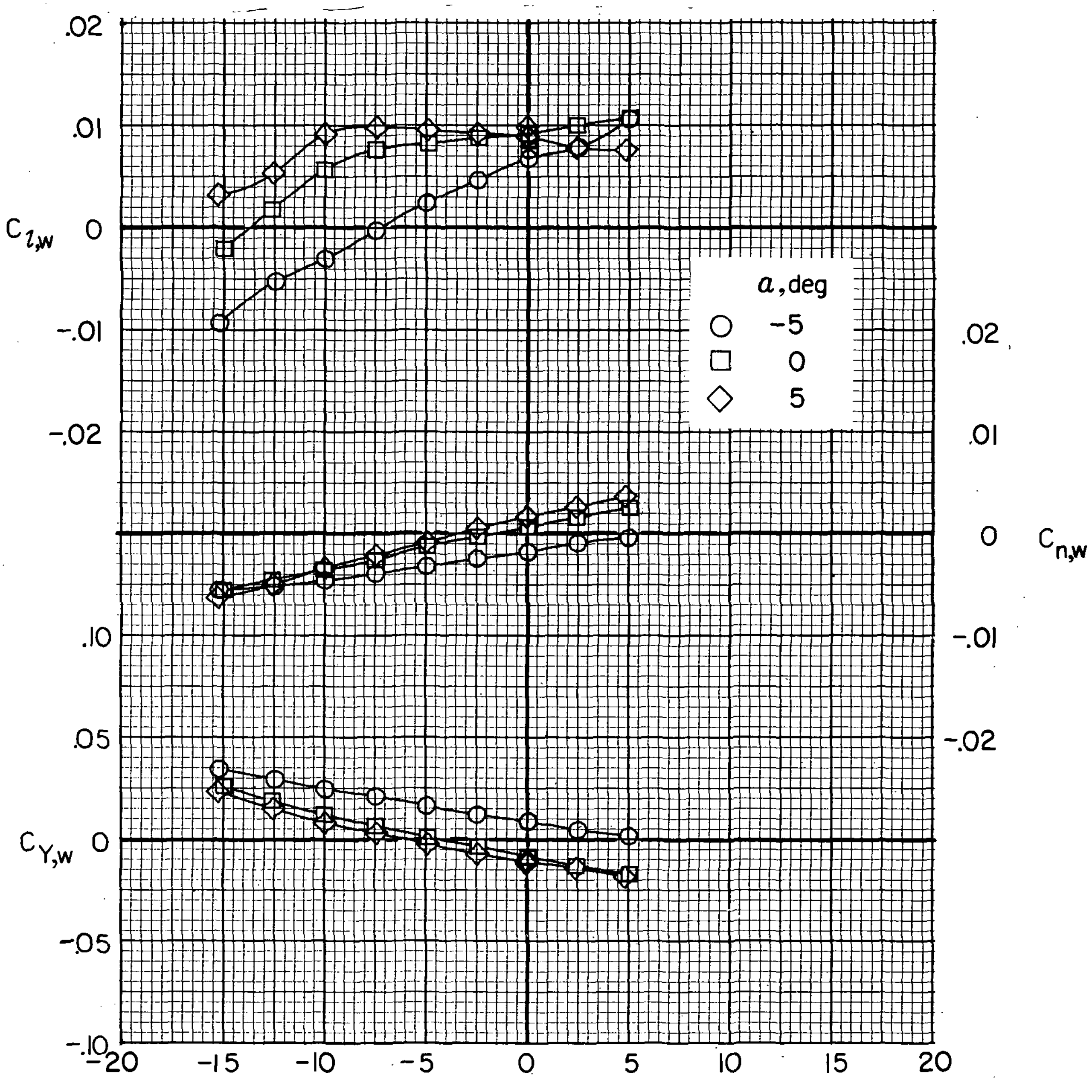

(d) Jets on ; $C_{T,J} \approx 0$; $i_w = 0^{\circ}$; $\delta_f = 30^{\circ}$; $F_1W_5VH_CJ_2$.

Figure 32.- Continued.

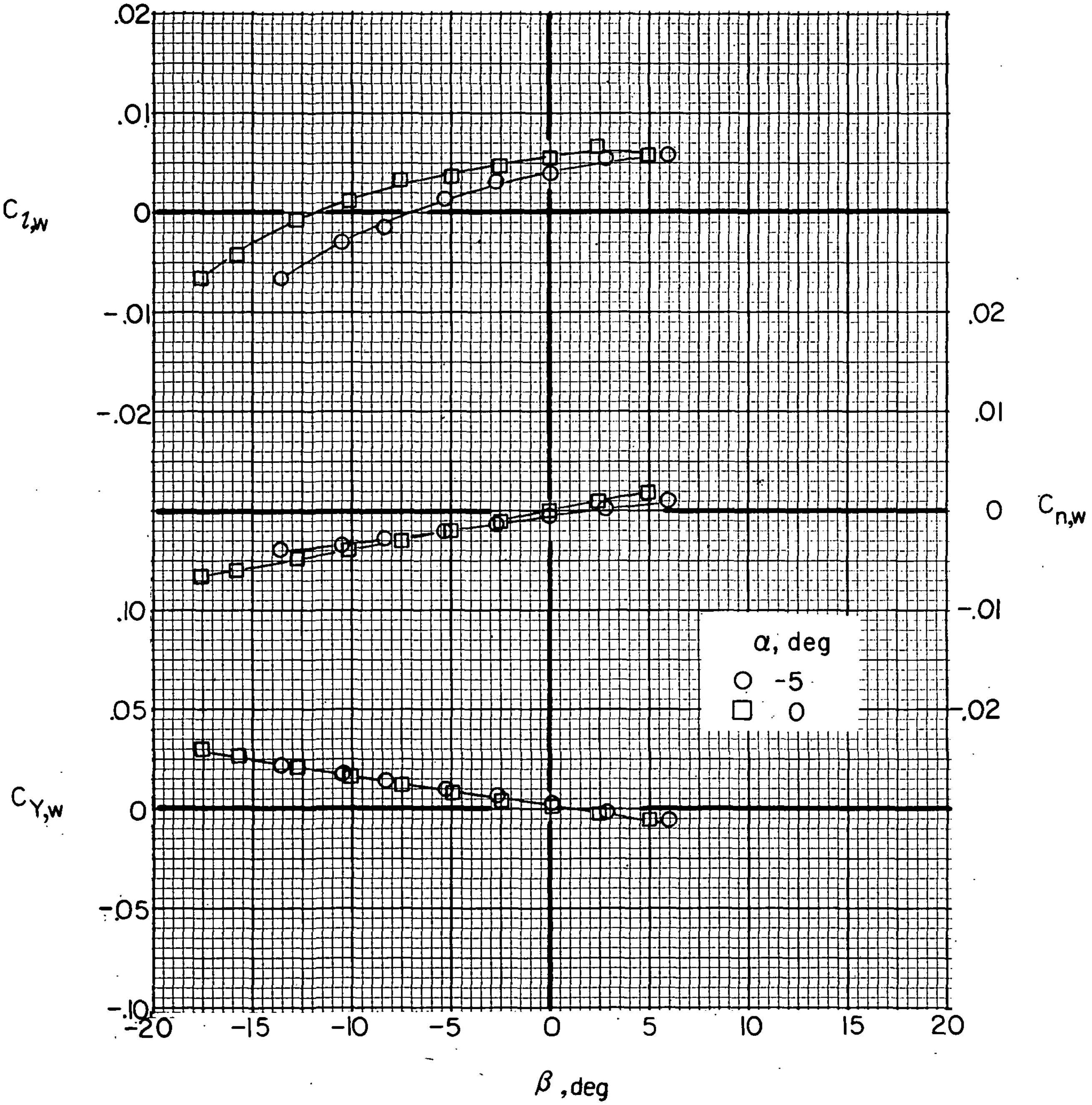

(e) Jets on; $C_{T,J} \approx 0$; $i_w = 7.5^o$; $\delta_f = 0^o$; $F_1W_2VH_CJ_2$.

Figure 32. - Continued.

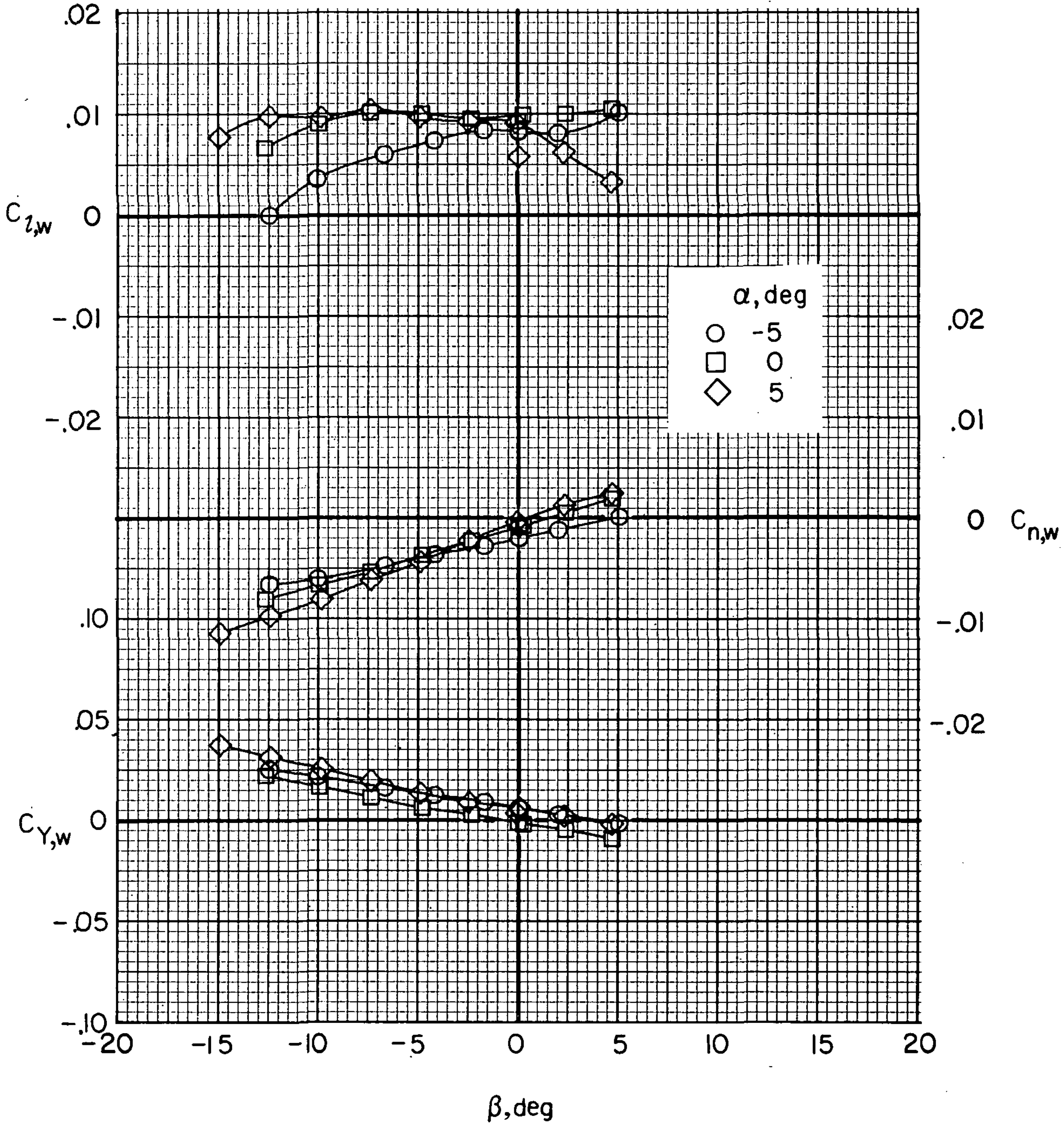

(f) Jets on; $C_{T,J} \approx 0$; $i_w = 7.5^{\circ}$; $\delta_f = 30^{\circ}$; $F_1W_6VH_CJ_2$.

Figure 32.- Concluded.

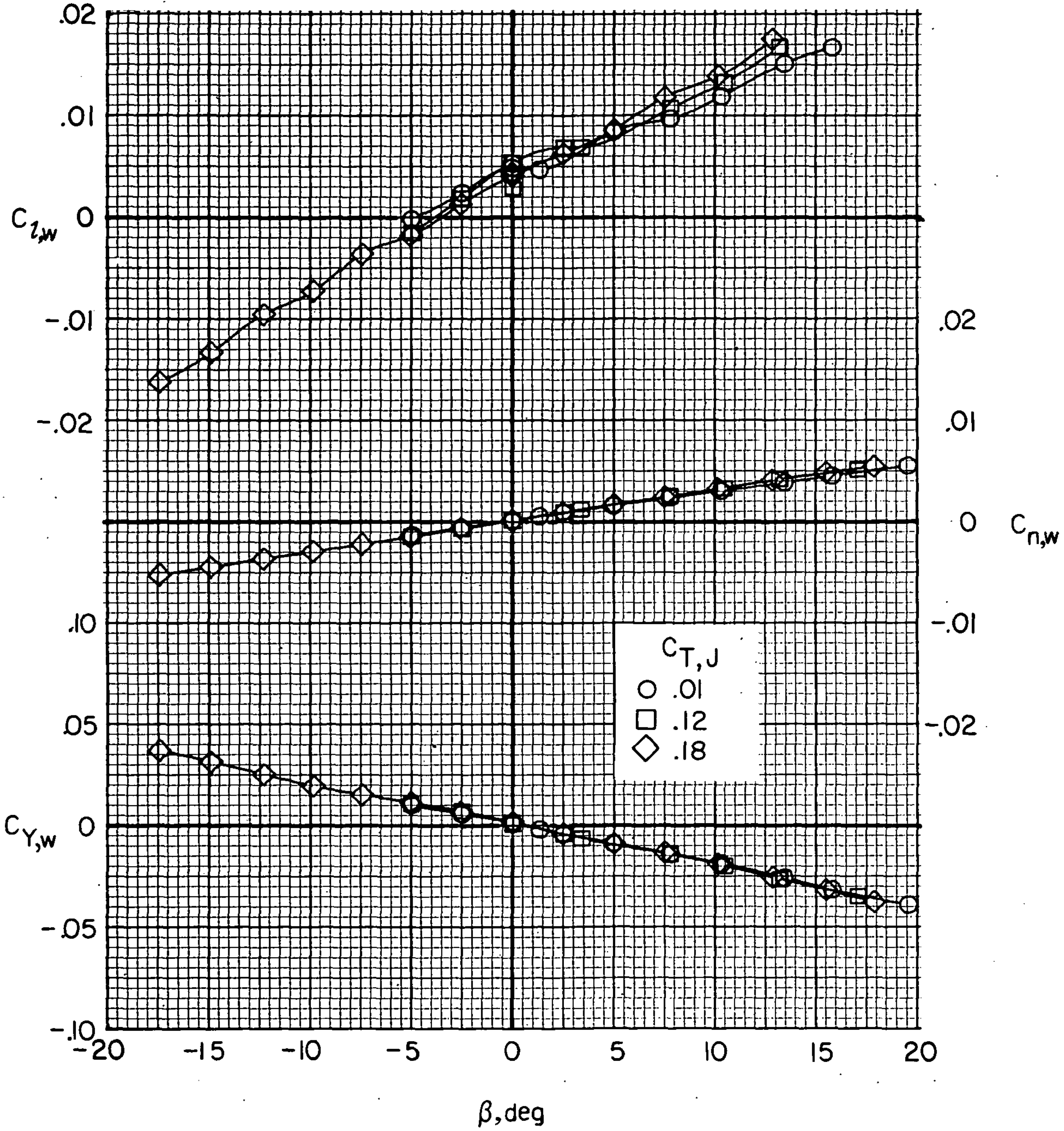

(a) $i_w = 0^\circ$; $\delta_f = 0^\circ$; $F_1W_1VH_CJ_2$.

Figure 33.- Effect of auxiliary engine thrust coefficient on wing lateral aerodynamics. $\alpha = 0^\circ$.

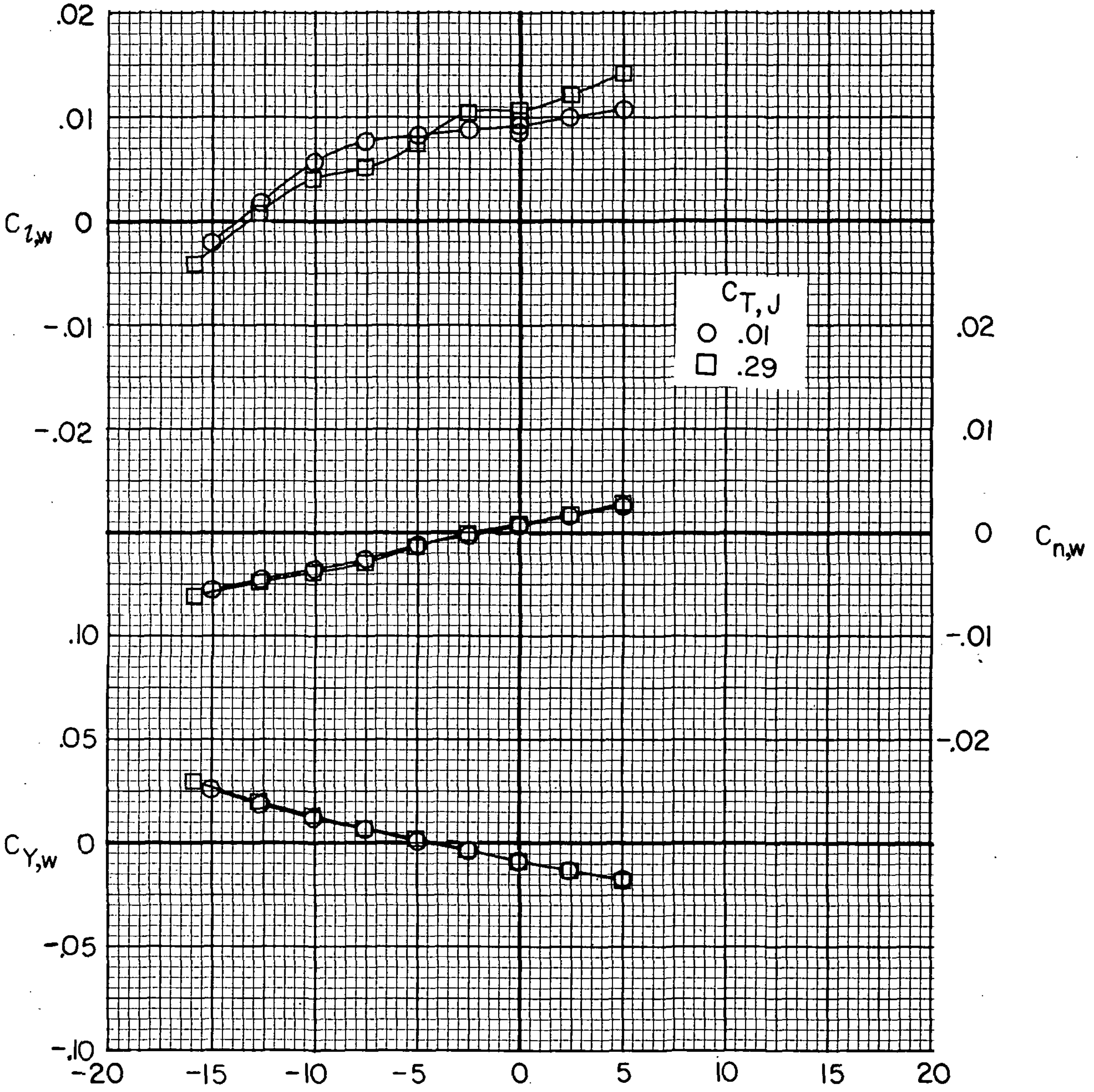

(b) $i_w = 0^\circ$; $\delta_f = 30^\circ$; $F_1W_5VH_CJ_2$.

Figure 33.- Continued.

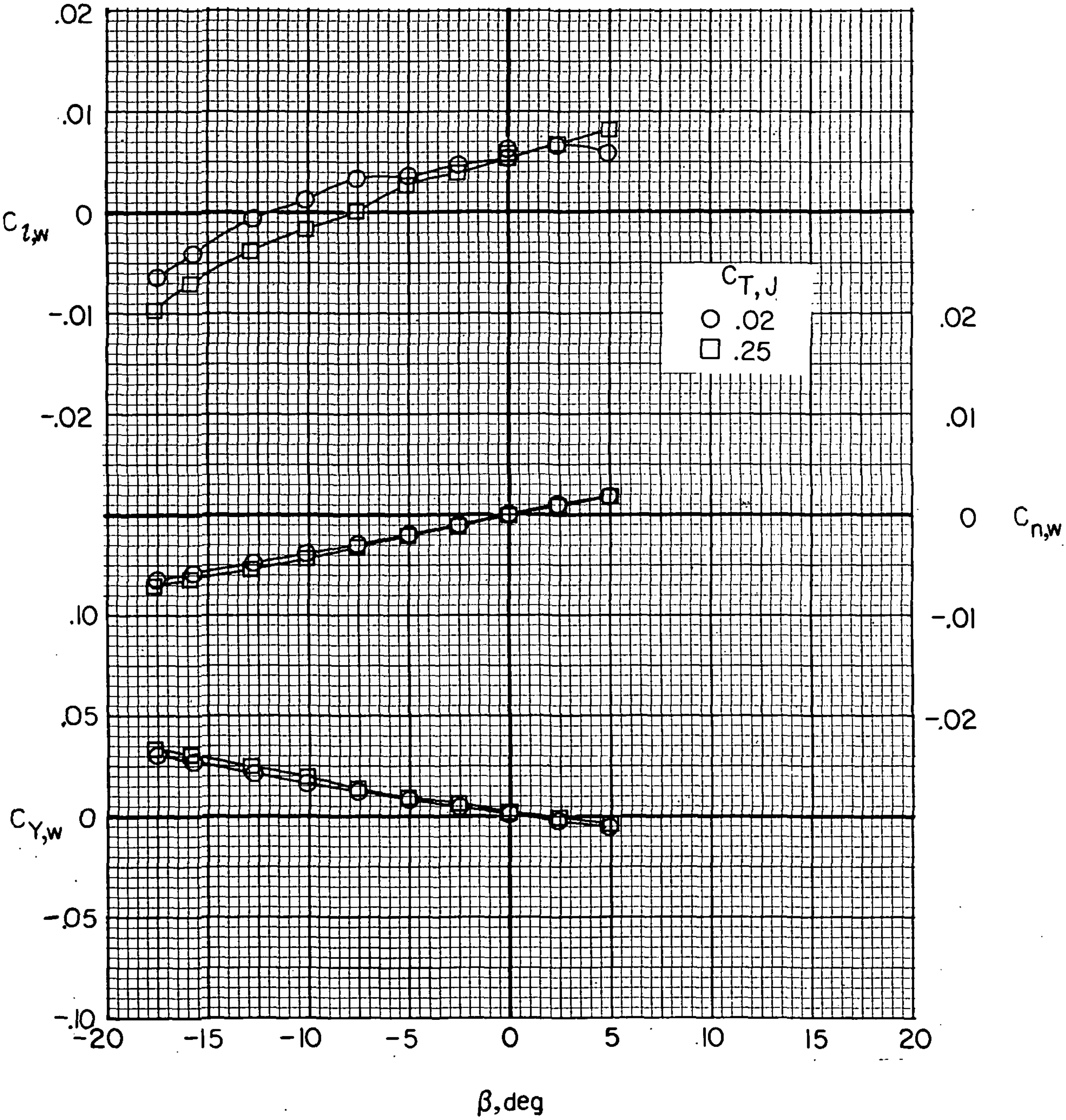

(c) $i_w = 7.5^{\circ}$; $\delta_f = 0^{\circ}$; $F_1W_2VH_CJ_2$.

Figure 33.- Continued.

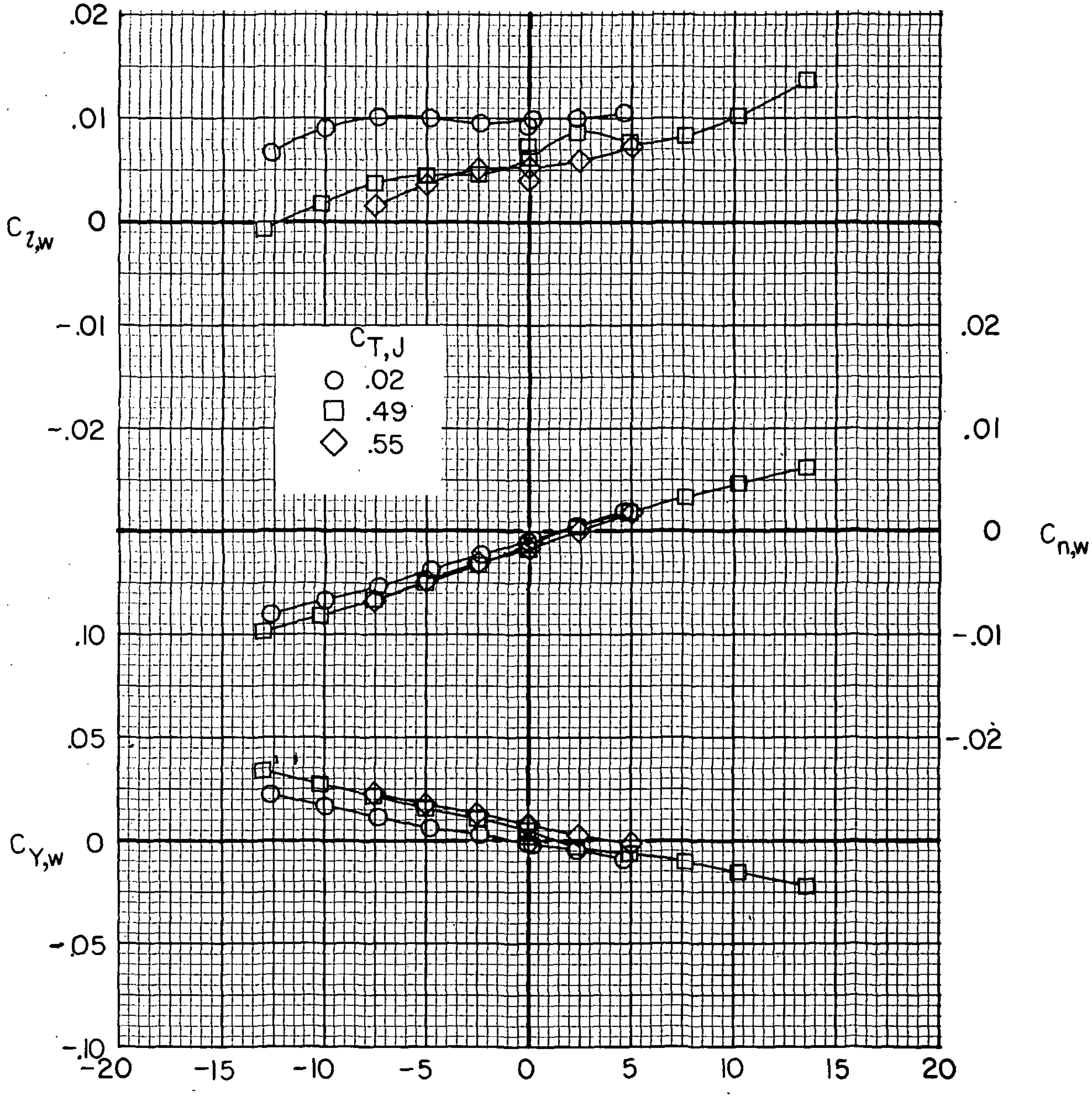

(d) $i_w = 7.5^\circ$; $\delta_f = 30^\circ$; $F_1W_6VH_CJ_2$.

Figure 33.- Concluded.

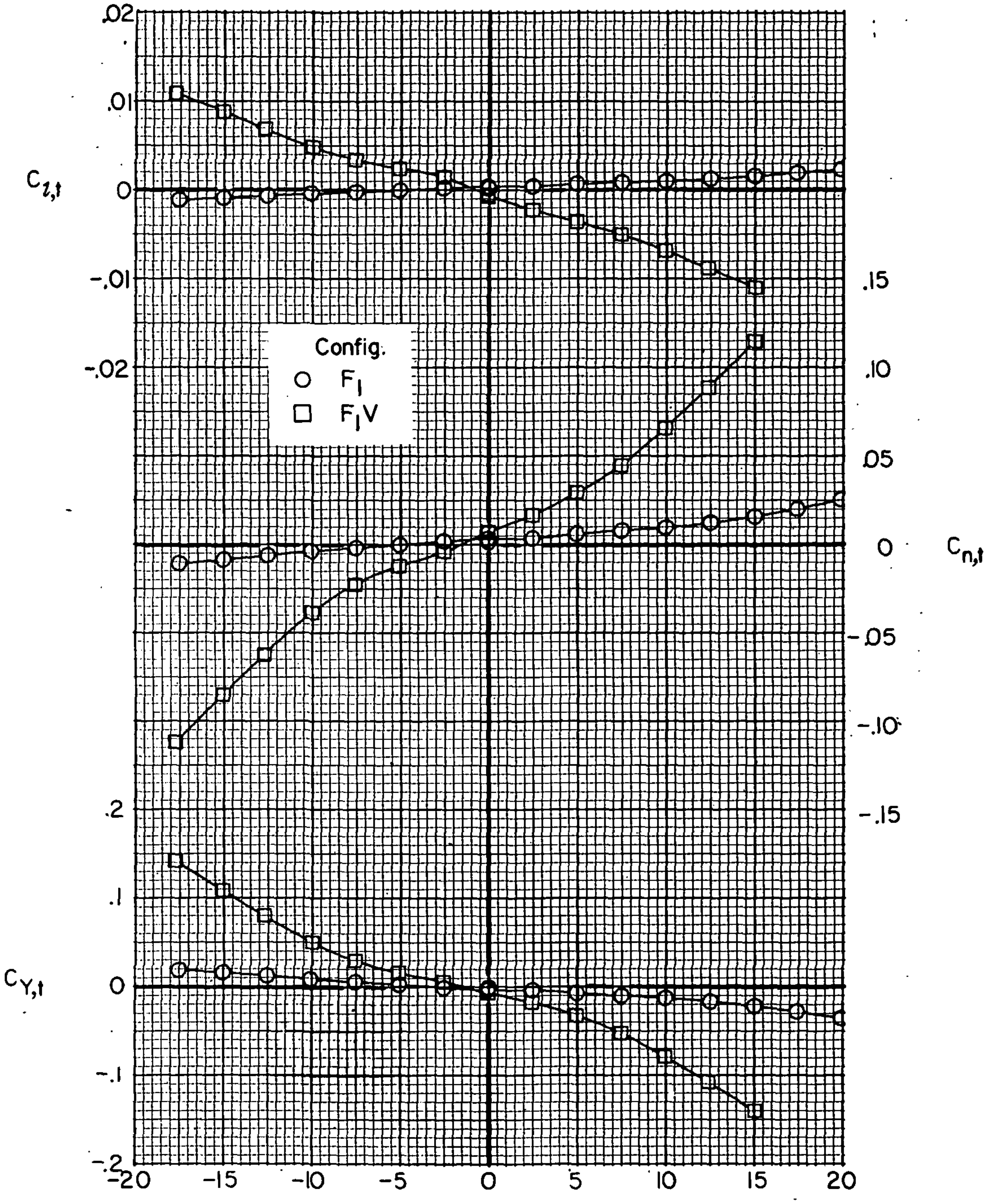

Figure 34.- Effect of vertical tail on tail lateral aerodynamics.

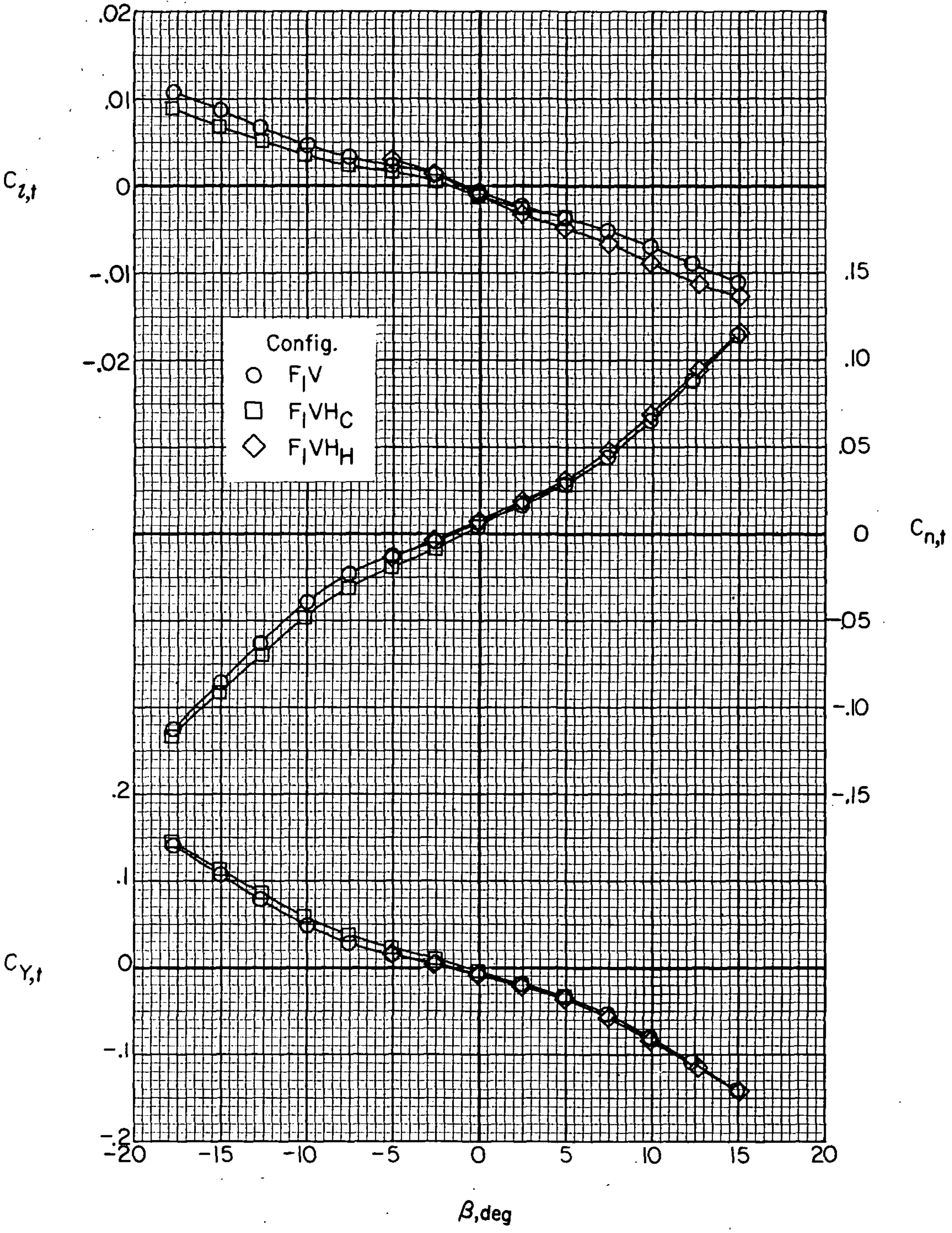

Figure 35.- Effect of horizontal tail on tail lateral aerodynamics.

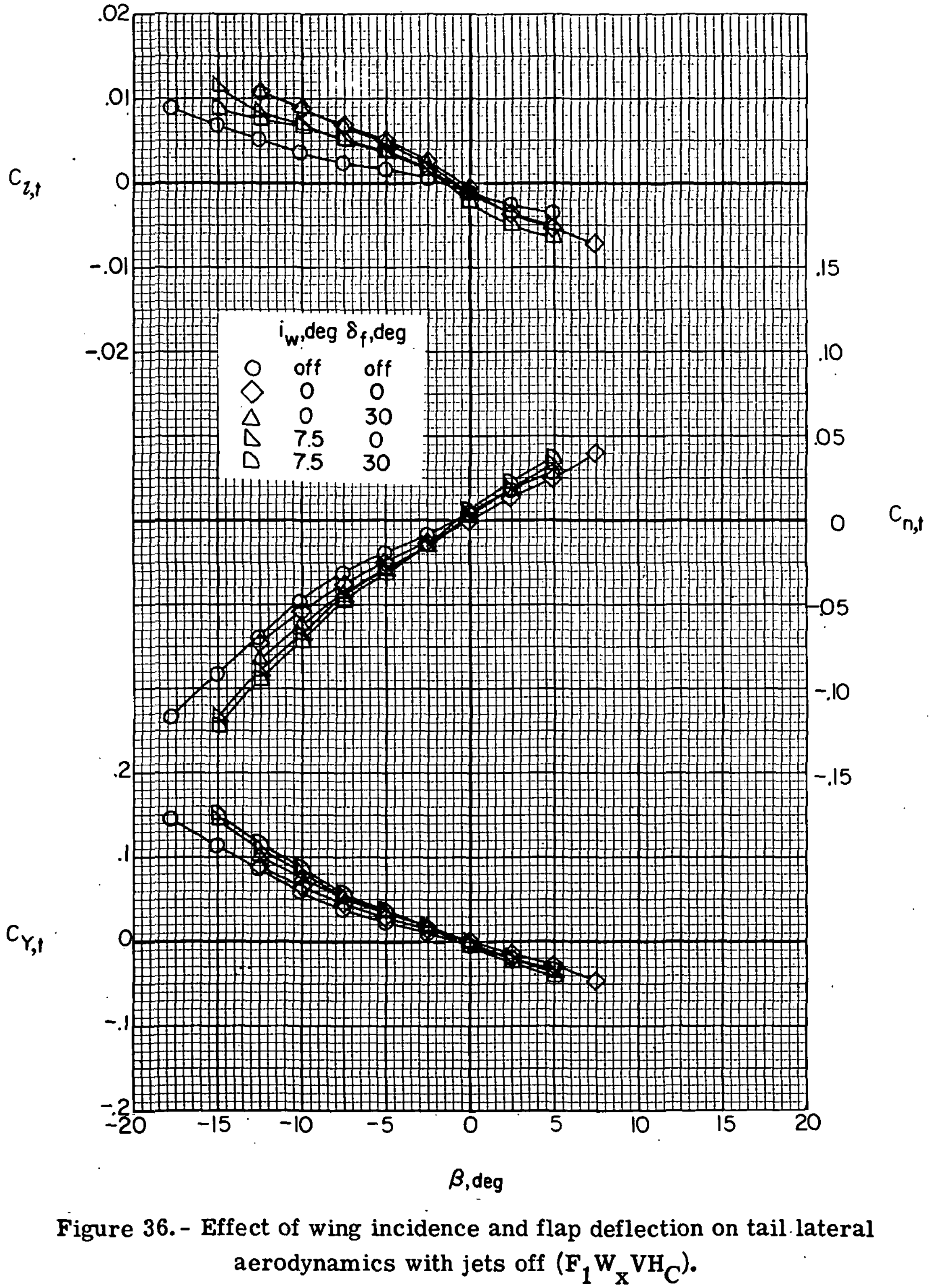

Figure 36.- Effect of wing incidence and flap deflection on tail lateral aerodynamics with jets off ($F_1W_xVH_C$).

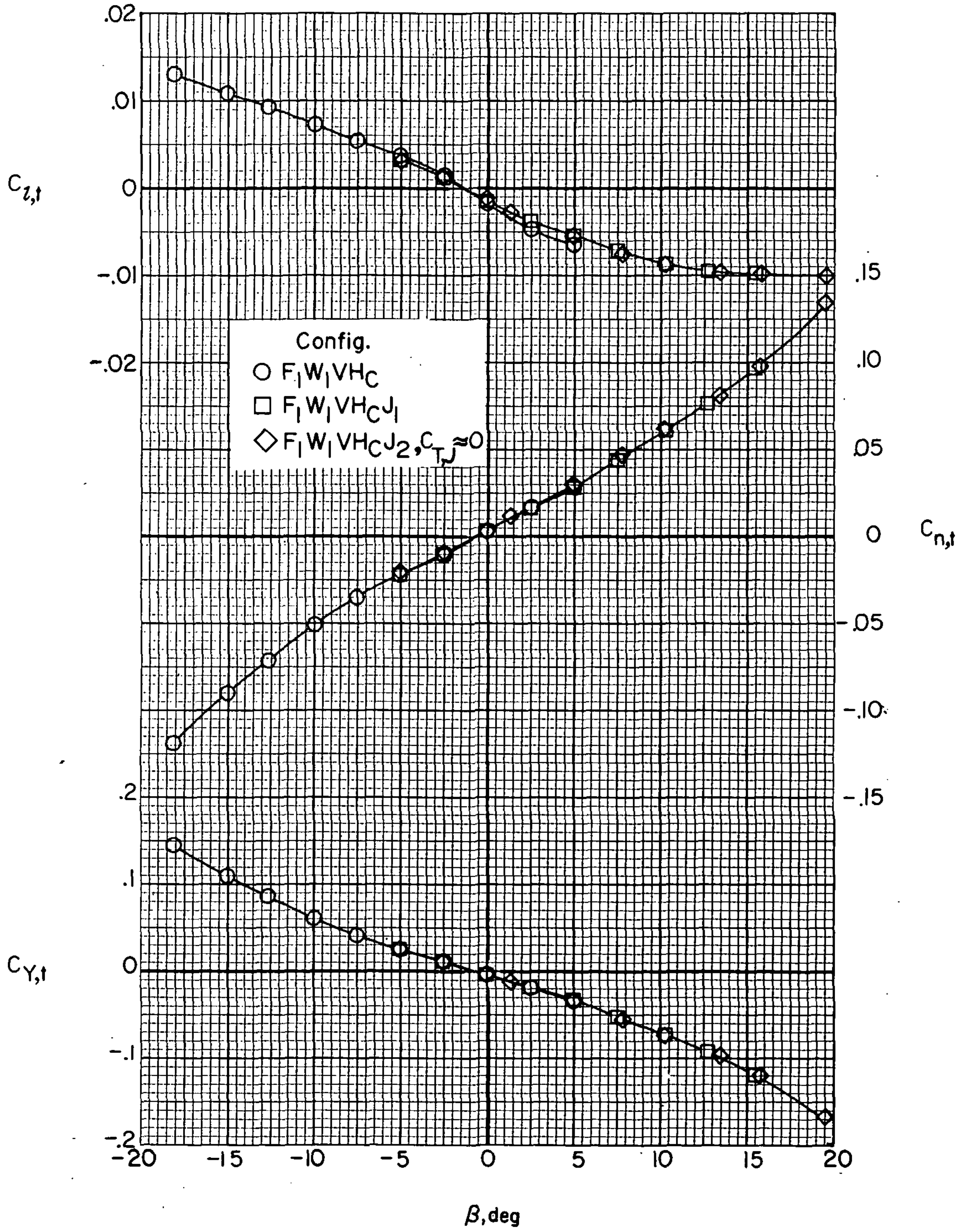

Figure 37.- Effect of engine nacelles on tail lateral aerodynamics.

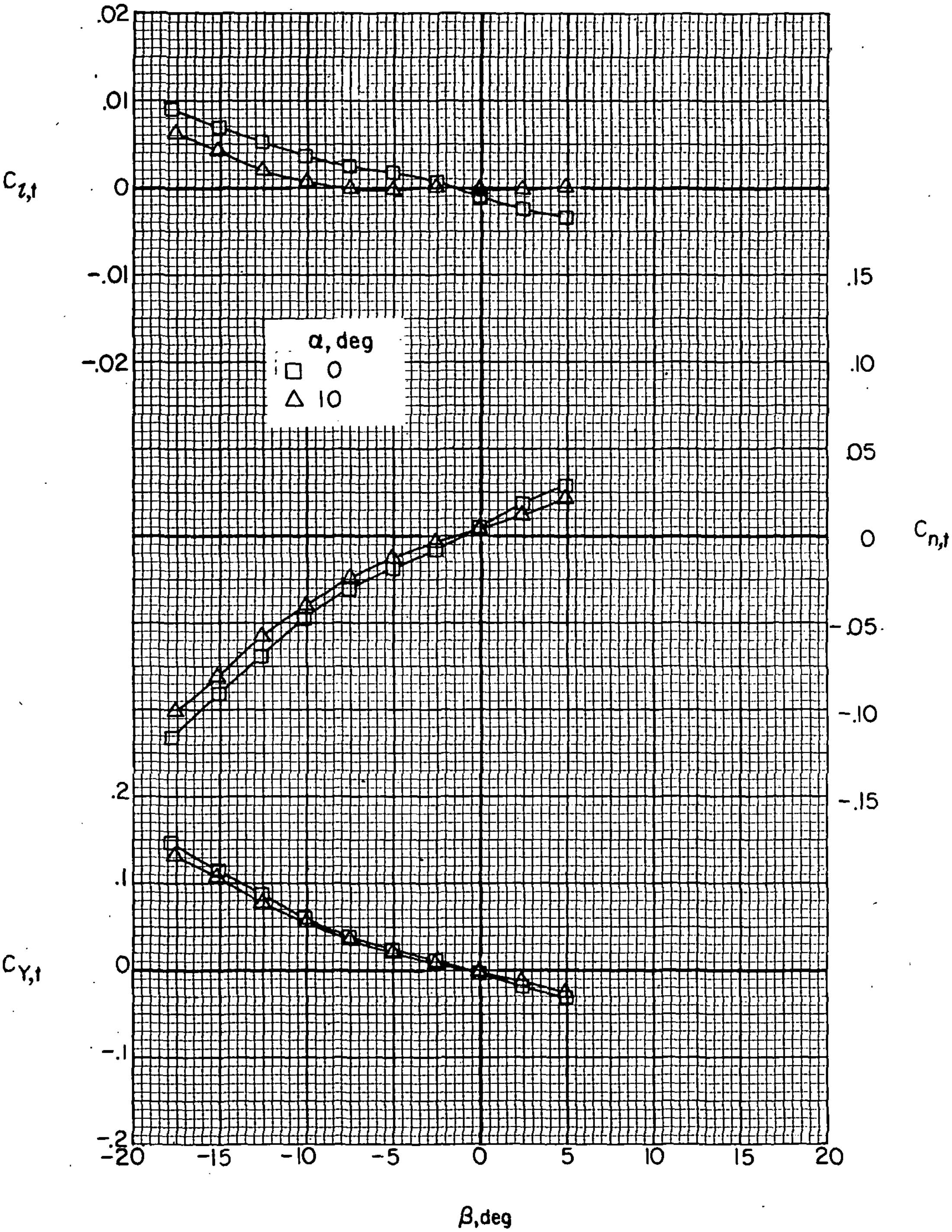

(a) Wing off; jets off; F_1VH_C.

Figure 38.- Effect of angle of attack on tail lateral aerodynamics.

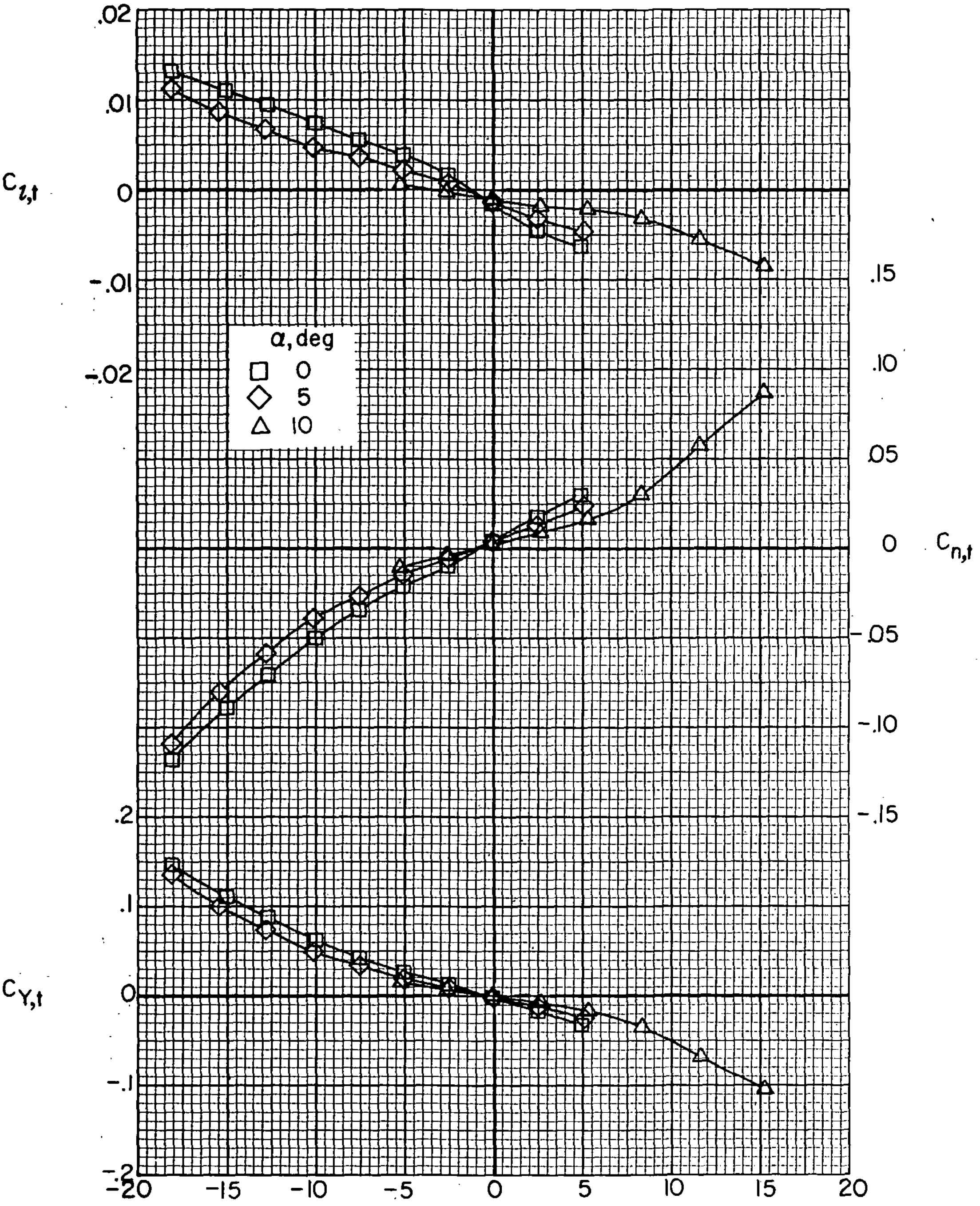

(b) Jets off; $i_w = 0^{\circ}$; $\delta_f = 0^{\circ}$; $F_1W_1VH_C$.

Figure 38. - Continued.

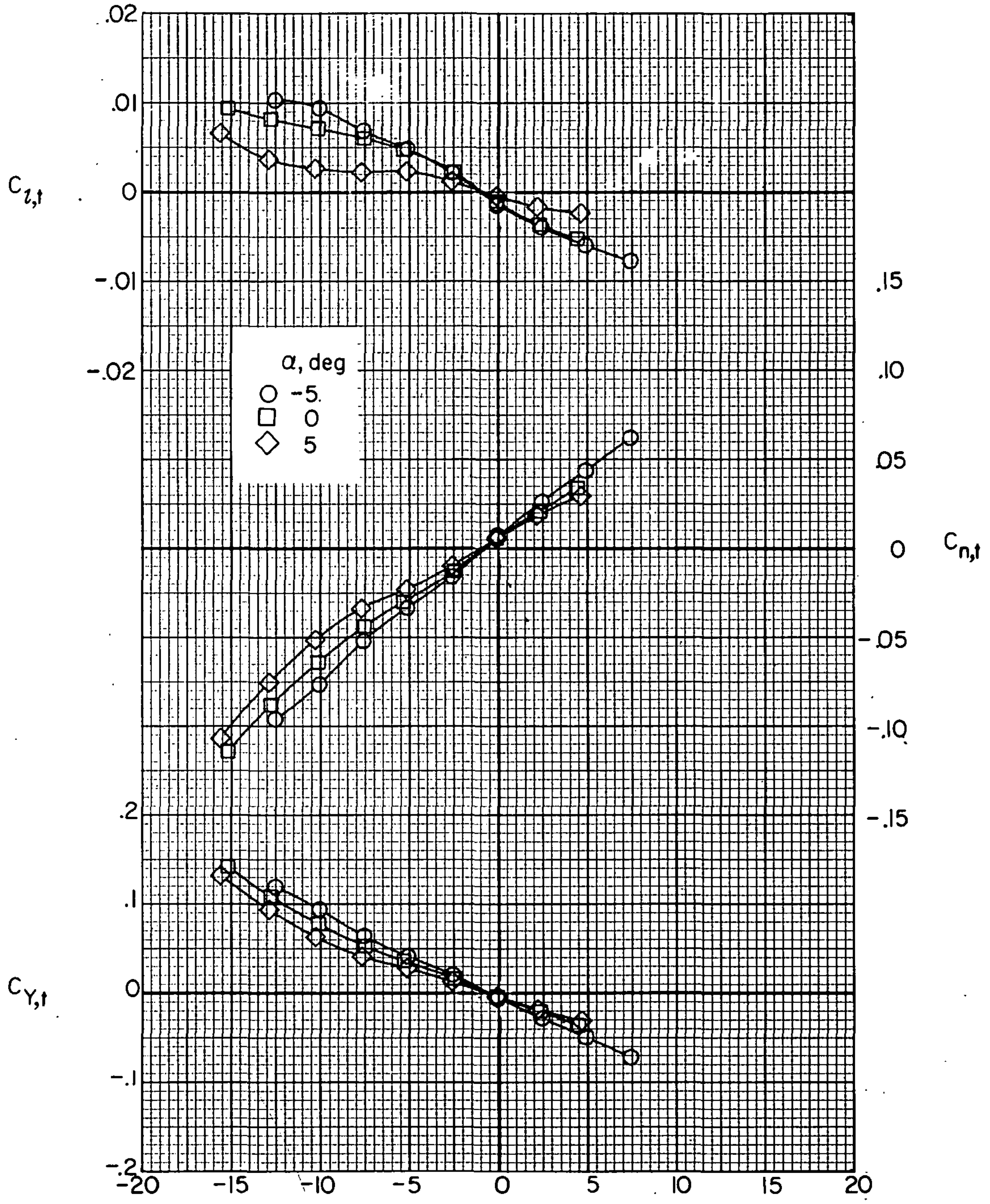

(c) Jets off; $i_w = 7.5^\circ$; $\delta_f = 30^\circ$; $F_1W_6VH_C$.

Figure 38.- Continued.

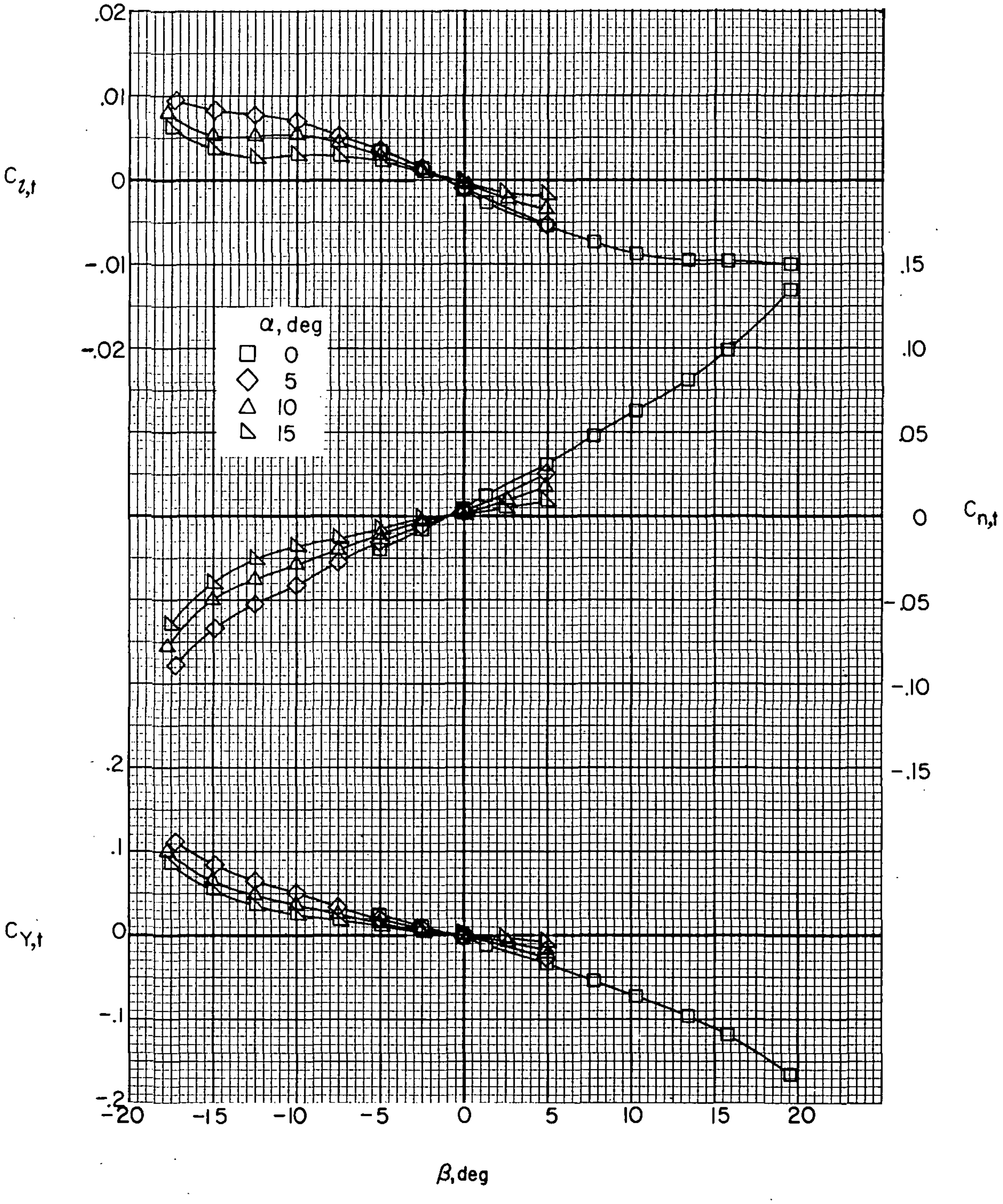

(d) Jets on; $C_{T,J} \approx 0$; $i_w = 0^{\circ}$; $\delta_f = 0^{\circ}$; $F_1W_1VH_CJ_2$.

Figure 38.- Continued.

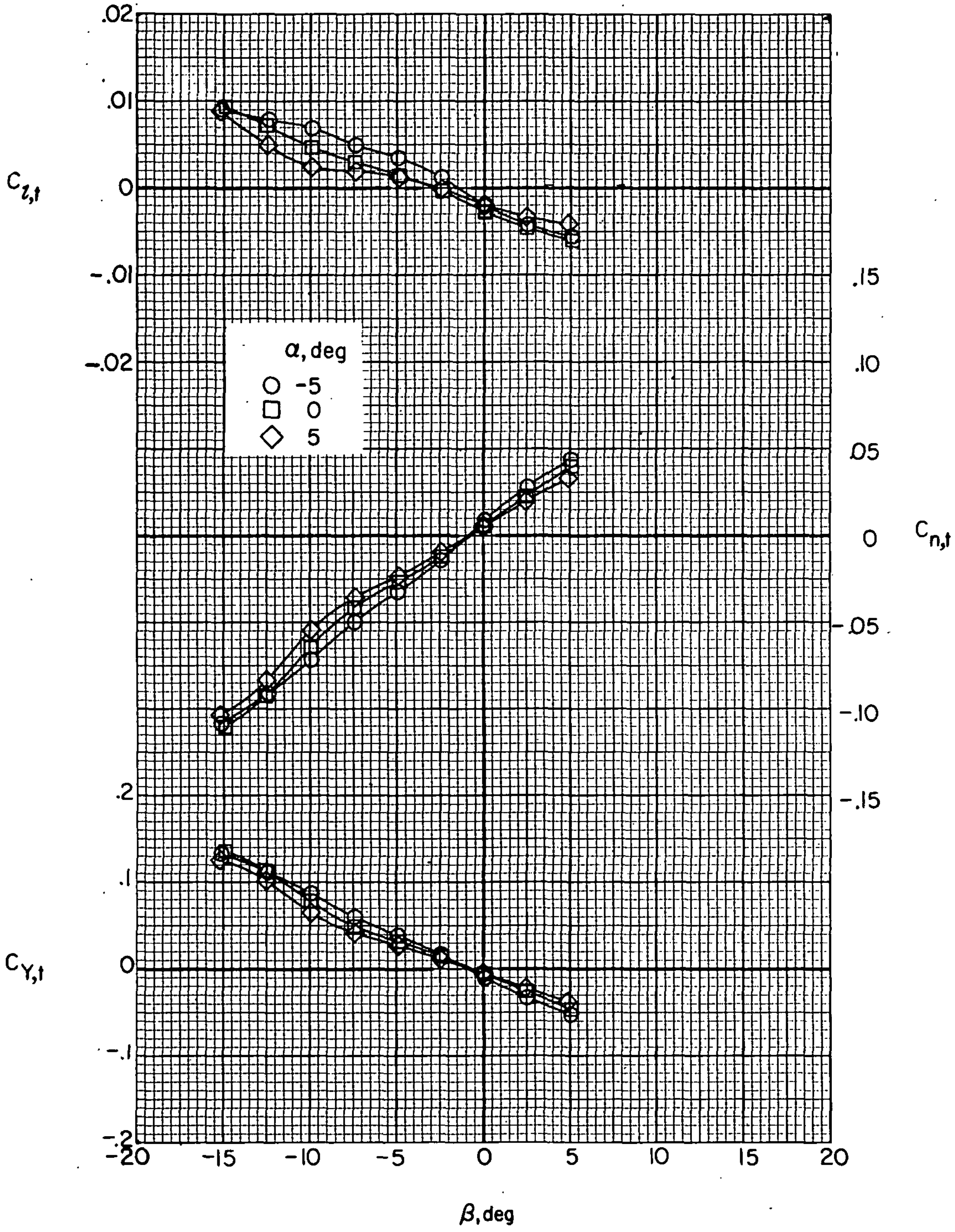

(e) Jets on; $C_{T,J} \approx 0$; $i_w = 0^o$; $\delta_f = 30^o$; $F_1W_5VH_CJ_2$.

Figure 38.- Continued.

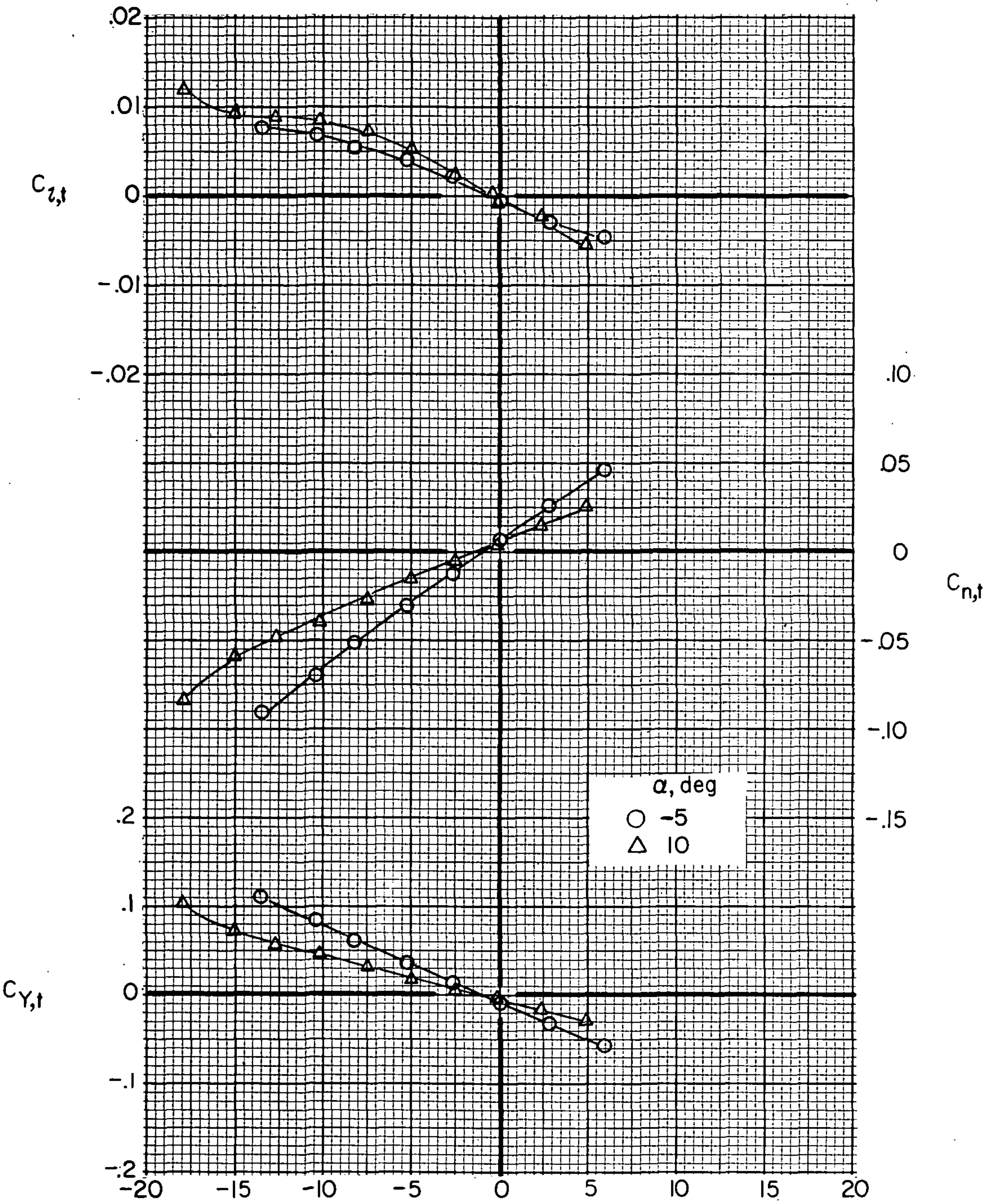

(f) Jets on; $C_{T,J} \approx 0$; $i_w = 7.5^{\circ}$; $\delta_f = 0^{\circ}$; $F_1W_2VH_CJ_2$.

Figure 38.- Concluded.

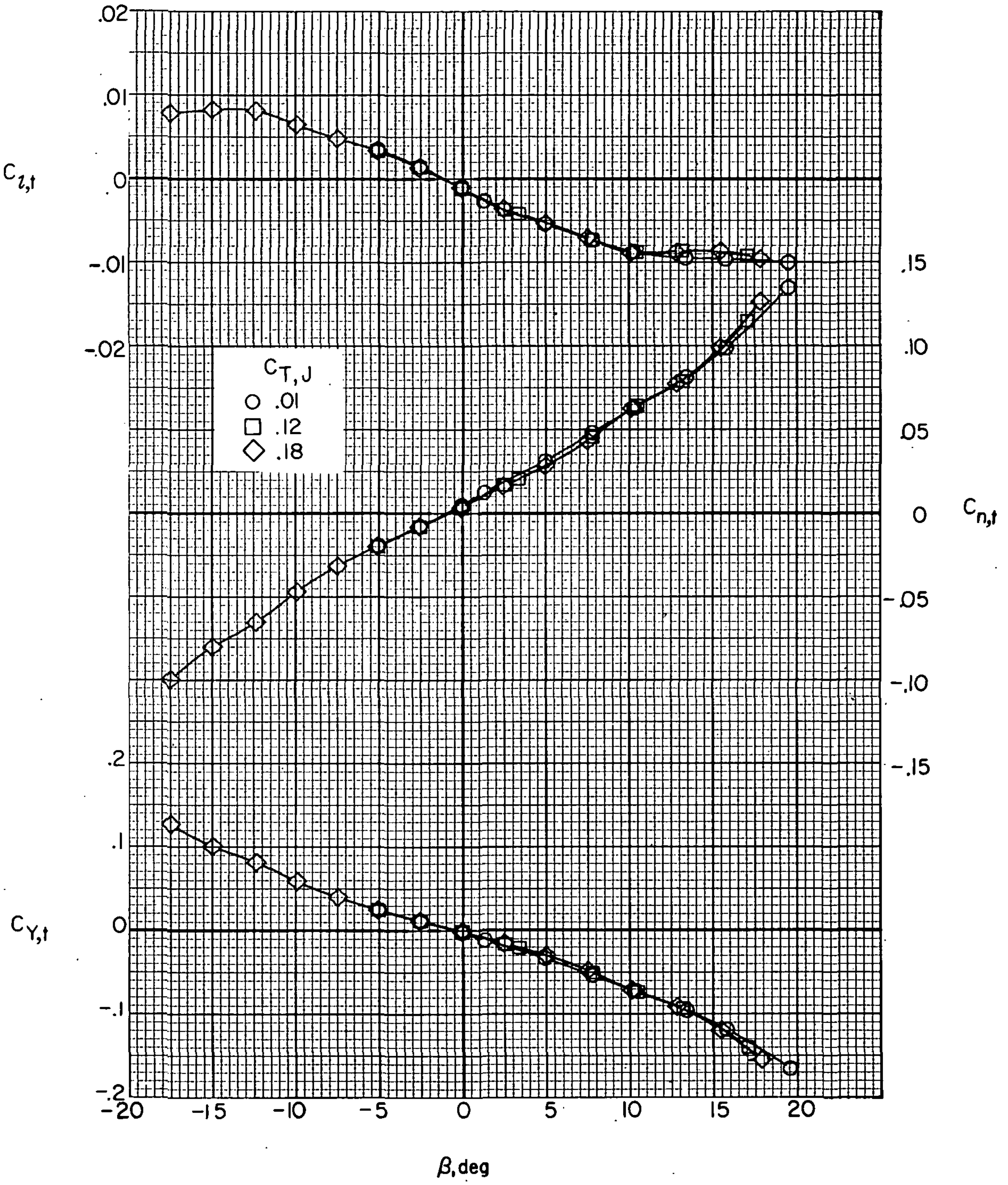

(a) $i_w = 0^\circ$; $\delta_f = 0^\circ$; $\alpha = 0^\circ$.

Figure 39.- Effect of auxiliary engine thrust coefficient on tail lateral aerodynamics. $F_1W_xVH_CJ_2$.

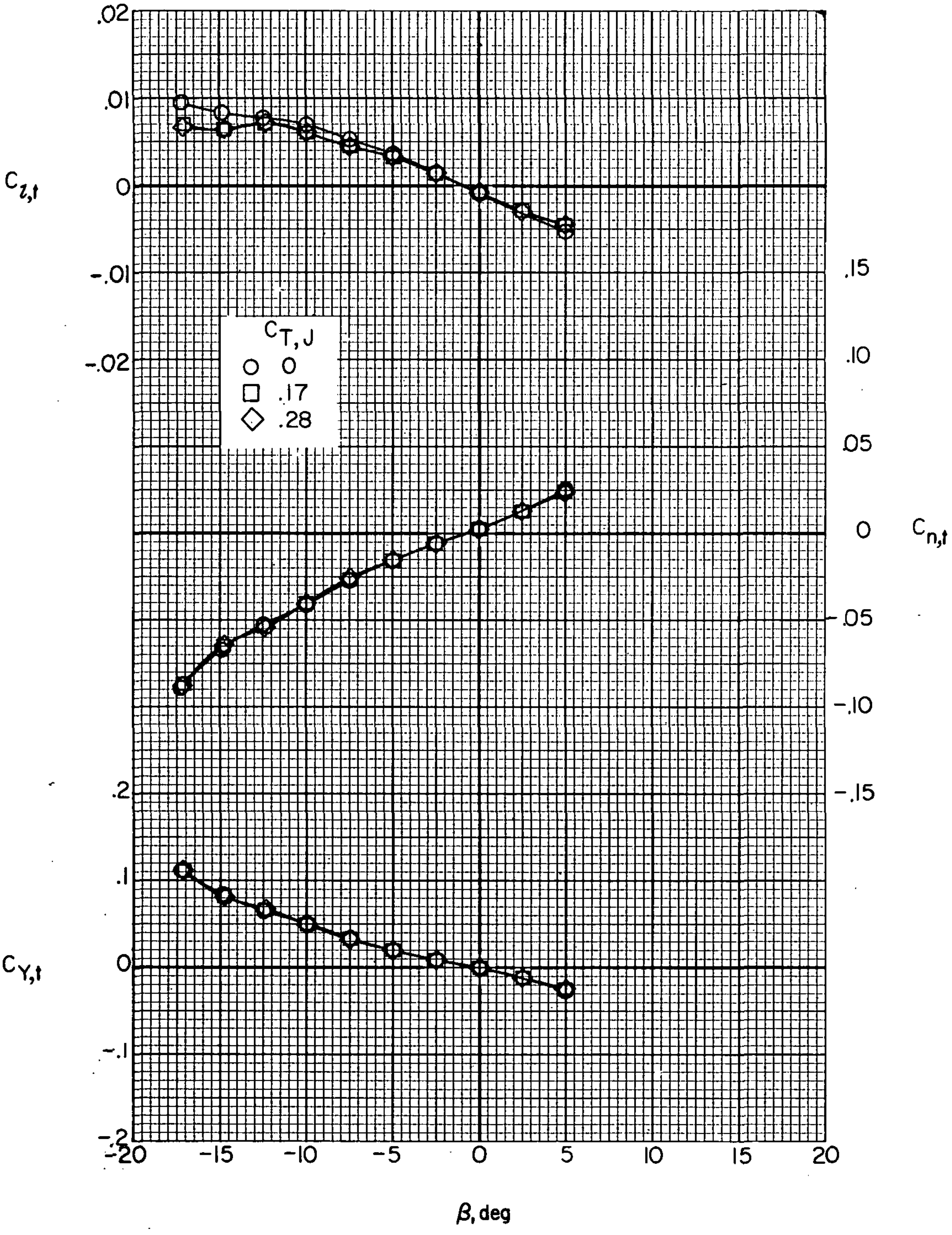

(b) $i_w = 0^\circ$; $\delta_f = 0^\circ$; $\alpha = 5^\circ$.

Figure 39.- Continued.

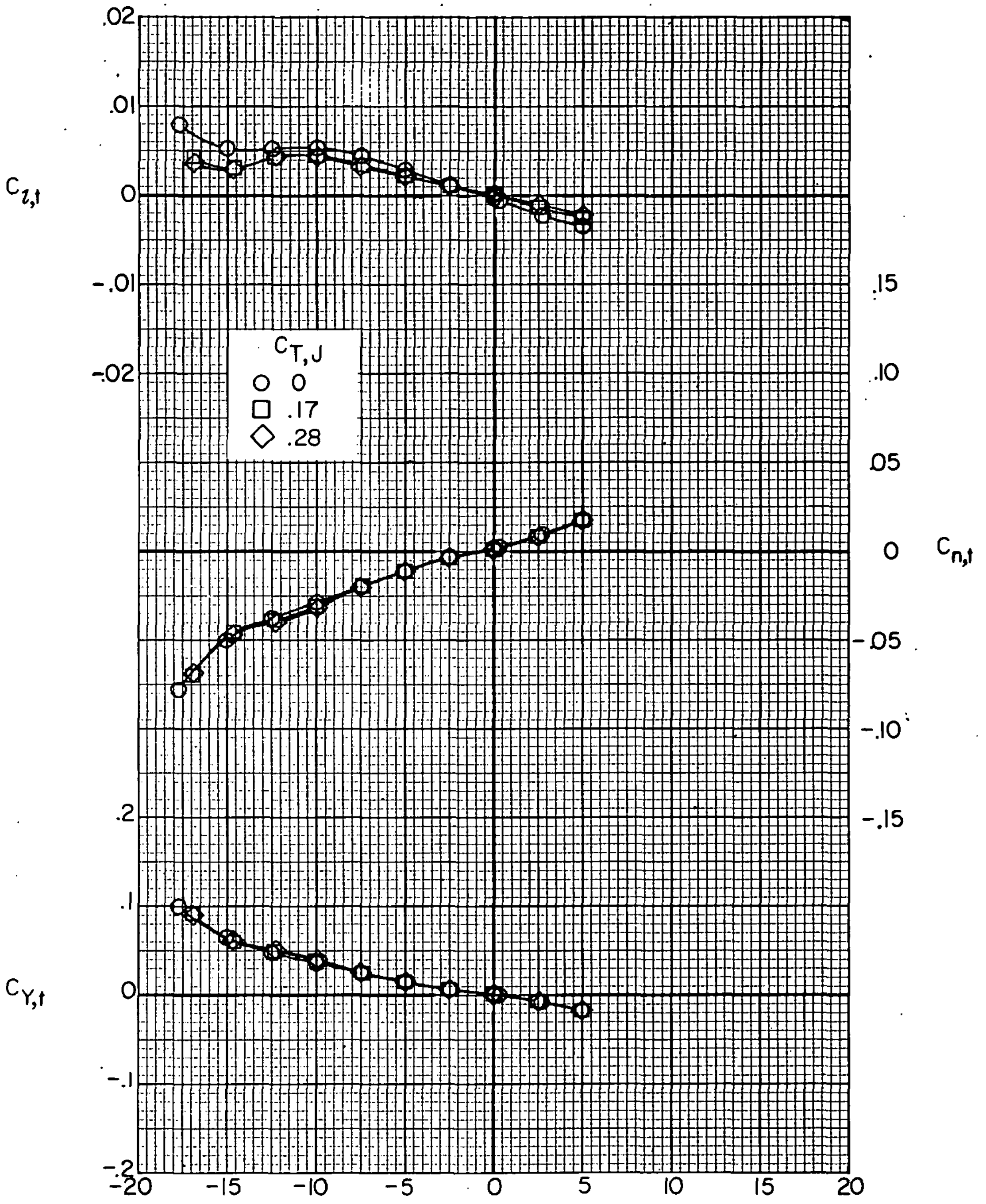

(c) $i_w = 0^\circ$; $\delta_f = 0^\circ$; $\alpha = 10^\circ$.

Figure 39.- Continued.

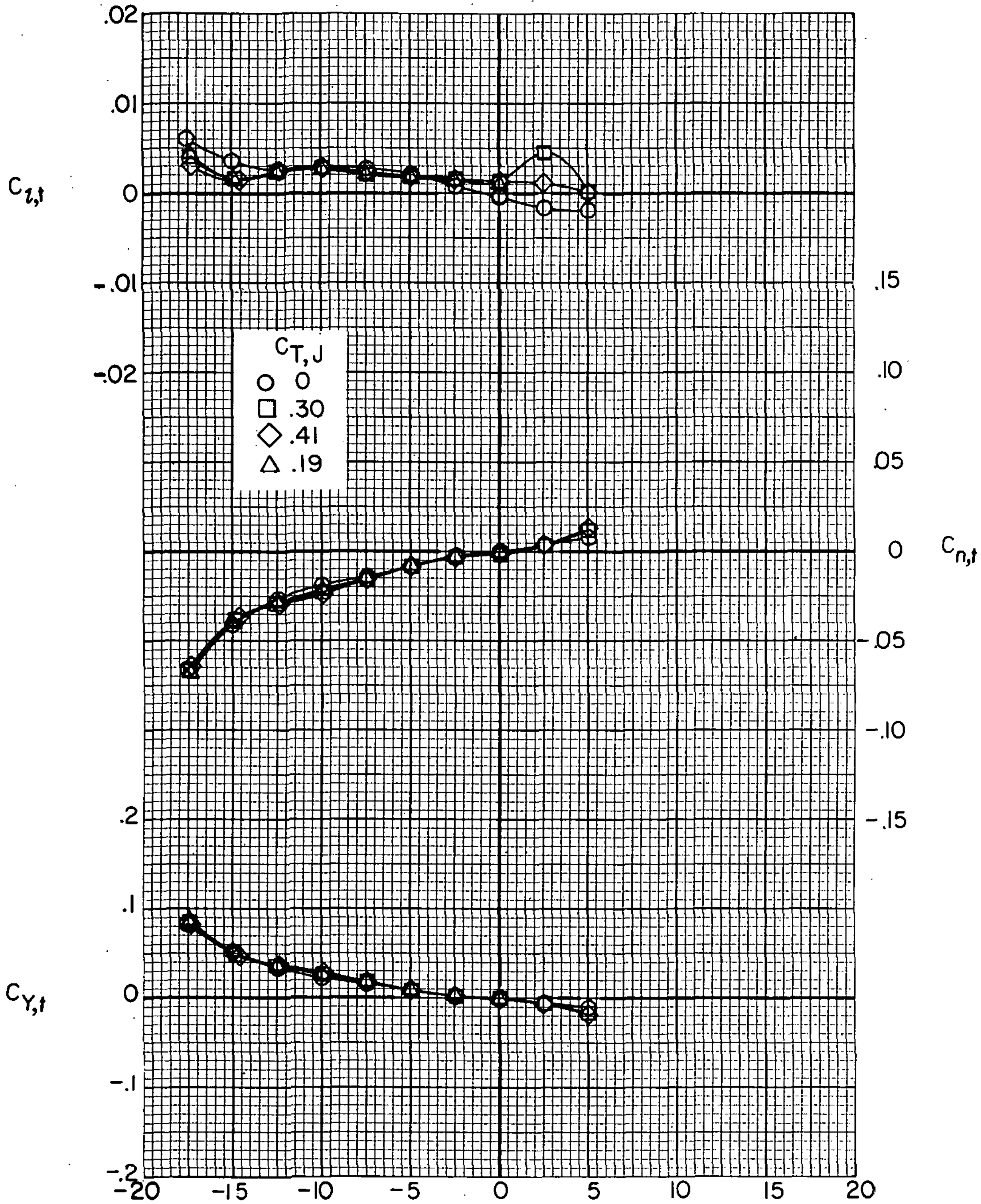

(d) $i_w = 0^\circ$; $\delta_f = 0^\circ$; $\alpha = 15^\circ$.

Figure 39.- Continued.

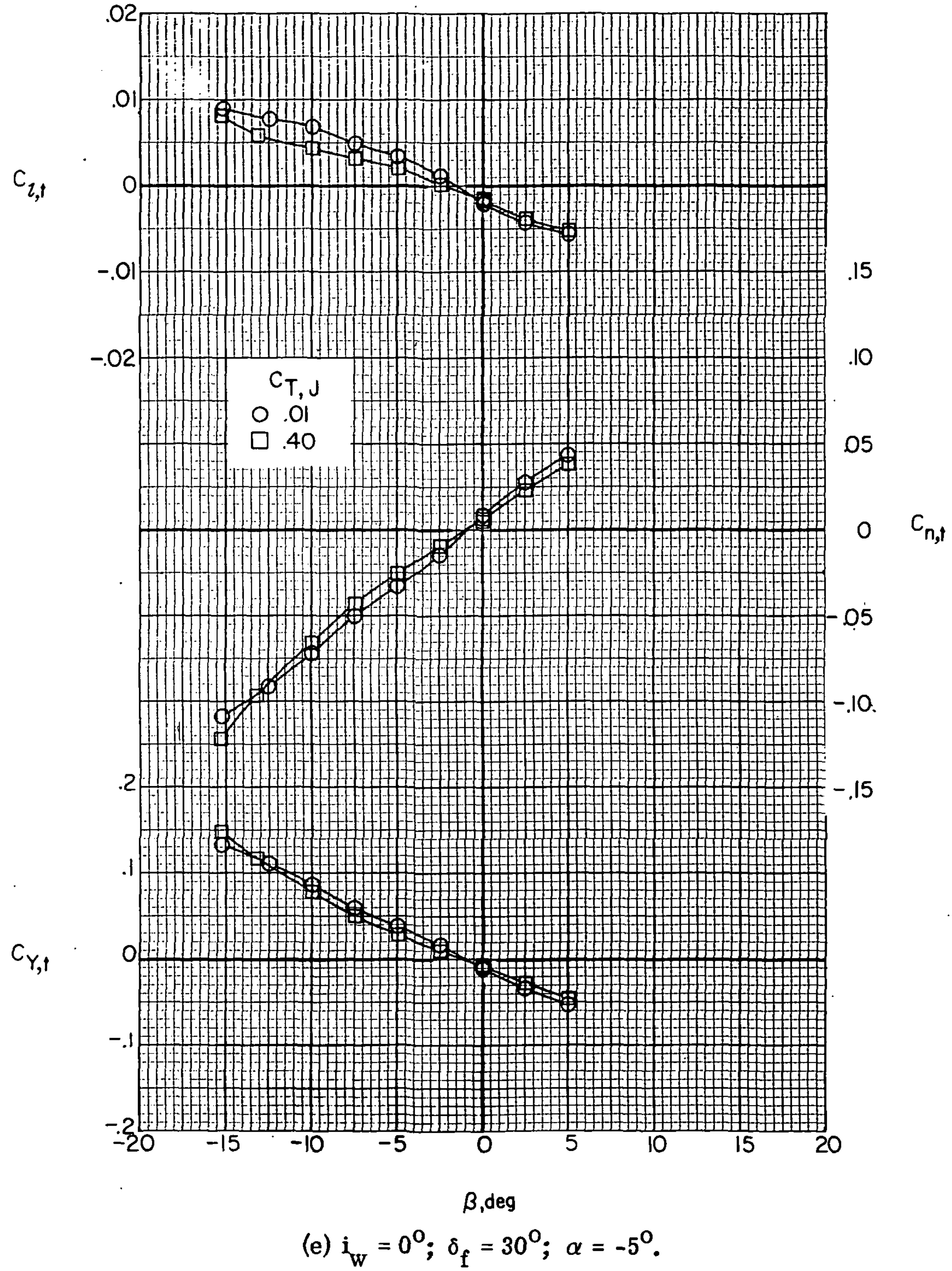

(e) $i_w = 0^\circ$; $\delta_f = 30^\circ$; $\alpha = -5^\circ$.

Figure 39.- Continued.

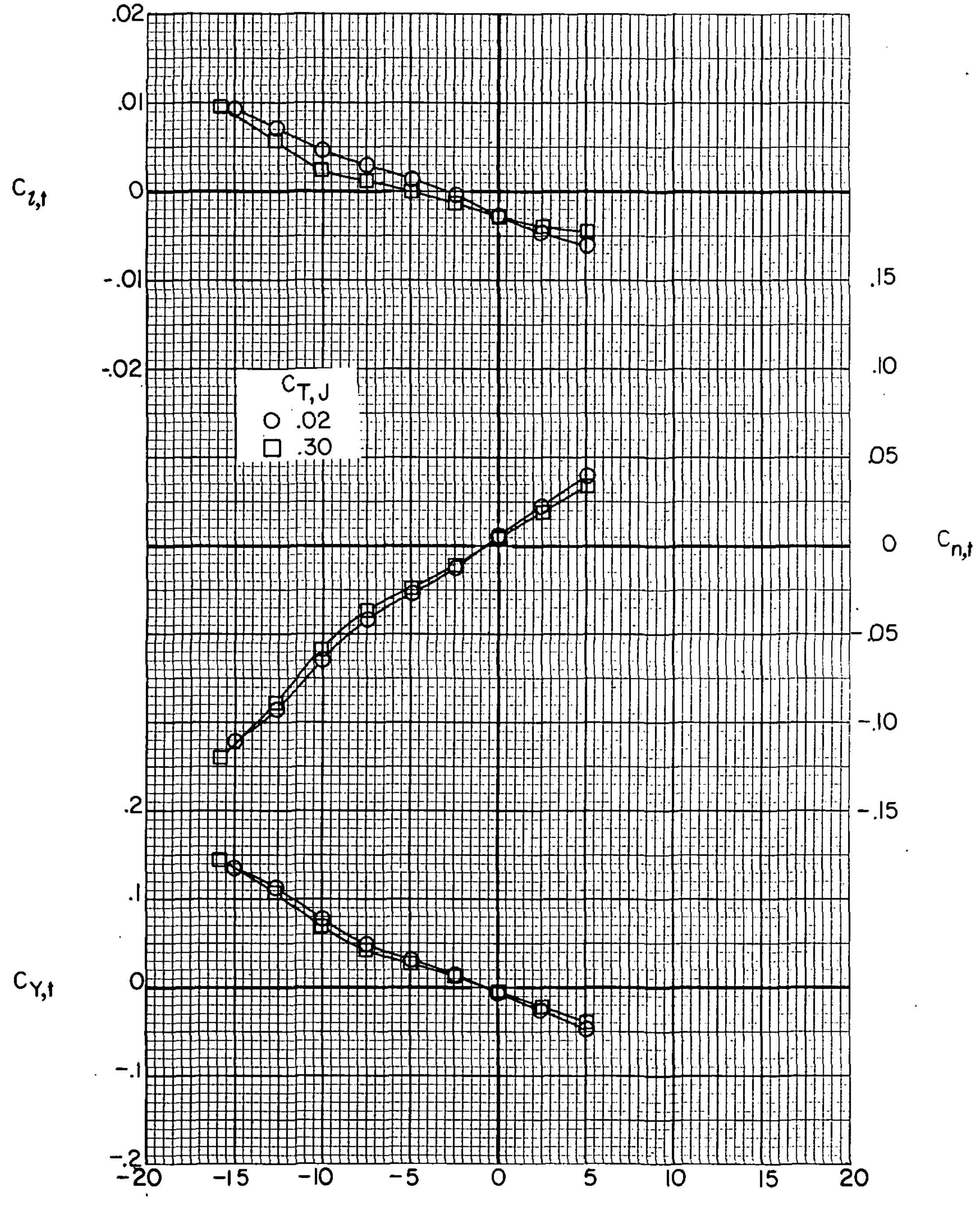

(f) $i_w = 0^\circ$; $\delta_f = 30^\circ$; $\alpha = 0^\circ$.

Figure 39.- Continued.

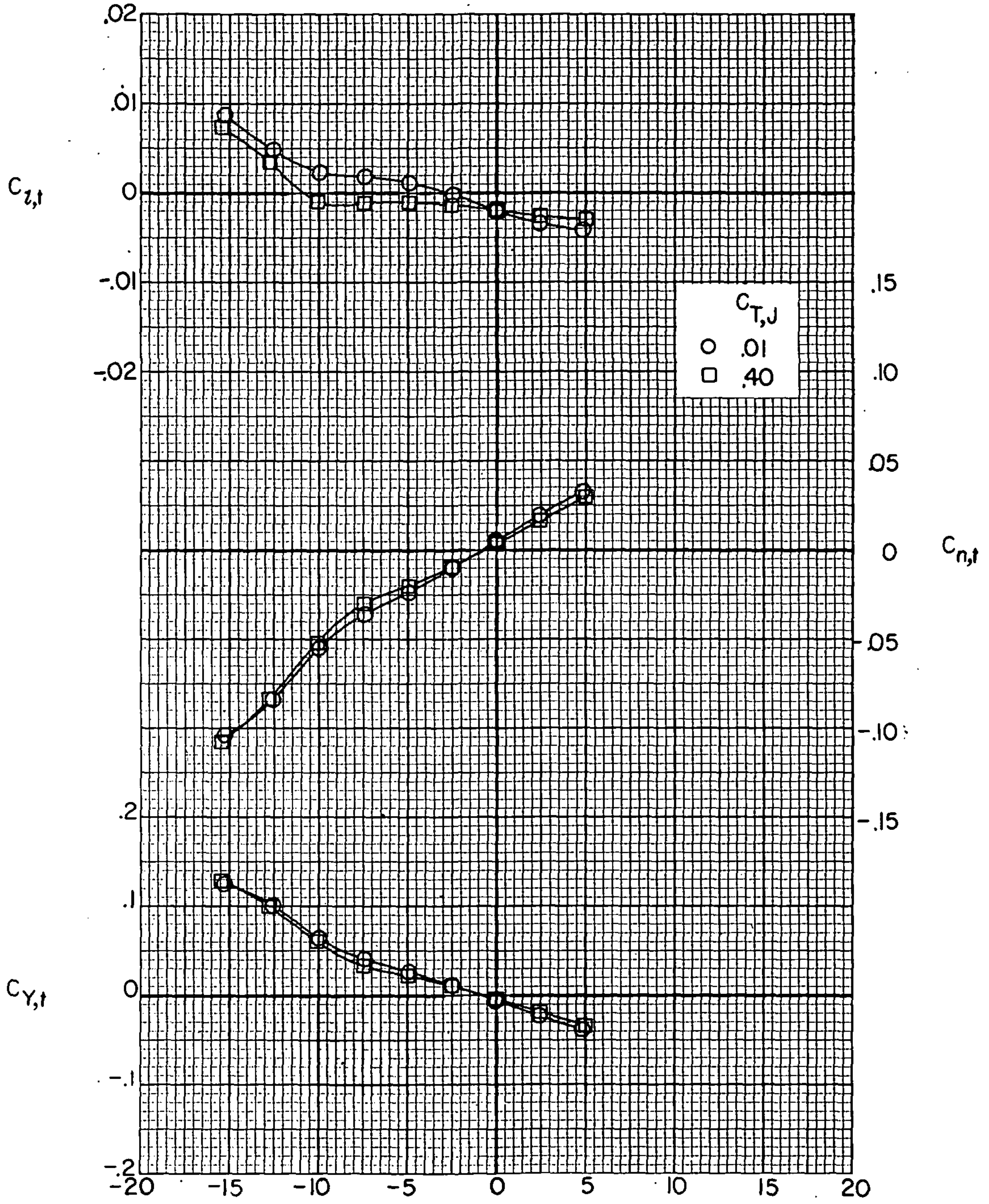

(g) $i_w = 0^\circ$; $\delta_f = 30^\circ$; $\alpha = 5^\circ$.

Figure 39. - Continued.

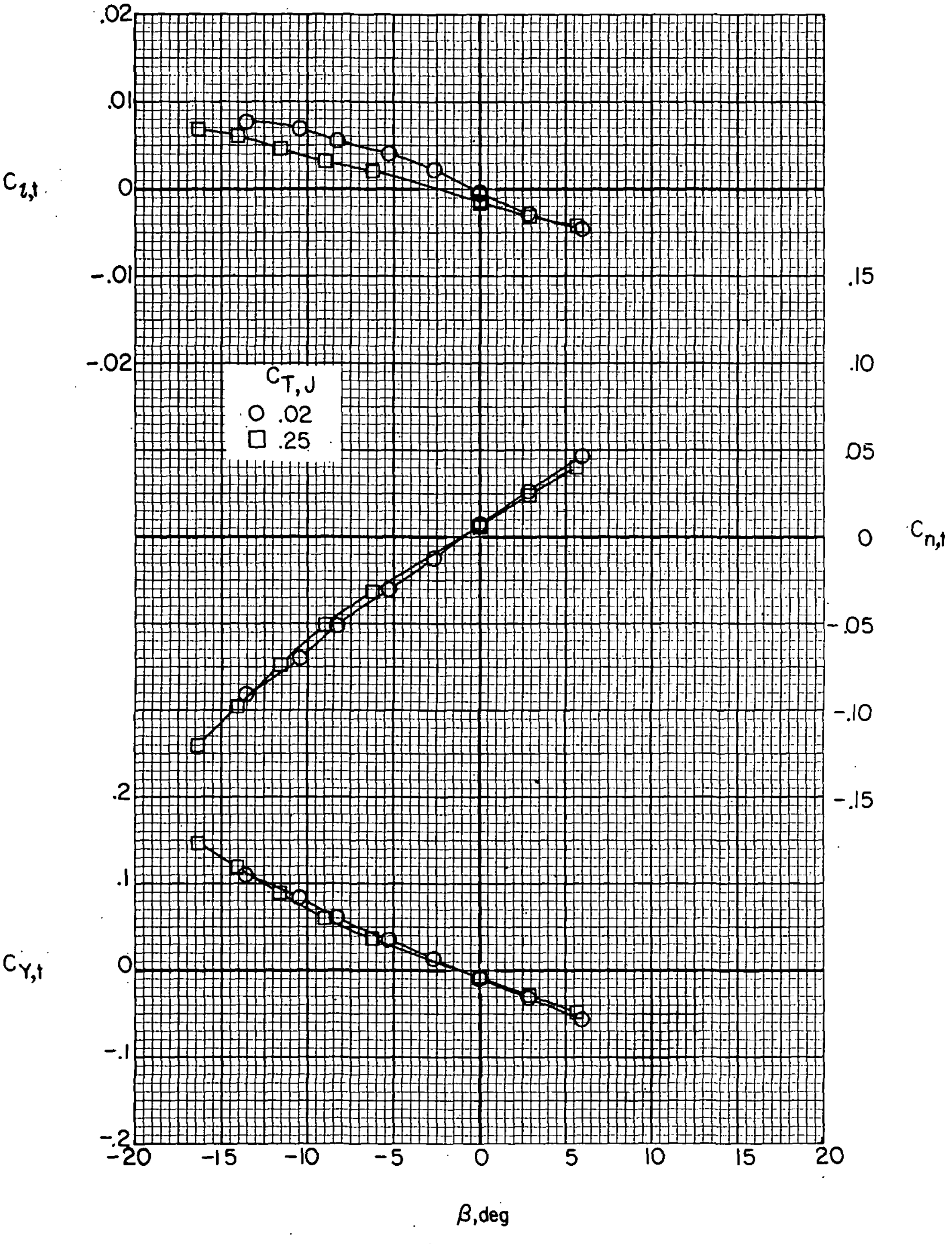

(h) $i_w = 7.5^\circ$; $\delta_f = 0^\circ$; $\alpha = -5^\circ$.

Figure 39.- Continued.

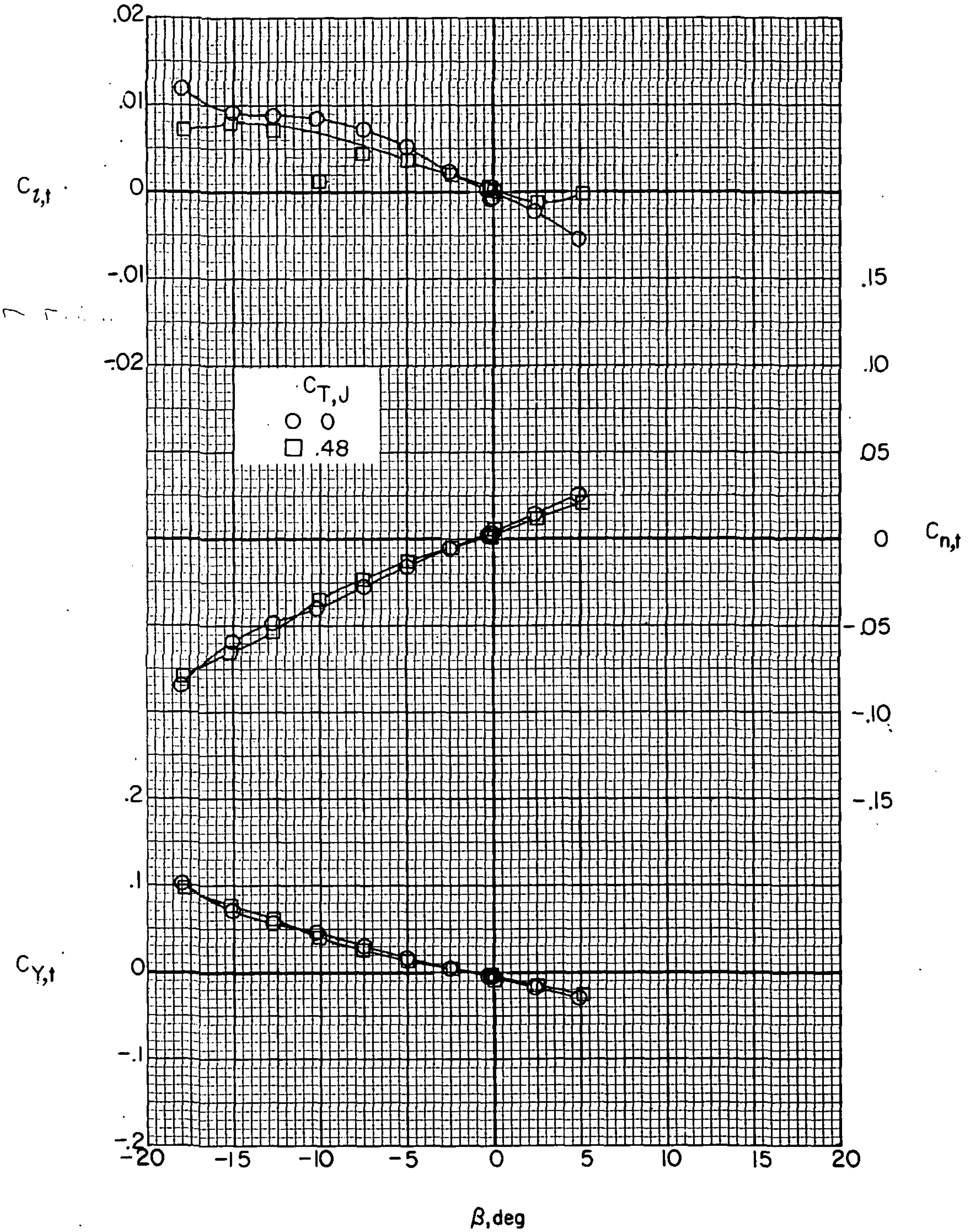

(i) $i_w = 7.5^\circ$; $\delta_f = 0^\circ$; $\alpha = 10^\circ$.

Figure 39.- Concluded.

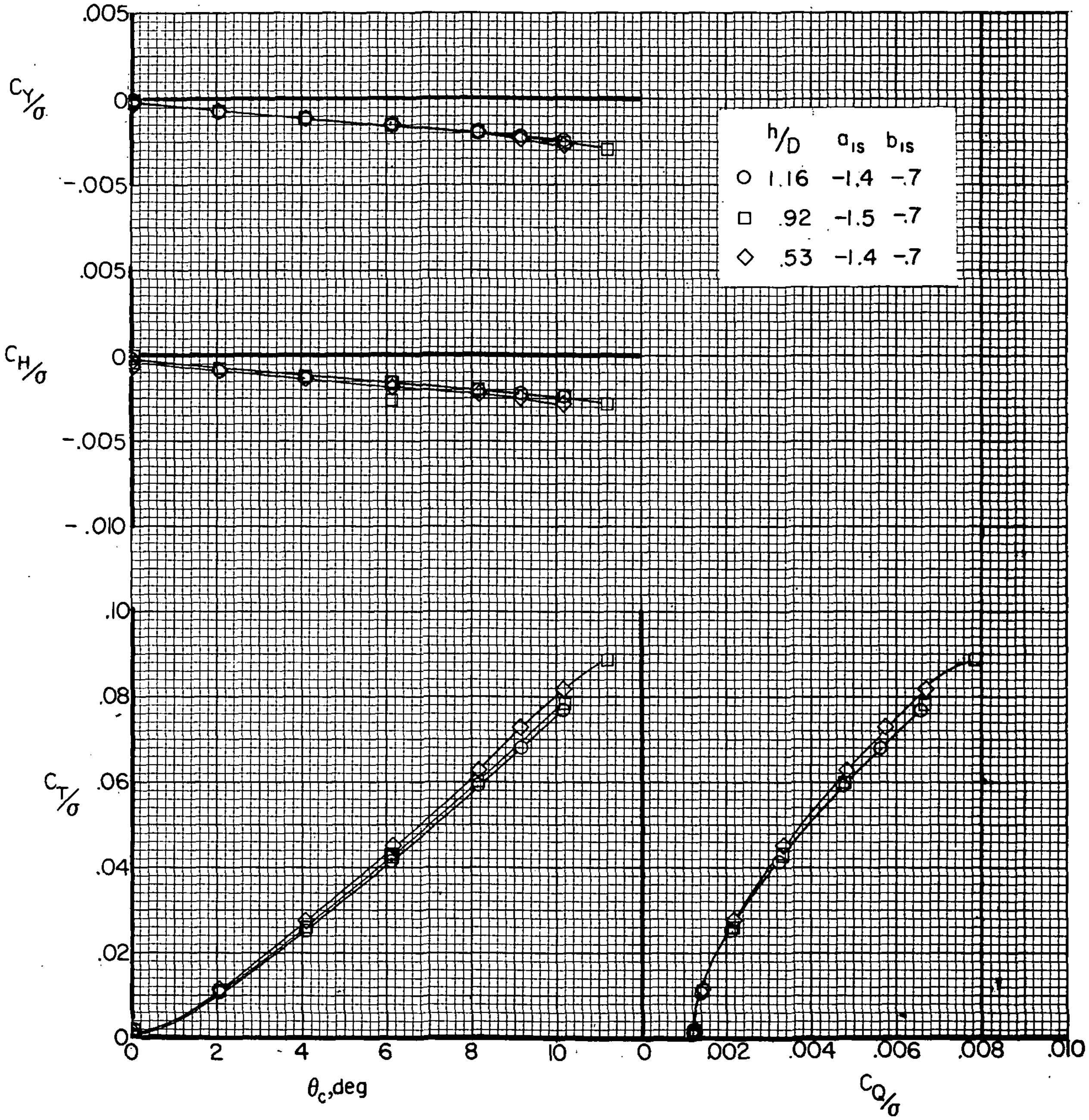

Figure 40.- Effect of ground proximity on rotor aerodynamics in hover. $F_1M_RW_1VH_CJ_2$; $C_{T,J} \approx 0$. (a_{1s} and b_{1s} are in degrees.)

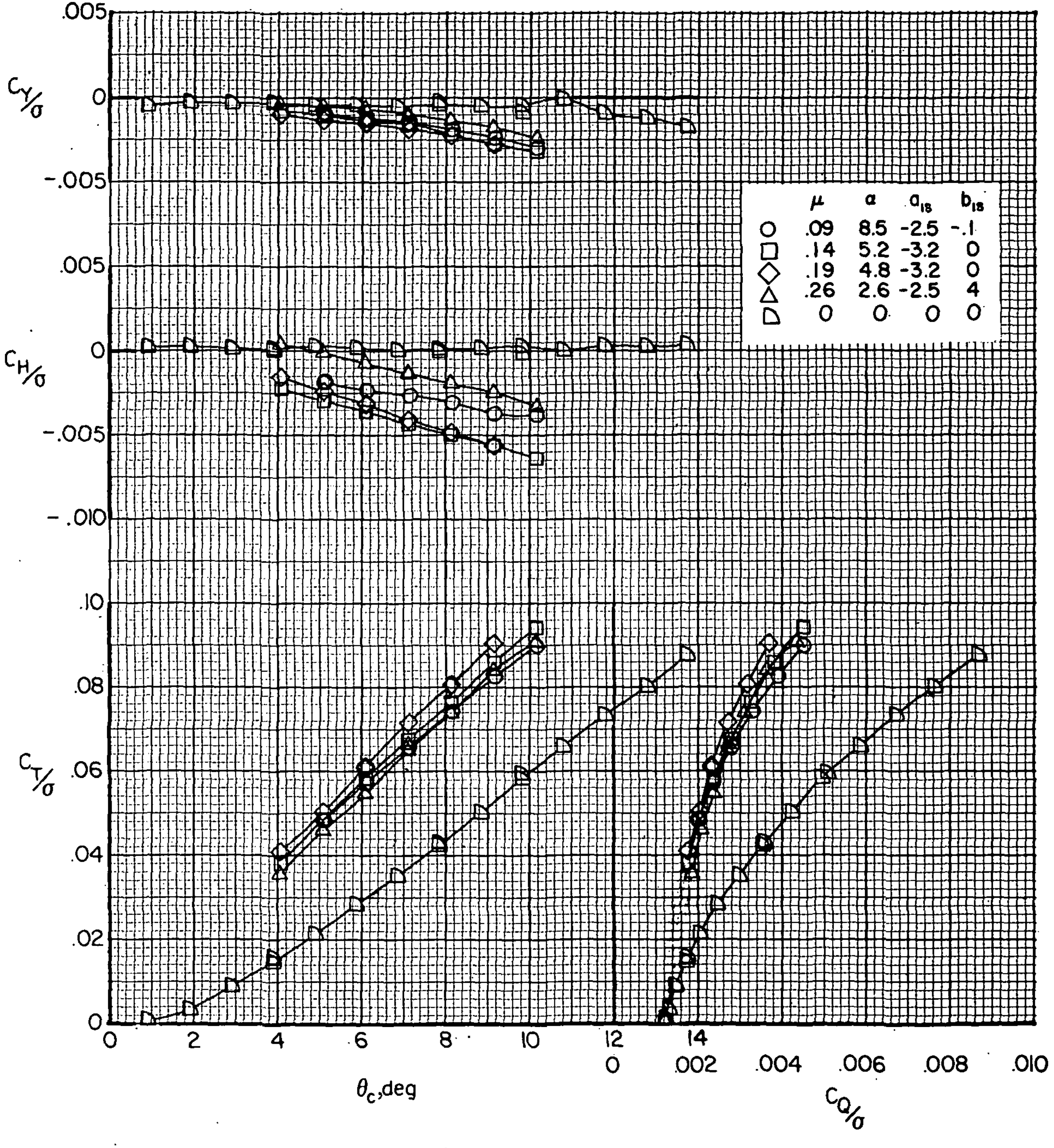

(a) $F_1M_RVH_H$.

Figure 41.- Effect of forward speed on rotor aerodynamics for a variation in rotor collective pitch angle with $\delta_3 = -27.6^\circ$. (α, a_{1s}, and b_{1s} are in degrees.)

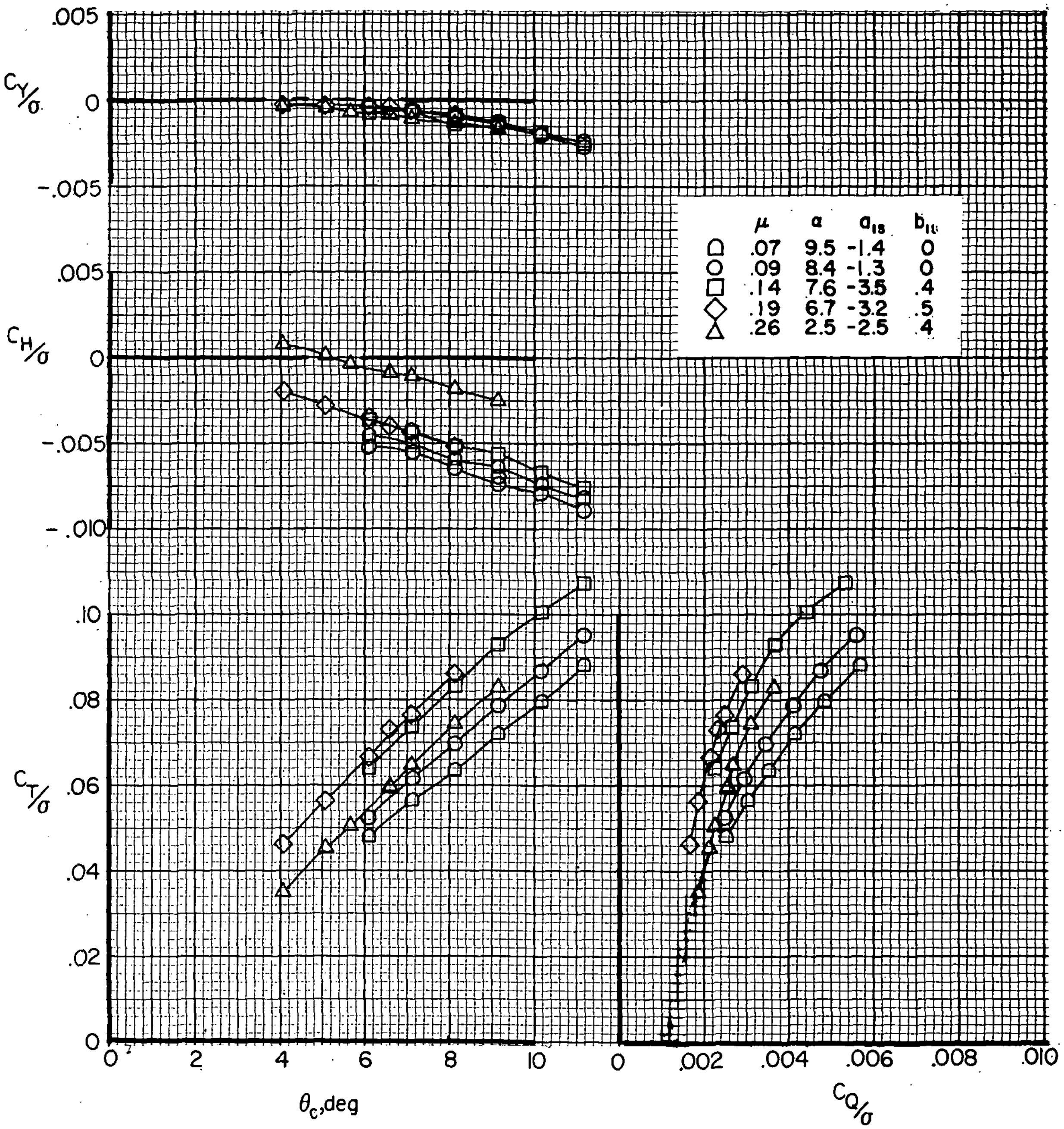

(b) $F_1M_RVH_C$.

Figure 41.- Continued.

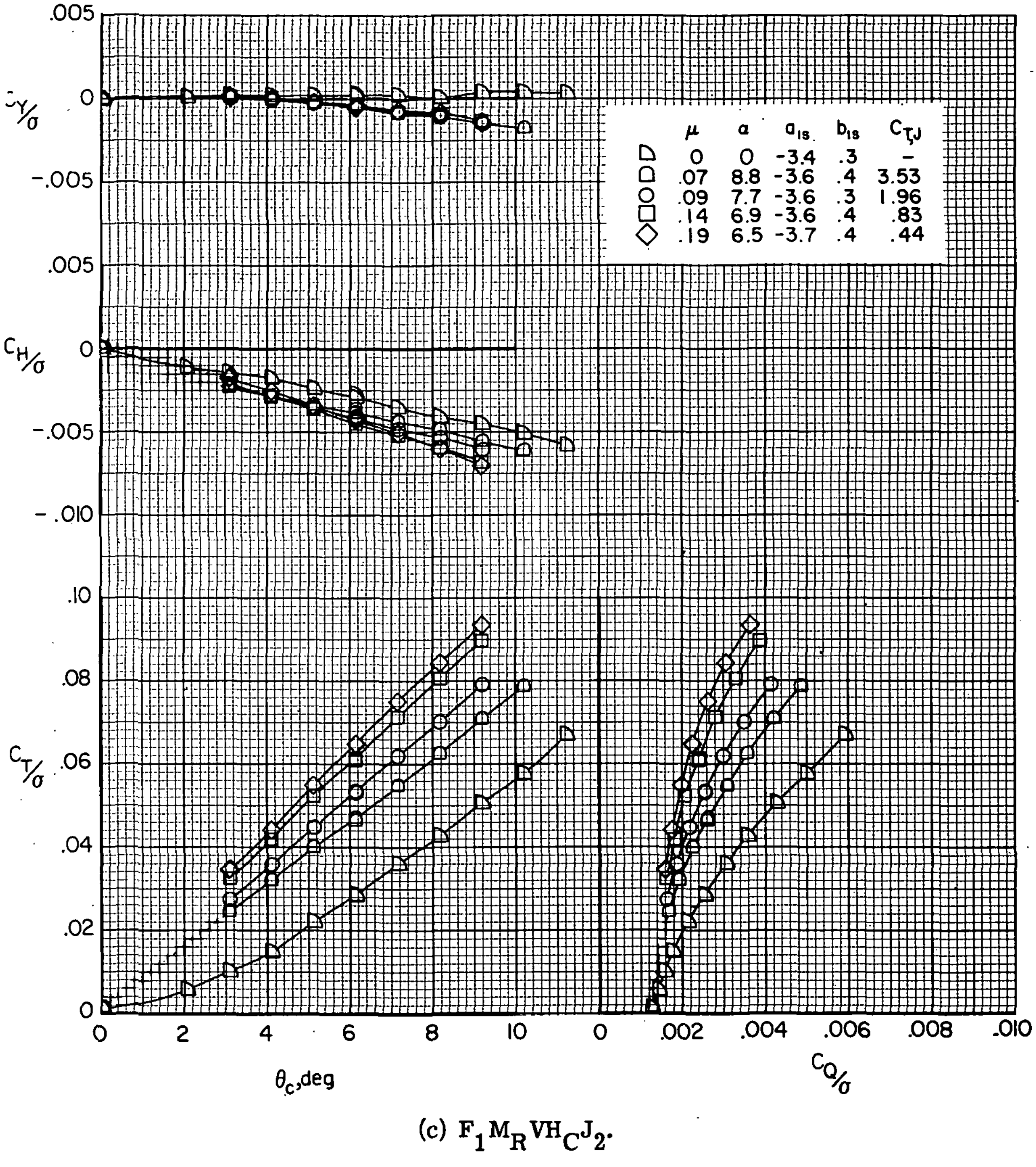

(c) $F_1M_RVH_CJ_2$.

Figure 41.- Continued.

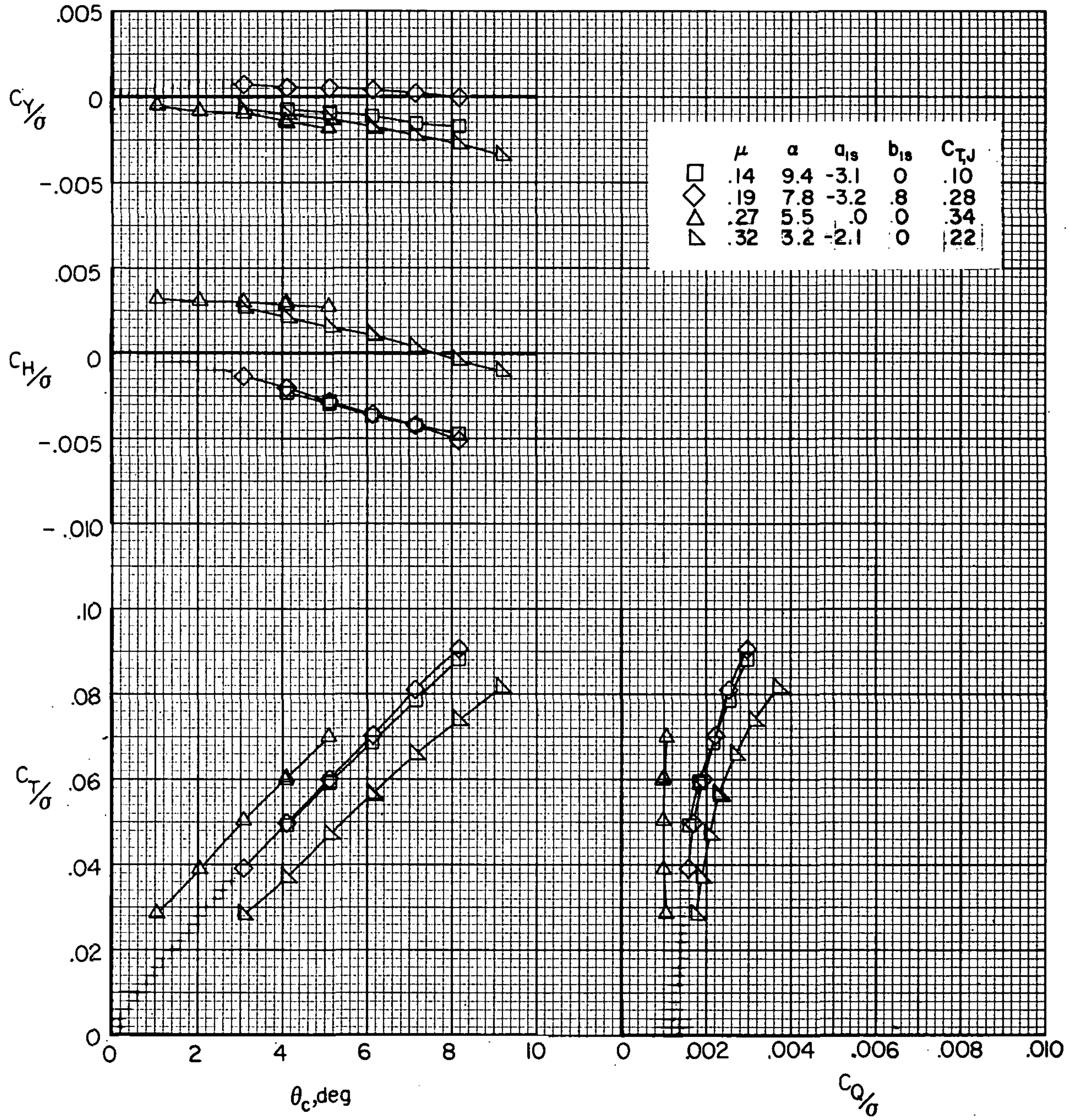

(d) $F_1M_RW_1VH_CJ_2$; high wing lift.

Figure 41.- Continued.

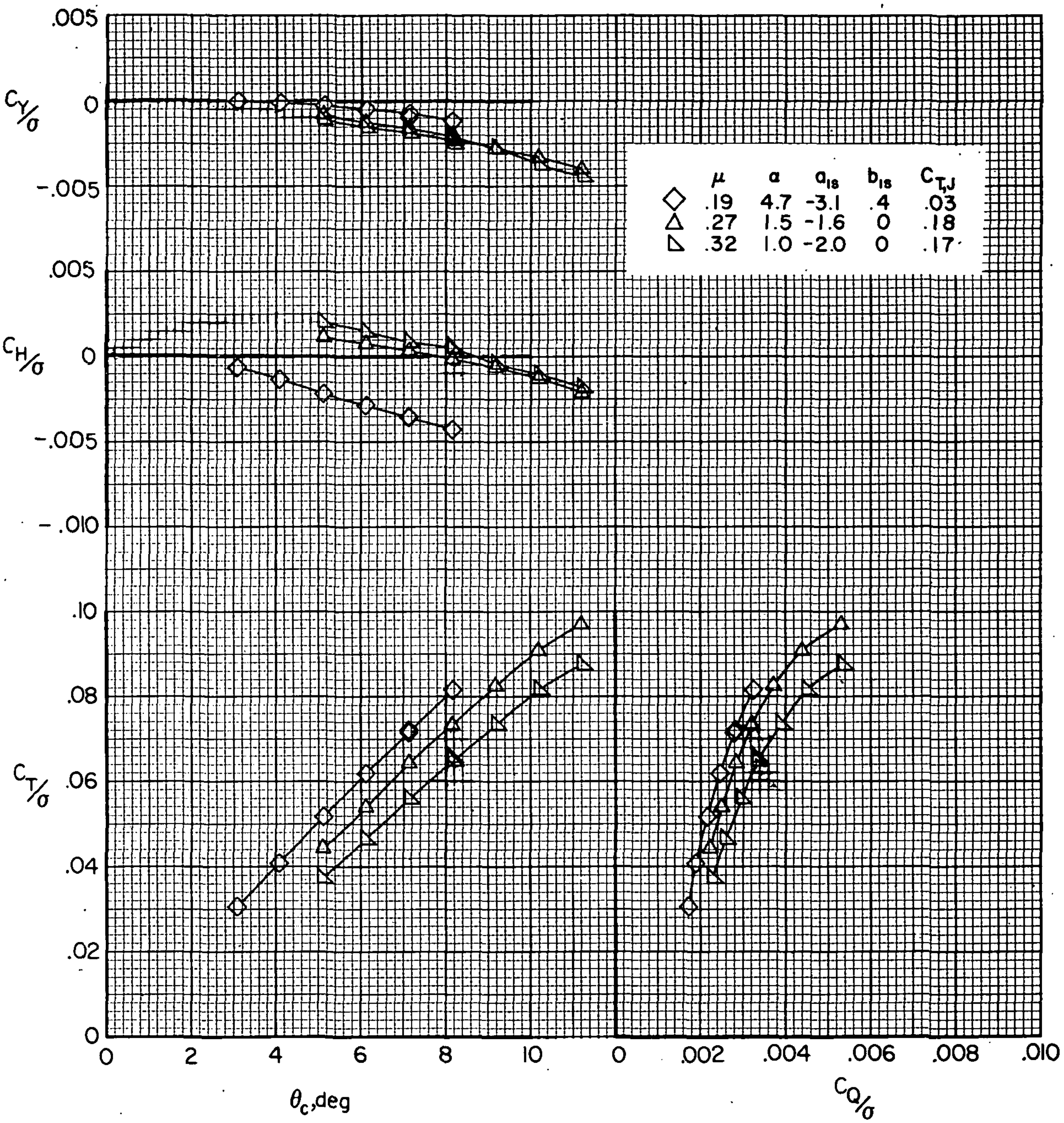

(e) $F_1M_RW_1VH_CJ_2$; low wing lift.

Figure 41.- Continued.

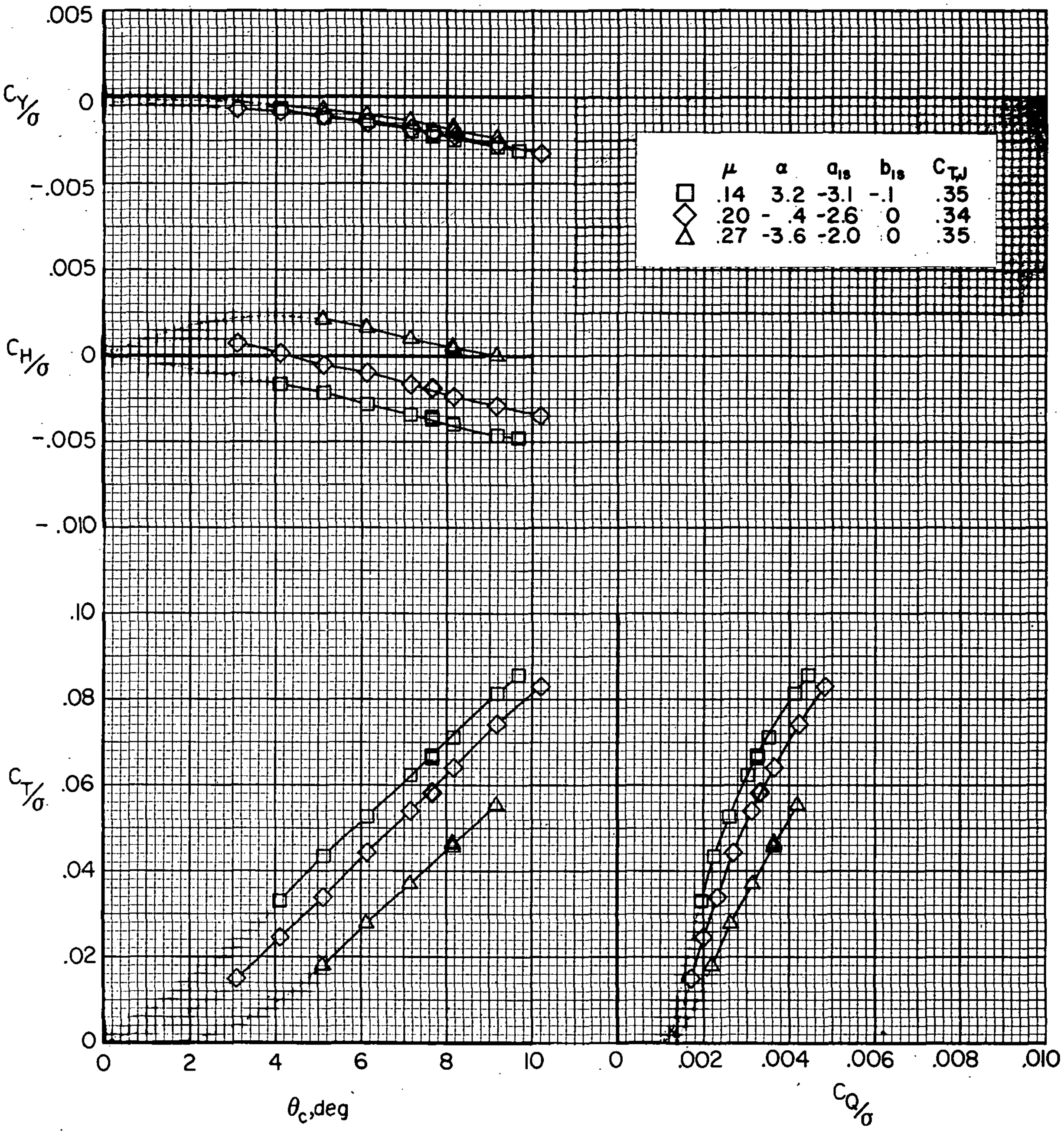

(f) $F_1M_RW_6VH_CJ_2$; high wing lift.

Figure 41.- Continued.

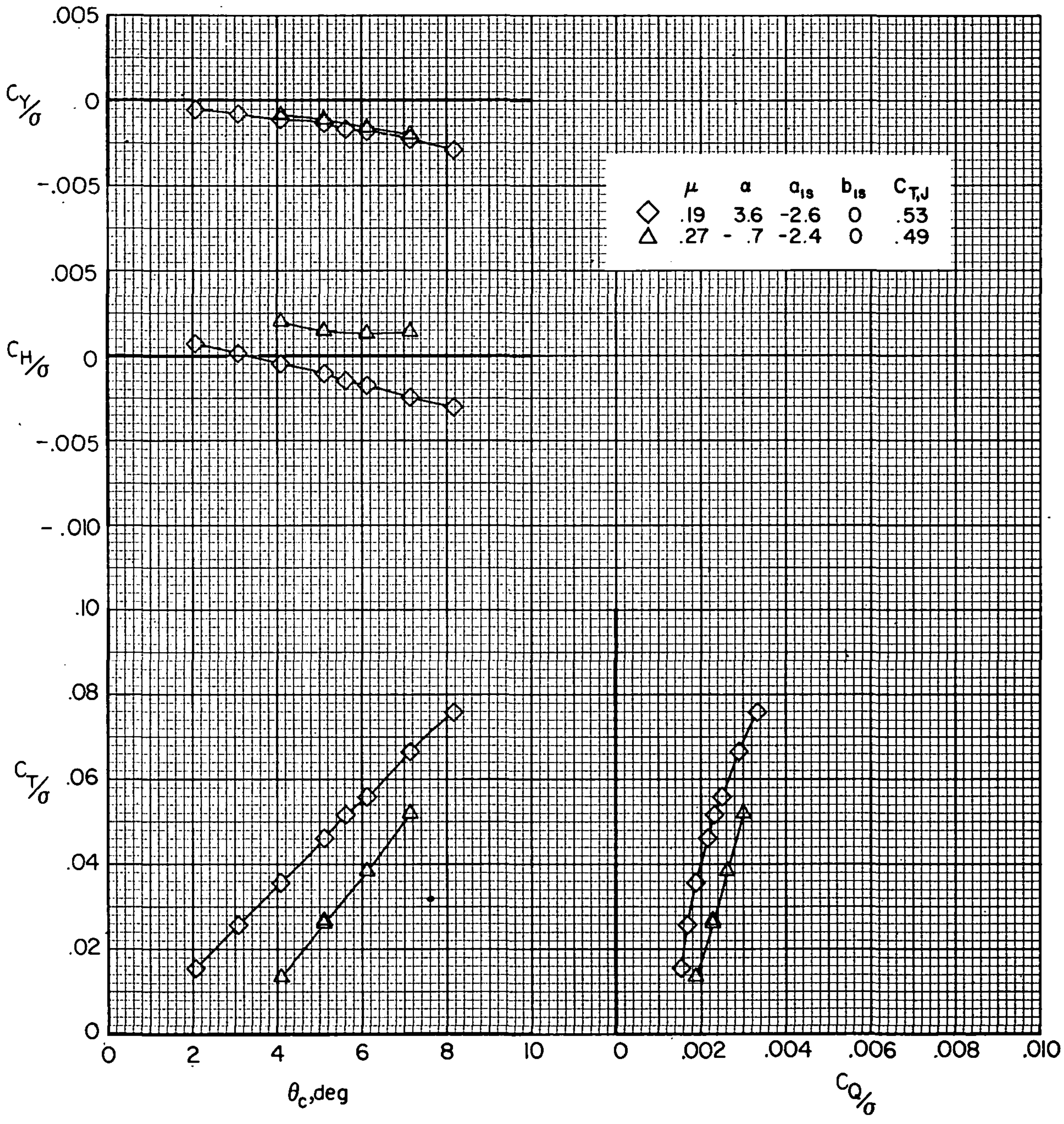

(g) $F_1M_RW_6VH_CJ_2$; low wing lift.

Figure 41.- Concluded.

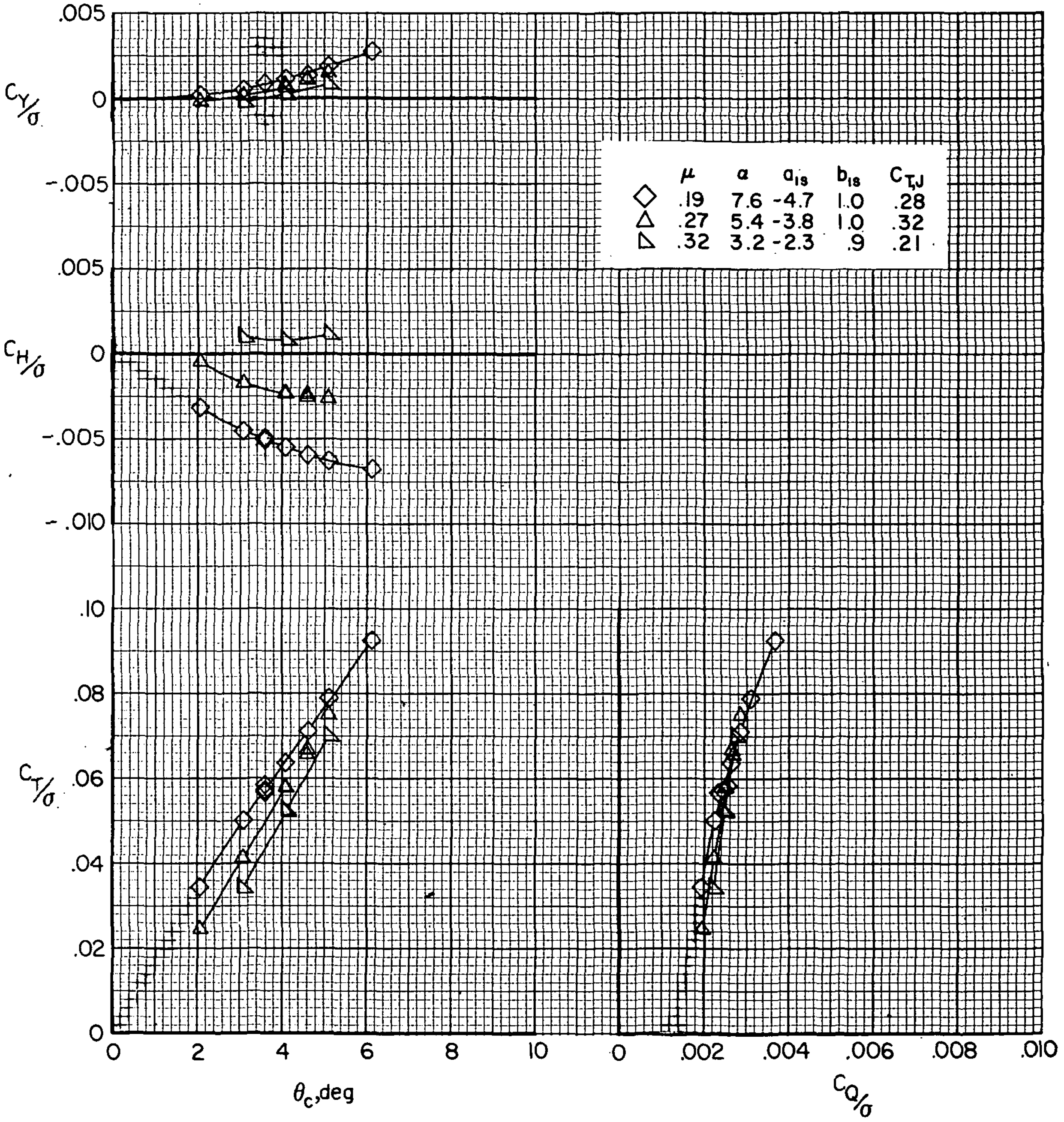

(a) $F_1M_RW_1VH_CJ_2$.

Figure 42.- Effect of forward speed on rotor aerodynamics for a variation in collective pitch angle with δ_3 = -2.0°. (α, a_{1s}, and b_{1s} are in degrees.)

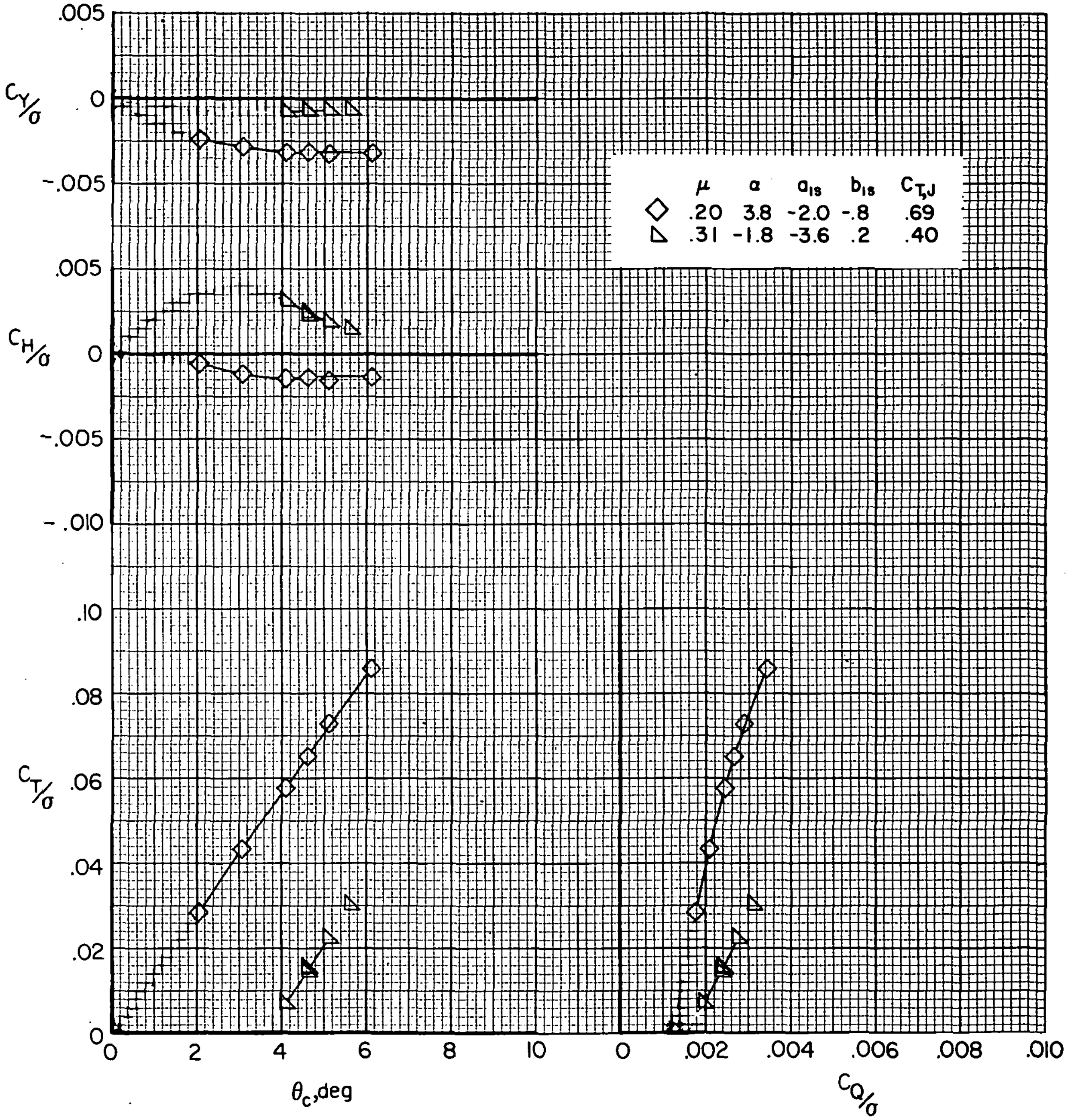

(b) $F_1M_RW_6VH_CJ_2$.

Figure 42.- Concluded.

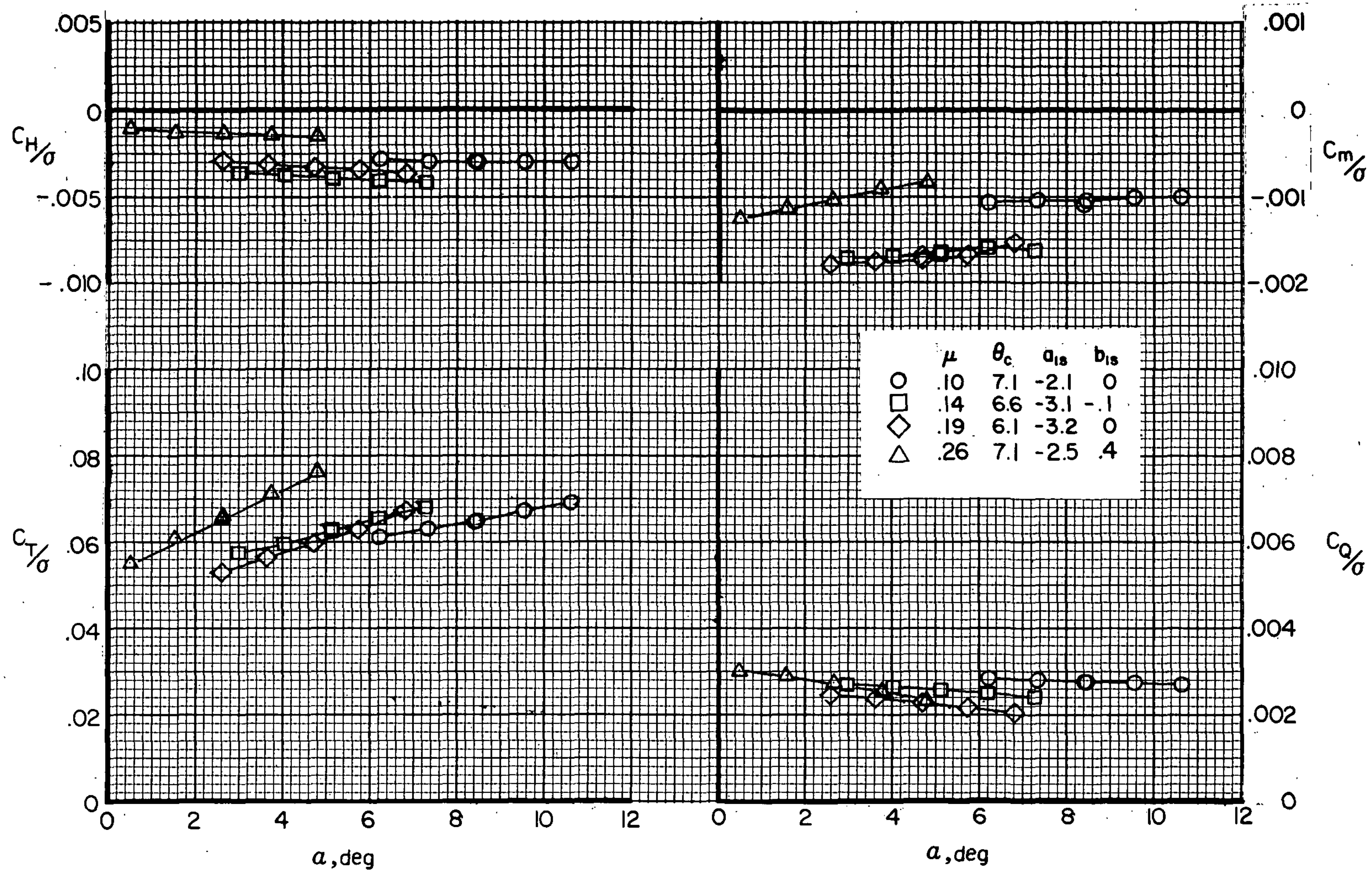

(a) $F_1M_RVH_H$.

Figure 43.- Effect of forward speed on rotor aerodynamics for an angle-of-attack variation with $\delta_3 = -27.6^\circ$. (θ_c, a_{1s}, and b_{1s} are in degrees.)

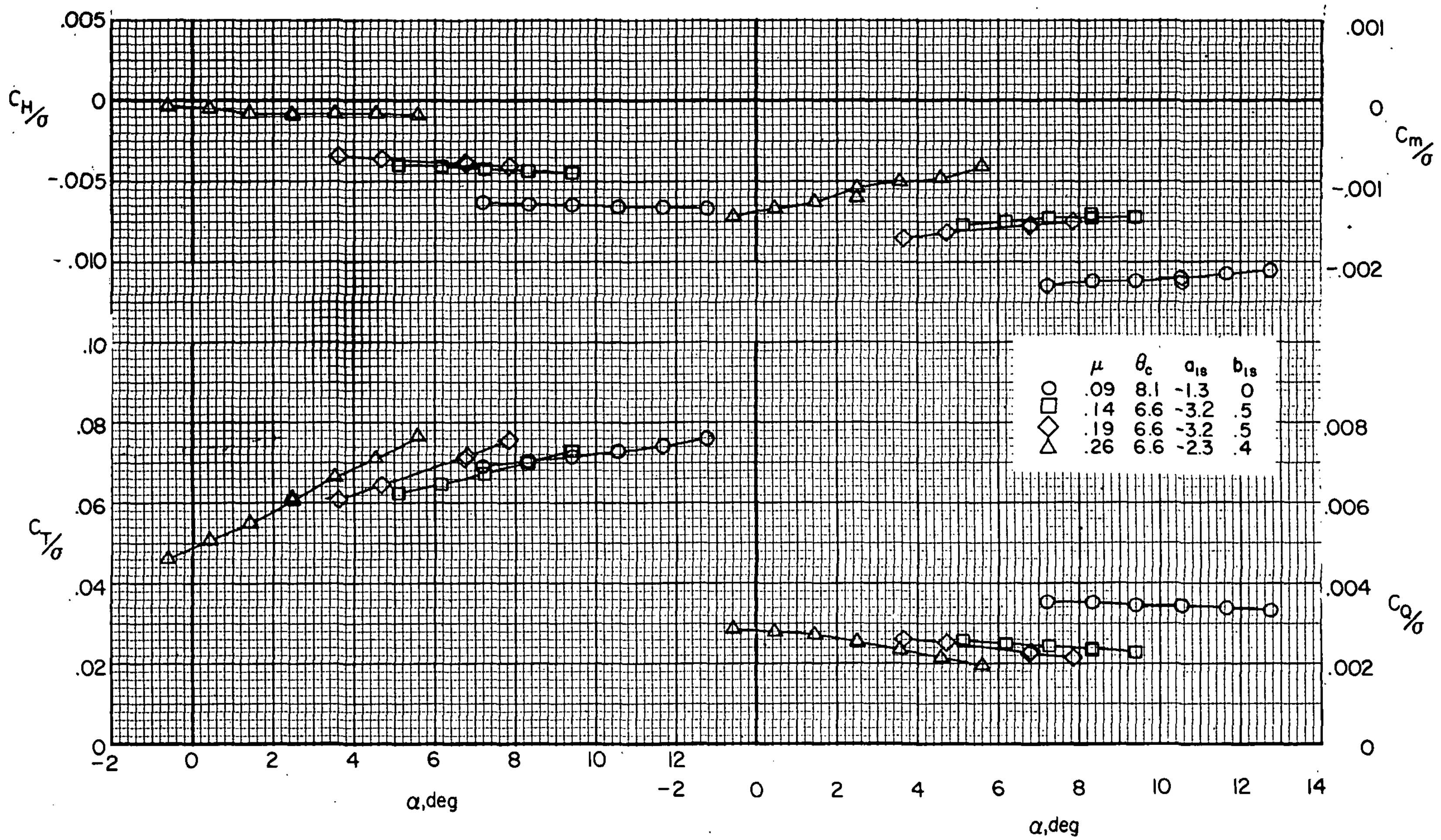

(b) $F_1M_RVH_C$.

Figure 43.- Continued.

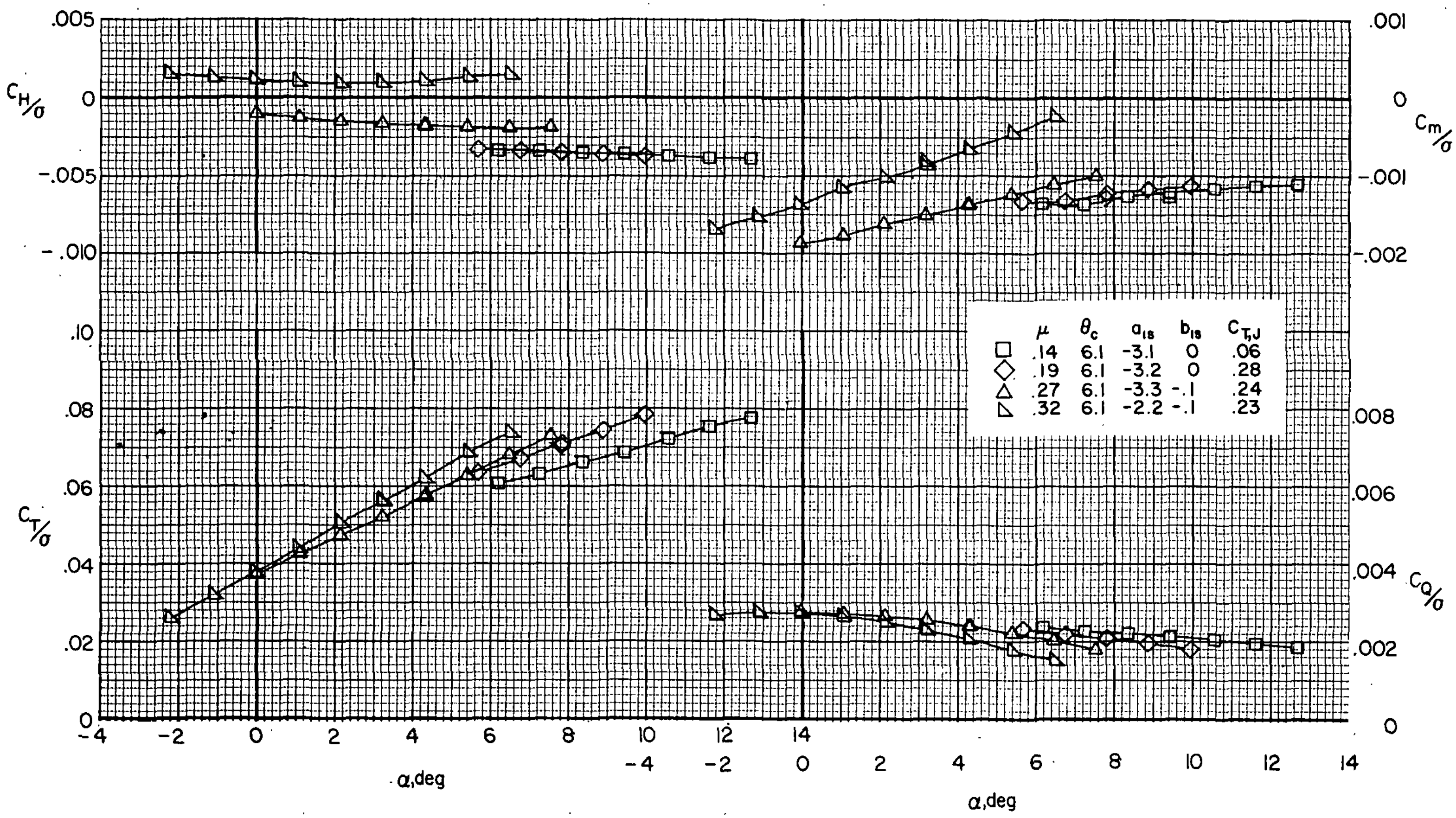

(c) $F_1M_RW_1VH_CJ_2$; high wing lift.

Figure 43.- Continued.

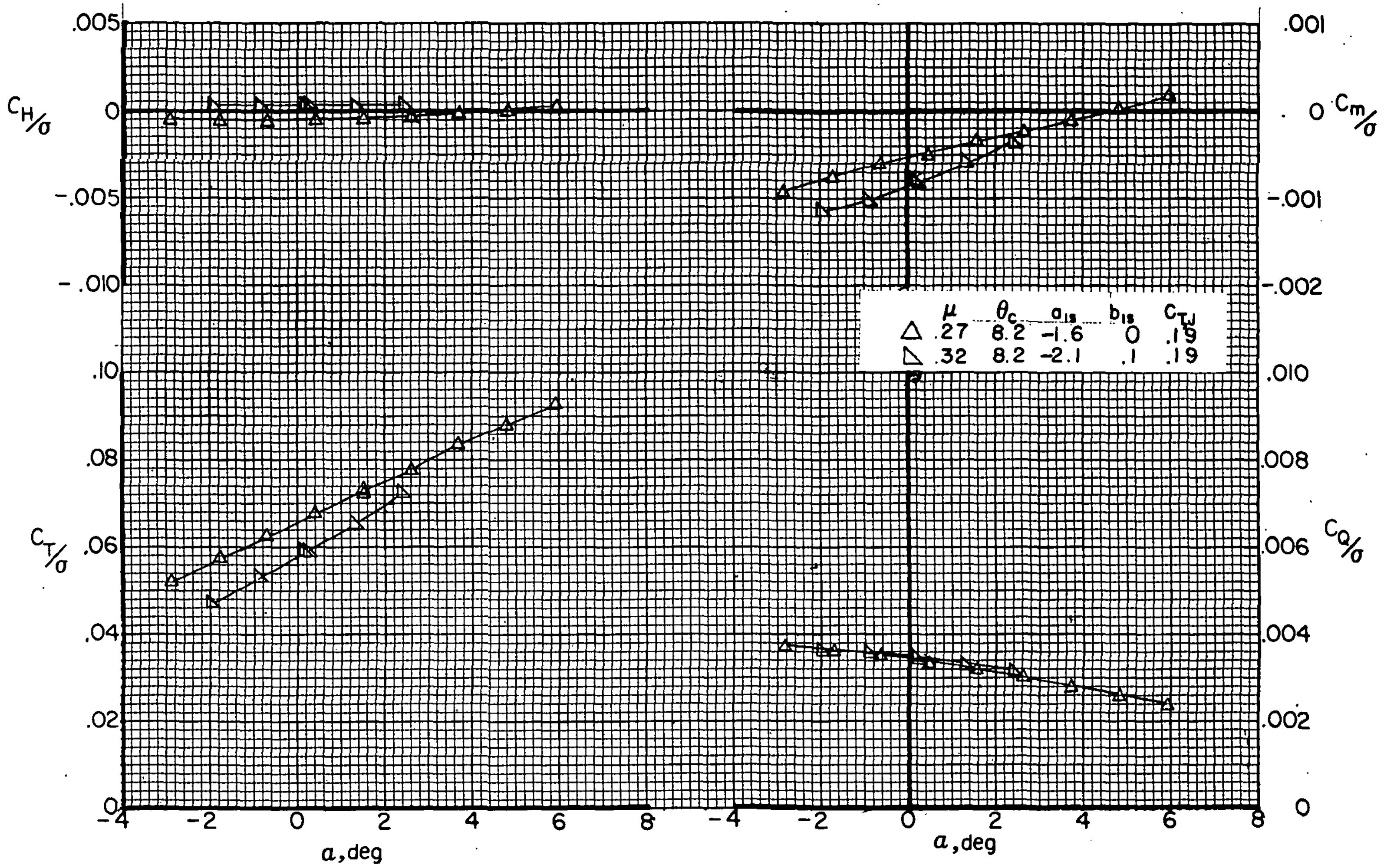

(d) $F_1 M_R W_1 VH_C J_2$; low wing lift.

Figure 43.- Continued.

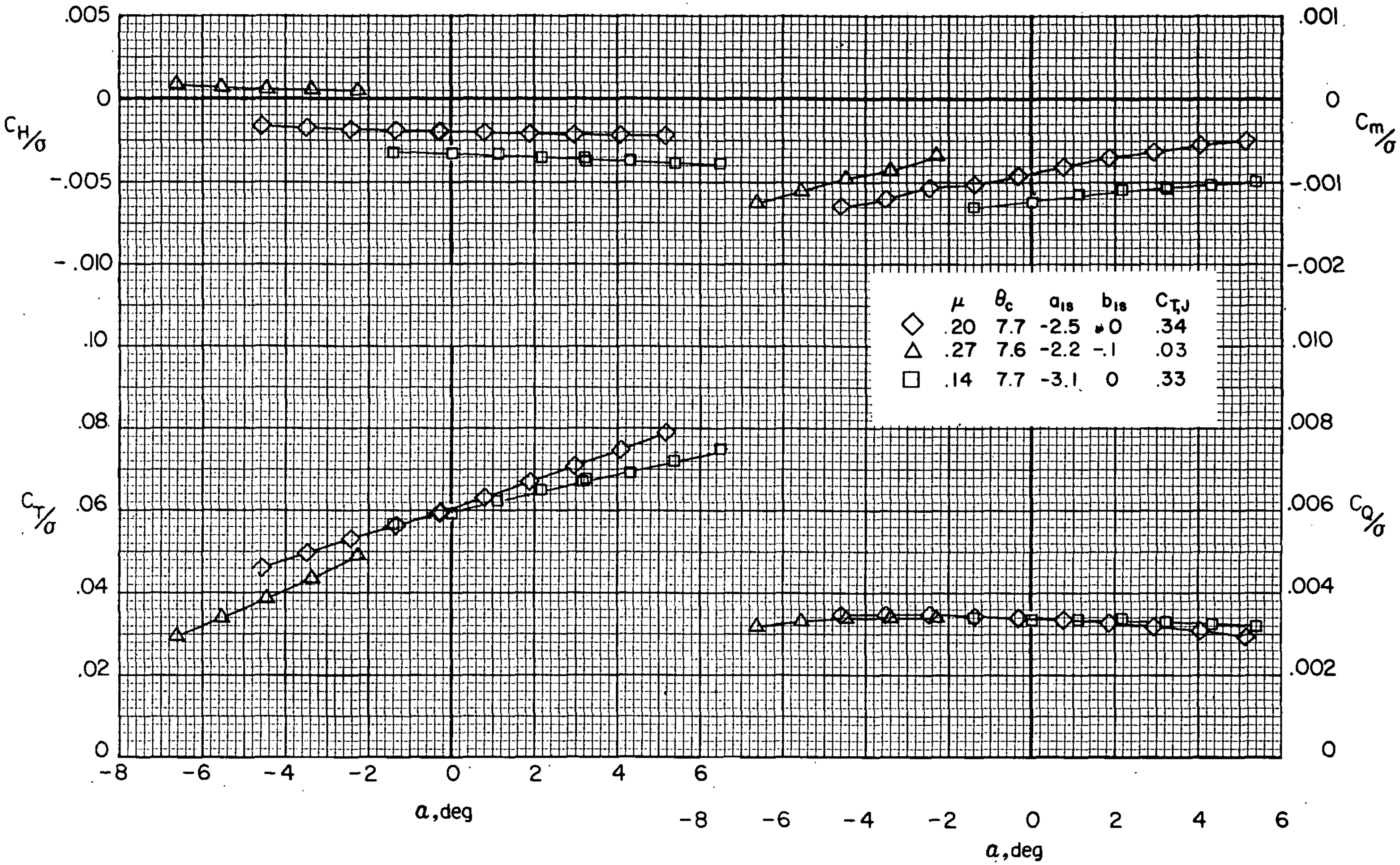

(e) $F_1M_RW_6VH_CJ_2$; high wing lift.

Figure 43.- Continued.

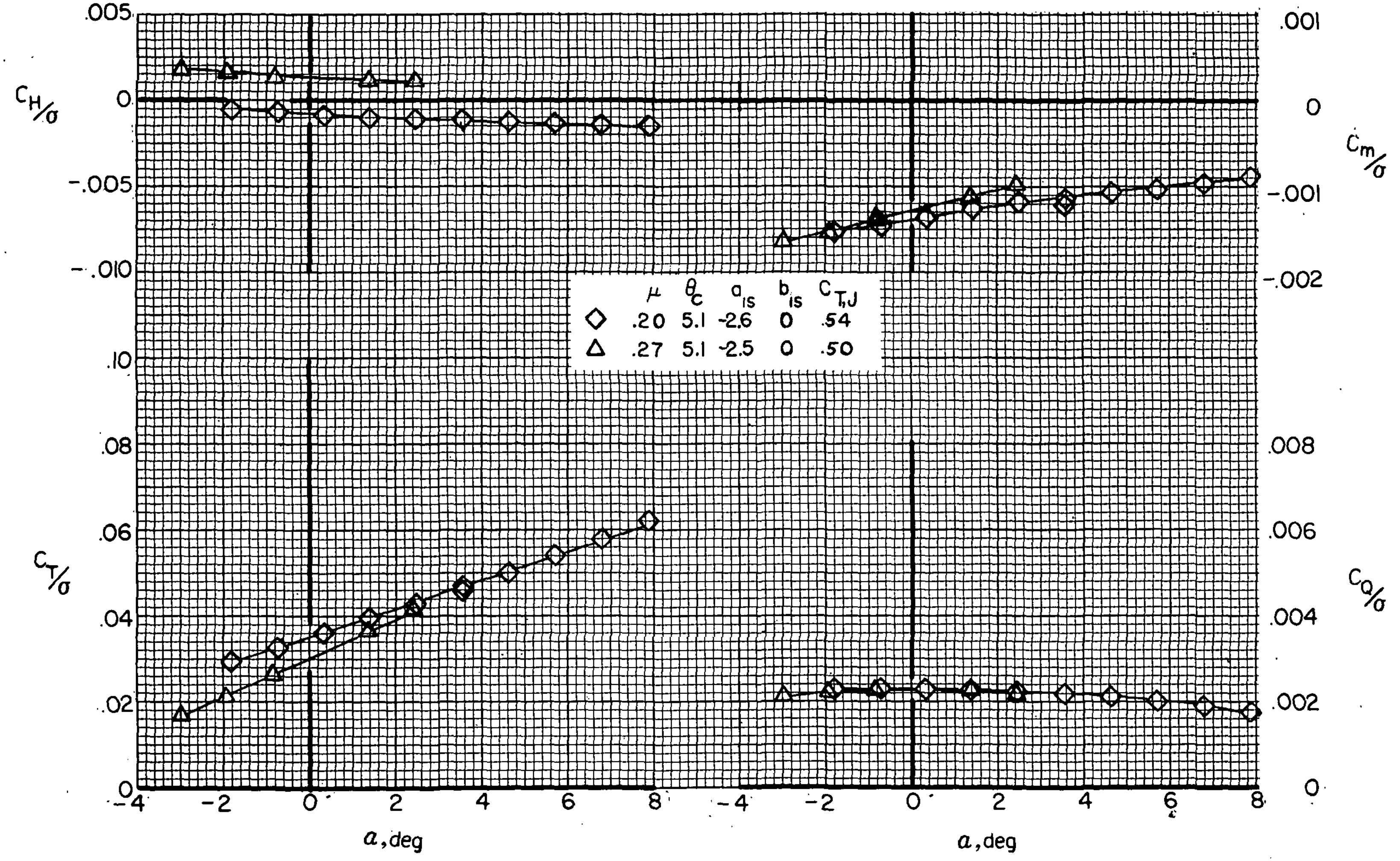

(f) $F_1M_RW_6VH_CJ_2$; low wing lift.

Figure 43.- Concluded.

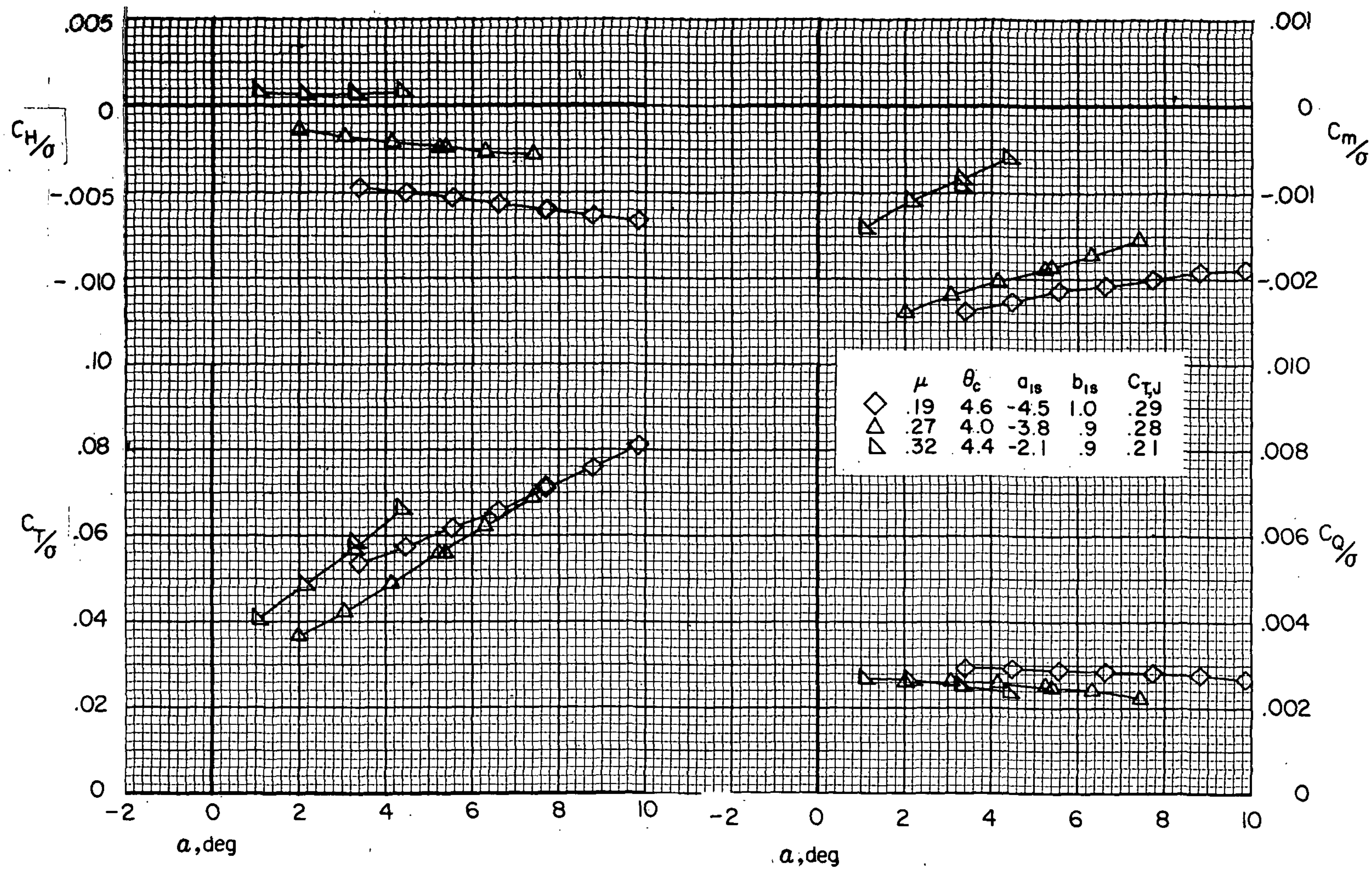

(a) $F_1M_RW_1VH_CJ_2$.

Figure 44.- Effect of forward speed on rotor aerodynamics for an angle-of-attack variation with $\delta_3 = -2.0^\circ$. (θ_c, a_{1s}, and b_{1s} are in degrees.)

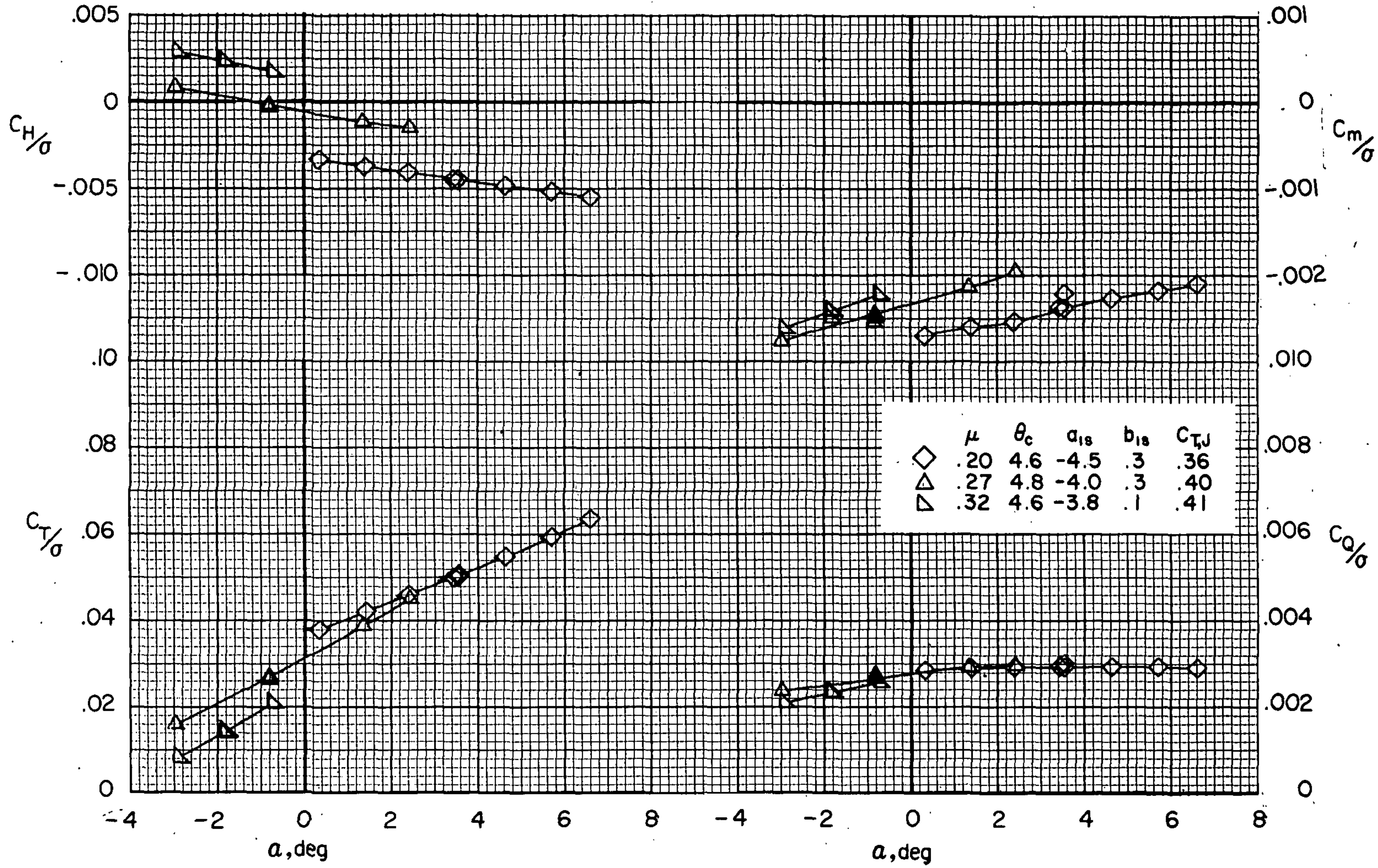

(b) $F_1M_RW_6VH_CJ_2$; high wing lift.

Figure 44.- Continued.

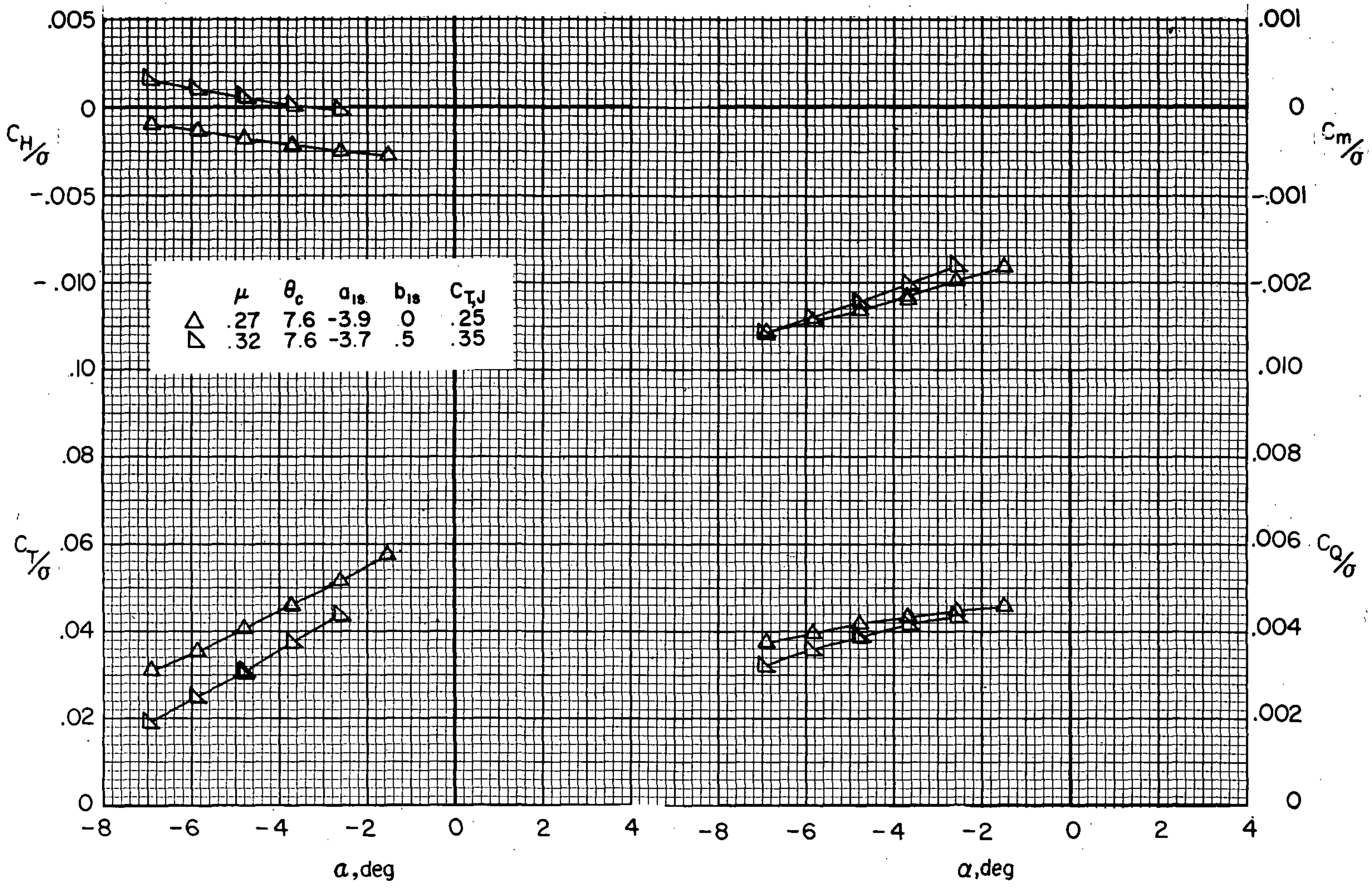

(c) $F_1M_RW_6VH_CJ_2$; low wing lift.

Figure 44.- Concluded.

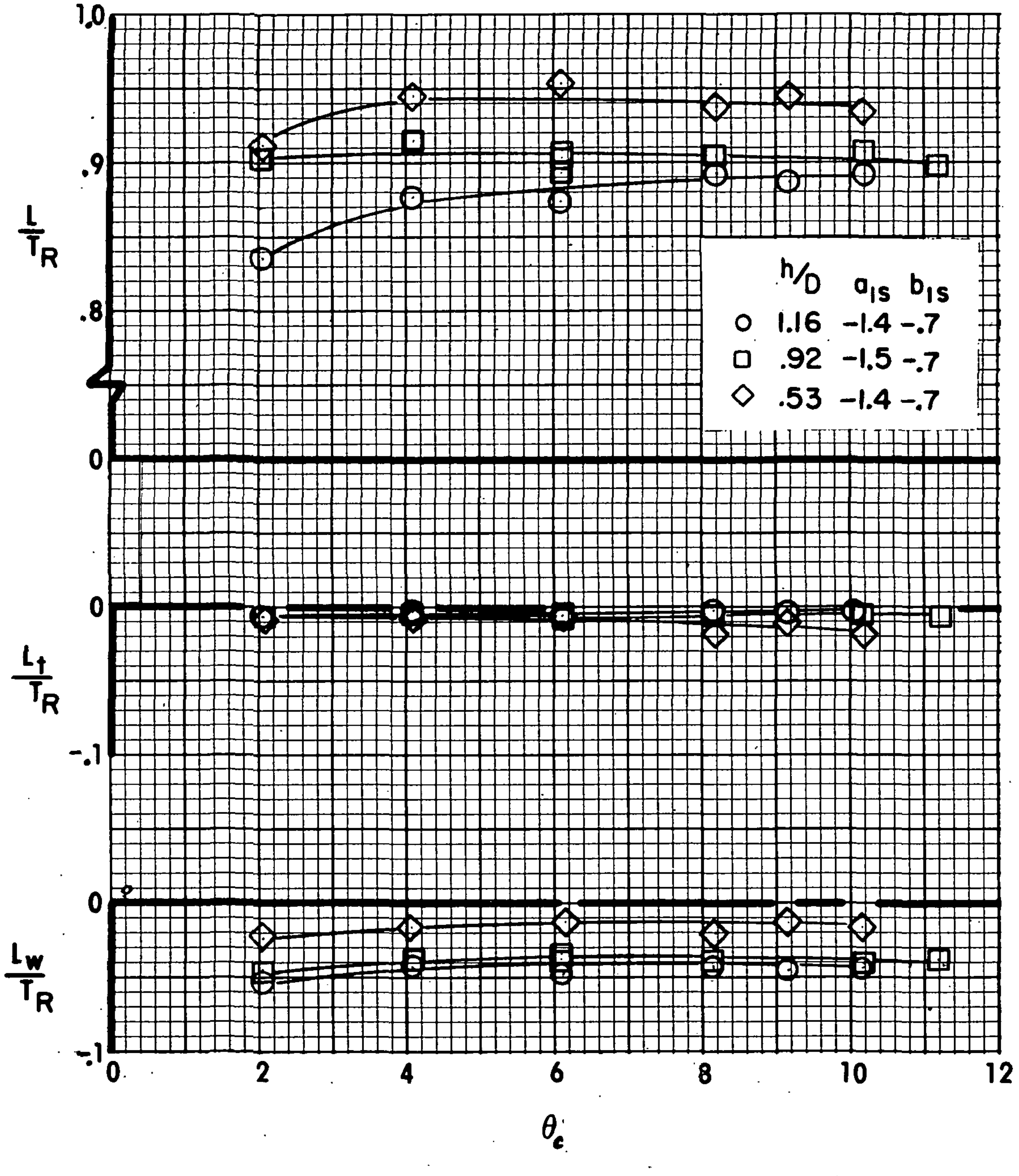

Figure 45.- Effect of ground proximity on the download in hover. $F_1M_RW_1VH_CJ_2$; $C_{T,J} \approx 0$. (a_{1s} and b_{1s} are in degrees.)

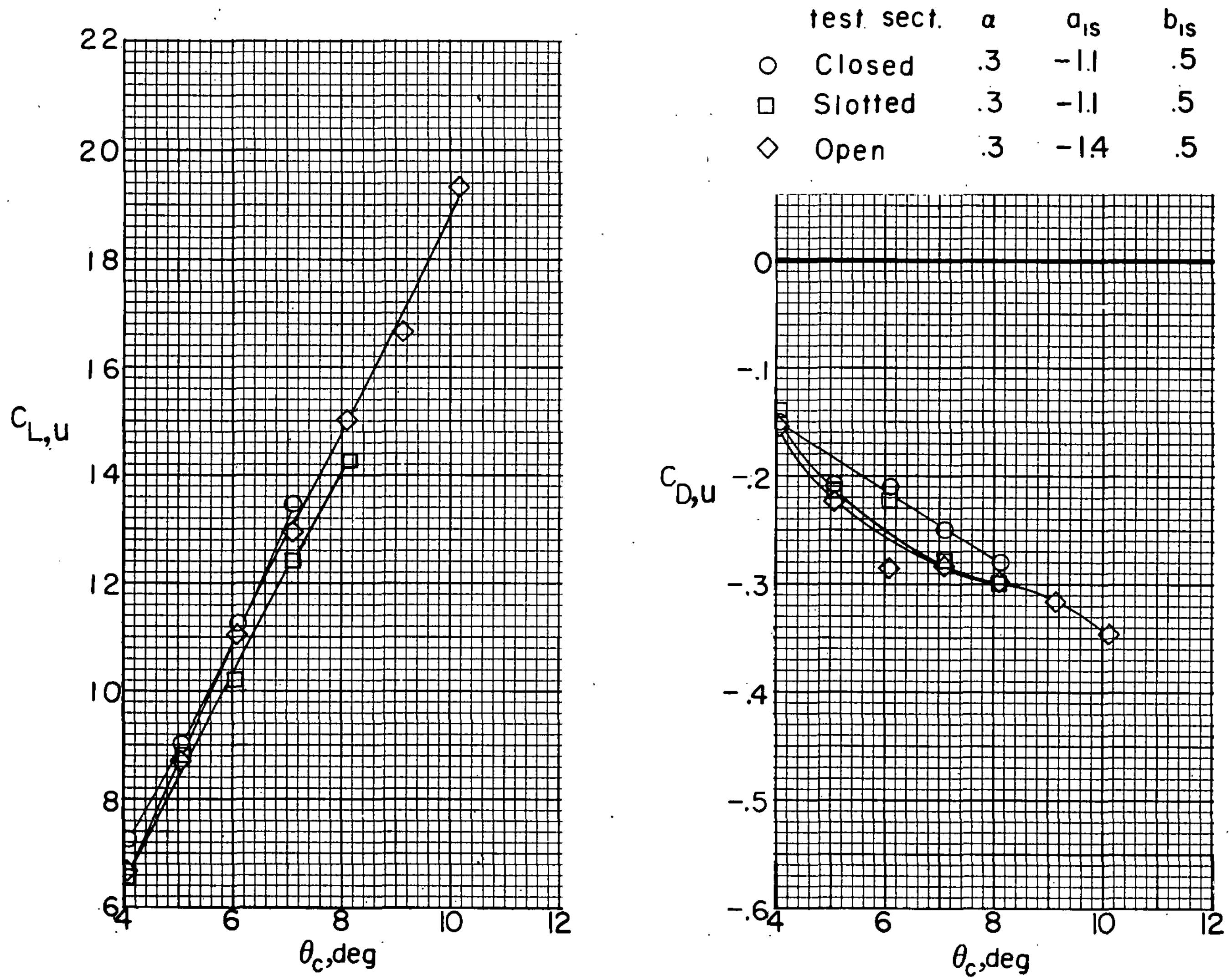

(a) No corrections for tunnel configuration.

Figure 46.- Effect of wind-tunnel test-section configuration on airframe aerodynamics. $F_1M_RVH_C$; $\mu = 0.07$. (α, a_{1s}, and b_{1s} are in degrees.)

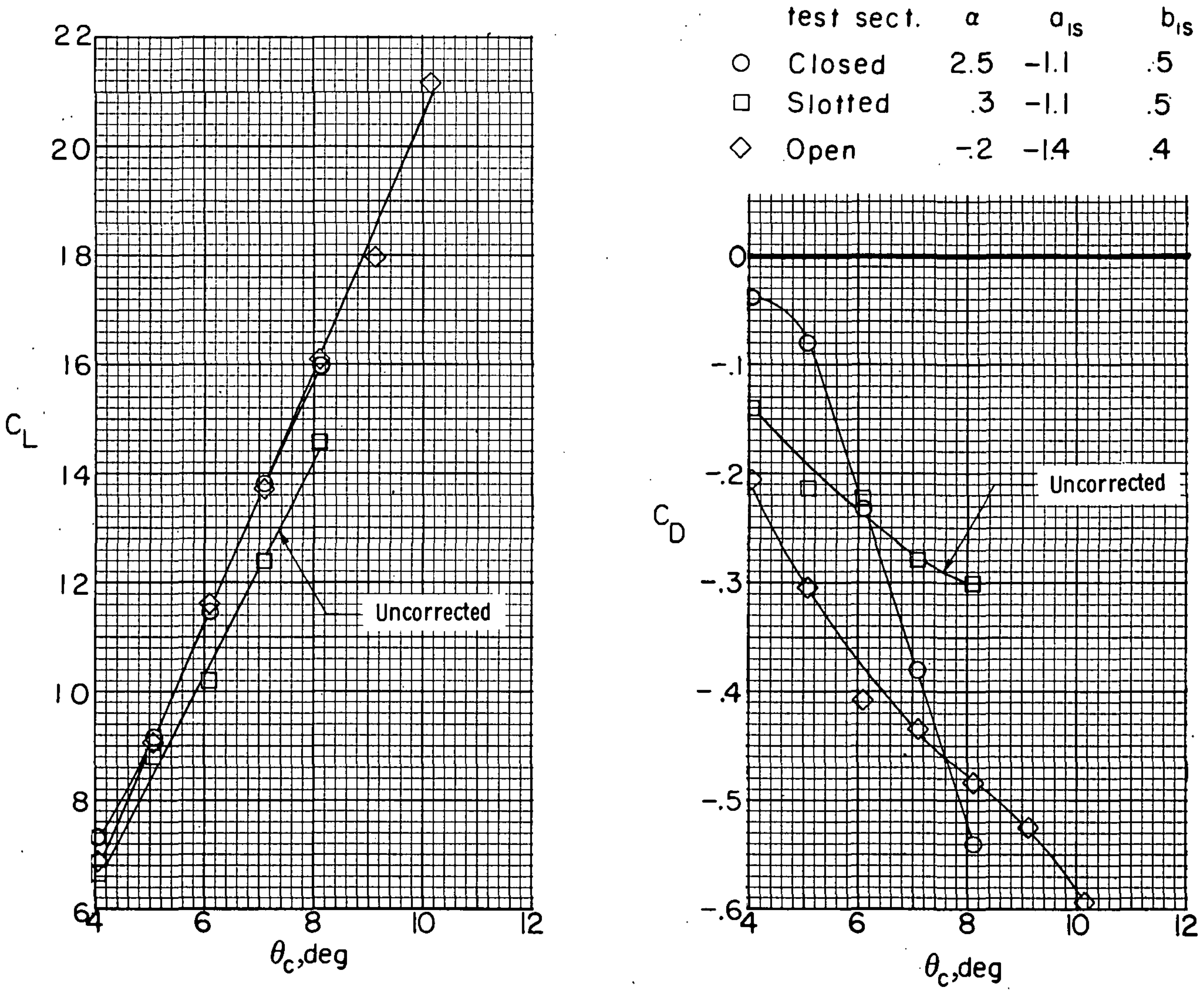

(b) Corrected for tunnel configuration.

Figure 46.- Continued.

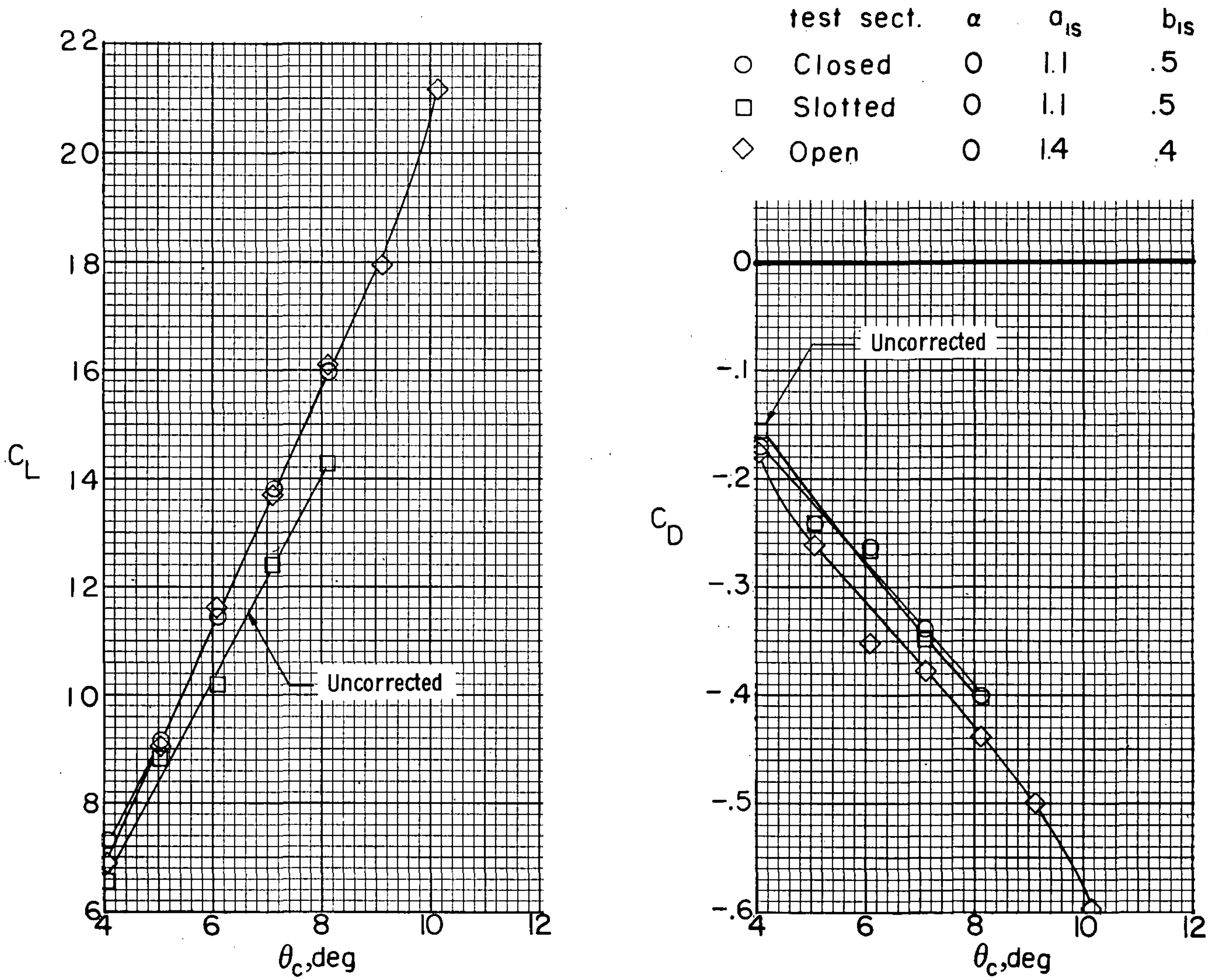

(c) Corrected for tunnel configuration and adjusted to same angle of attack.

Figure 46.- Concluded.

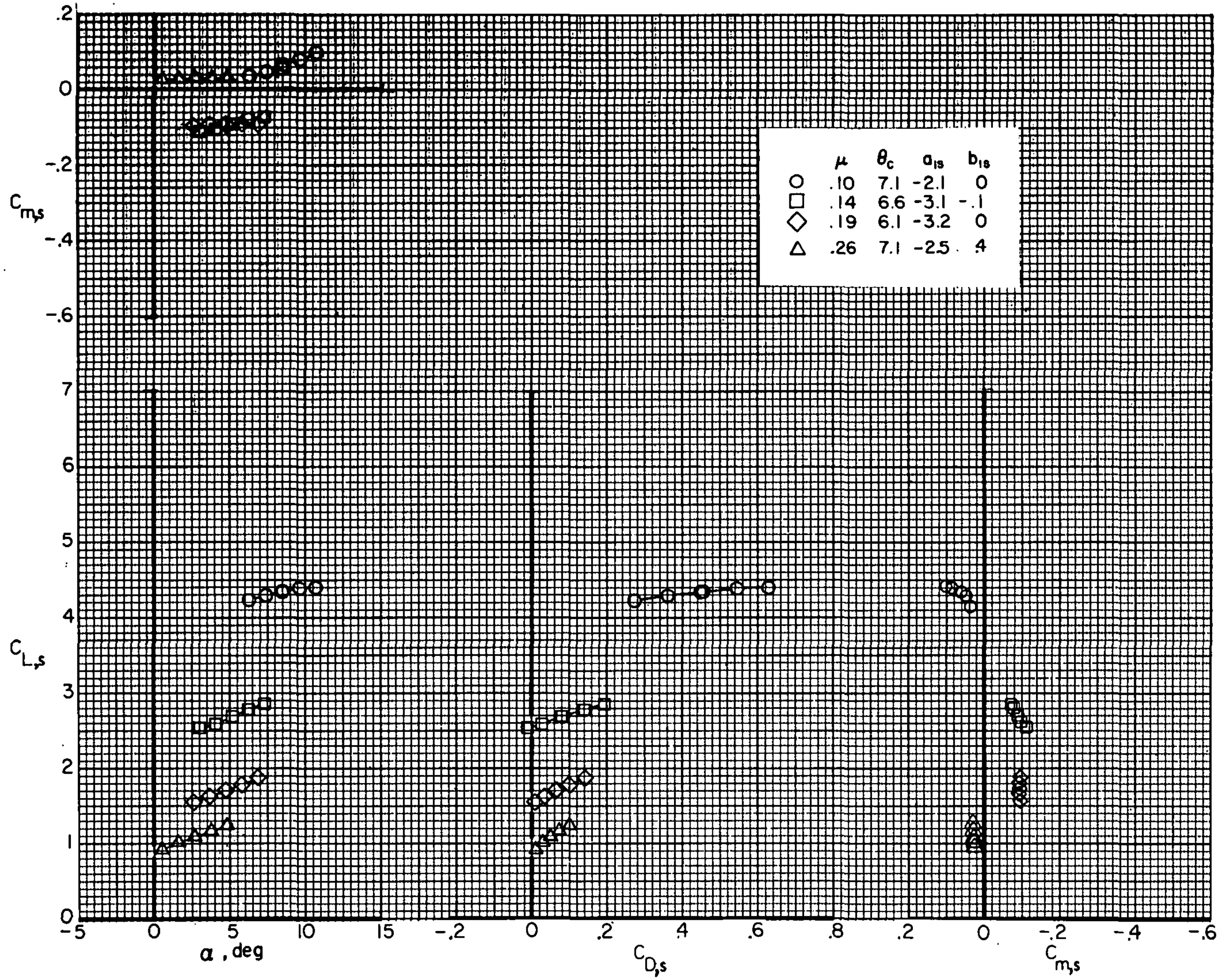

(a) $F_1M_RVH_H$.

Figure 47.- Effect of forward speed on airframe longitudinal aerodynamics with the rotor on for $\delta_3 = -27.6^{\circ}$. (θ_c, a_{1s}, and b_{1s} are in degrees.)

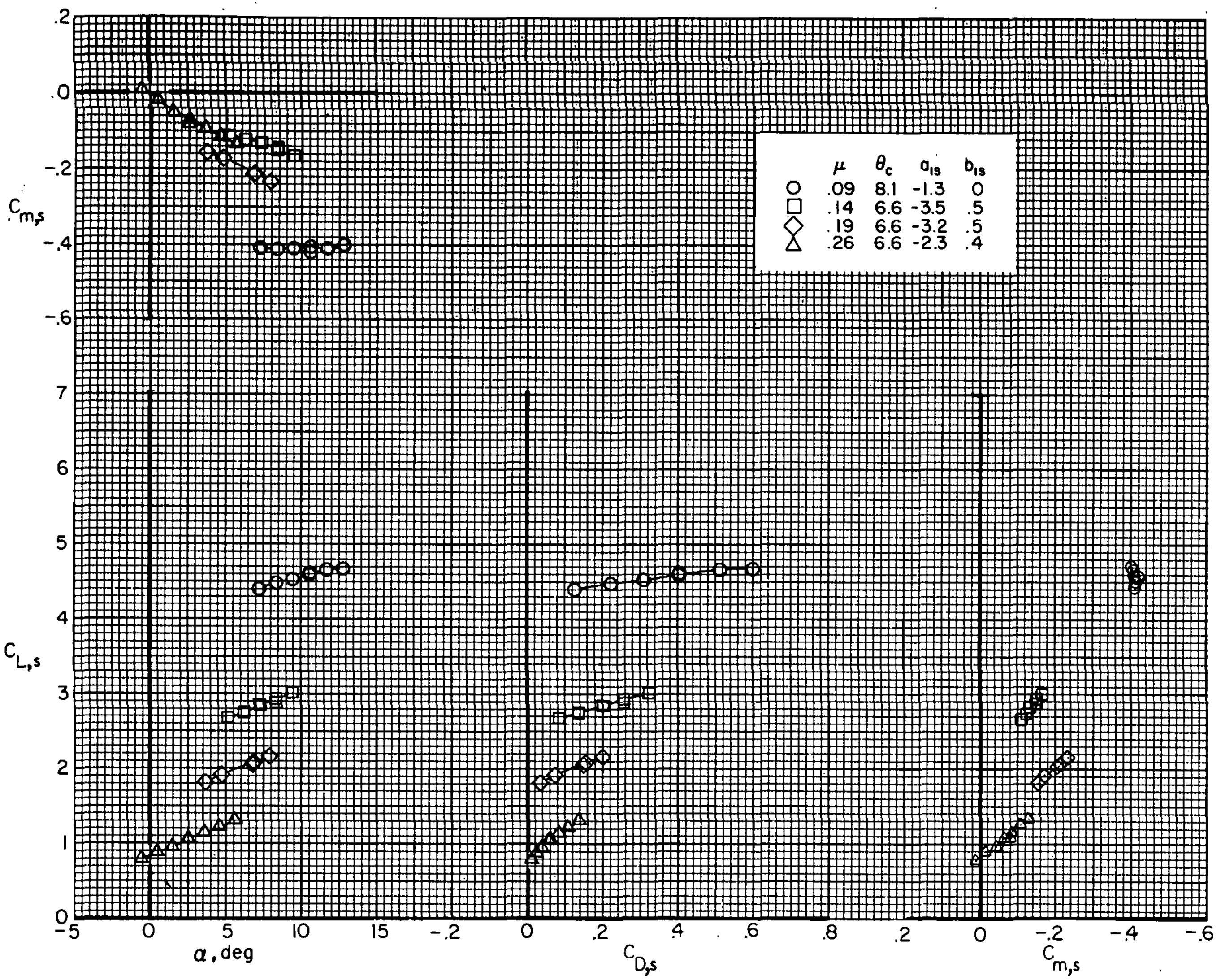

(b) $F_1 M_R VH_C$.

Figure 47.- Continued.

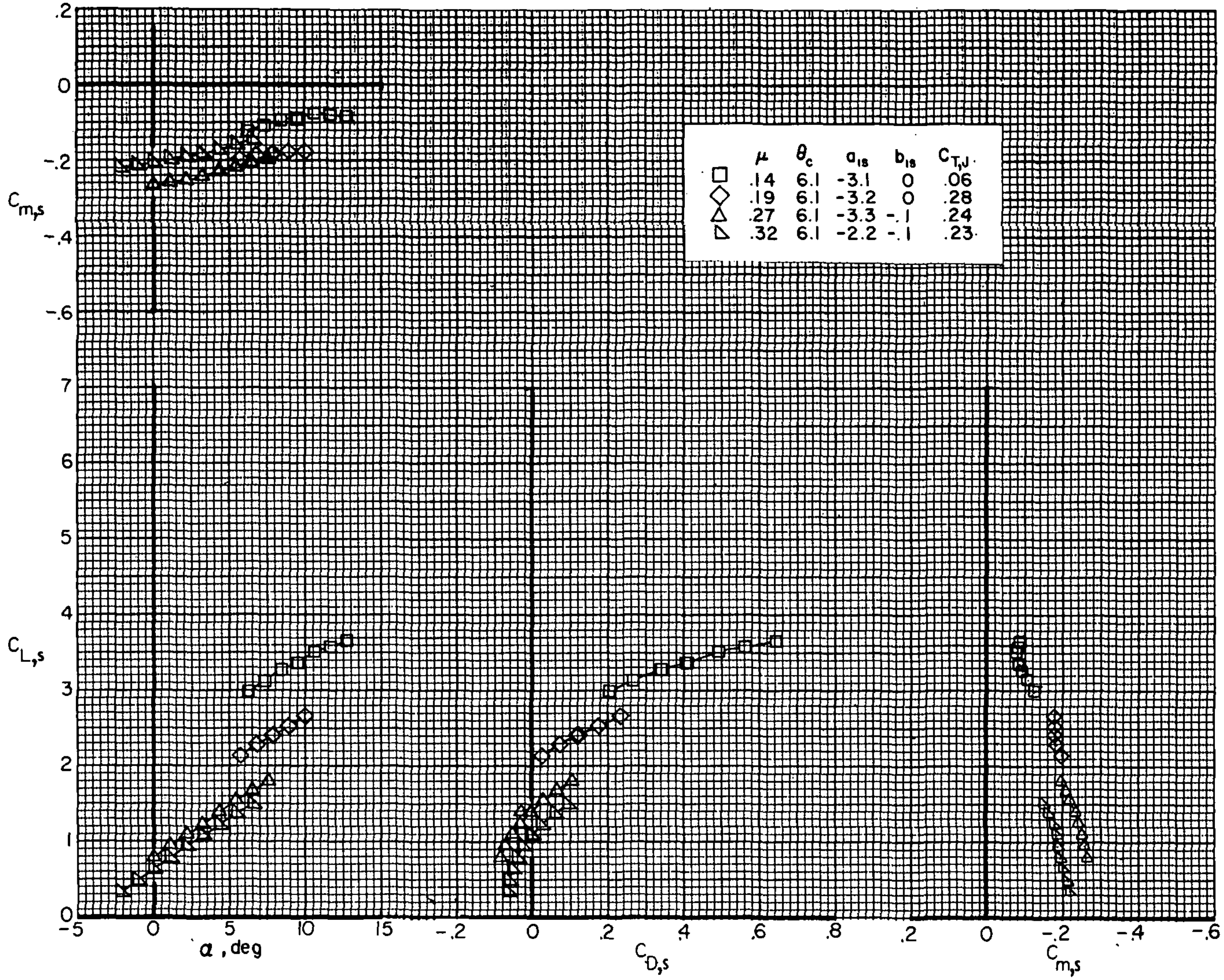

(c) $F_1M_RW_1VH_CJ_2$; high wing lift.

Figure 47.- Continued.

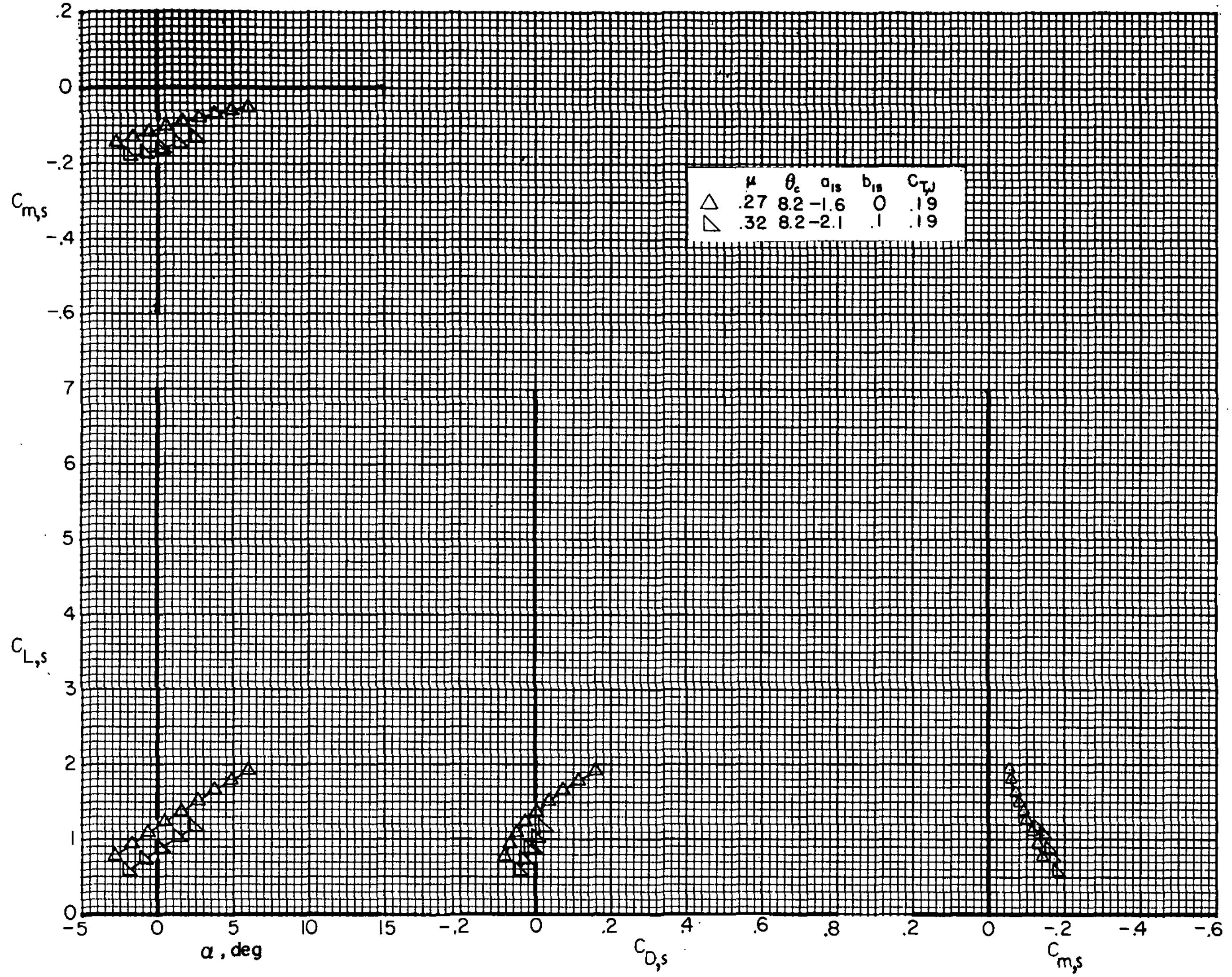

(d) $F_1 M_R W_1 V H_C J_2$; low wing lift.

Figure 47.- Continued.

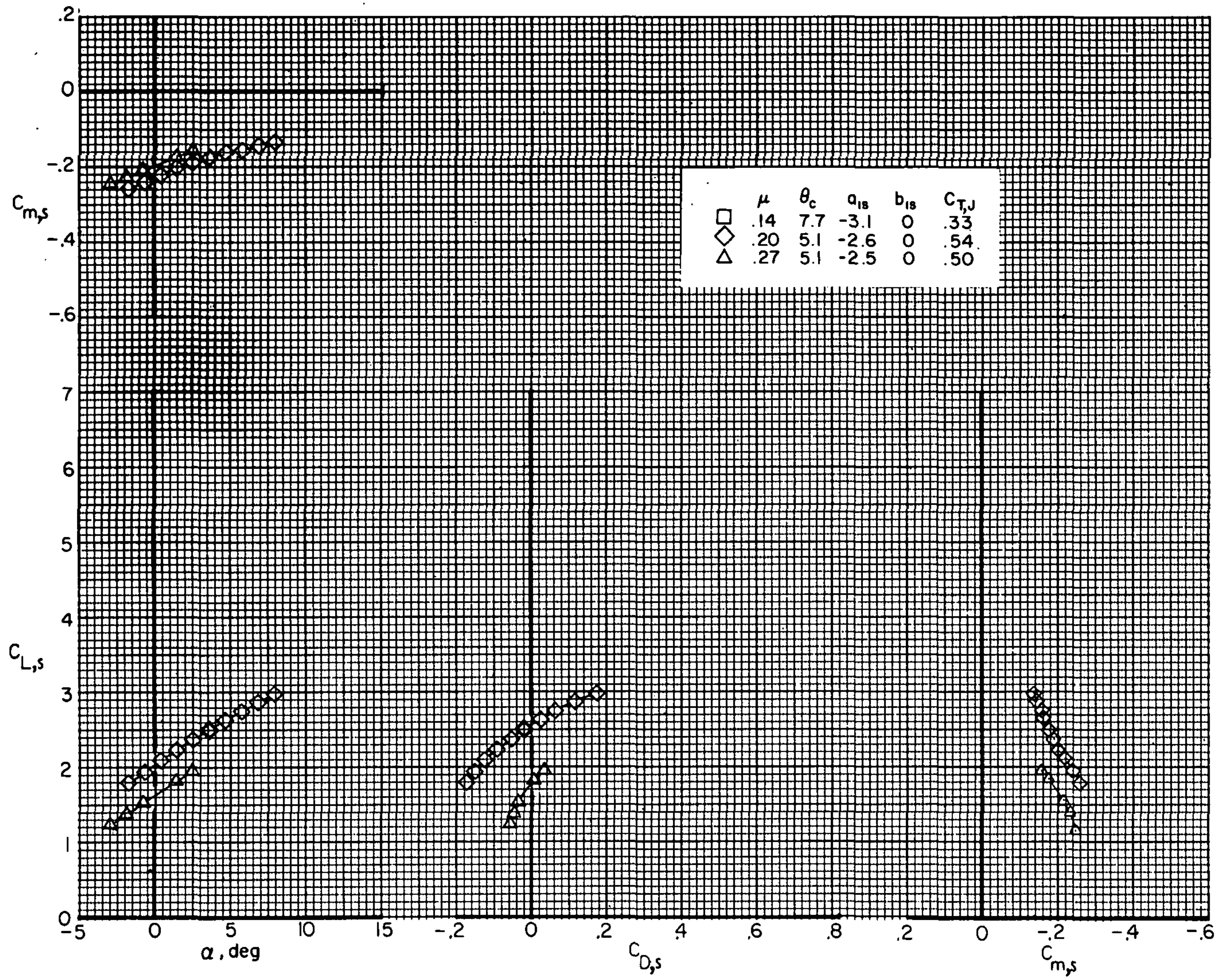

(e) $F_1M_RW_6VH_CJ_2$; high wing lift.

Figure 47.- Continued.

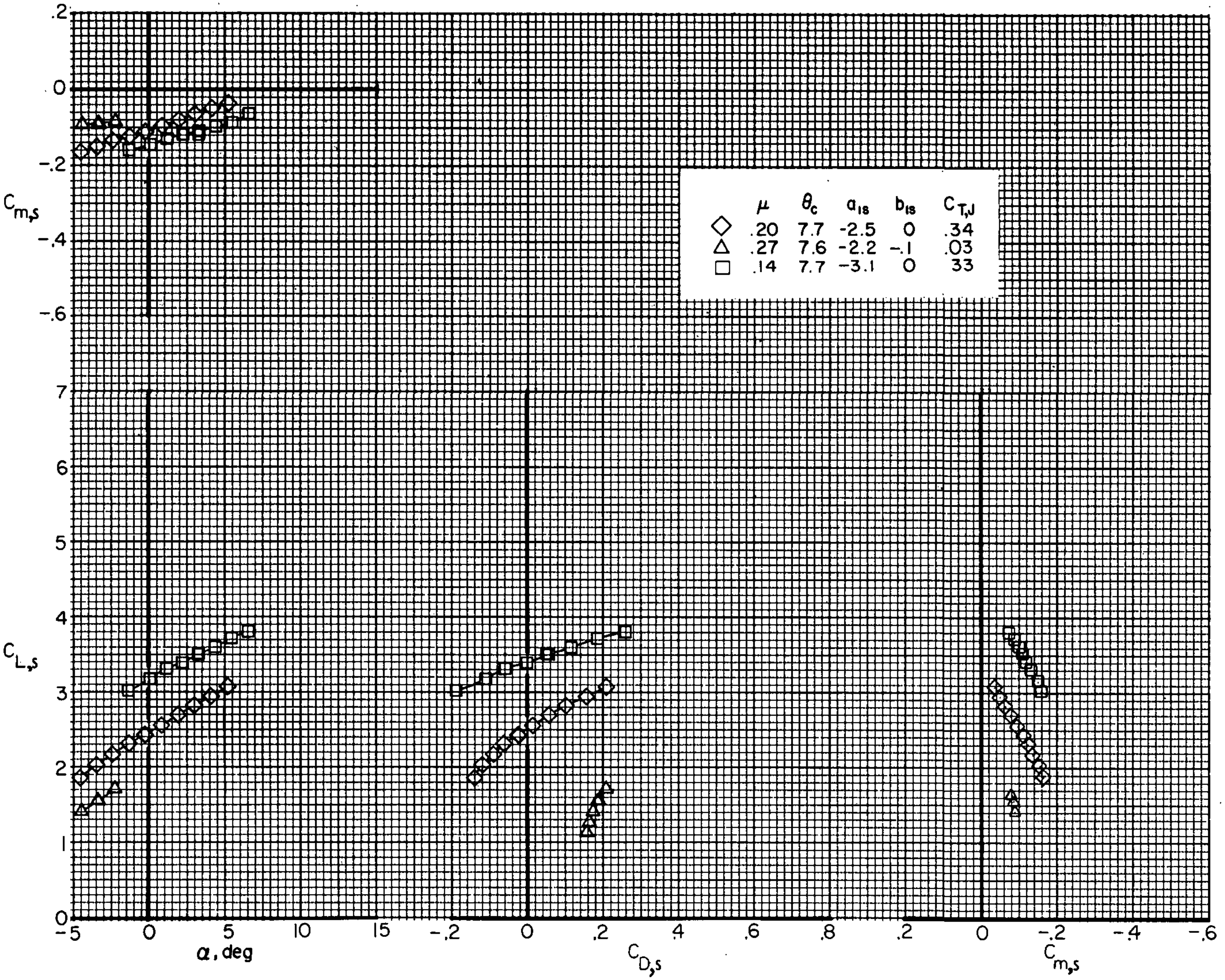

(f) $F_1M_RW_6VH_CJ_2$; low wing lift.

Figure 47. - Concluded.

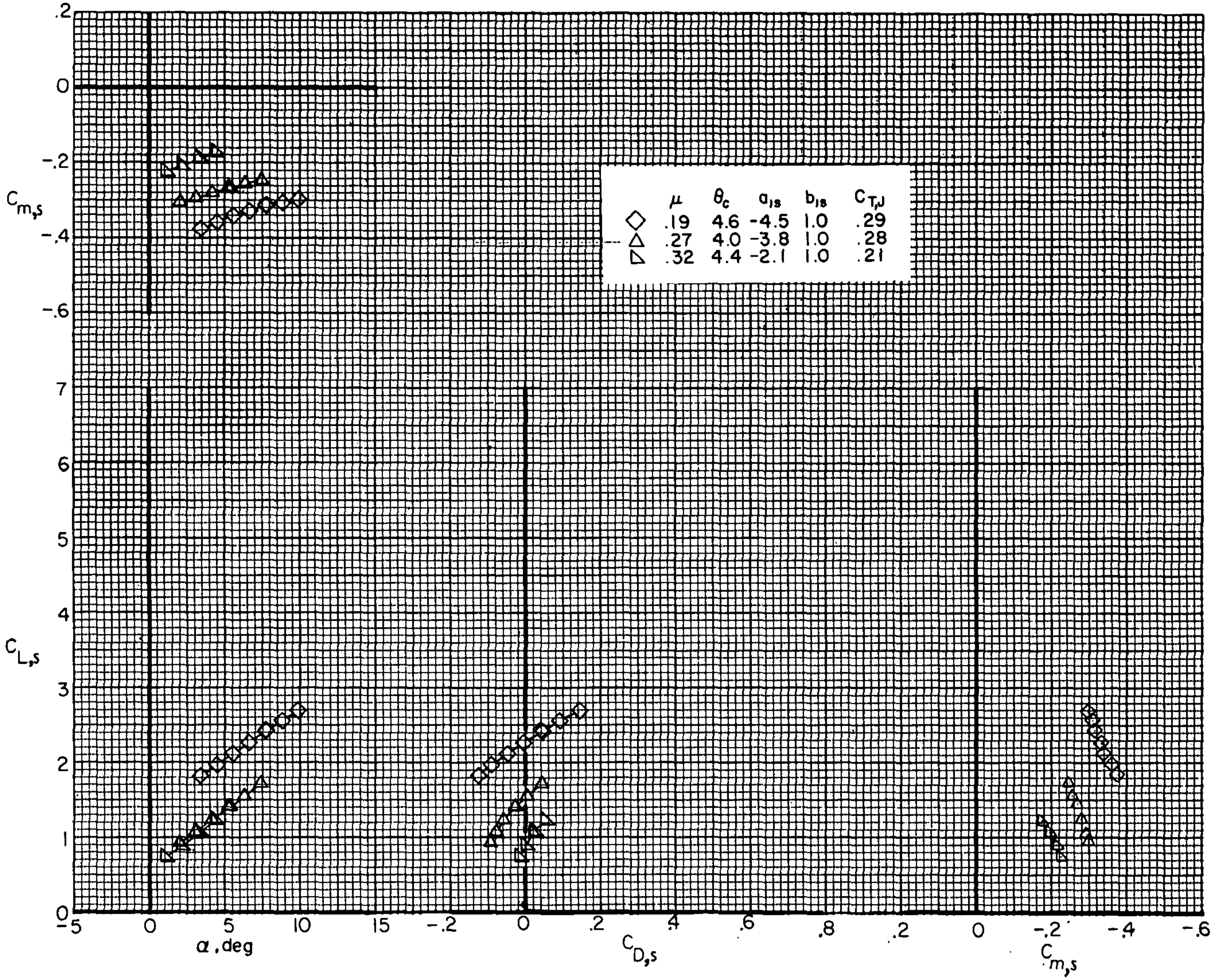

(a) $F_1M_RW_1VH_CJ_2$.

Figure 48.- Effect of forward speed on airframe longitudinal aerodynamics with the rotor on for $\delta_3 = -2.0^{\circ}$. (θ_c, a_{1s}, and b_{1s} are in degrees.)

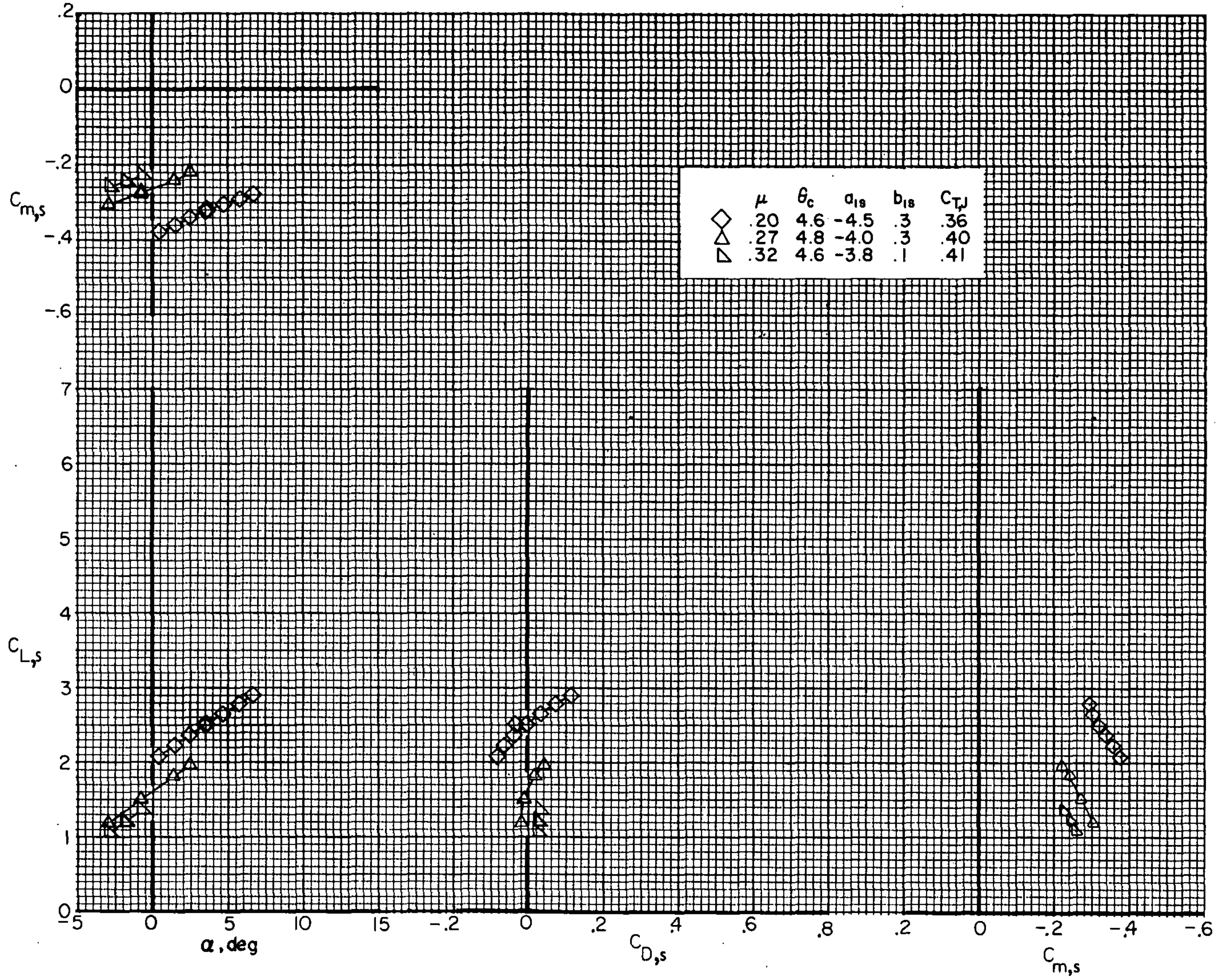

(b) $F_1 M_R W_6 V H_C J_2$; high wing lift.

Figure 48.- Continued.

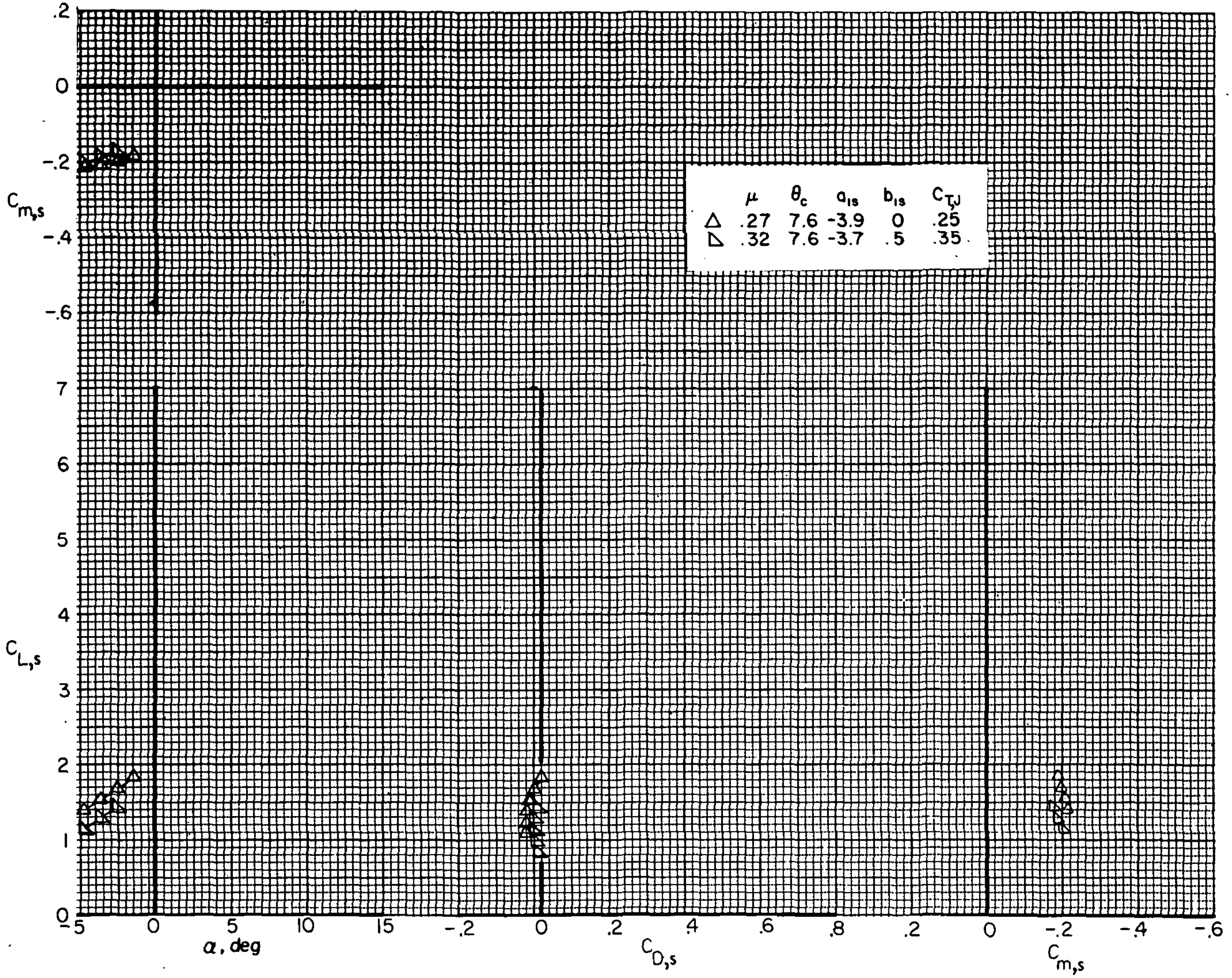

(c) $F_1 M_R W_6 V H_C J_2$; low wing lift.

Figure 48.- Concluded.

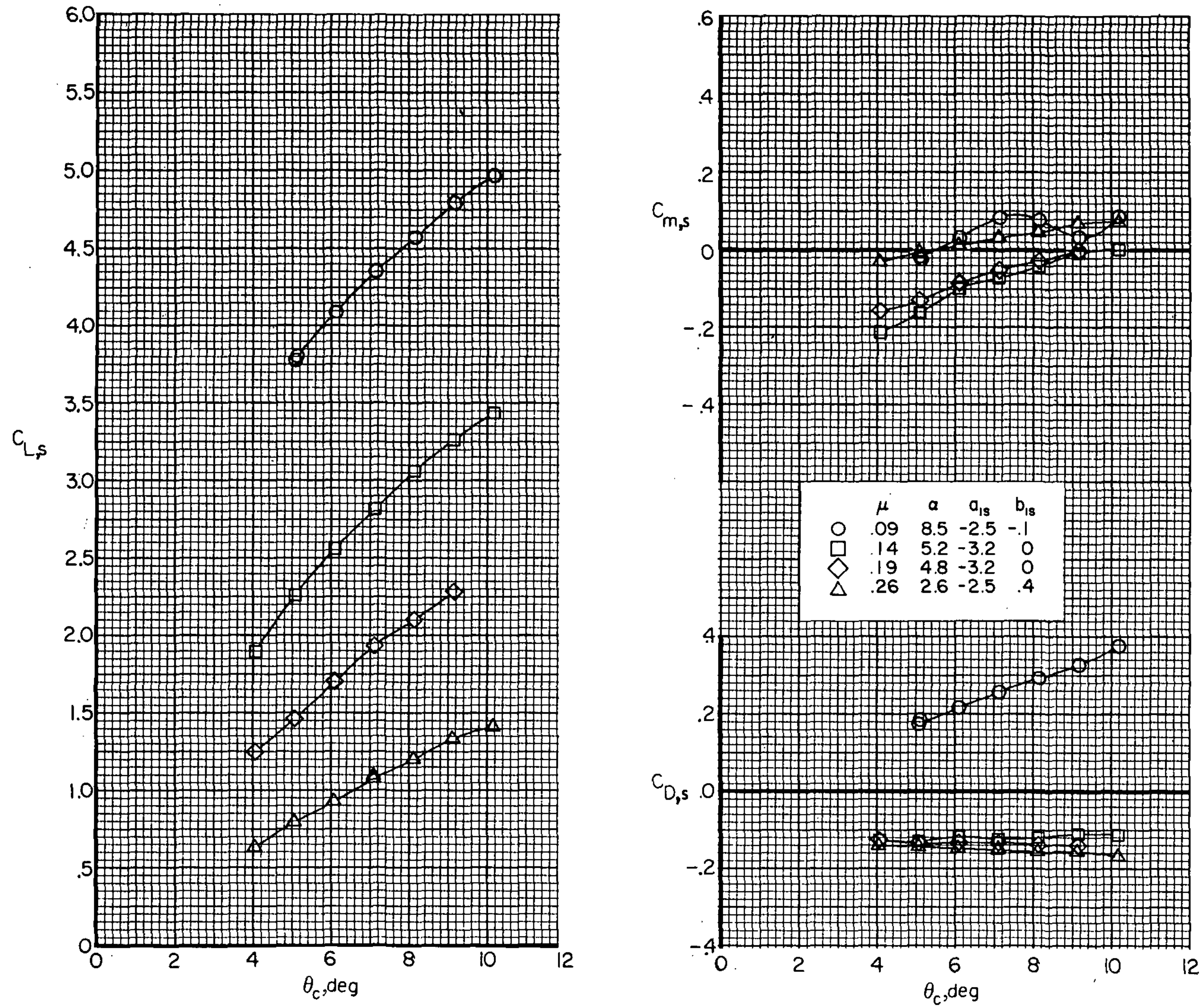

(a) $F_1 M_R V H_H$.

Figure 49.- Variation of airframe longitudinal aerodynamics with collective pitch angle with the rotor at several forward speeds for $\delta_3 = -27.6^{\circ}$. (α, a_{1s}, and b_{1s} are in degrees.)

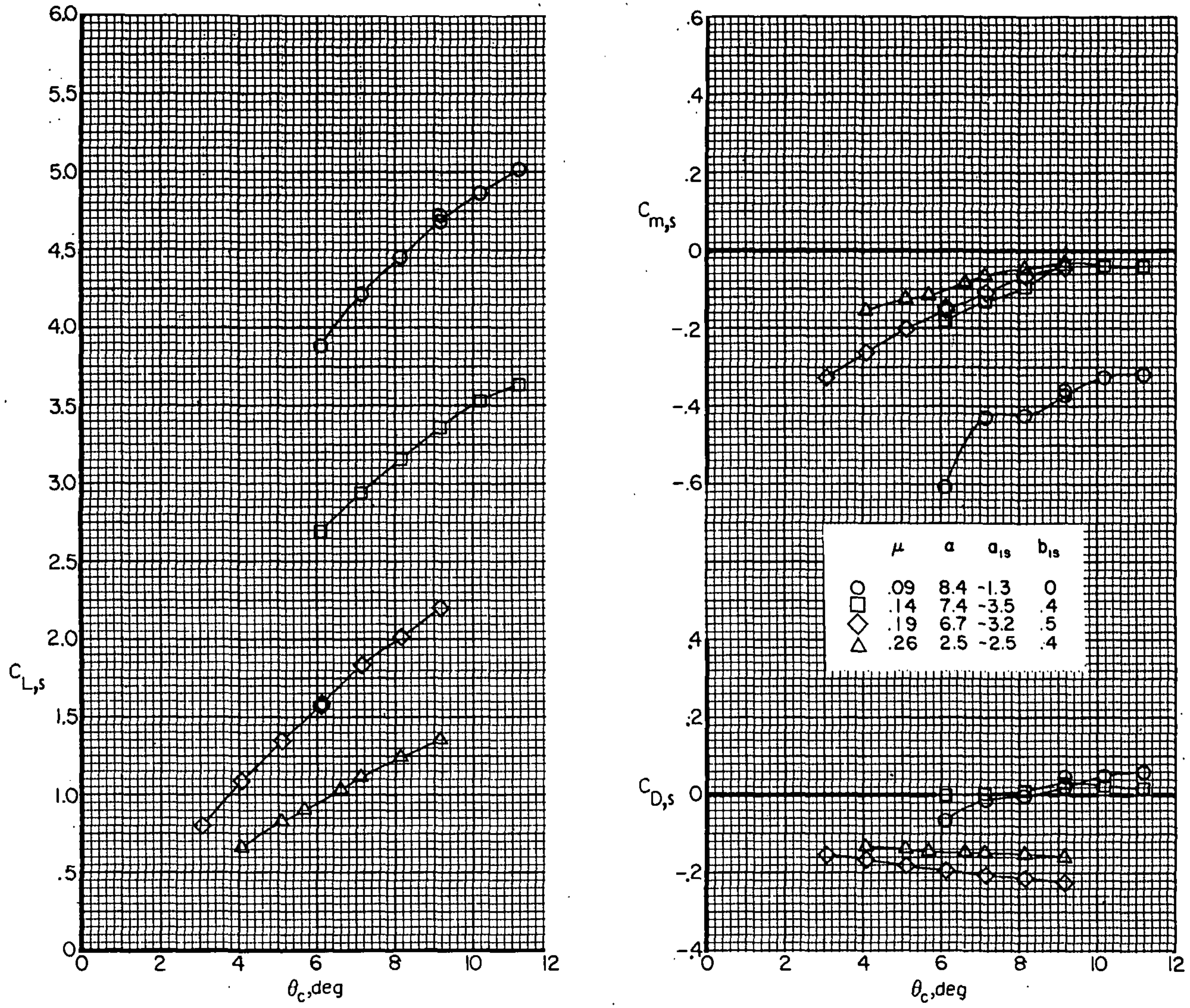

(b) $F_1M_RVH_C$.

Figure 49.- Continued.

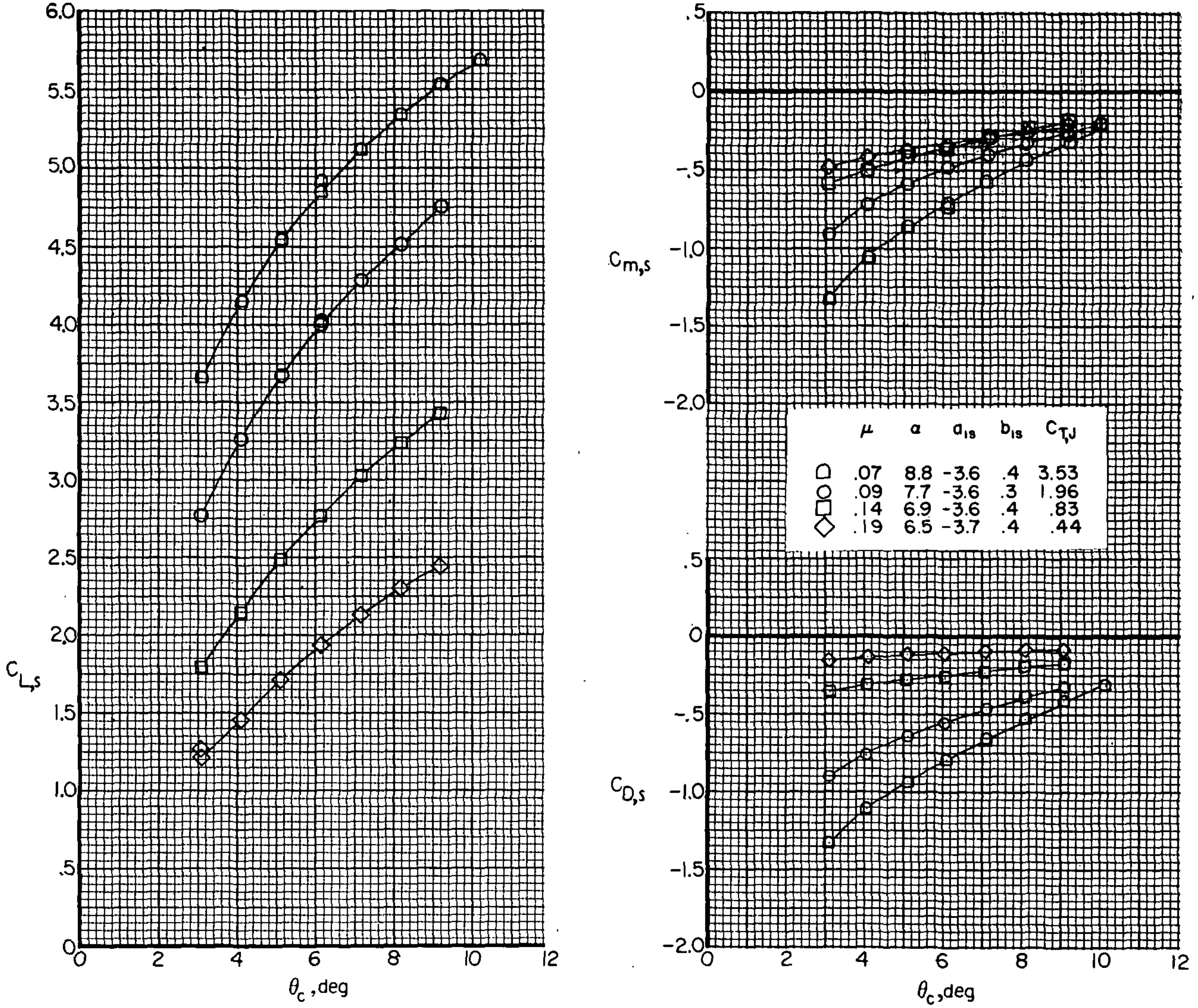

(c) $F_1M_RVH_CJ_2$.

Figure 49.- Continued.

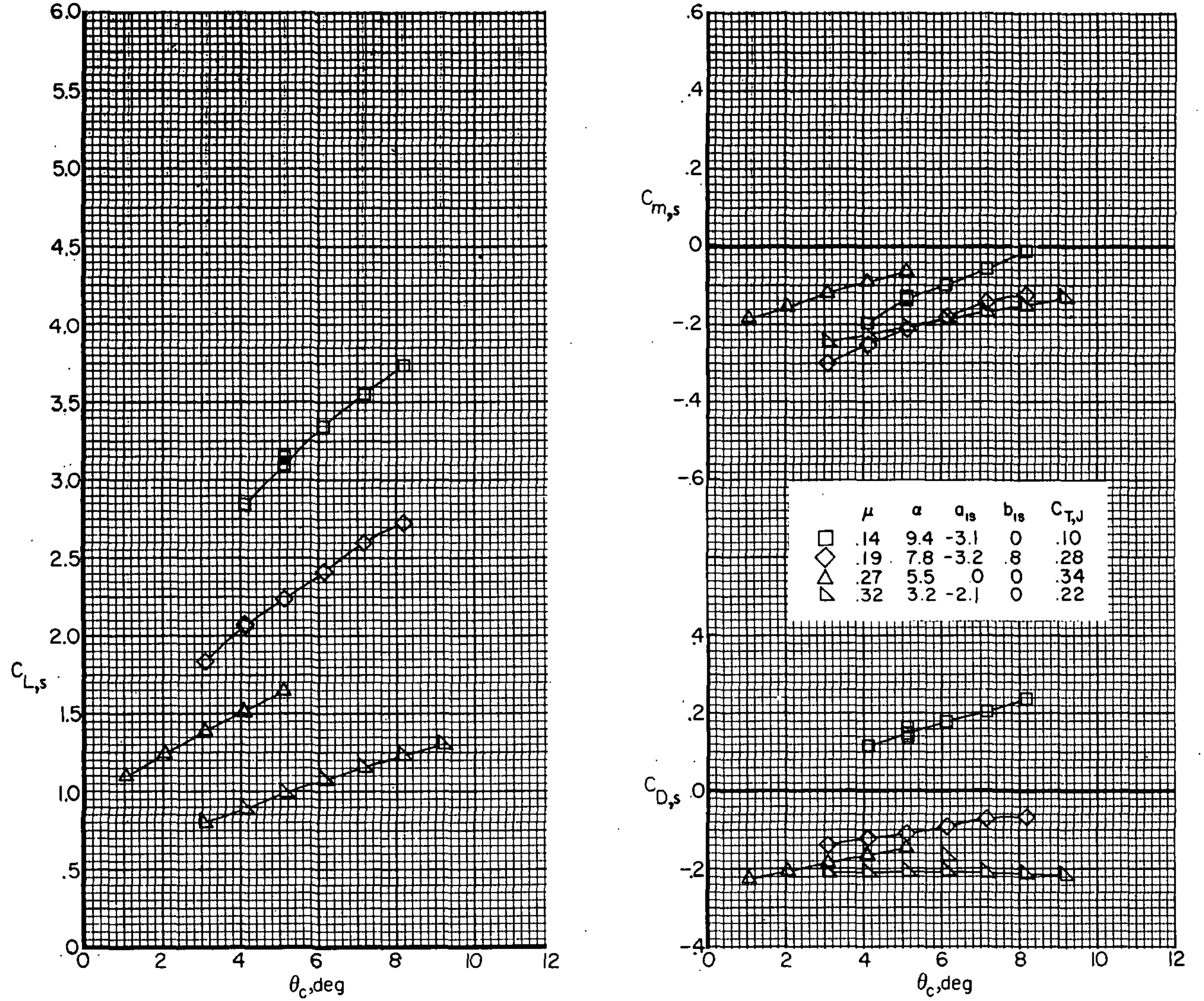

(d) $F_1M_RW_1VH_CJ_2$; high wing lift.

Figure 49.- Continued.

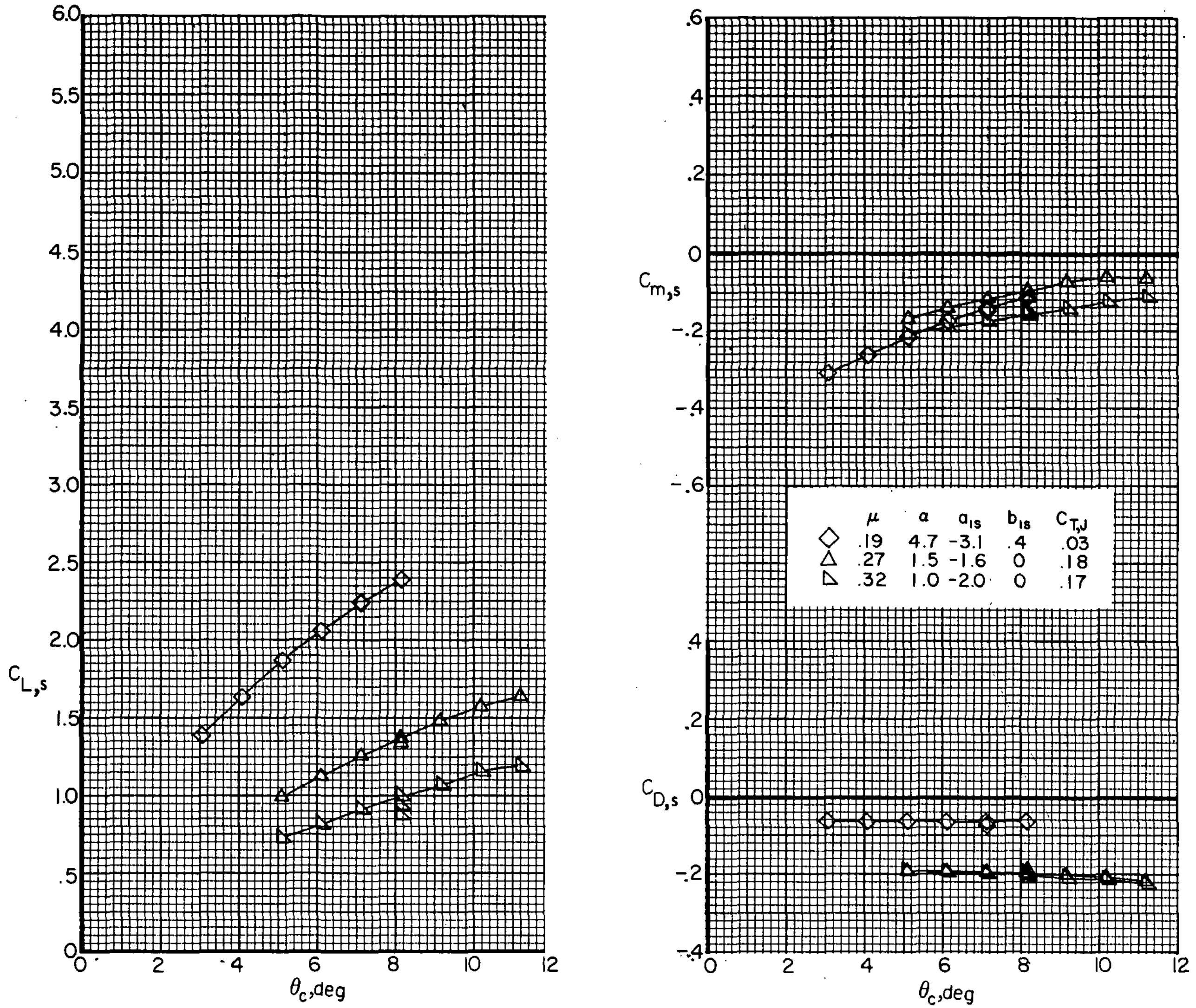

(e) $F_1M_RW_1VH_CJ_2$; low wing lift.

Figure 49.- Continued.

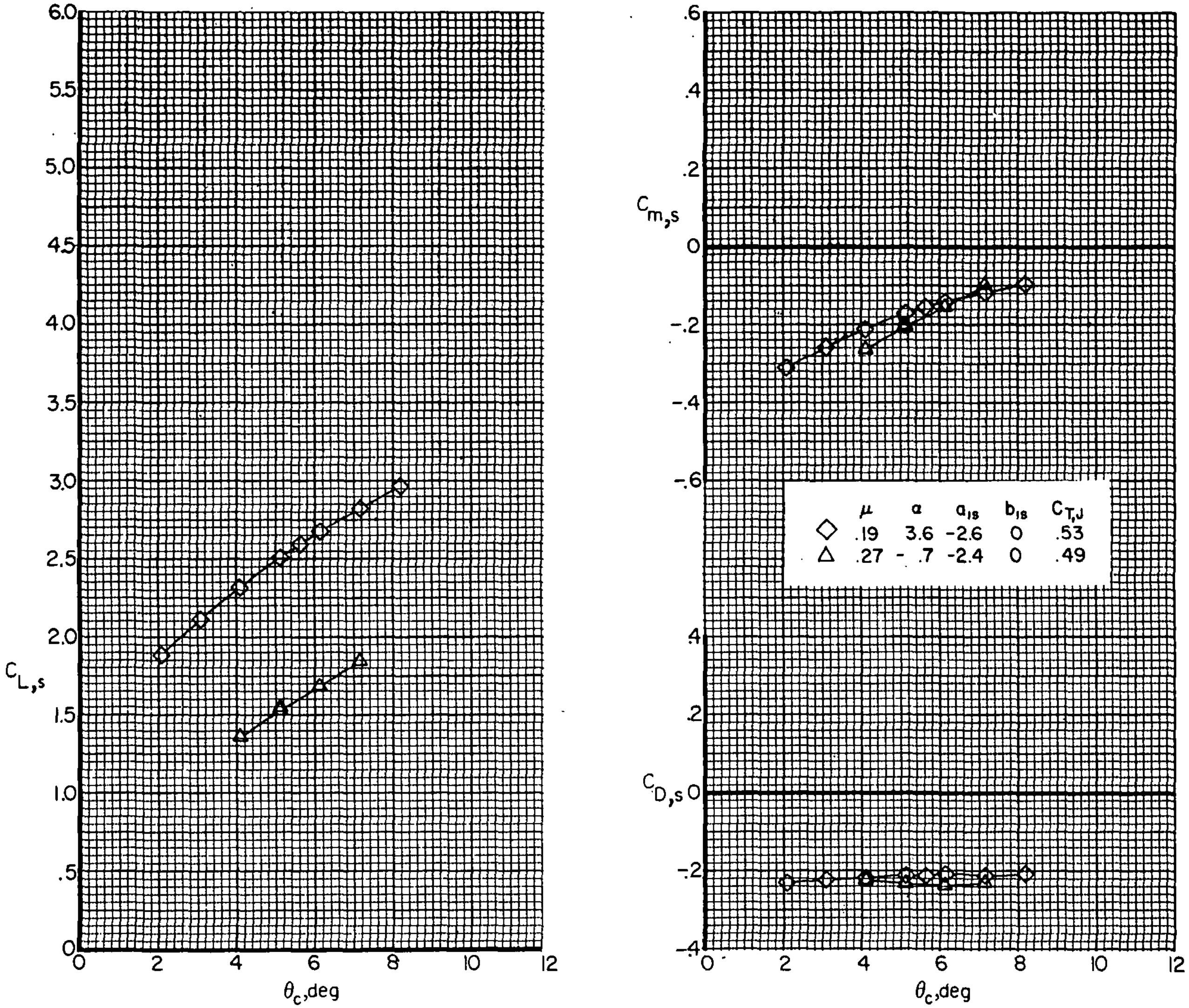

(f) $F_1M_RW_6VH_CJ_2$; high wing lift.

Figure 49.- Continued.

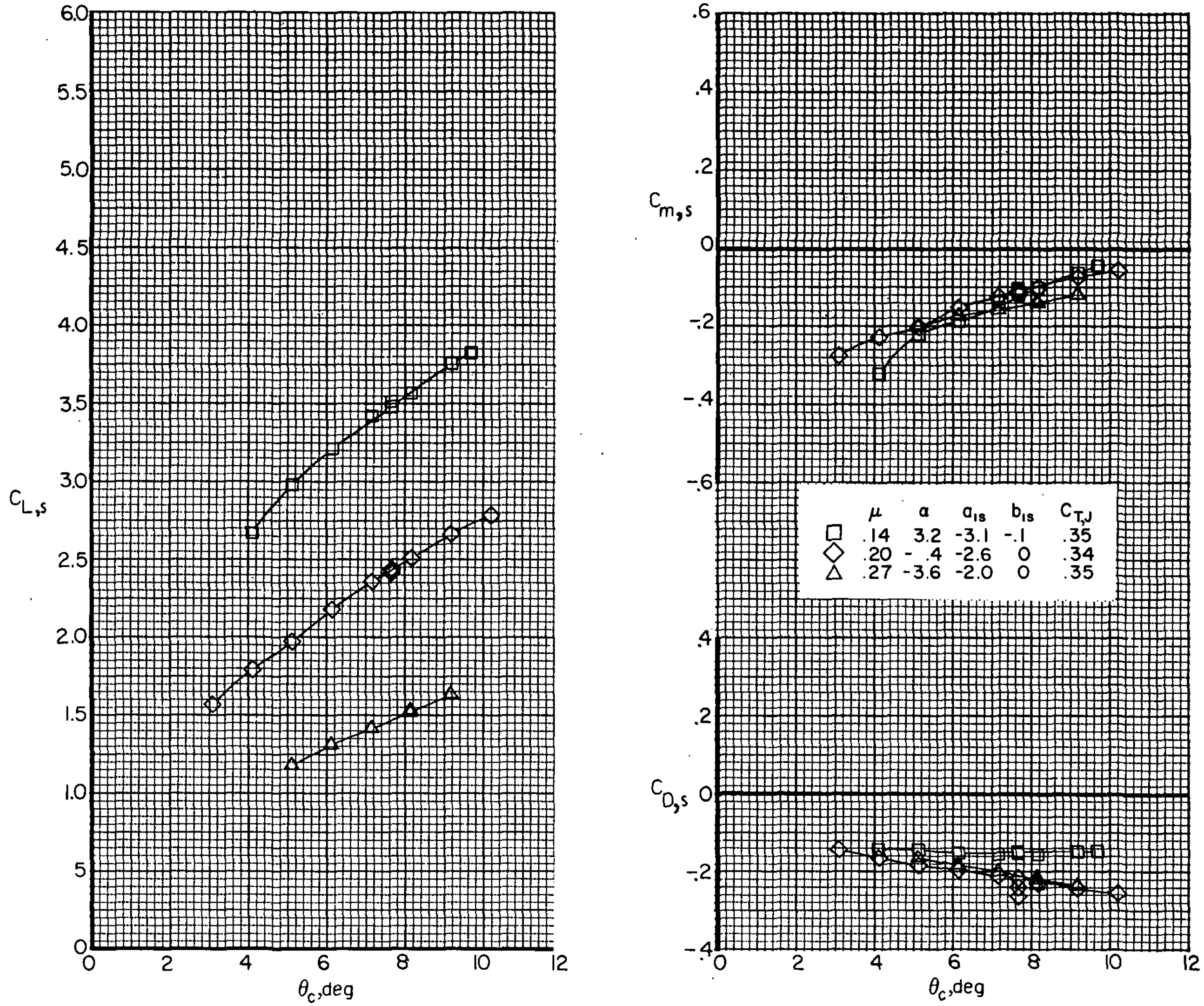

(g) $F_1M_RW_6VH_CJ_2$; low wing lift.

Figure 49.- Concluded.

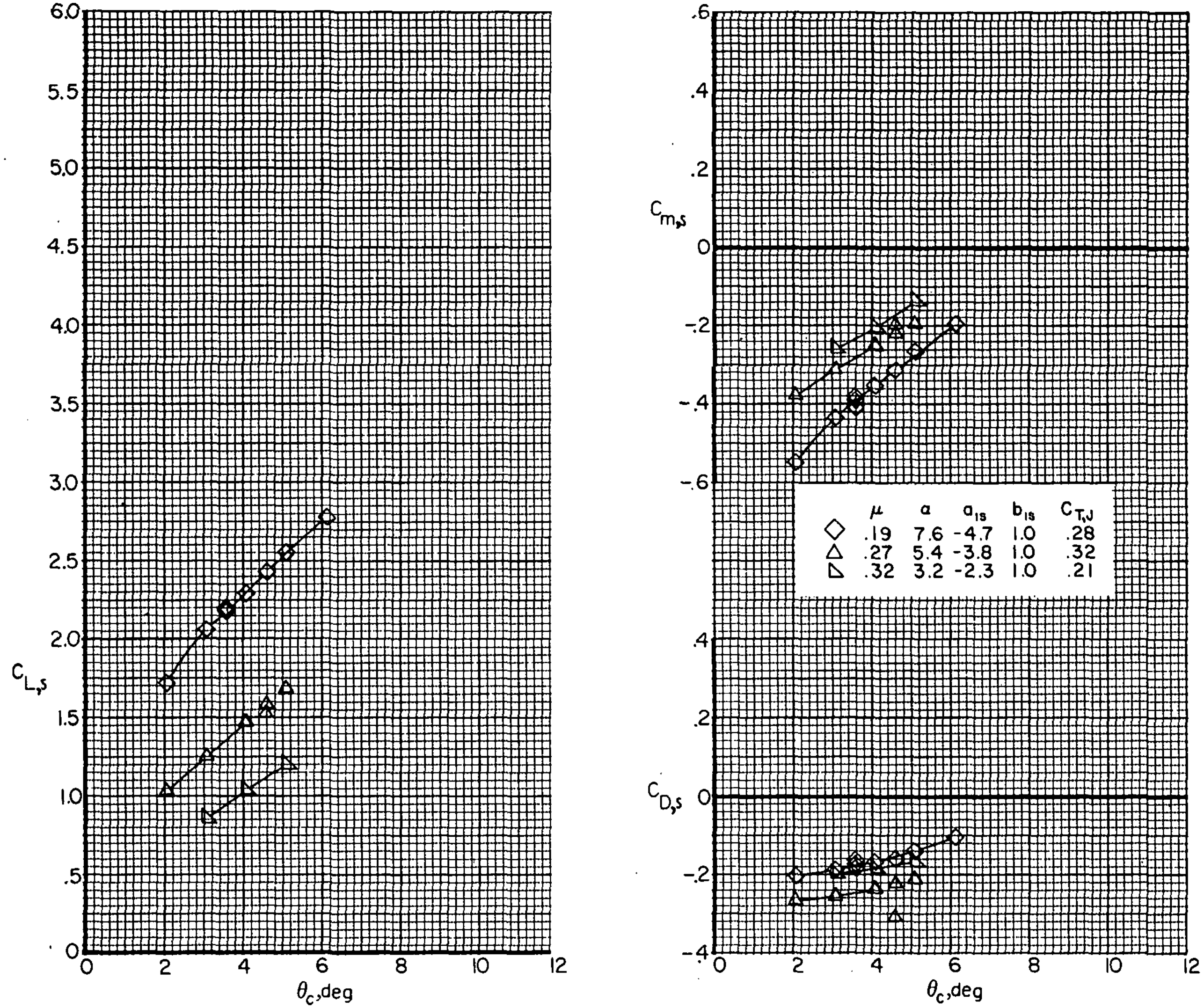

(a) $F_1 M_R W_1 VH_C J_2$.

Figure 50.- Variation of airframe longitudinal aerodynamics with collective pitch angle with the rotor at several forward speeds for $\delta_3 = -2.0^{\circ}$. (α, a_{1s}, and b_{1s} are in degrees.)

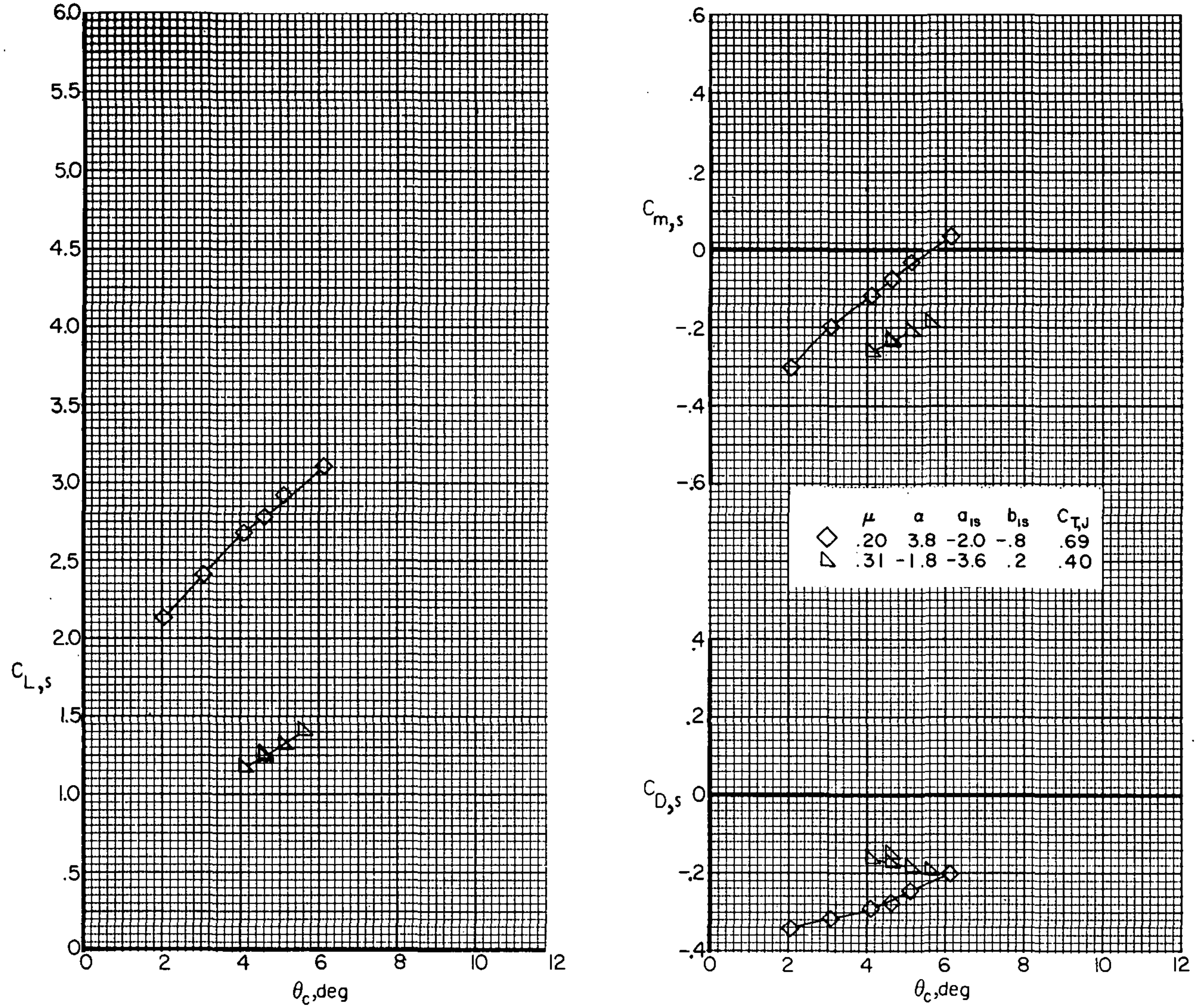

(b) $F_1M_RW_6VH_CJ_2$.

Figure 50.- Concluded.

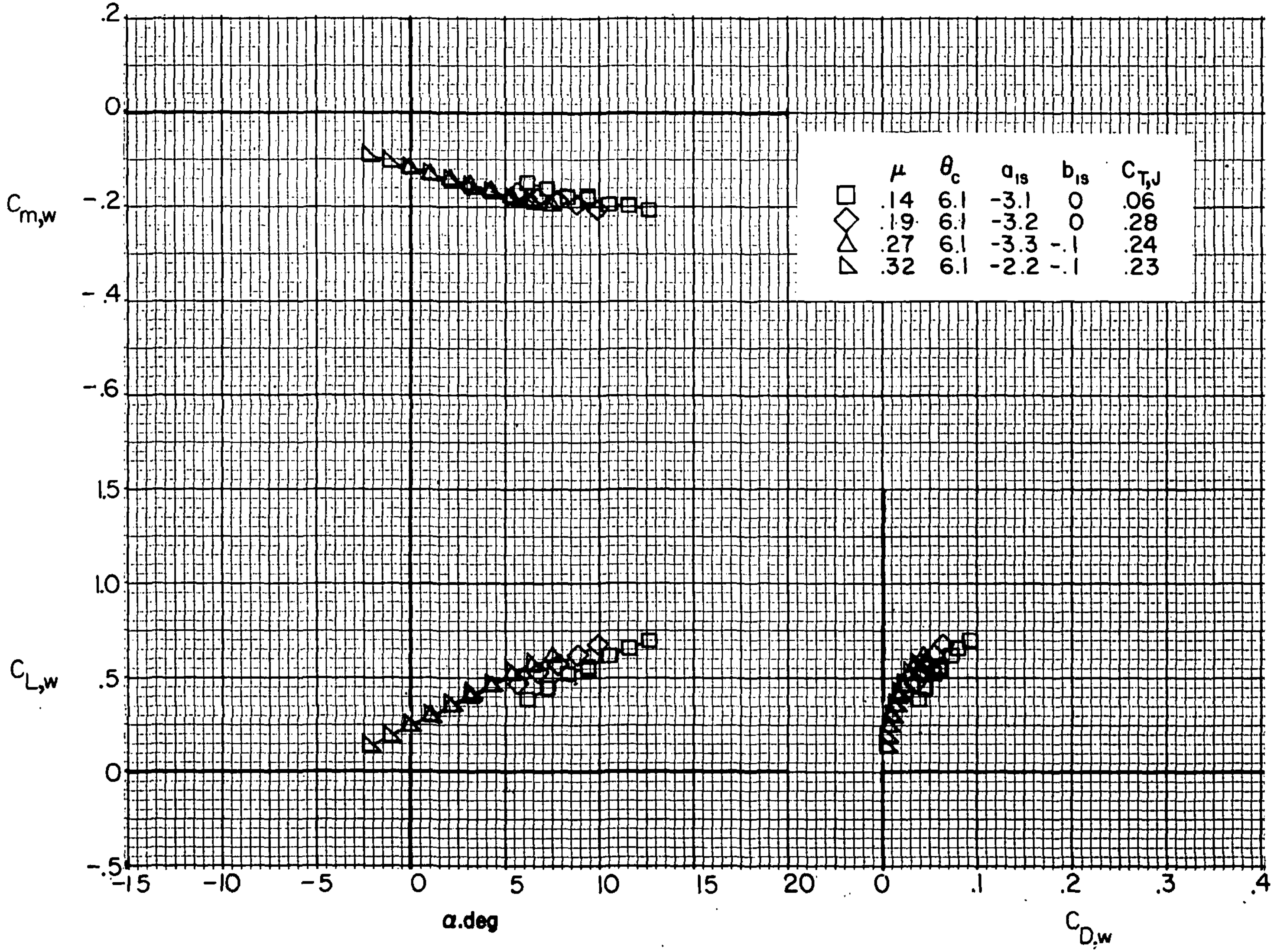

(a) $F_1M_RW_1VH_CJ_2$; high wing lift.

Figure 51.- *Effect of forward speed on wing longitudinal aerodynamics with the rotor on for* $\delta_3 = -27.6^{\circ}$. (θ_c, a_{1s}, and b_{1s} are in degrees.)

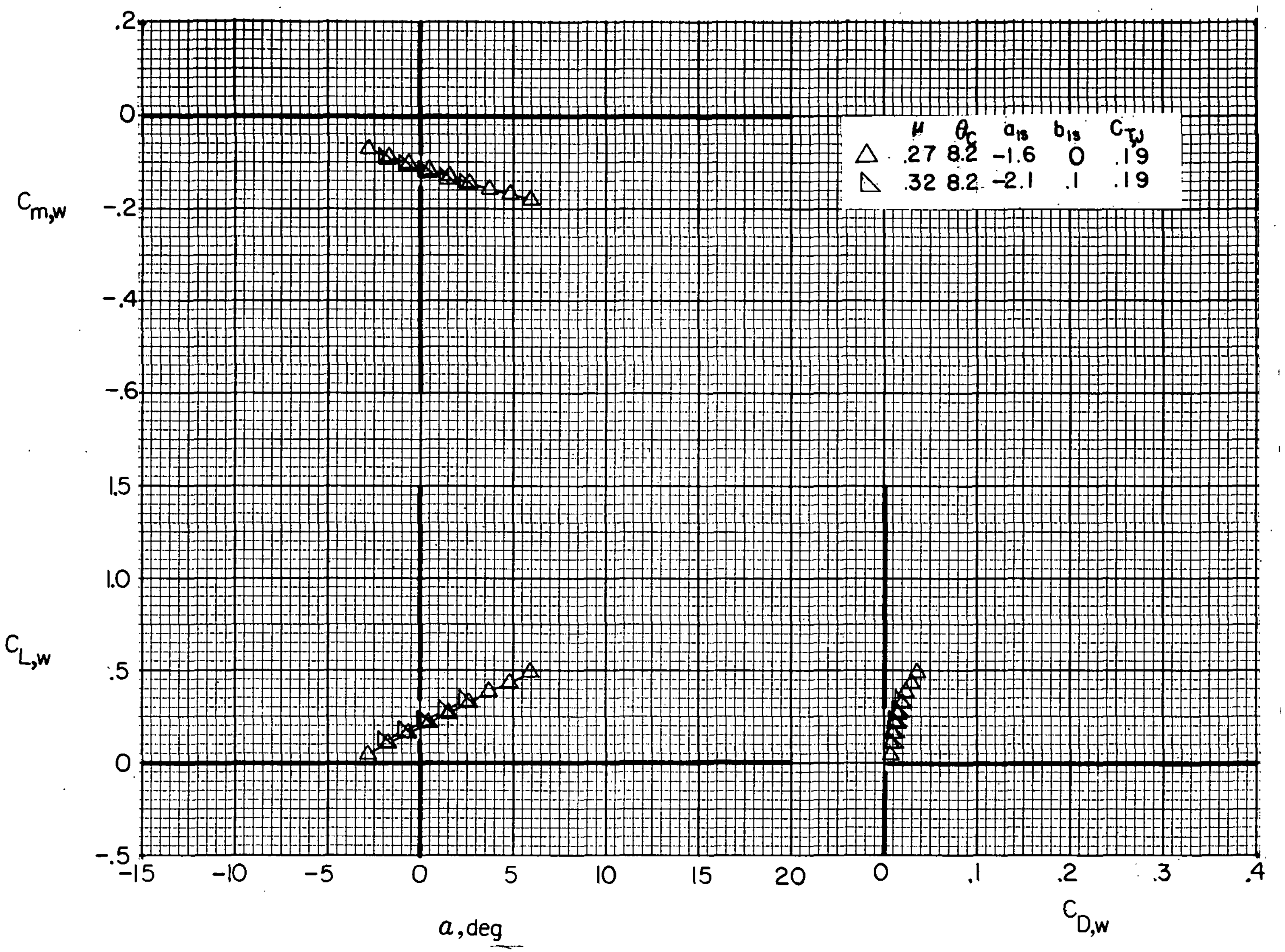

(b) $F_1 M_R W_1 V H_C J_2$; low wing lift.

Figure 51.- Continued.

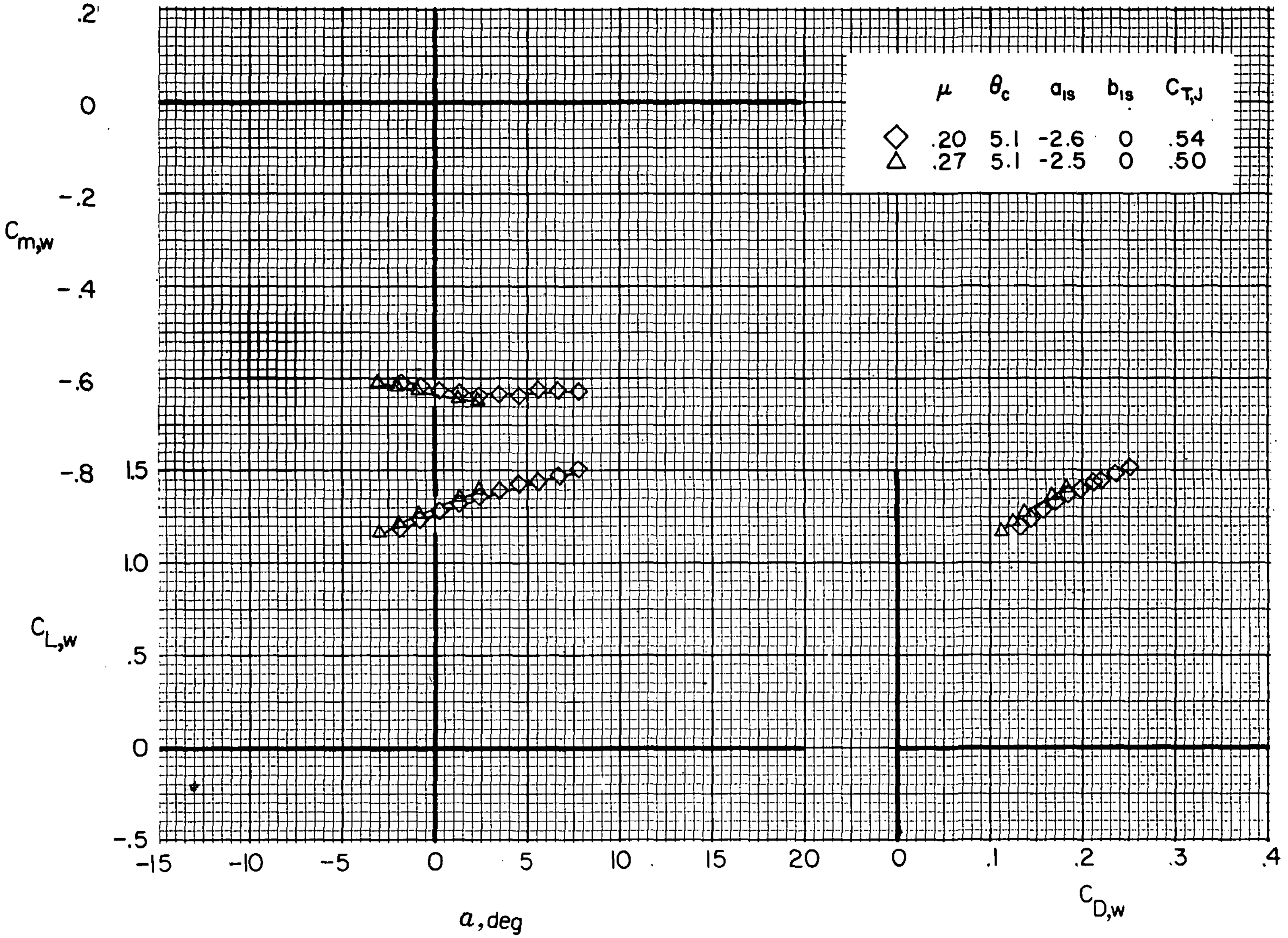

(c) $F_1M_RW_6VH_CJ_2$; high wing lift.

Figure 51.- Continued.

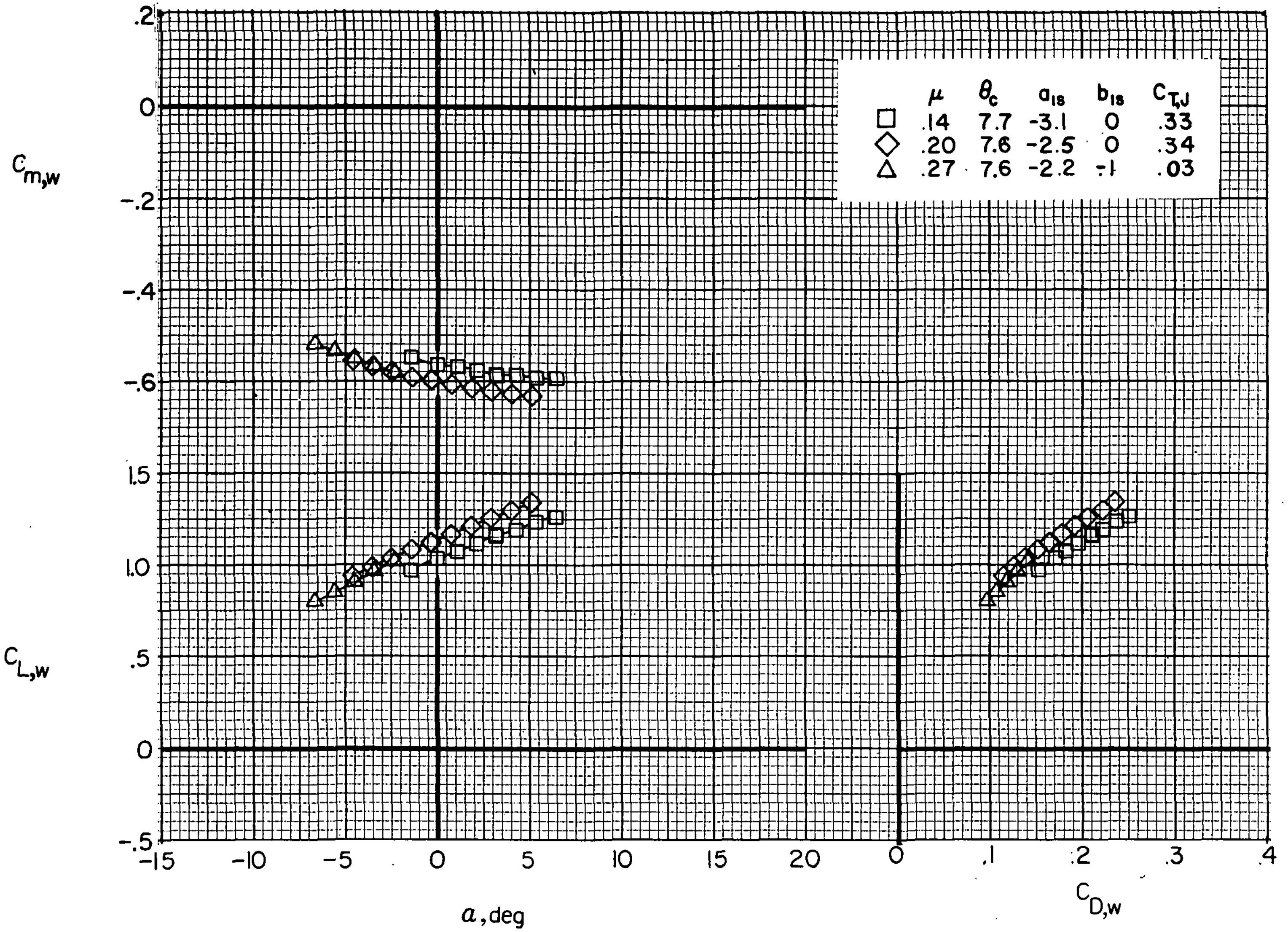

(d) $F_1M_RW_6VH_CJ_2$; low wing lift.

Figure 51.- Concluded.

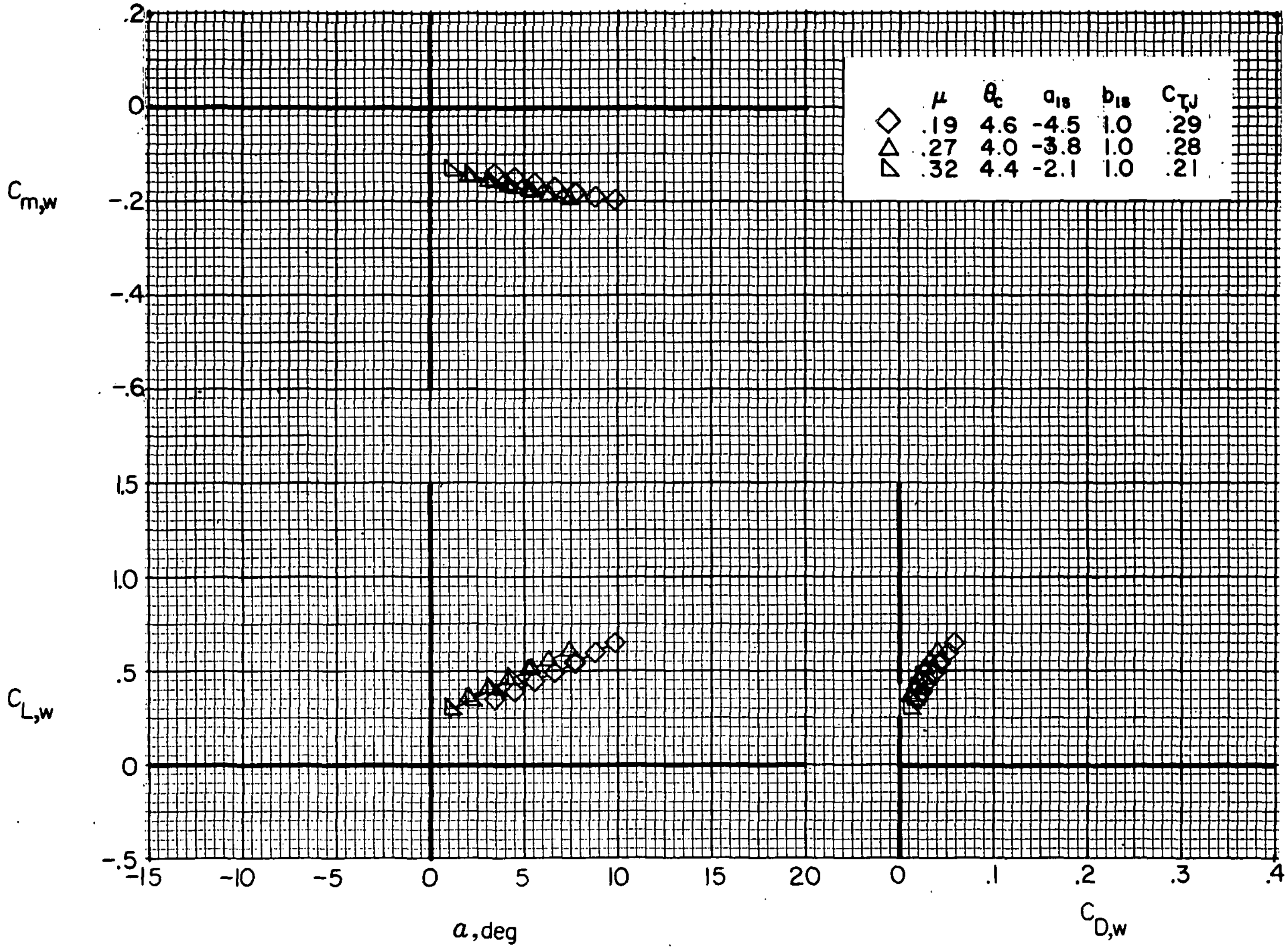

(a) $F_1 M_R W_1 VH_C J_2$.

Figure 52.- Effect of forward speed on wing longitudinal aerodynamics with the rotor on for $\delta_3 = -2.0^\circ$. (θ_c, a_{1s}, and b_{1s} are in degrees.)

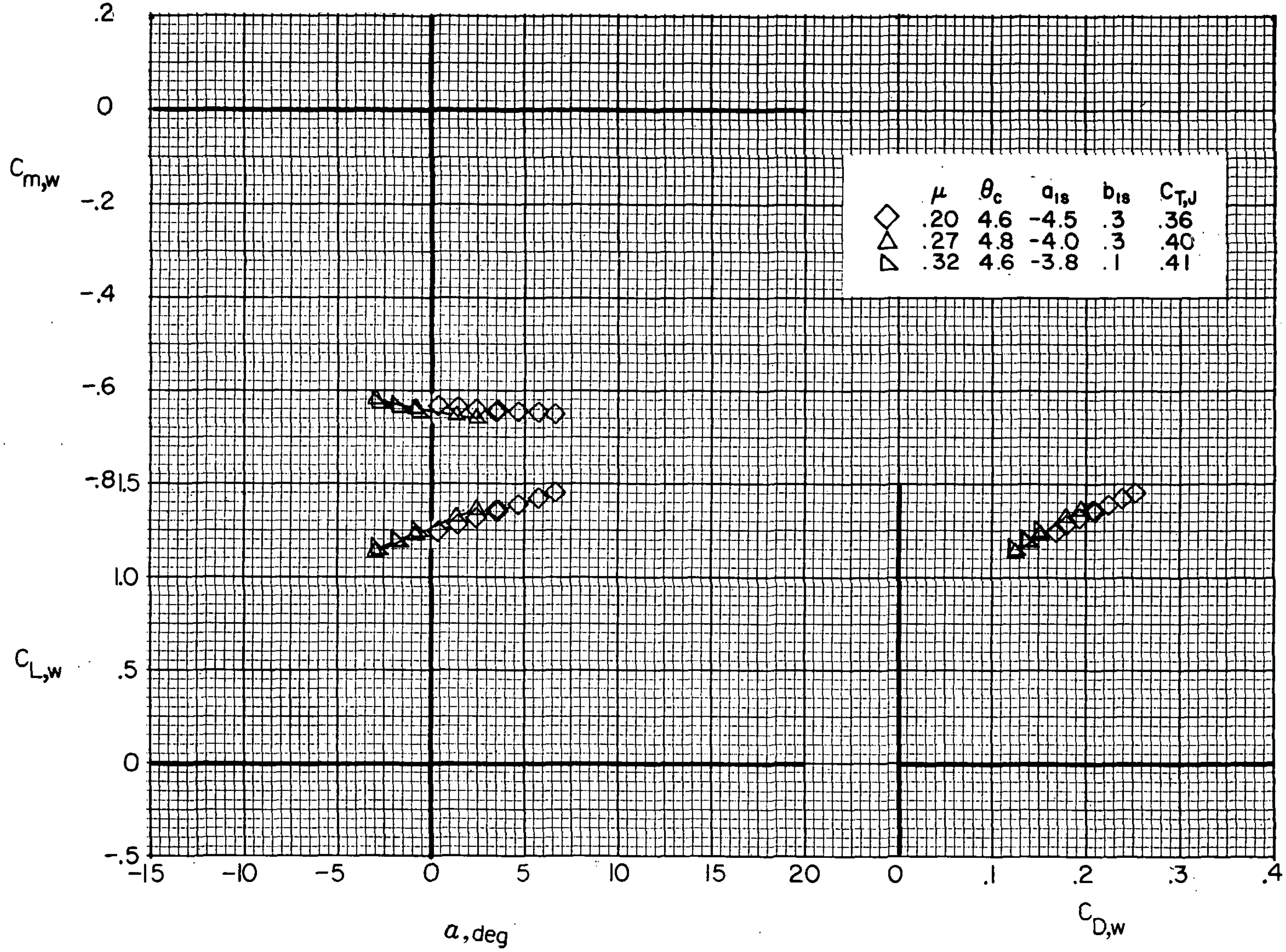

(b) $F_1M_RW_6VH_CJ_2$; high wing lift.

Figure 52. - Continued.

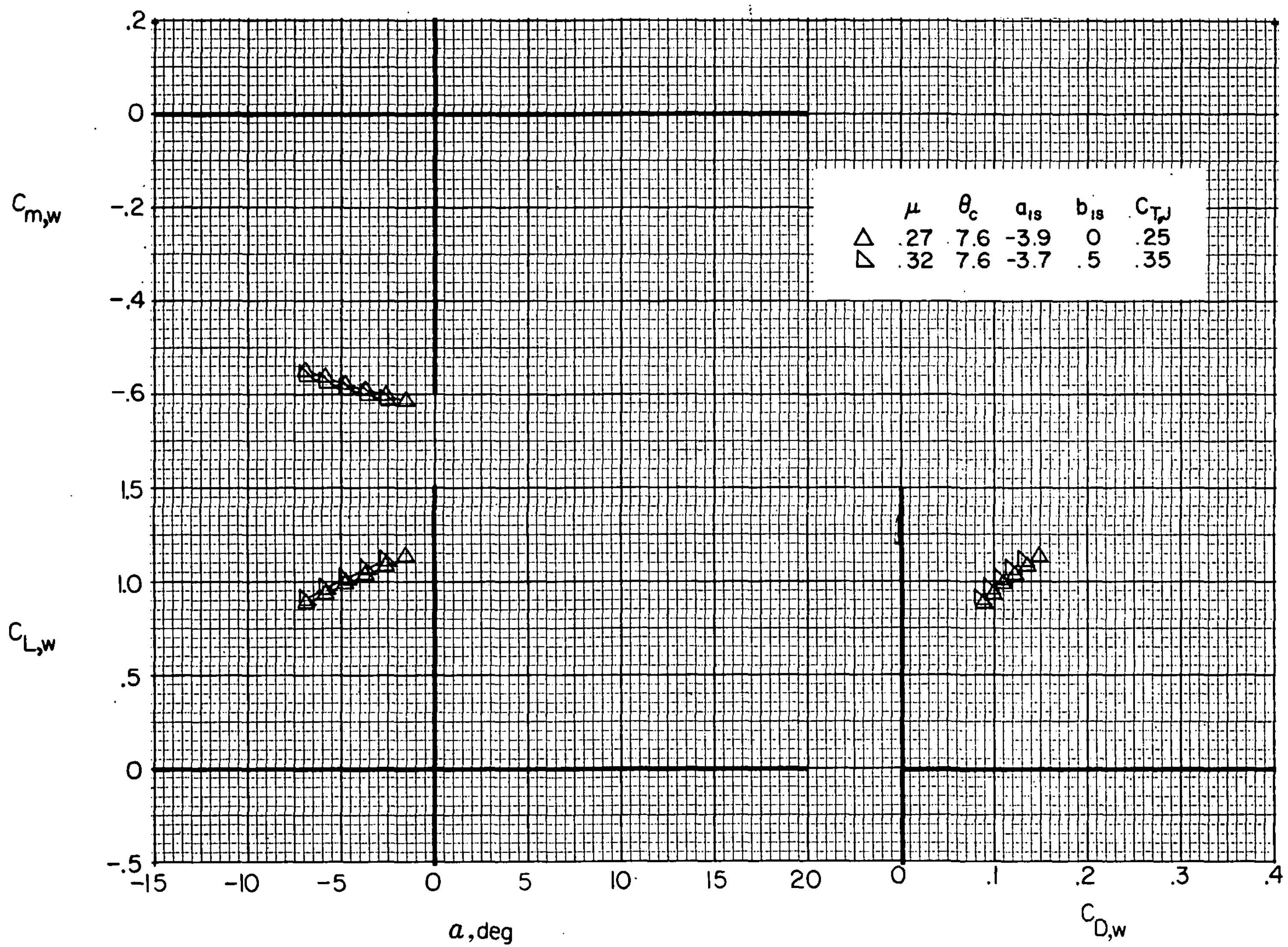

(c) $F_1M_RW_6VH_CJ_2$; low wing lift.

Figure 52.- Concluded.

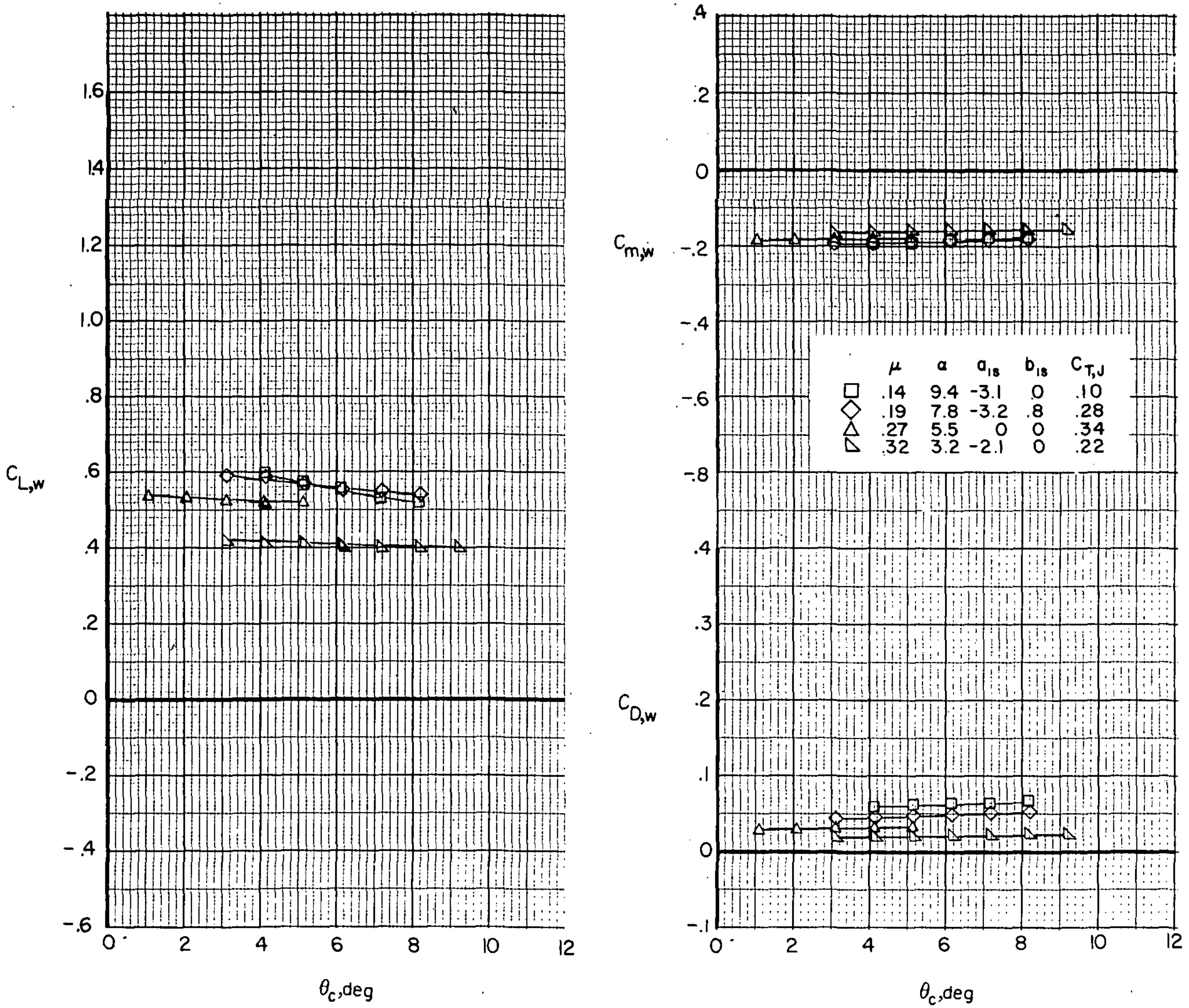

(a) $F_1M_RW_1VH_CJ_2$; high wing lift.

Figure 53.- Variation of wing longitudinal aerodynamics with collective pitch angle with the rotor on for $\delta_3 = -27.6^{\circ}$. (α, a_{1s}, and b_{1s} are in degrees.)

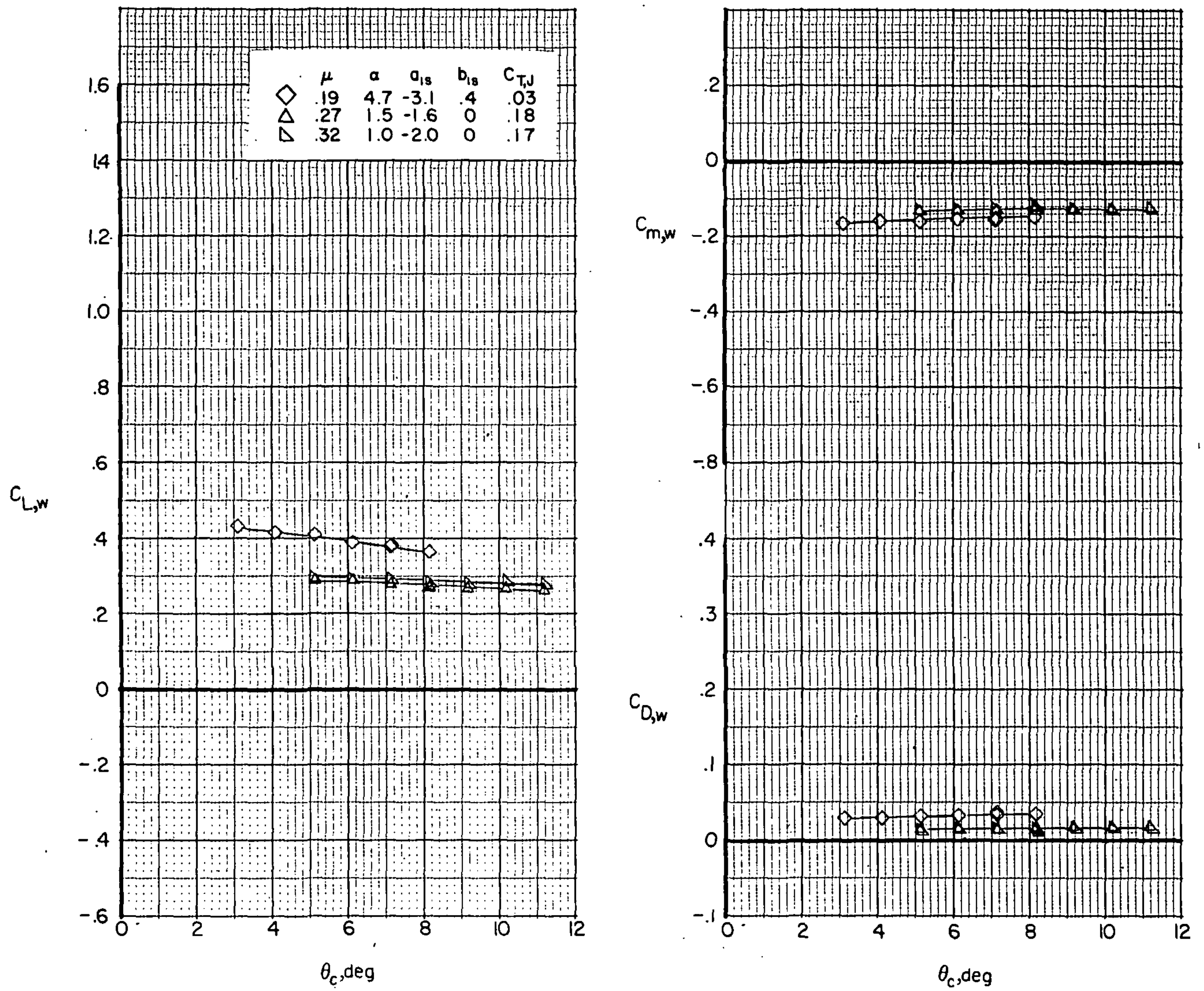

(b) $F_1 M_R W_1 VH_C J_2$; low wing lift.

Figure 53.- Continued.

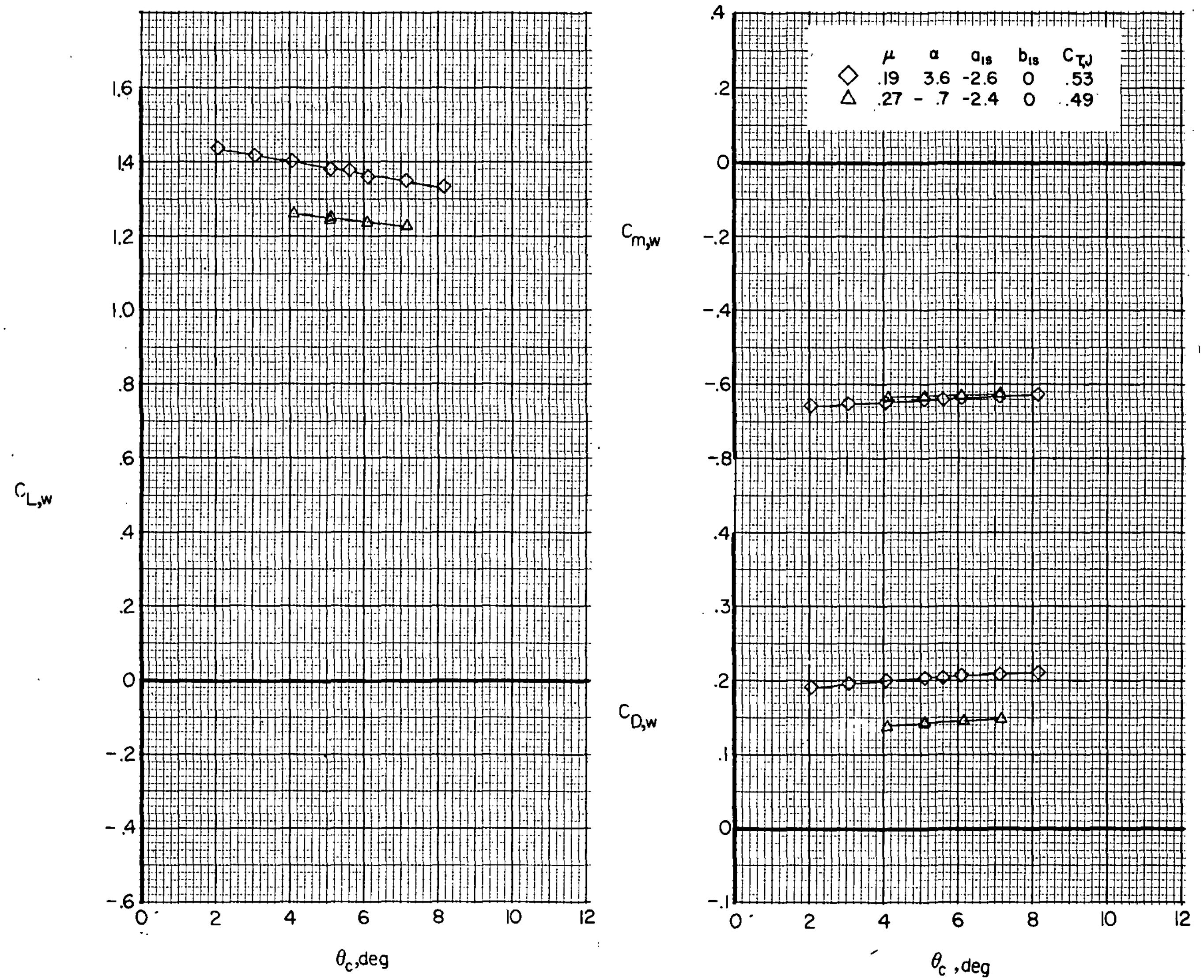

(c) $F_1M_RW_6VH_CJ_2$; high wing lift.

Figure 53.- Continued.

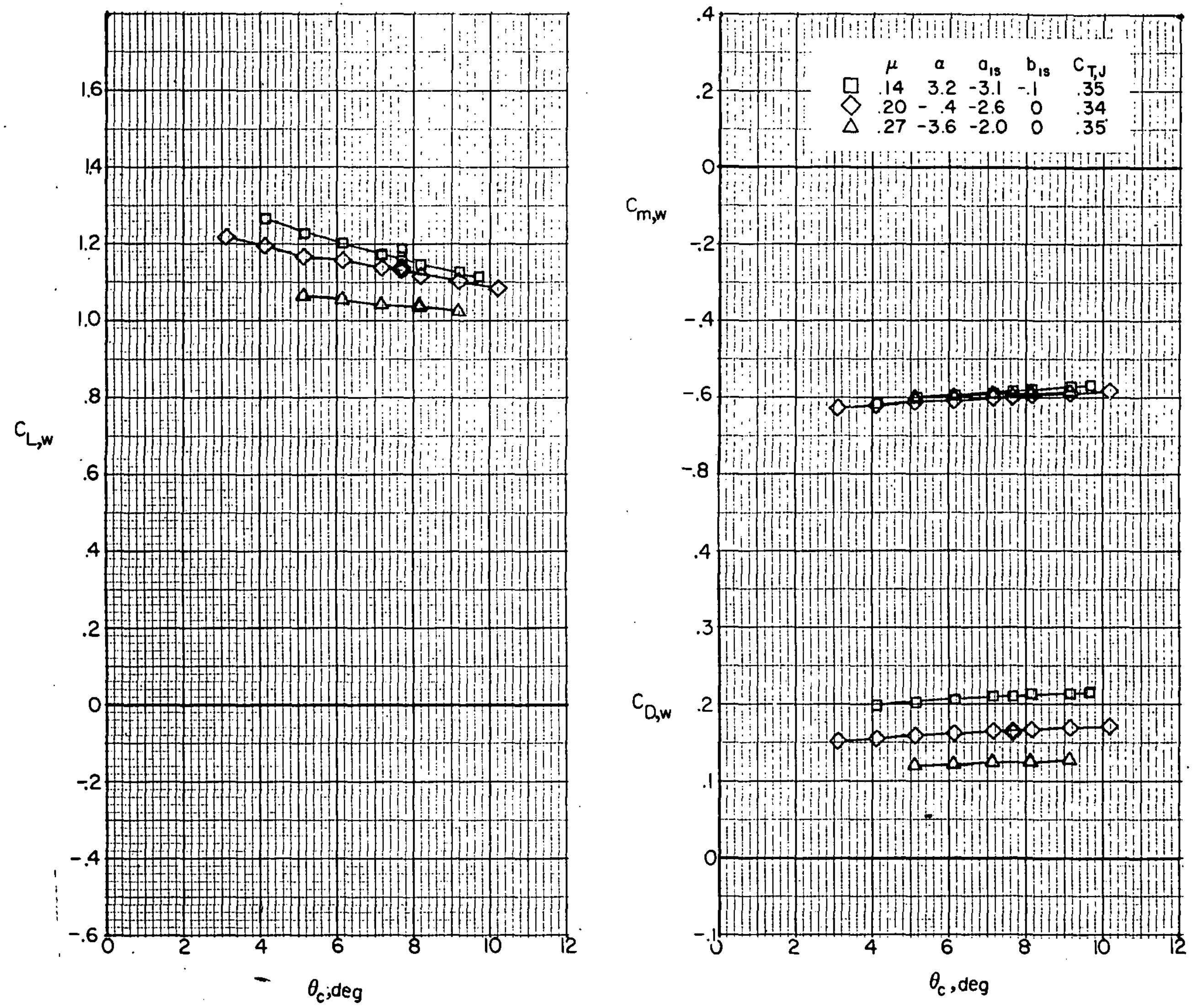

(d) $F_1M_RW_6VH_CJ_2$; low wing lift.

Figure 53.- Concluded.

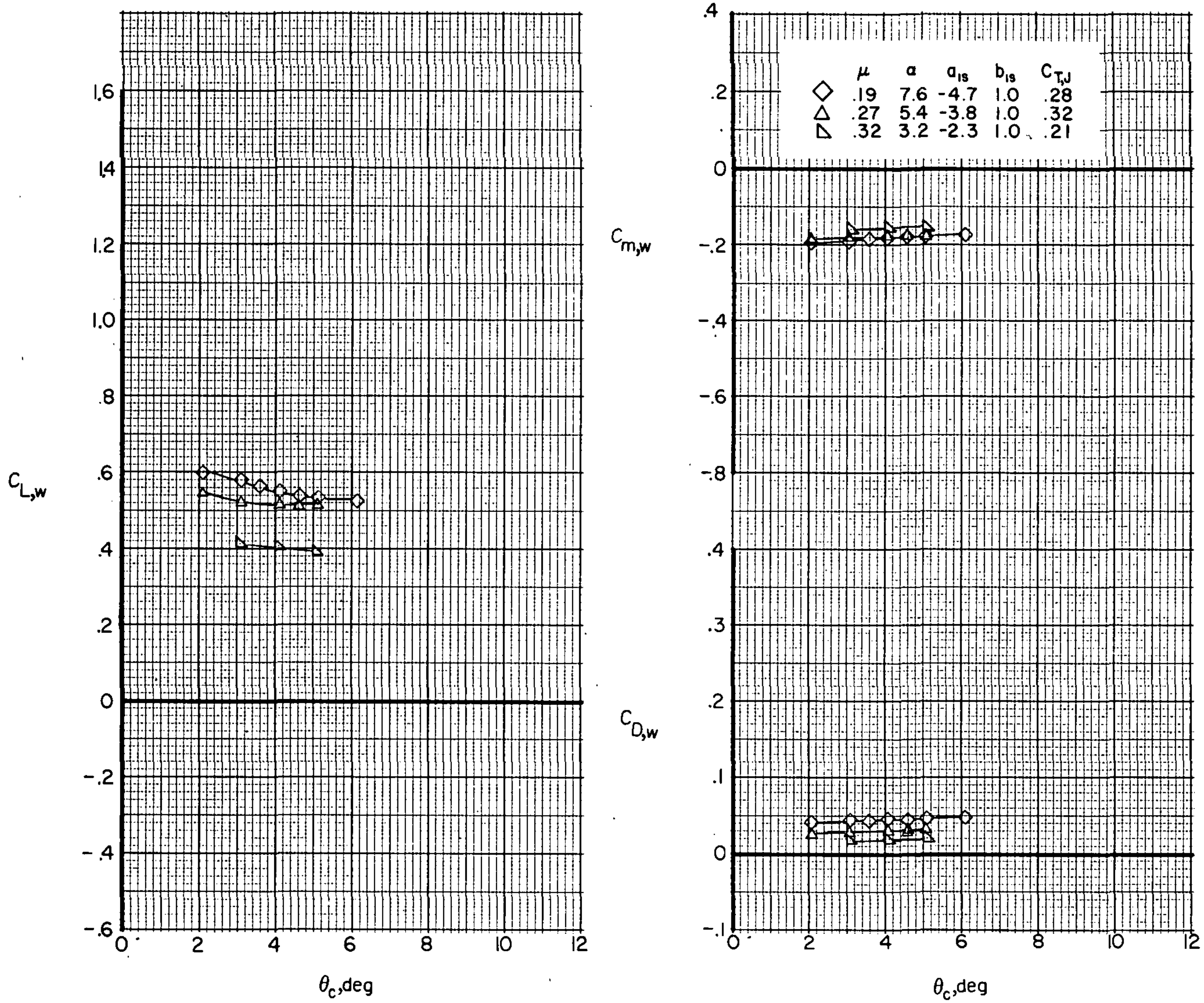

(a) $F_1M_RW_1VH_CJ_2$.

Figure 54.- Variation of wing longitudinal aerodynamics with collective pitch angle with the rotor on for $\delta_3 = -2.0^{\circ}$. (α, a_{1s}, and b_{1s} are in degrees.)

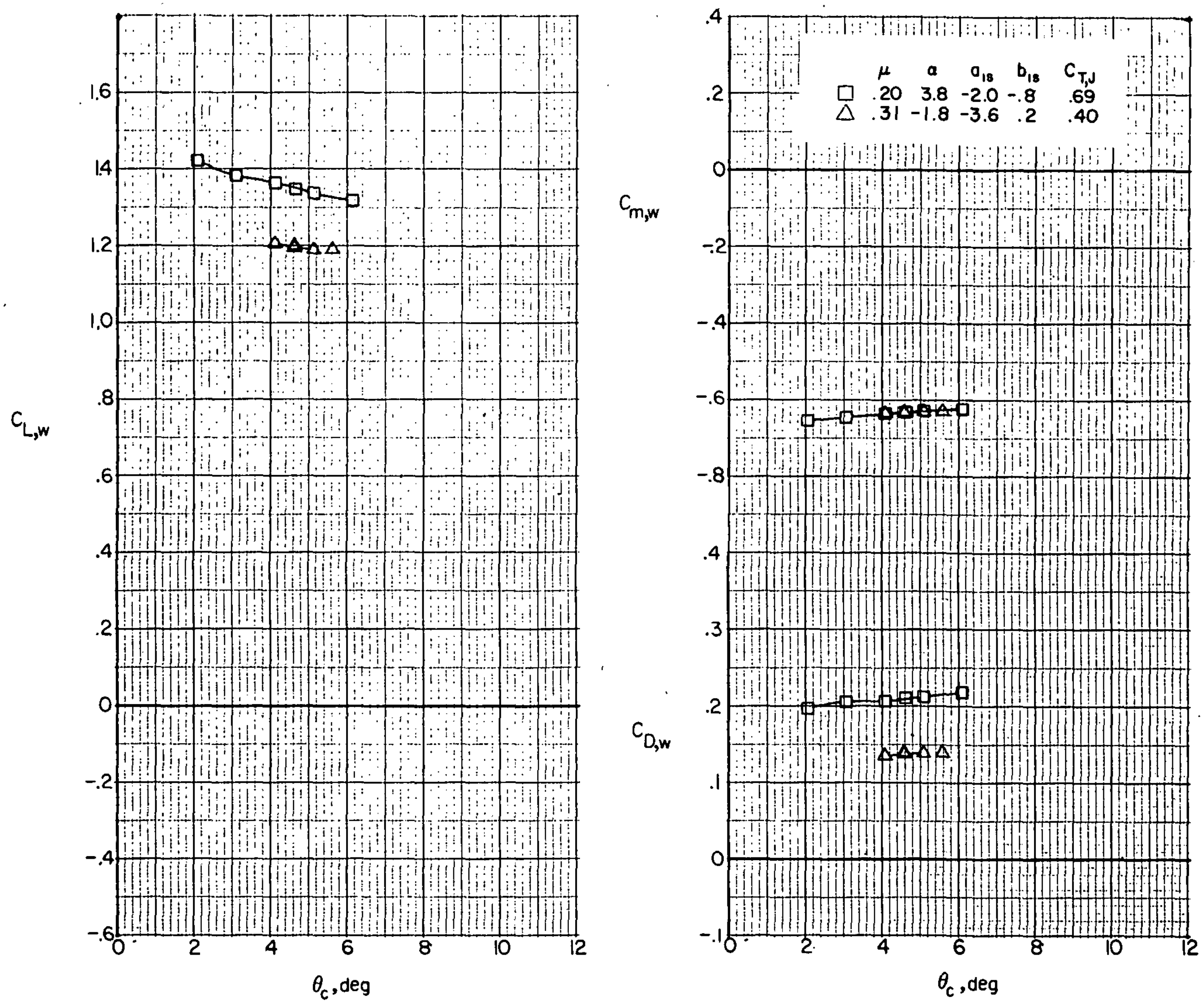

(b) $F_1 M_R W_6 V H_C J_2$.

Figure 54.- Concluded.

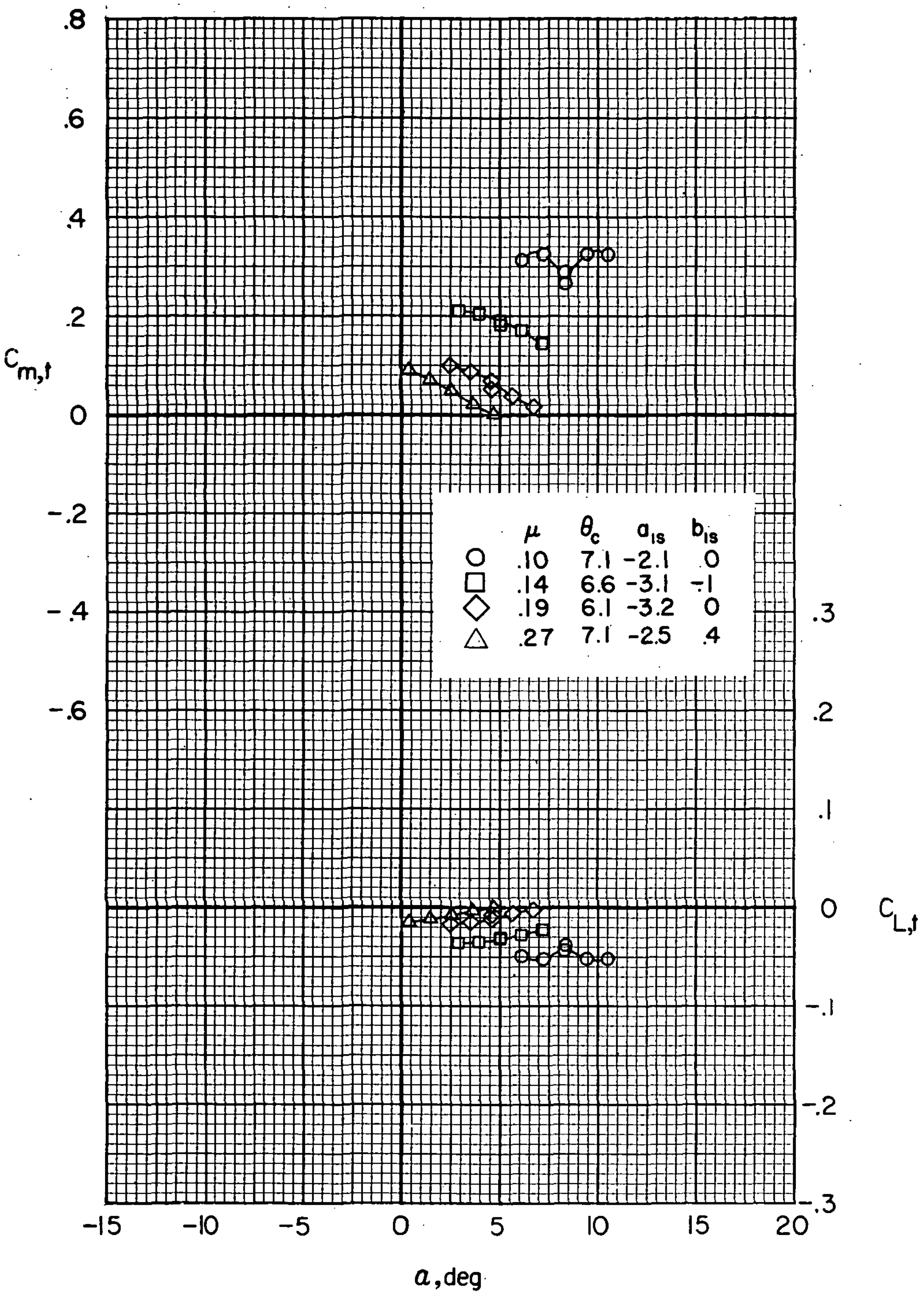

(a) $F_1M_RVH_H$.

Figure 55.- Effect of forward speed on tail longitudinal aerodynamics with the rotor on for $\delta_3 = -27.6^\circ$. (θ_c, a_{1s}, and b_{1s} are in degrees.)

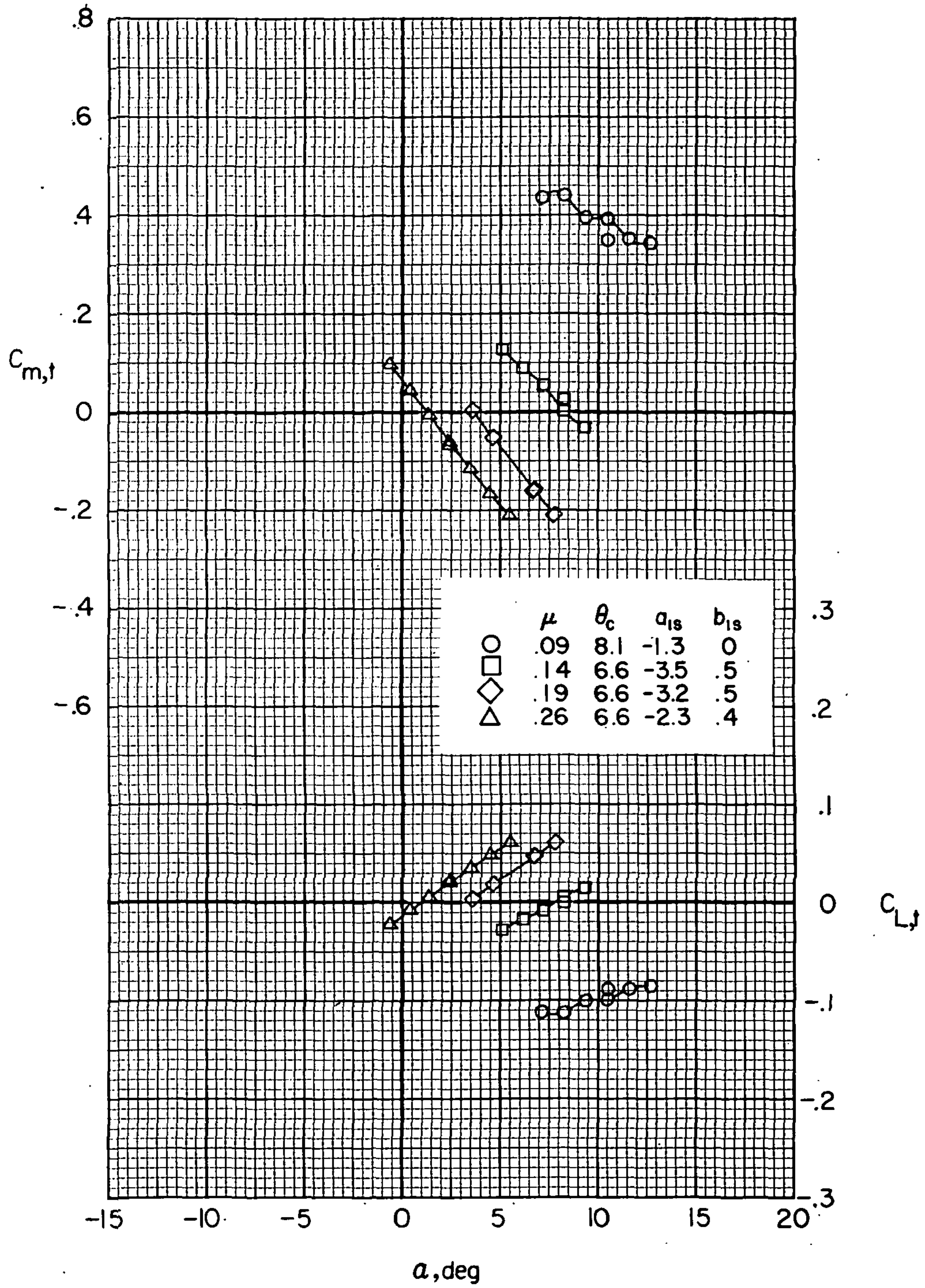

(b) $F_1M_RVH_C$.

Figure 55.- Continued.

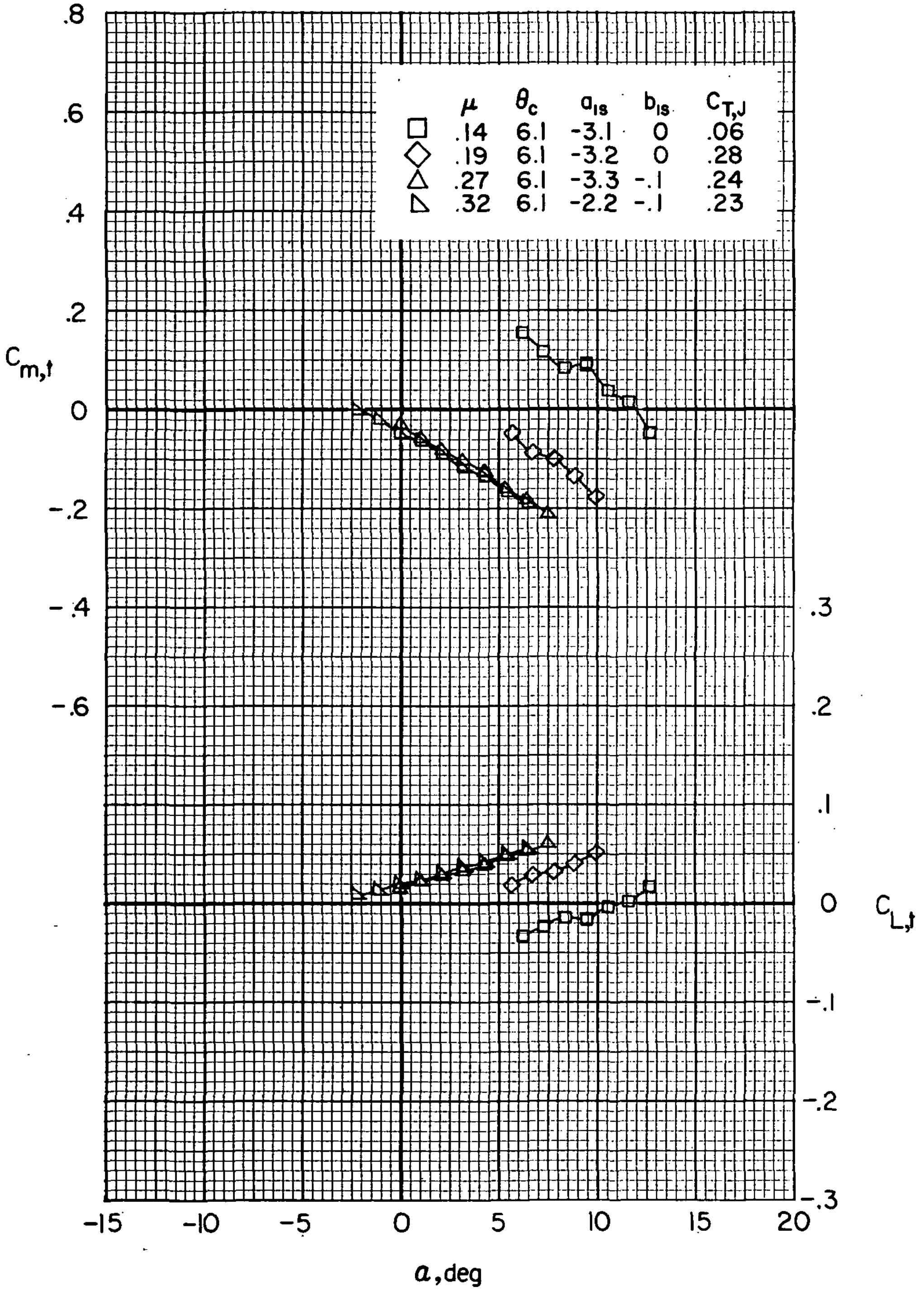

(c) $F_1M_RW_1VH_CJ_2$; high wing lift.

Figure 55.- Continued.

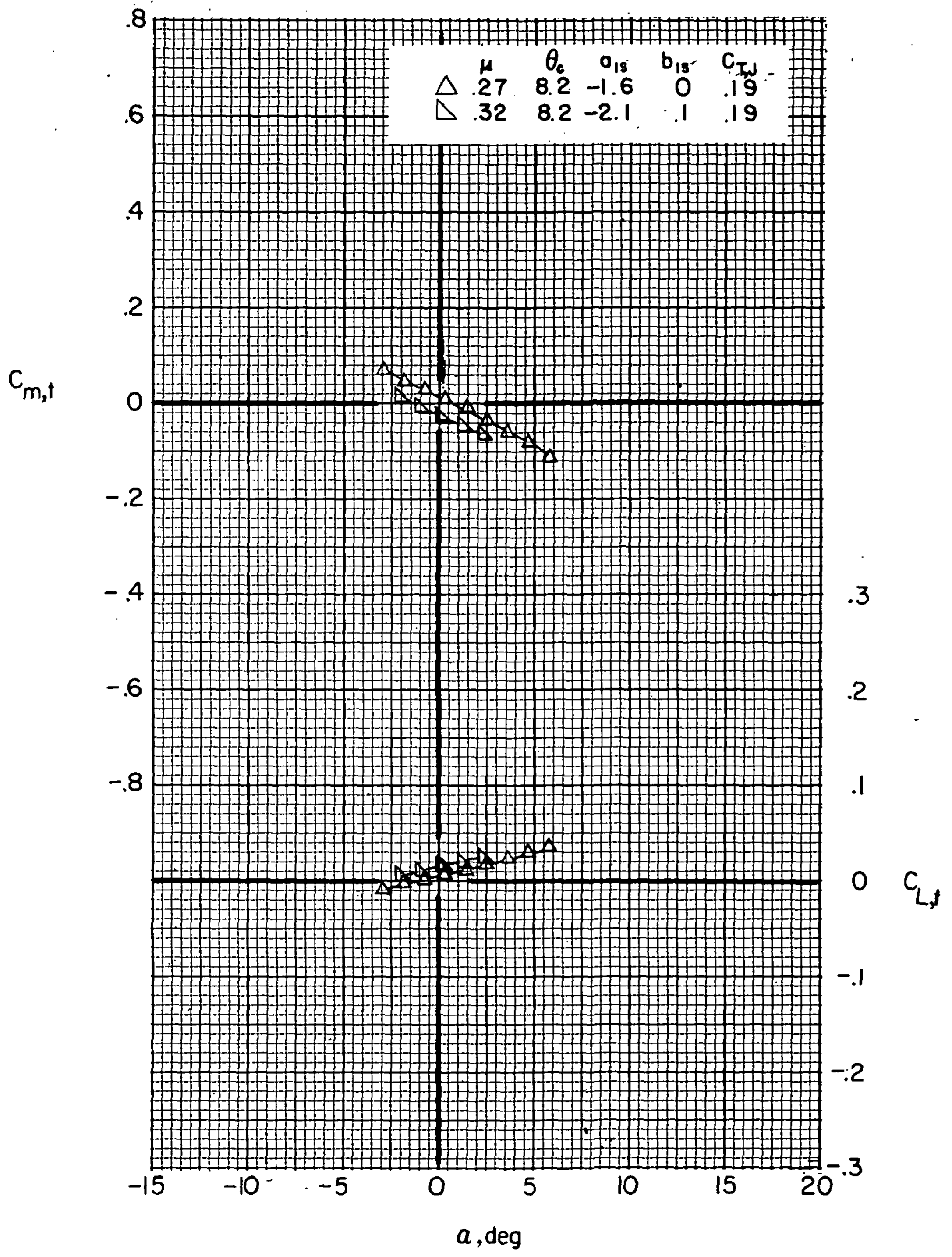

(d) $F_1M_RW_1VH_CJ_2$; low wing lift.

Figure 55.- Continued.

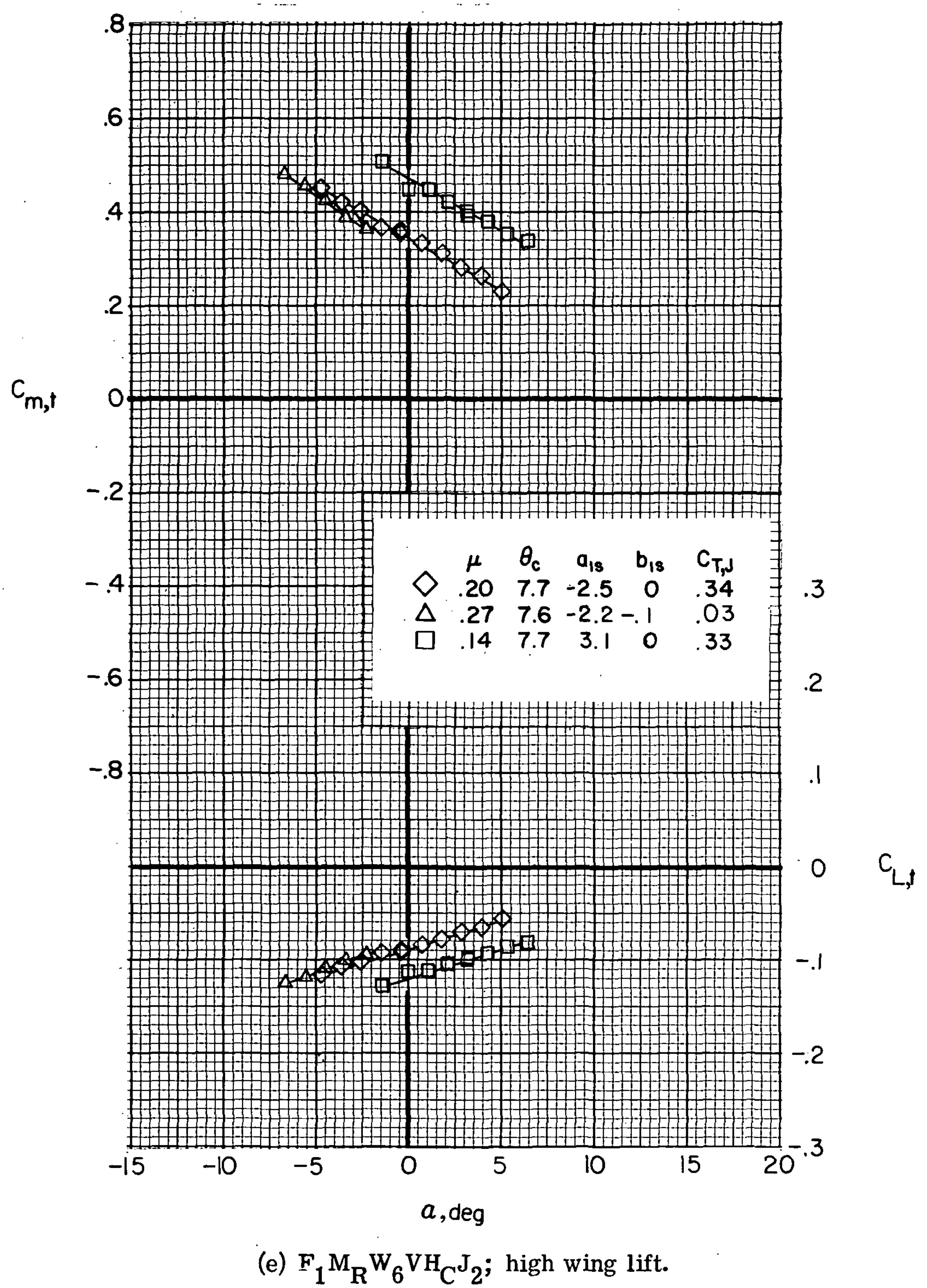

(e) $F_1M_RW_6VH_CJ_2$; high wing lift.

Figure 55.- Continued.

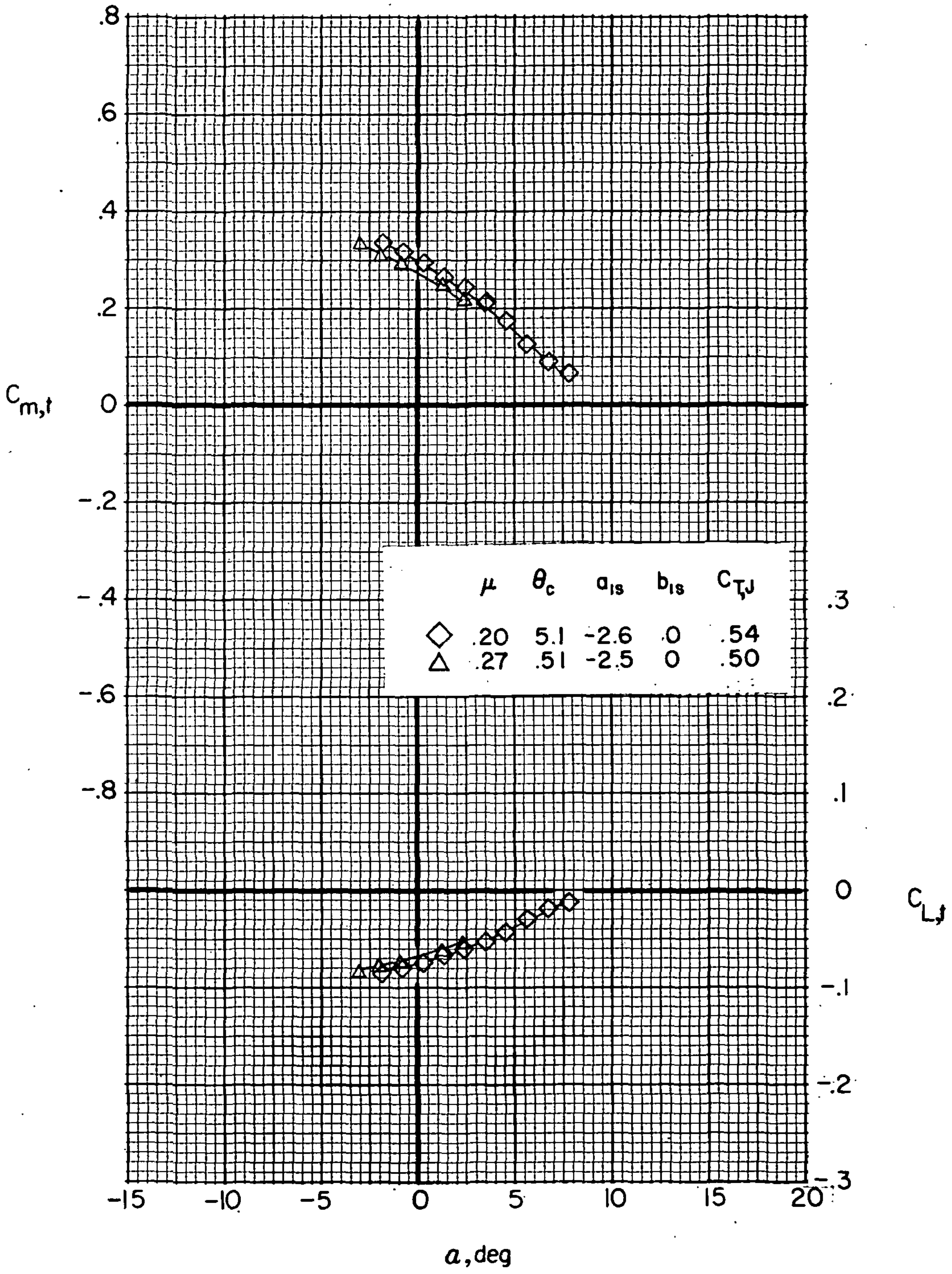

(f) $F_1M_RW_6VH_CJ_2$; low wing lift.

Figure 55.- Concluded.

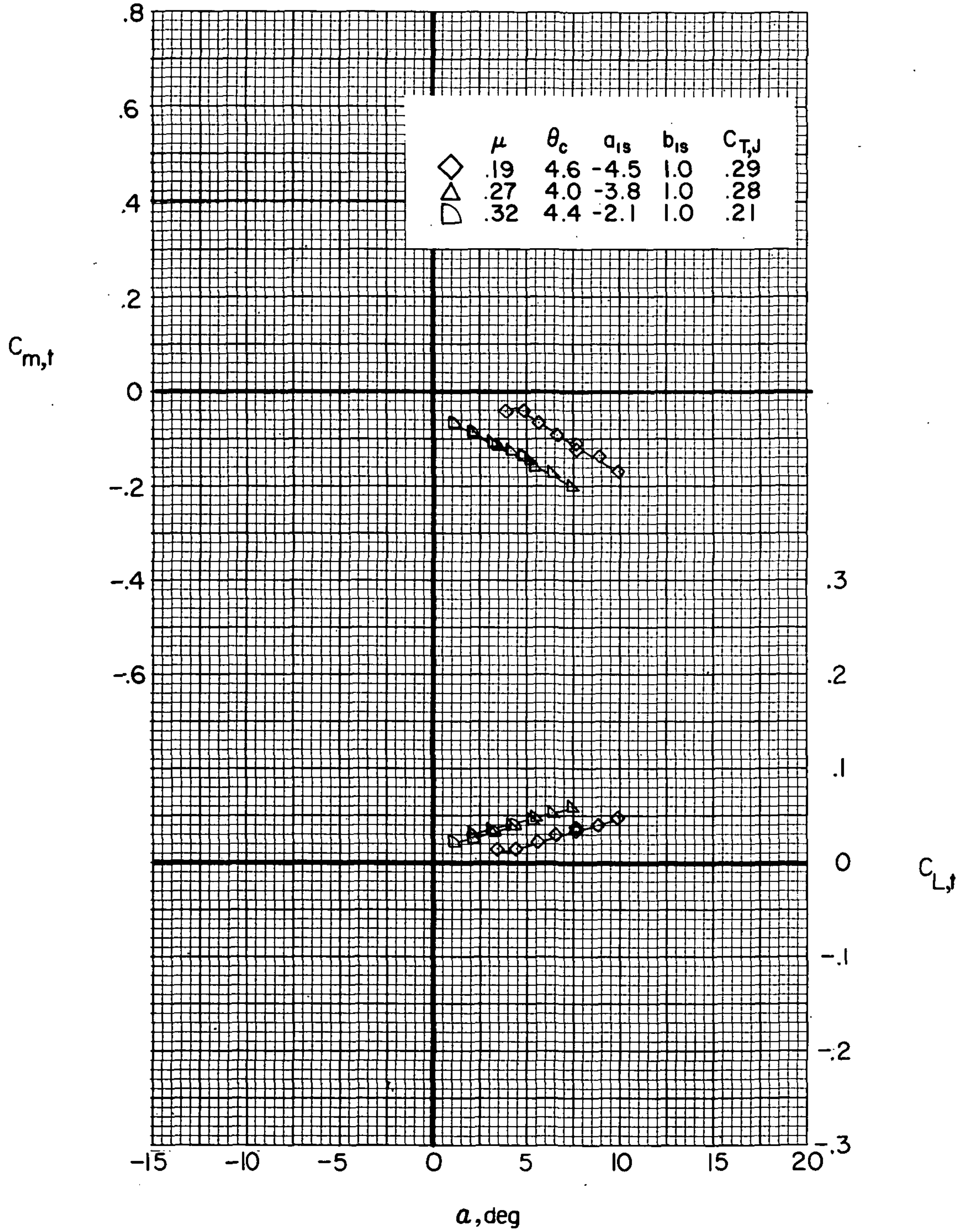

(a) $F_1M_RW_1VH_CJ_2$.

Figure 56.- Effect of forward speed on tail longitudinal aerodynamics with the rotor on for $\delta_3 = -2.0^{\circ}$. (θ_c, a_{1s}, and b_{1s} are in degrees.)

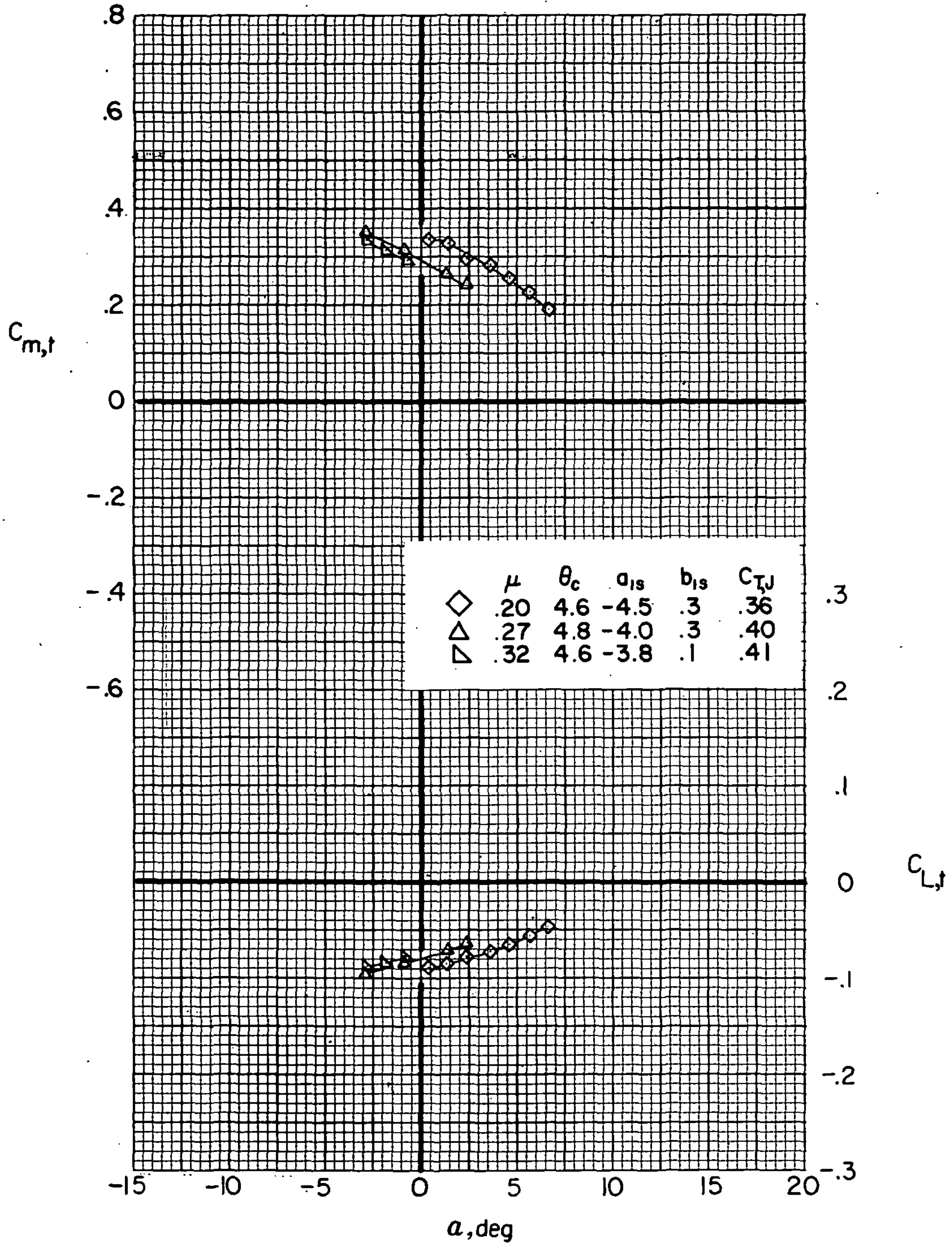

(b) $F_1M_RW_6VH_CJ_2$; high wing lift.

Figure 56.- Continued.

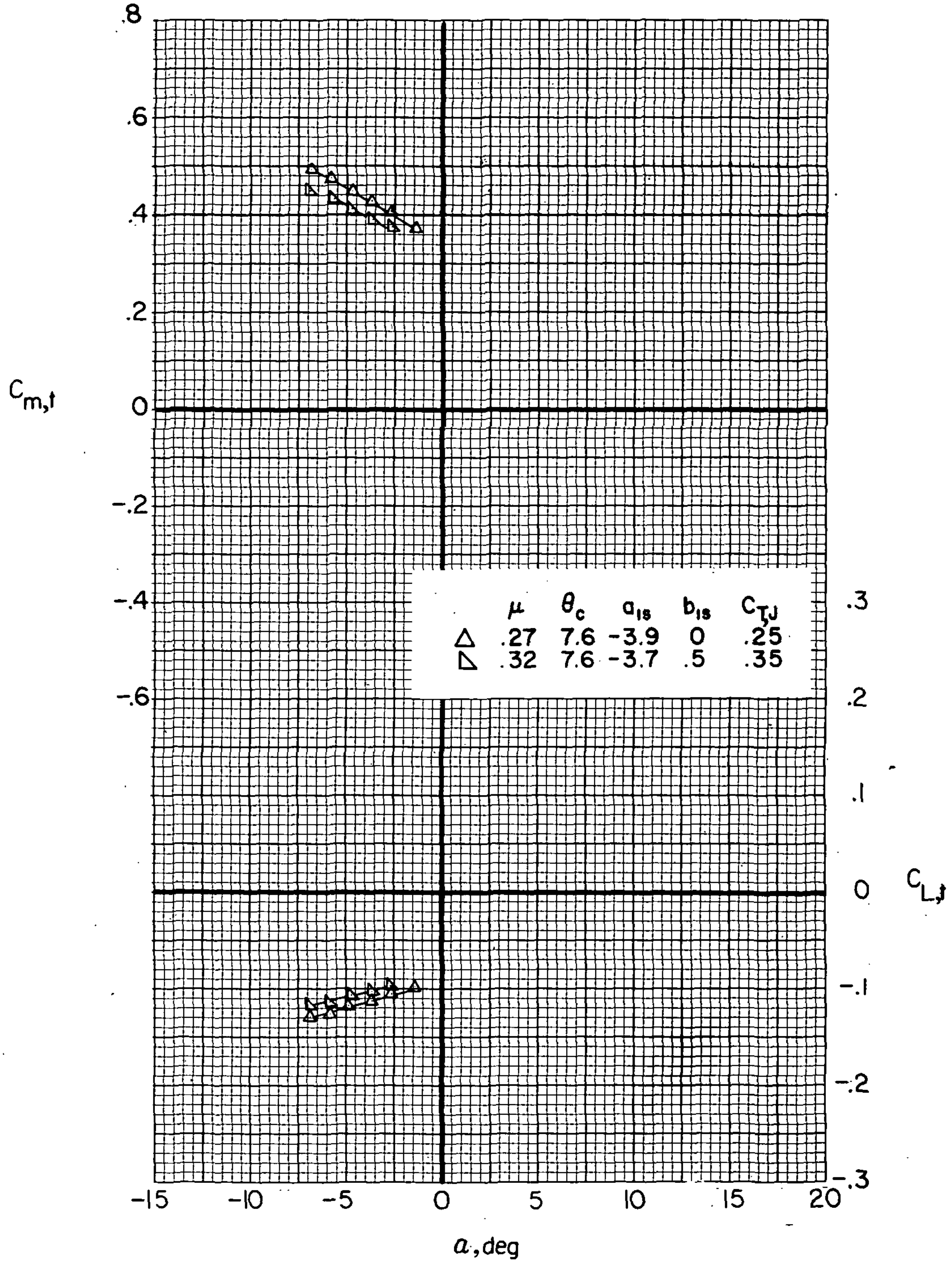

(c) $F_1M_RW_6VH_CJ_2$; low wing lift.

Figure 56.- Concluded.

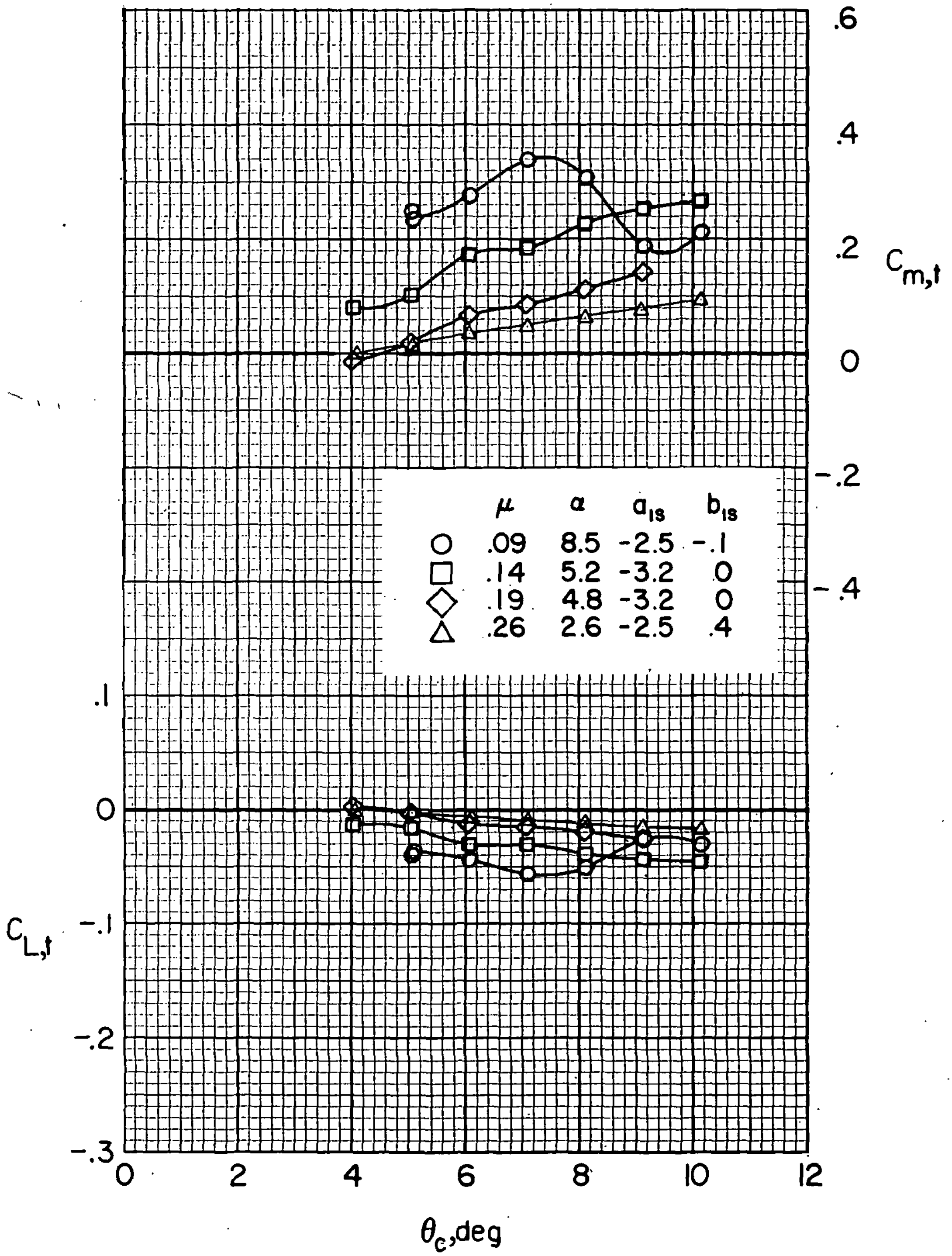

(a) $F_1M_RVH_H$.

Figure 57.- Variation of tail longitudinal aerodynamics with collective pitch angle with the rotor on for $\delta_3 = -27.6^\circ$. (α, a_{1s}, and b_{1s} are in degrees.)

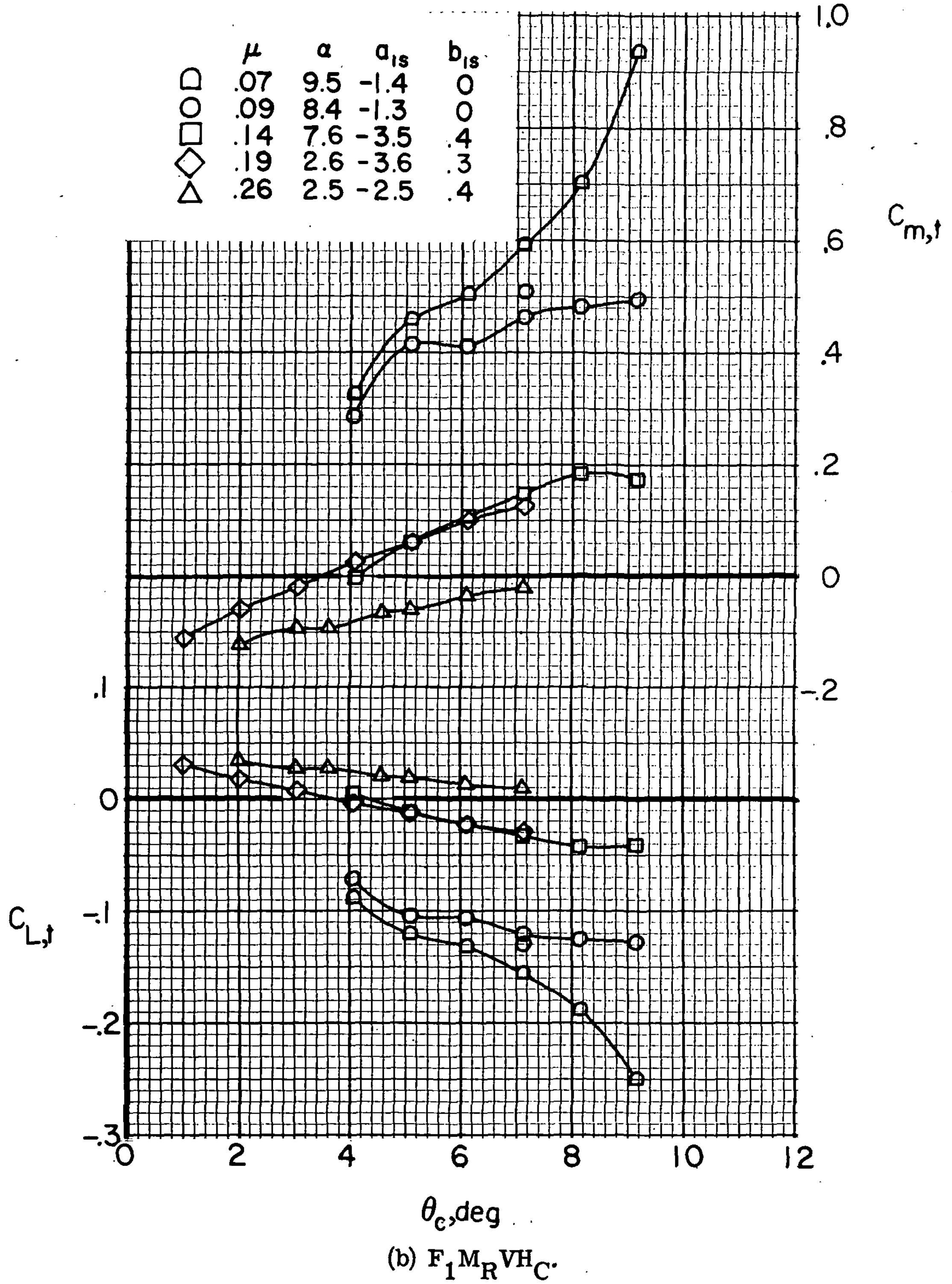

(b) $F_1M_RVH_C$.

Figure 57. - Continued.

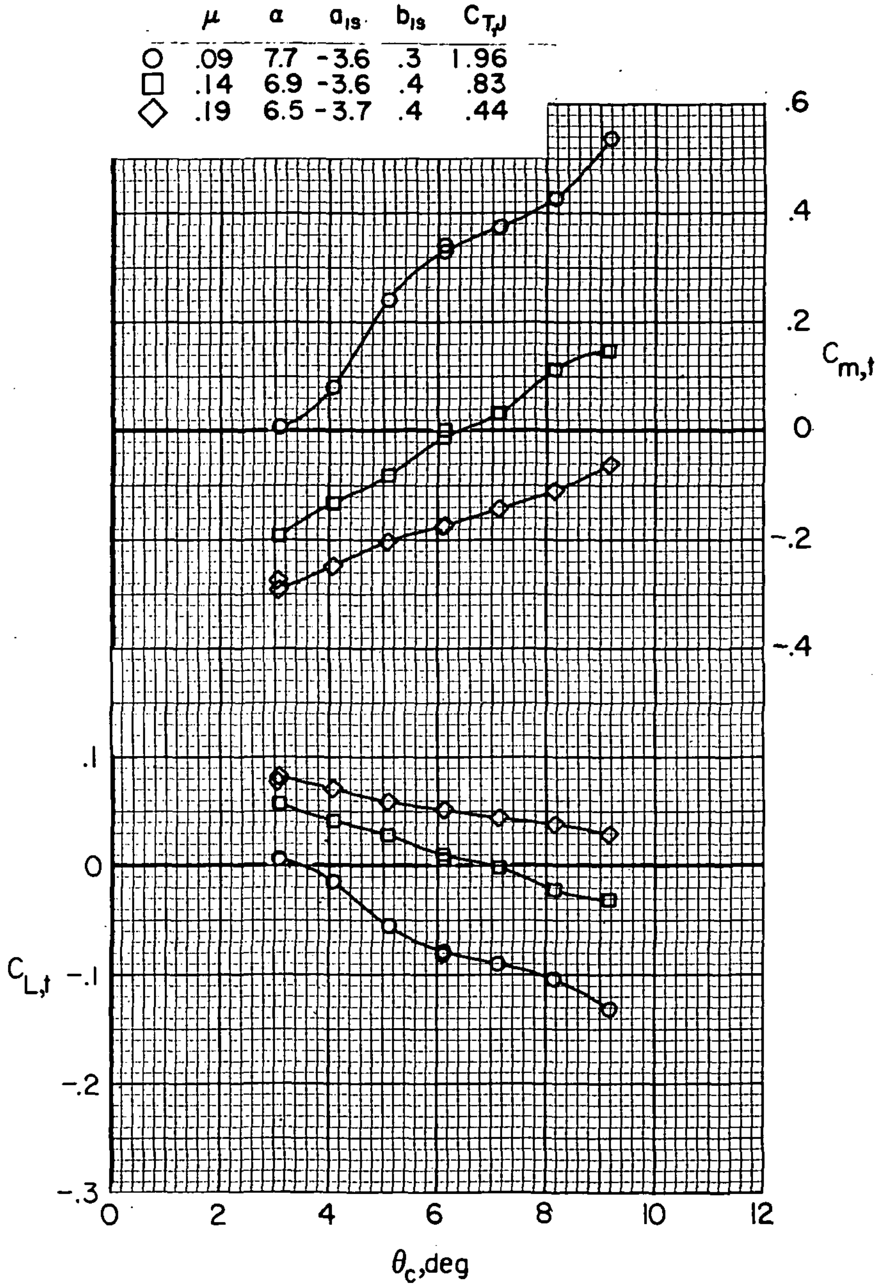

(c) $F_1M_RVH_CJ_2$.

Figure 57.- Continued.

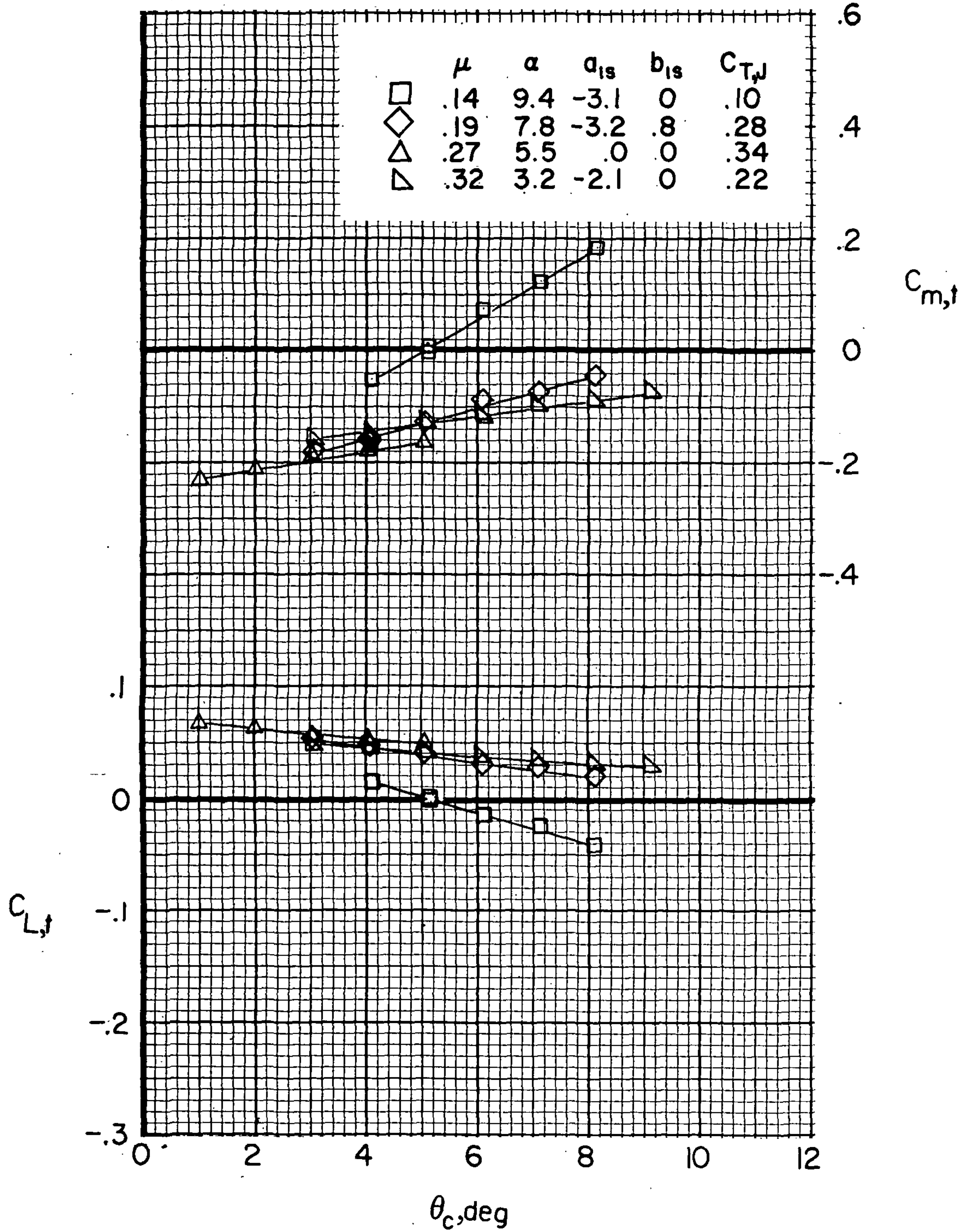

(d) $F_1M_RW_1VH_CJ_2$; high wing lift.

Figure 57.- Continued.

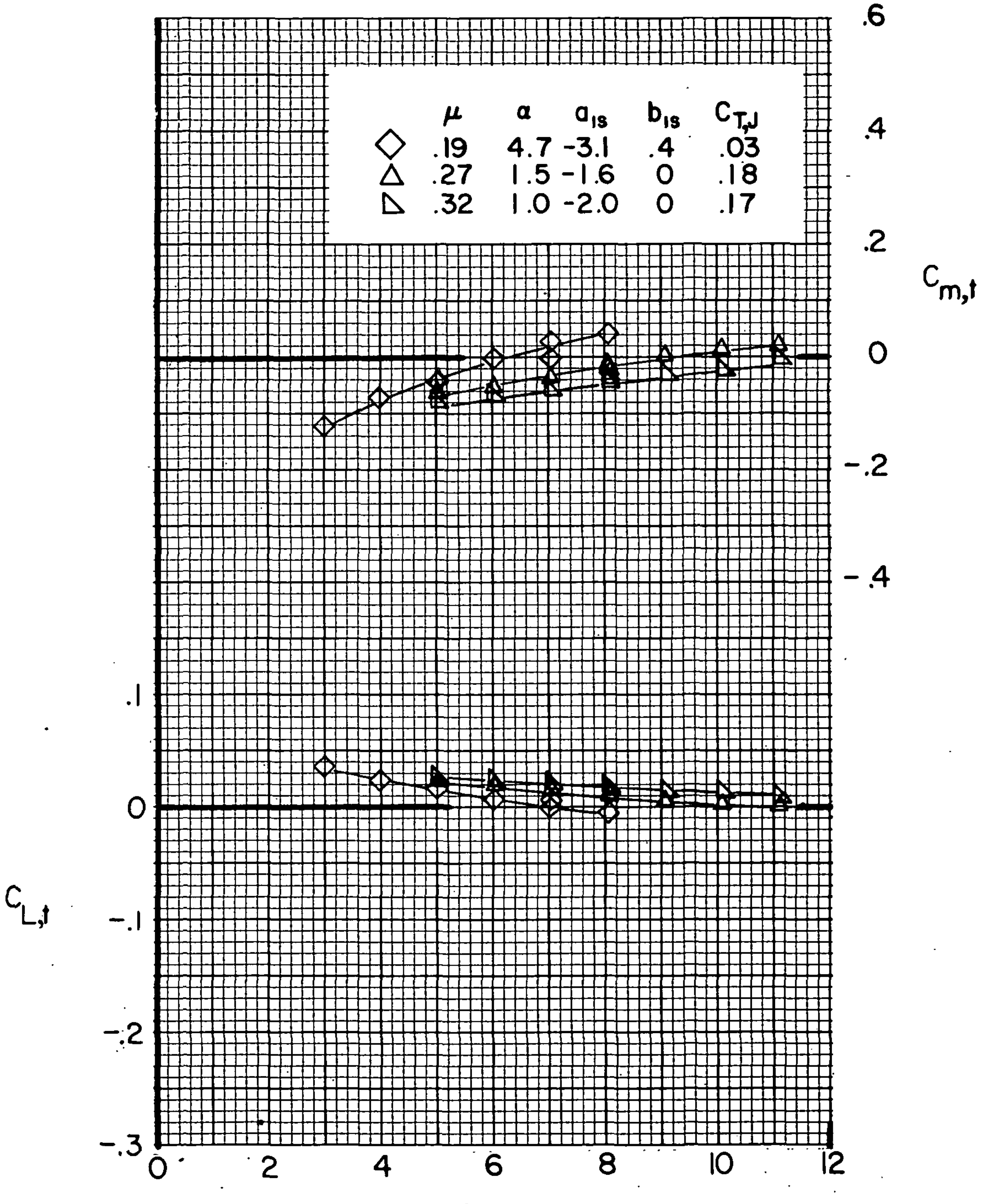

(e) $F_1M_RW_1VH_CJ_2$; low wing lift.

Figure 57.- Continued.

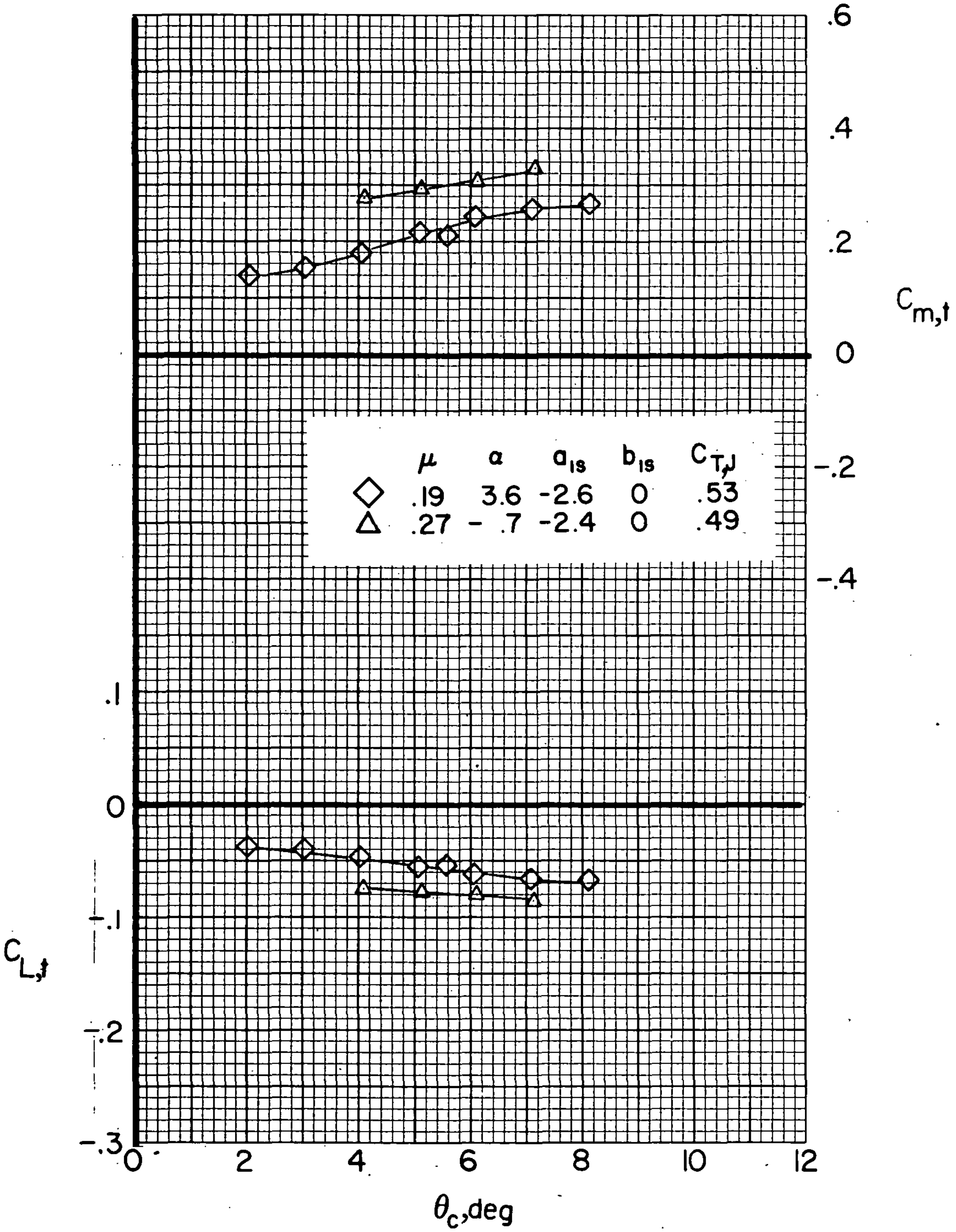

(f) $F_1M_RW_6VH_CJ_2$; high wing lift.

Figure 57. - Continued.

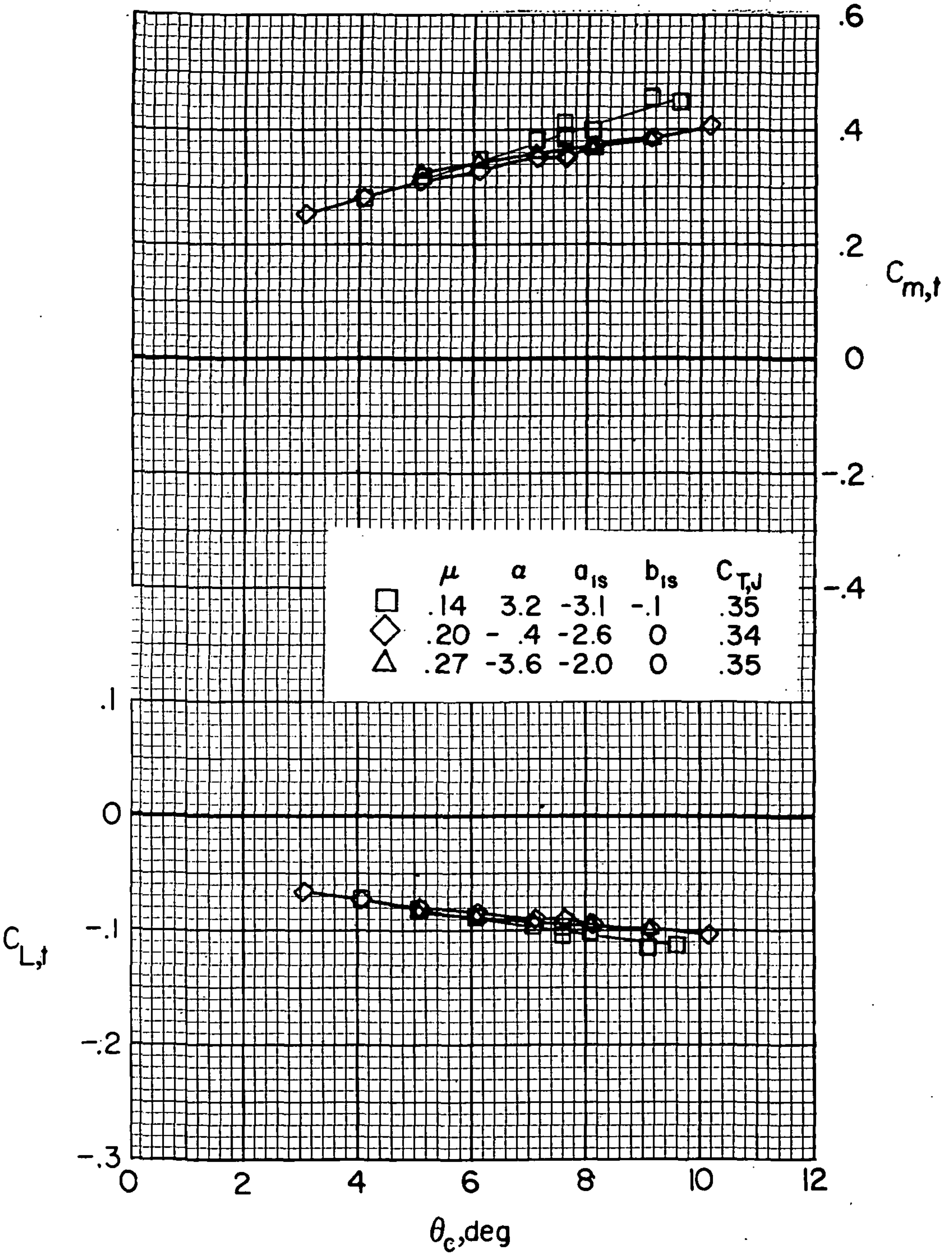

(g) $F_1M_RW_6VH_CJ_2$; low wing lift.

Figure 57.- Concluded.

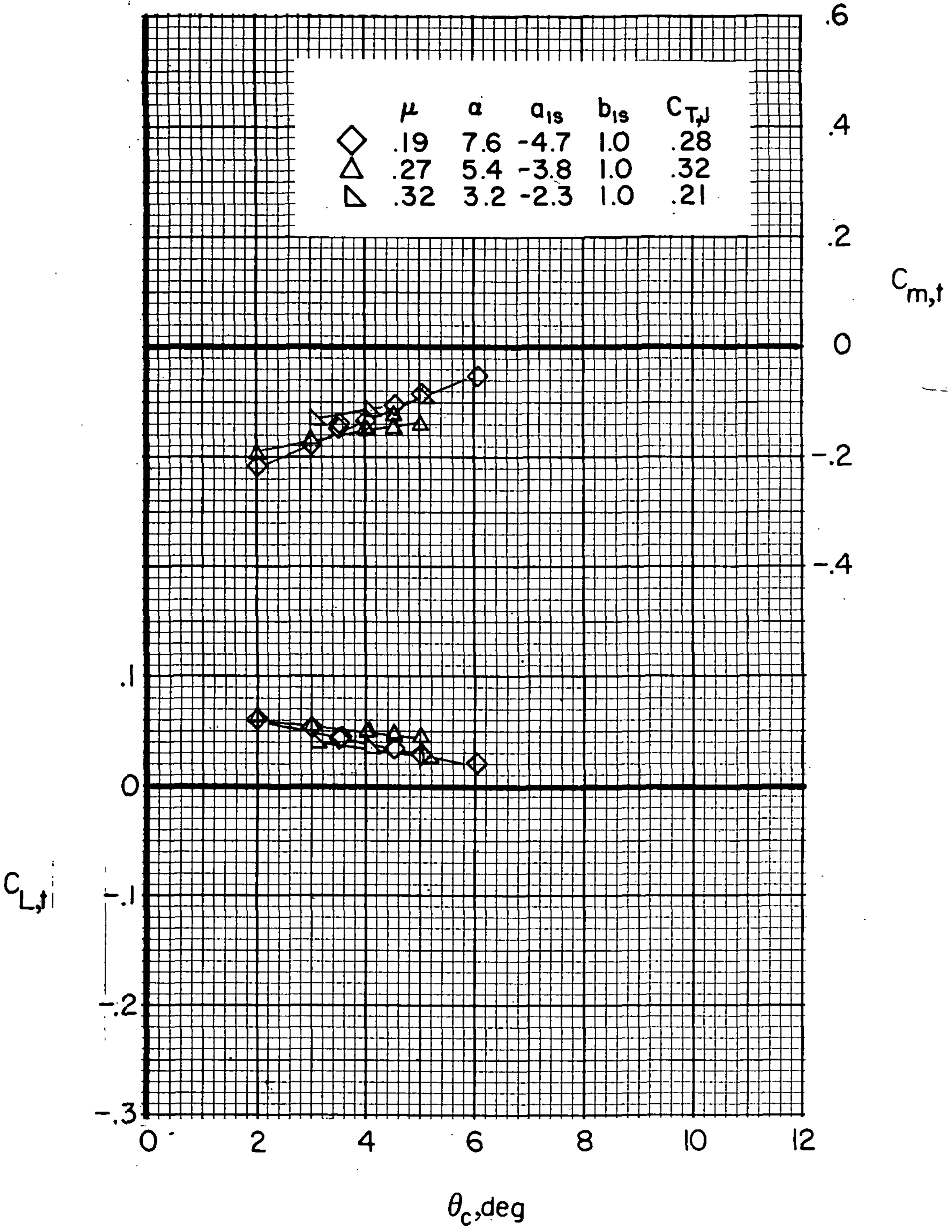

(a) $F_1M_RW_1VH_CJ_2$.

Figure 58.- Variation of tail longitudinal aerodynamics with collective pitch angle with the rotor on for $\delta_3 = -2.0^\circ$. (α, a_{1s}, and b_{1s} are in degrees.)

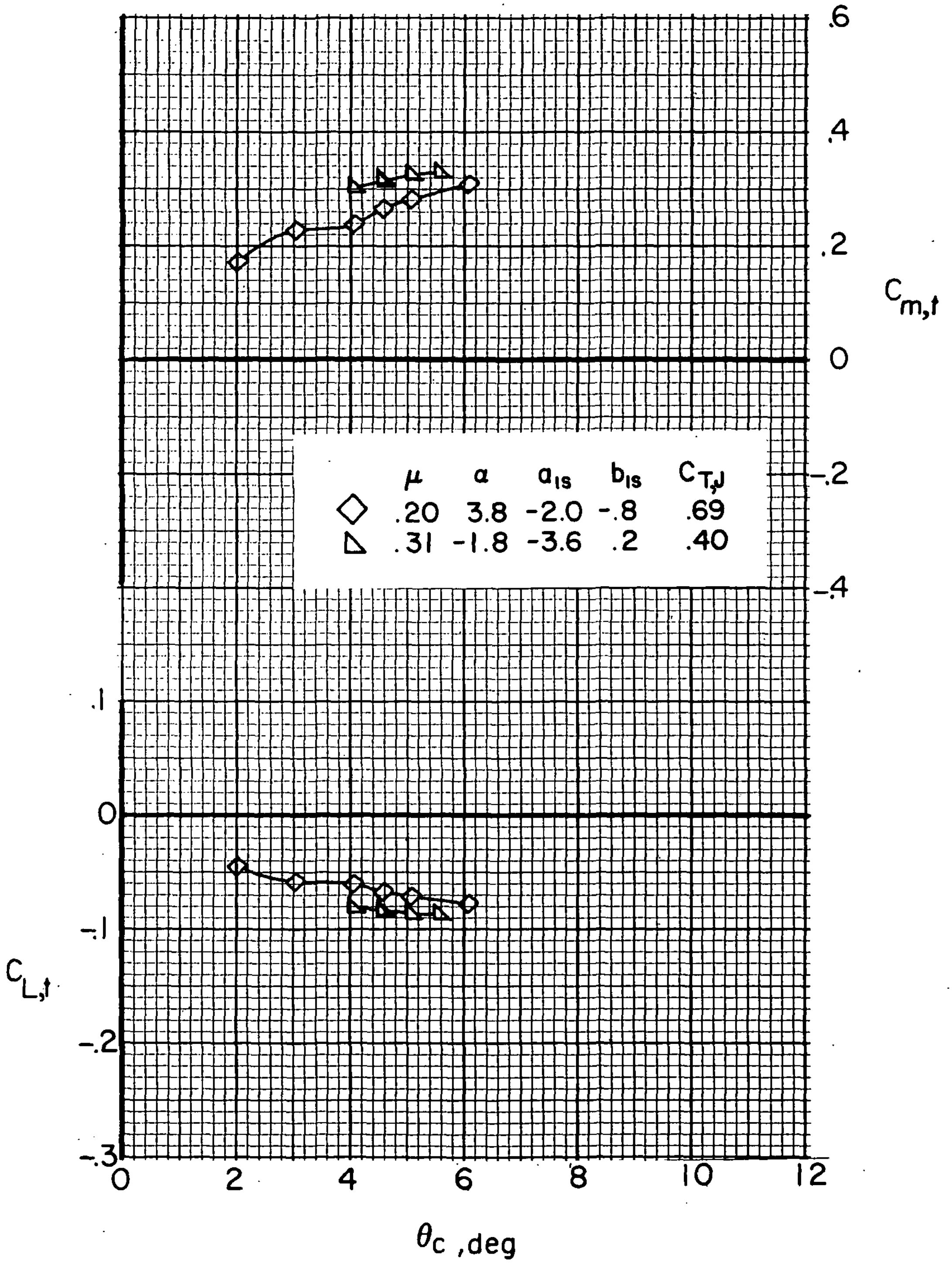

(b) $F_1M_RW_6VH_CJ_2$.

Figure 58. - Concluded.

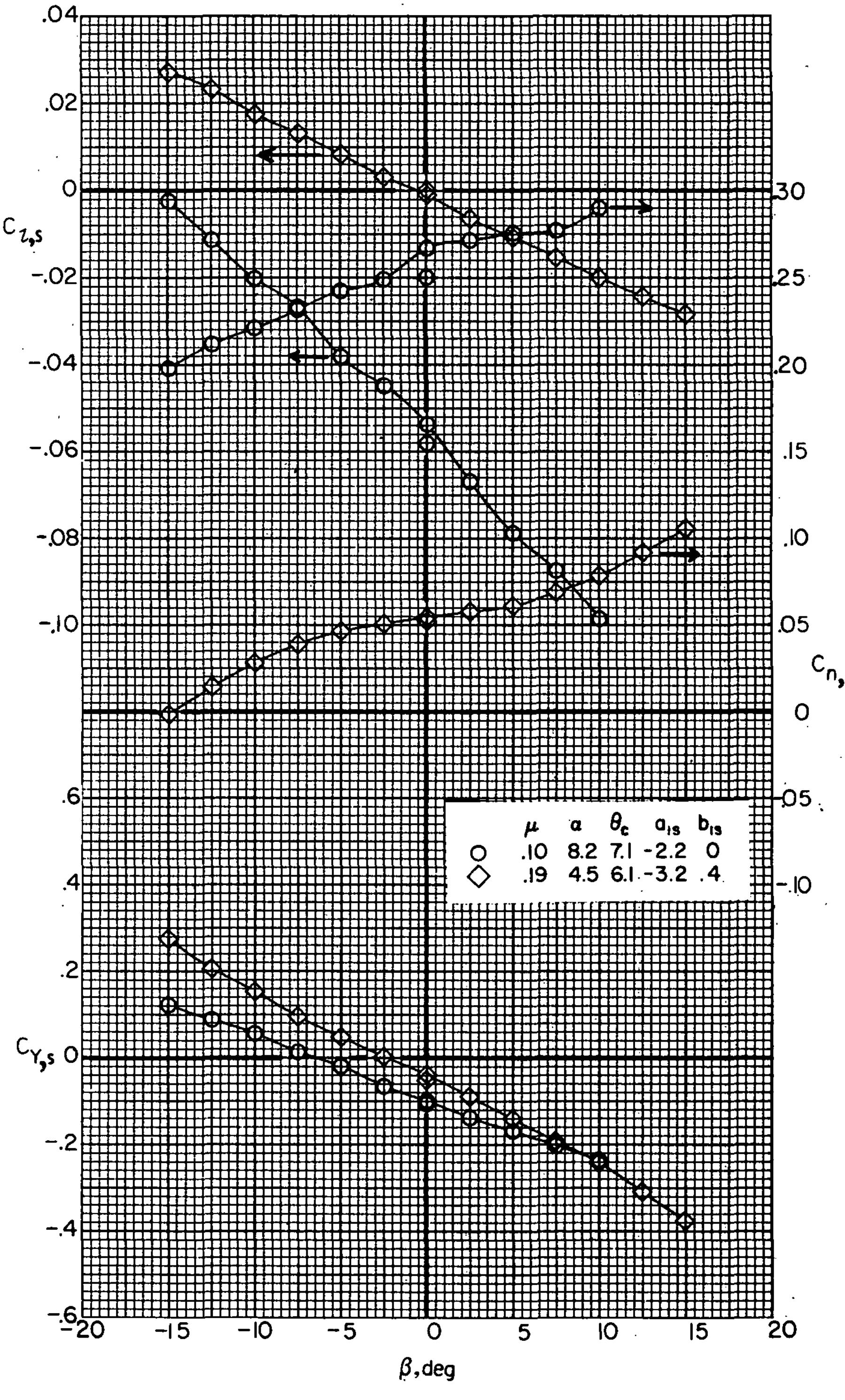

(a) $F_1 M_R V H_H$.

Figure 59.- Effect of forward speed on airframe lateral aerodynamics with the rotor on for δ_3 = -27.6°. (α, θ_c, a_{1s}, and b_{1s} are in degrees.)

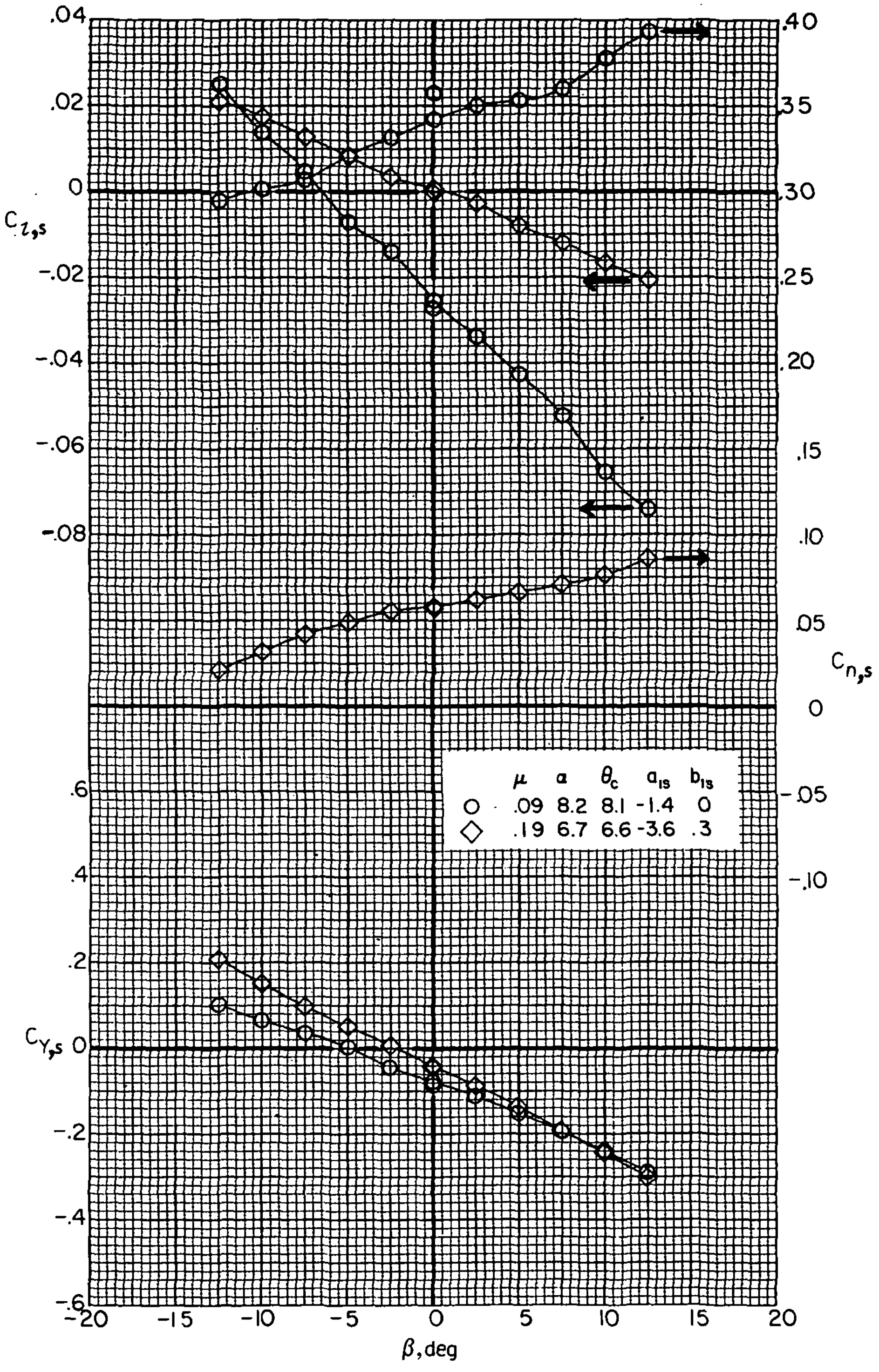

(b) $F_1M_RVH_C$.

Figure 59.- Continued.

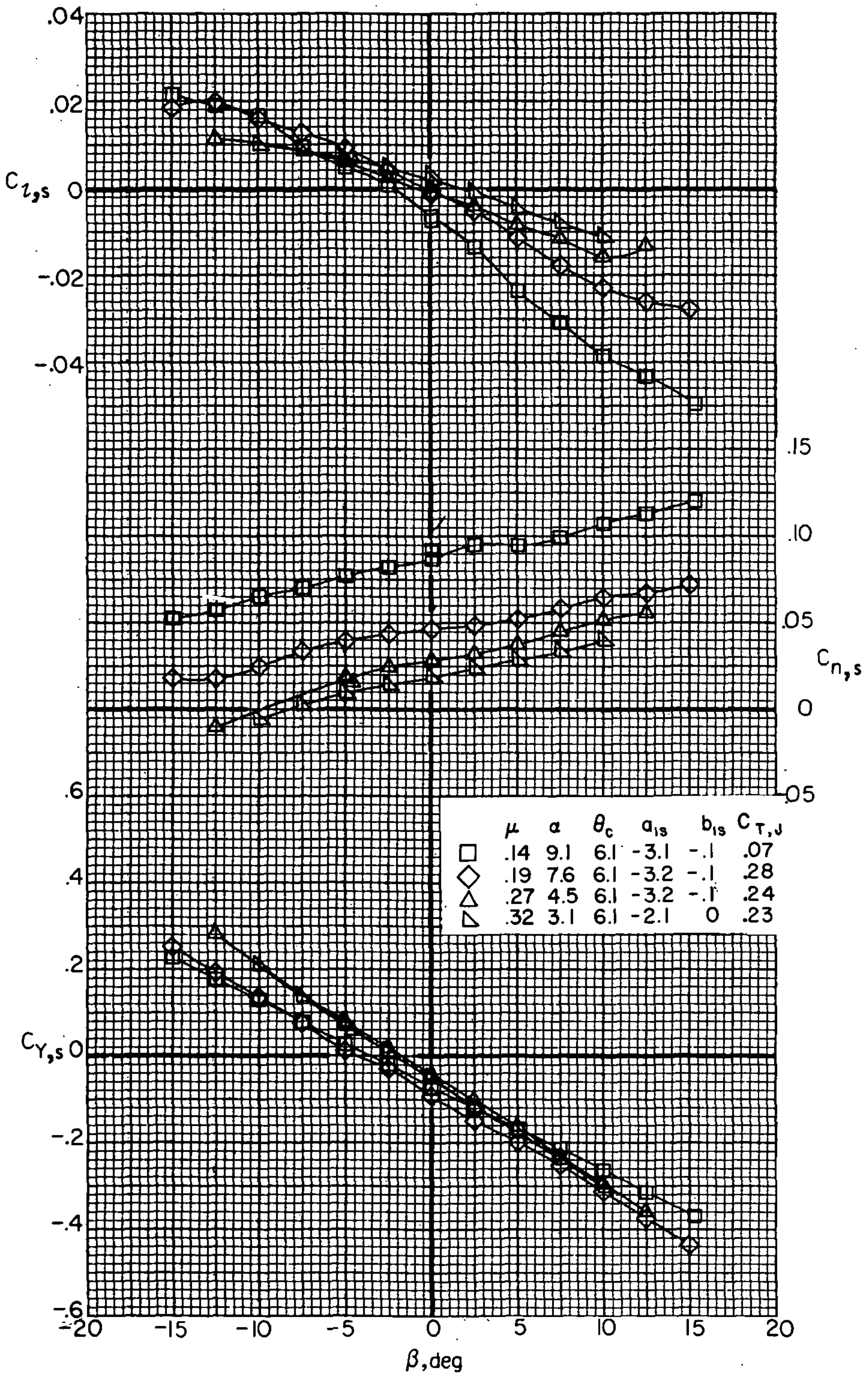

(c) $F_1M_RW_1VH_CJ_2$; high wing lift.

Figure 59.- Continued.

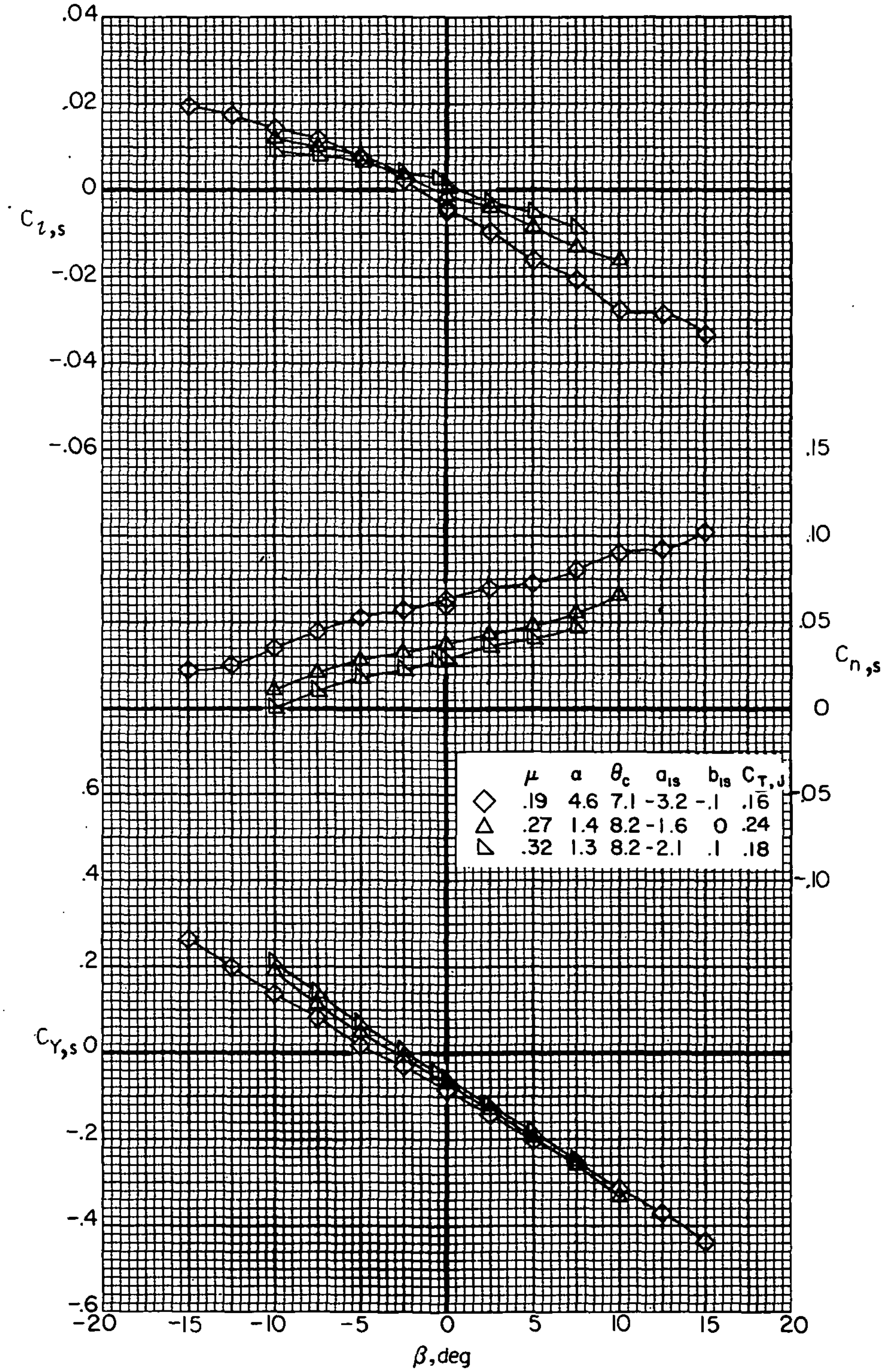

(d) $F_1M_RW_1VH_CJ_2$; low wing lift.

Figure 59.- Continued.

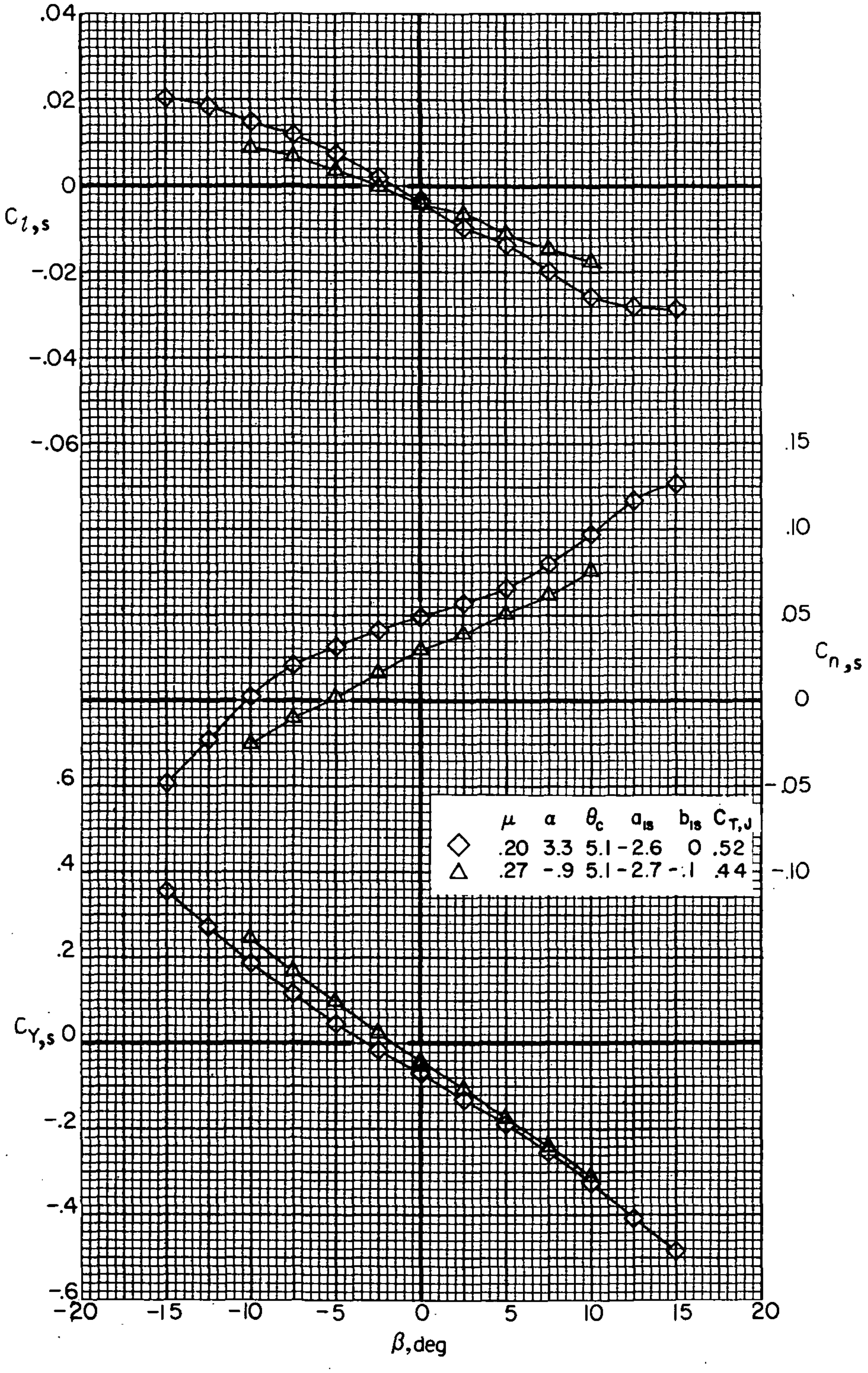

(e) $F_1M_RW_6VH_CJ_2$; high wing lift.

Figure 59.- Continued.

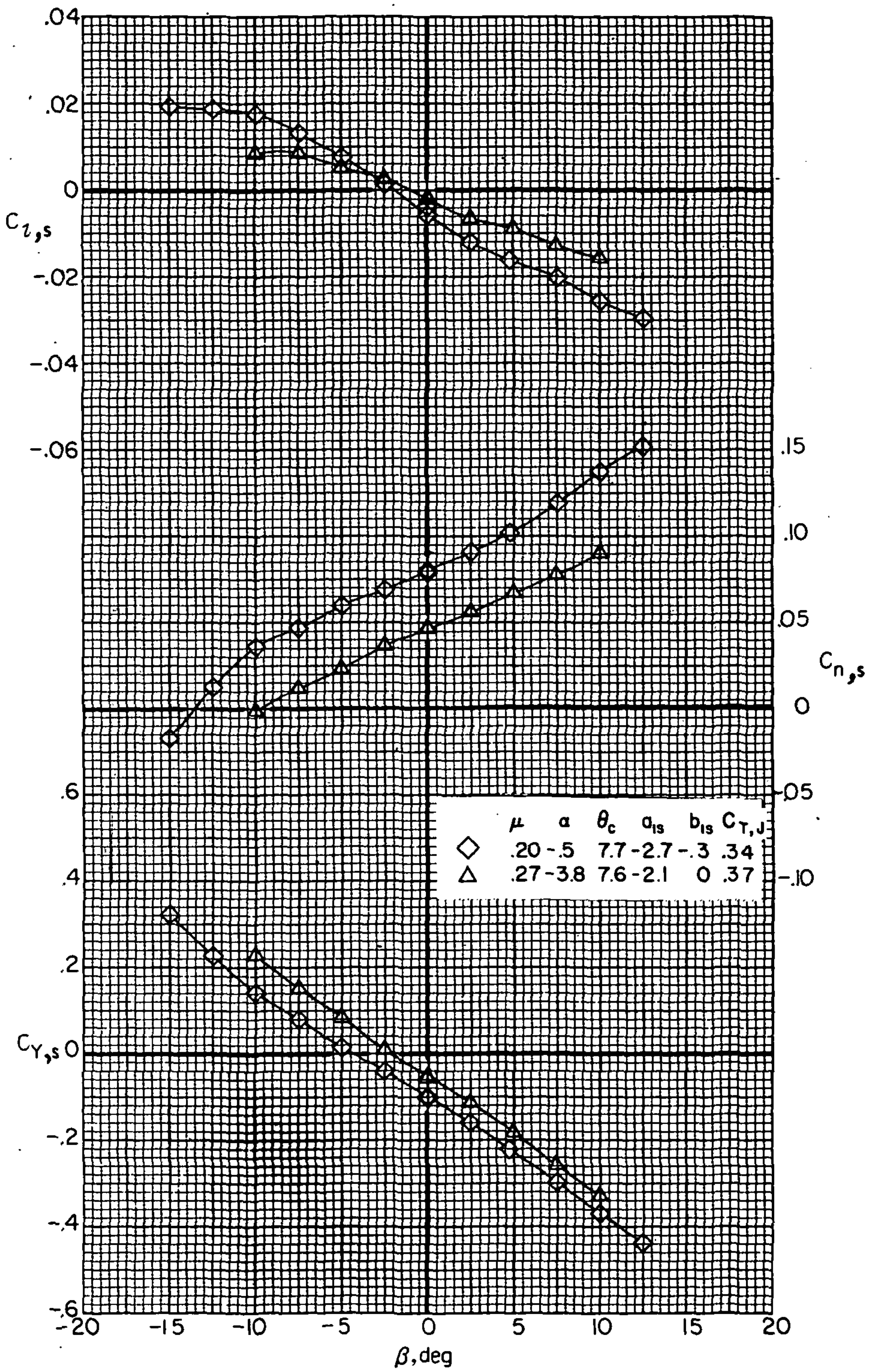

(f) $F_1M_RW_6VH_CJ_2$; low wing lift.

Figure 59.- Concluded.

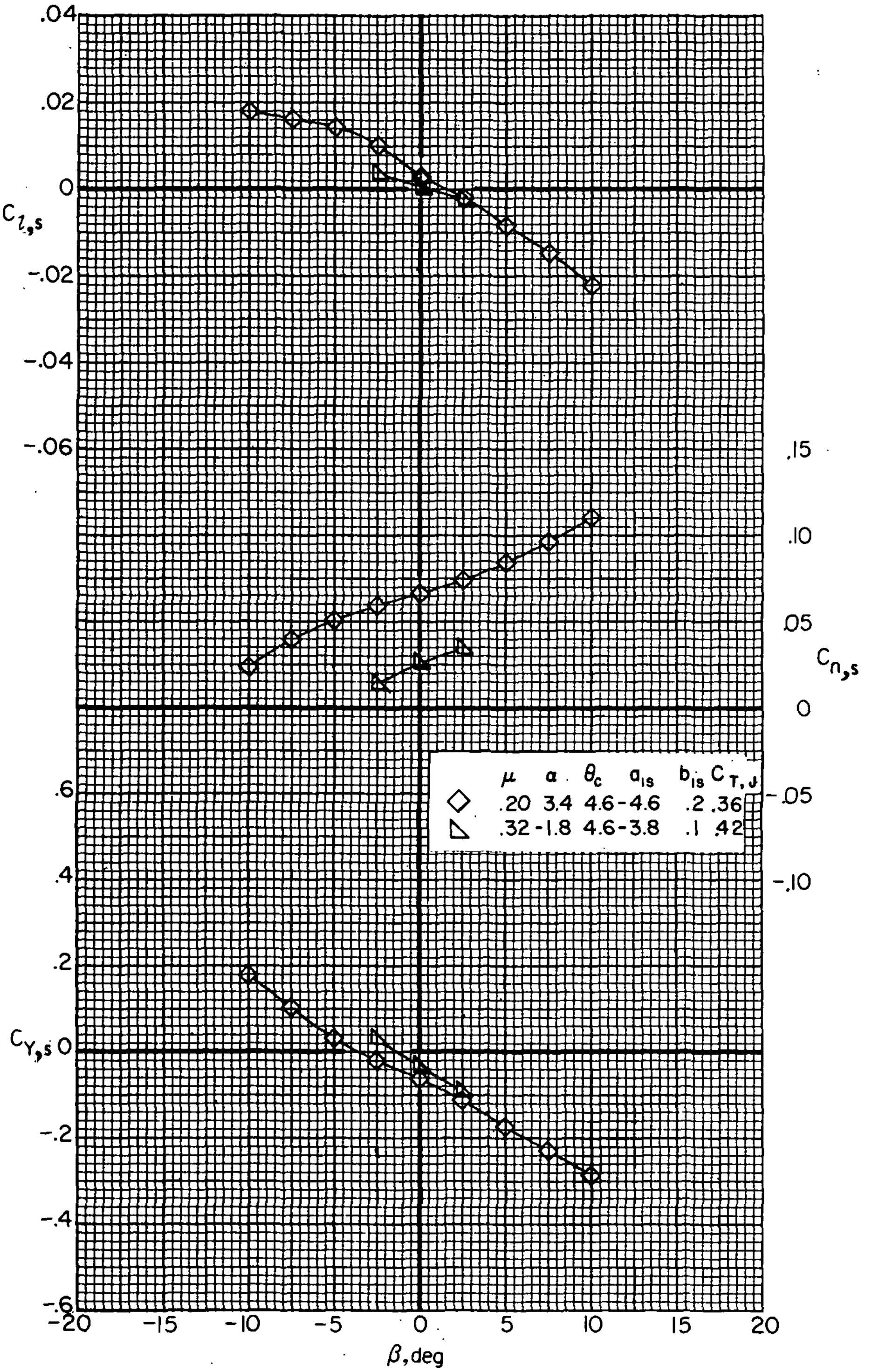

Figure 60.- Effect of forward speed on lateral aerodynamics with the rotor on for $\delta_3 = -2.0^\circ$. $F_1M_RW_6VH_CJ_2$. (α, θ_c, a_{1s}, and b_{1s} are in degrees.)

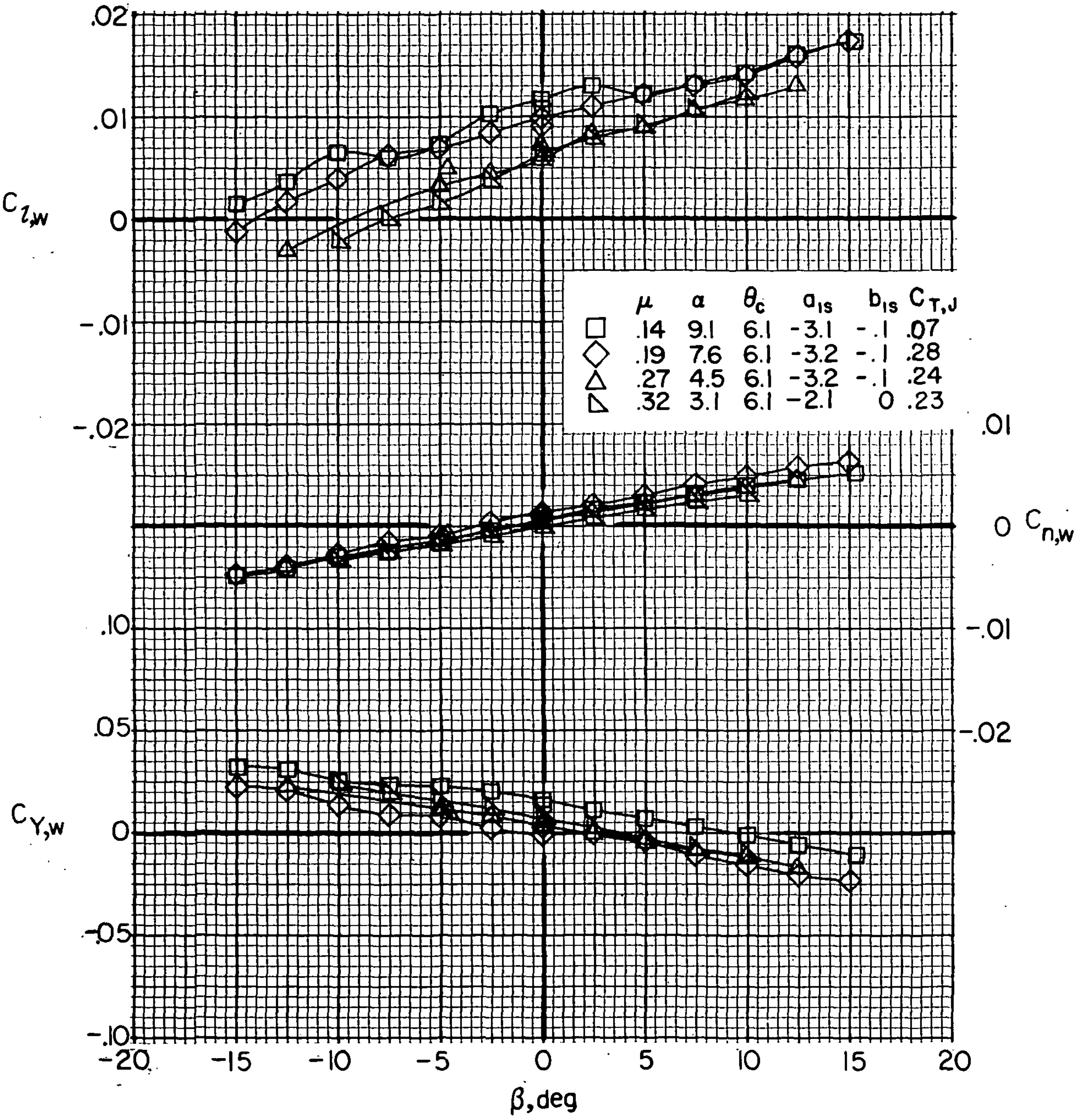

(a) $F_1M_RW_1VH_CJ_2$; high wing lift.

Figure 61.- Effect of forward speed on wing lateral aerodynamics with the rotor on for $\delta_3 = -27.6^{\circ}$. (α, θ_c, a_{1s}, and b_{1s} are in degrees.)

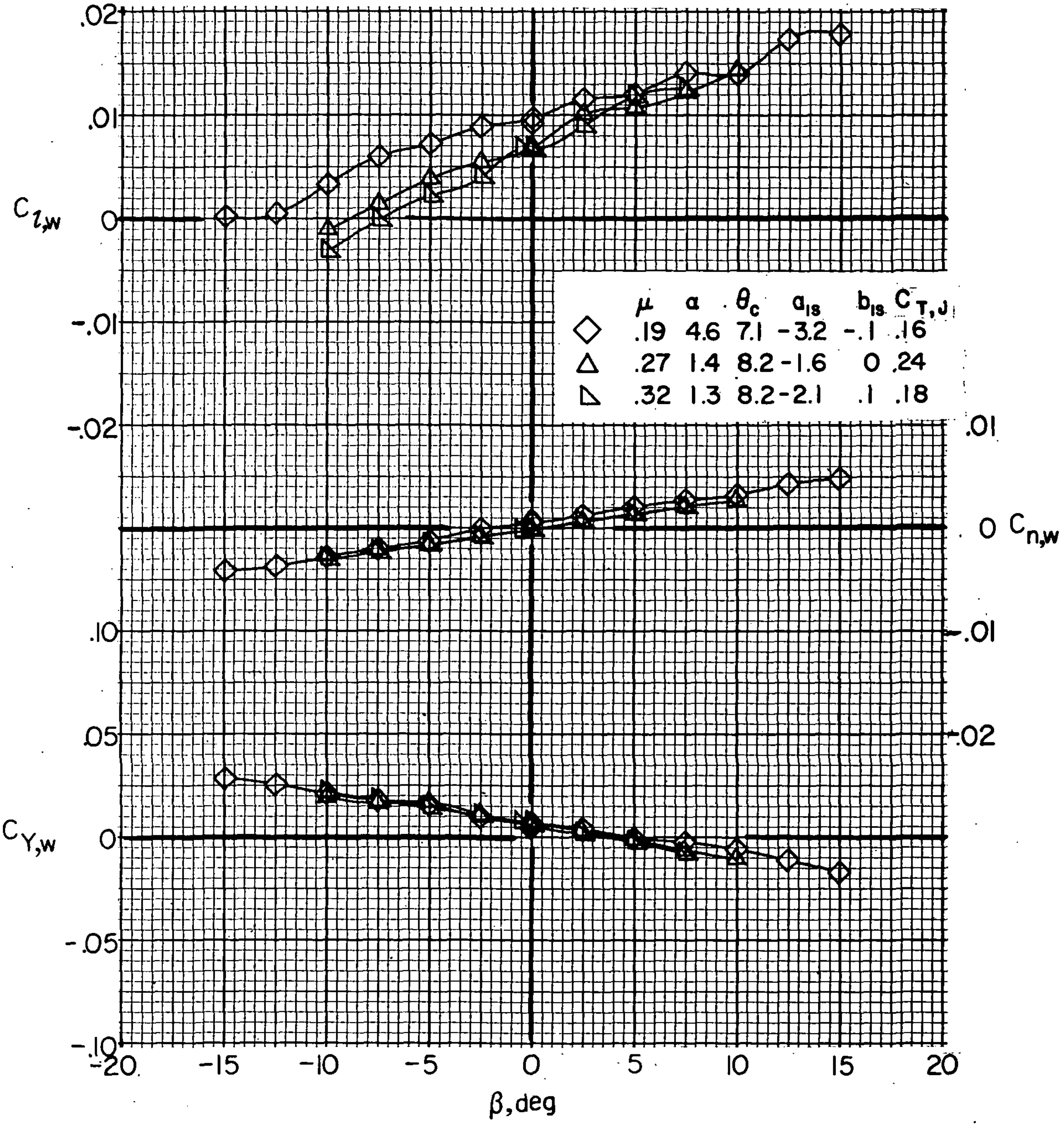

(b) $F_1M_RW_1VH_CJ_2$; low wing lift.

Figure 61.- Continued.

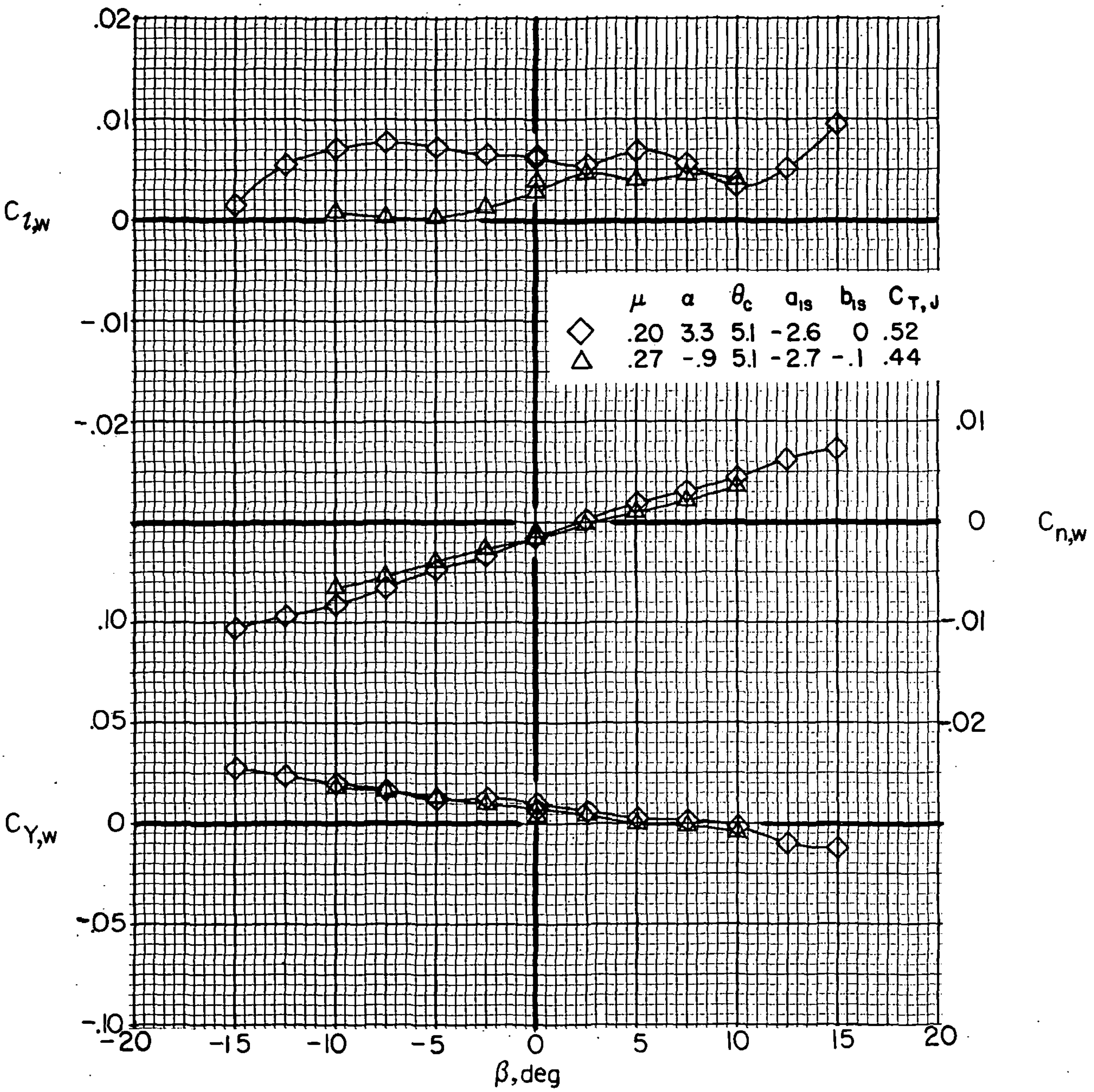

(c) $F_1M_RW_6VH_CJ_2$; high wing lift.

Figure 61.- Continued.

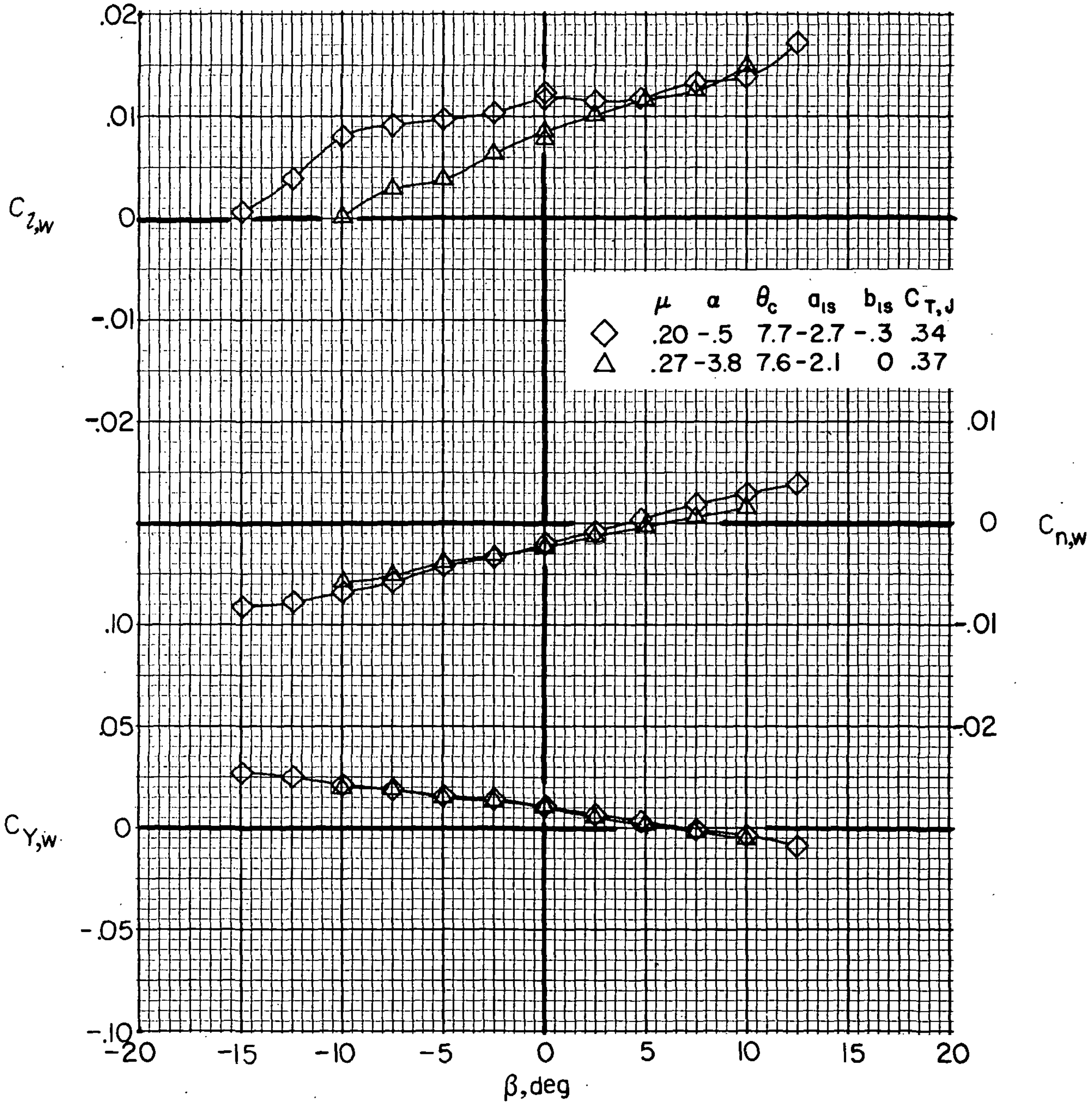

(d) $F_1M_RW_6VH_CJ_2$; low wing lift.

Figure 61.- Concluded.

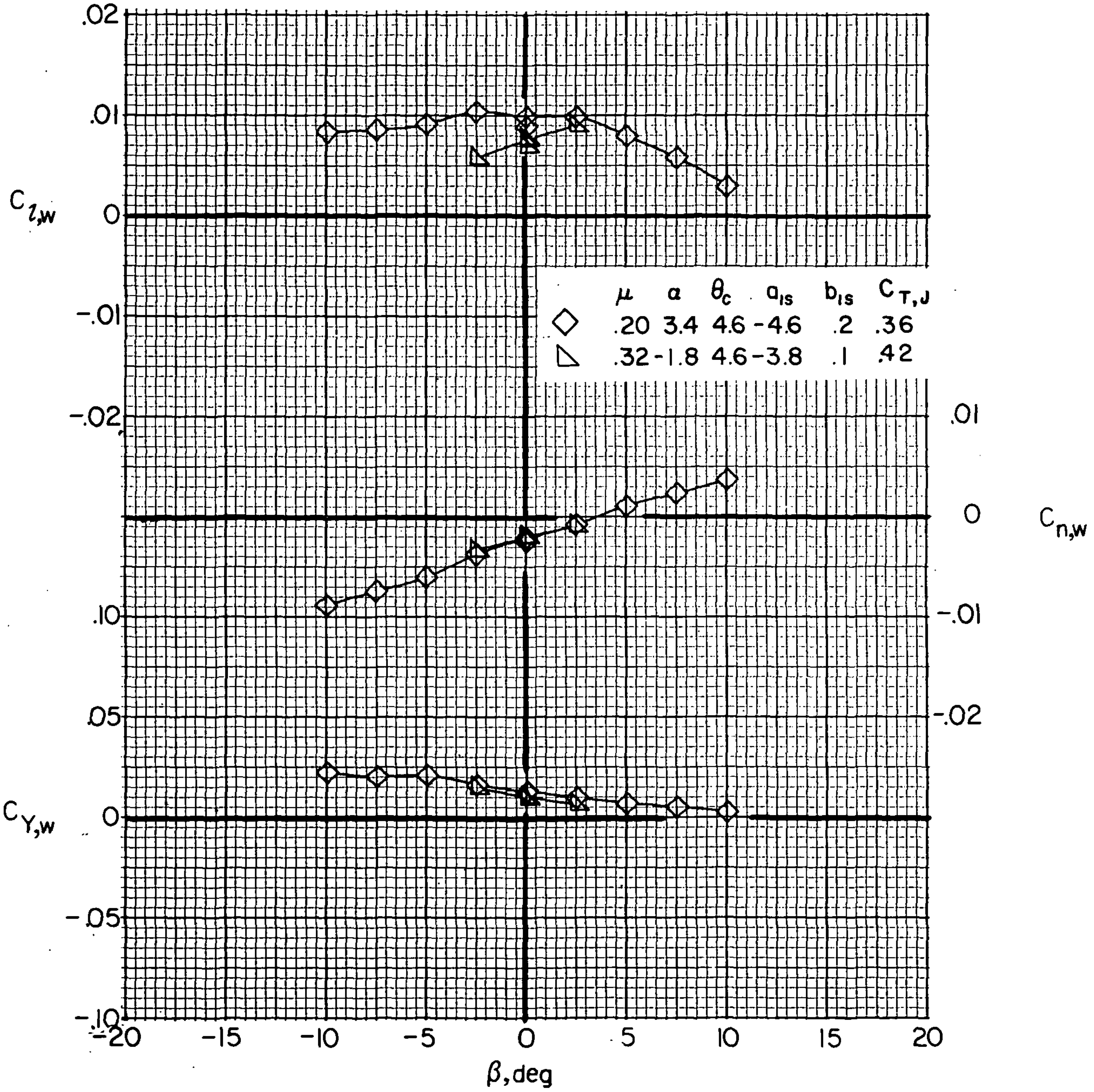

Figure 62.- Effect of forward speed on wing lateral aerodynamics with the rotor on for $\delta_3 = -2.0^\circ$. $F_1M_RW_6VH_CJ_2$. (α, θ_c, a_{1s}, and b_{1s} are in degrees.)

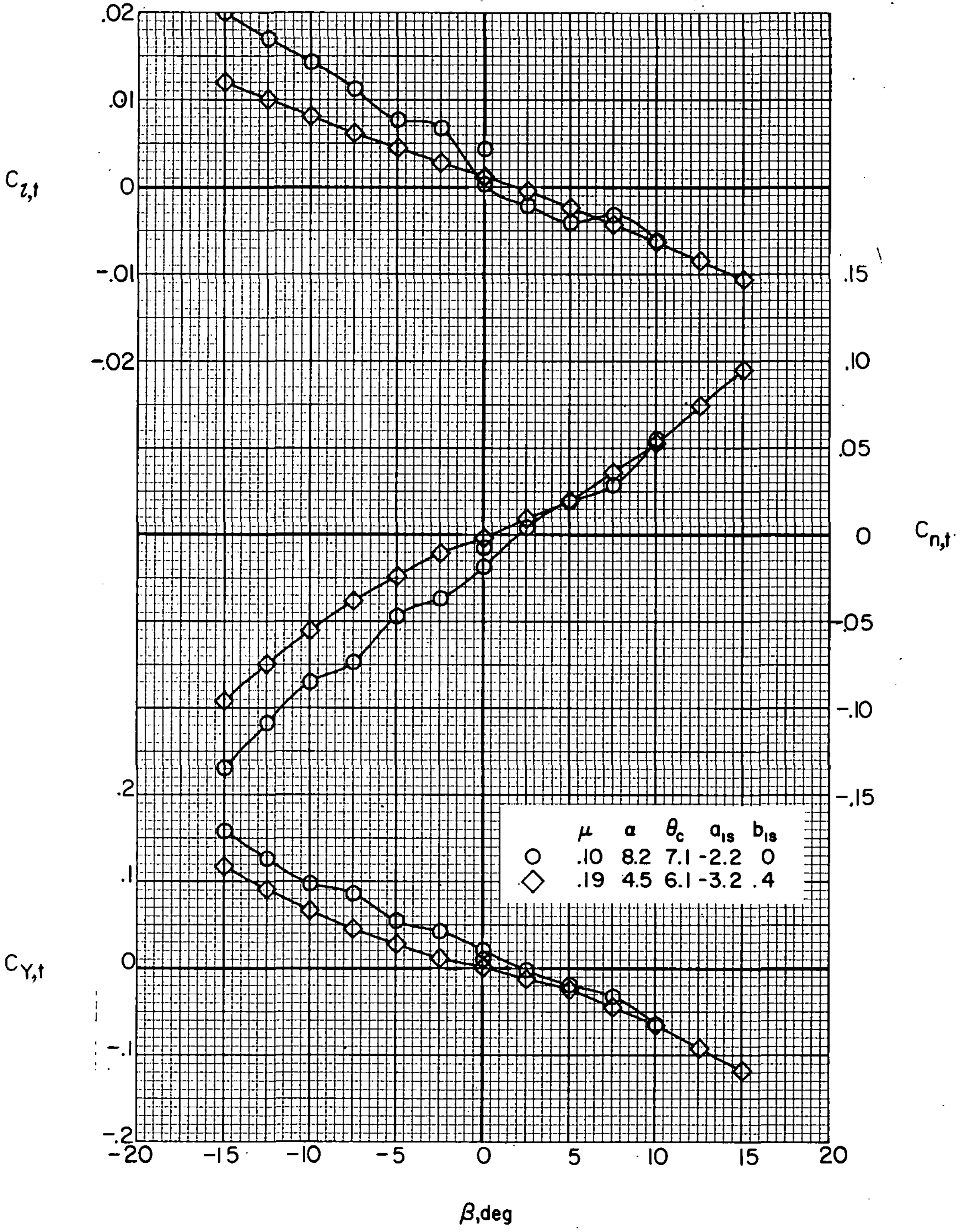

(a) $F_1M_RVH_H$.

Figure 63.- Effect of forward speed on tail lateral aerodynamics with the rotor on for $\delta_3 = -27.6^{\circ}$. (α, θ_c, a_{1s}, and b_{1s} are in degrees.)

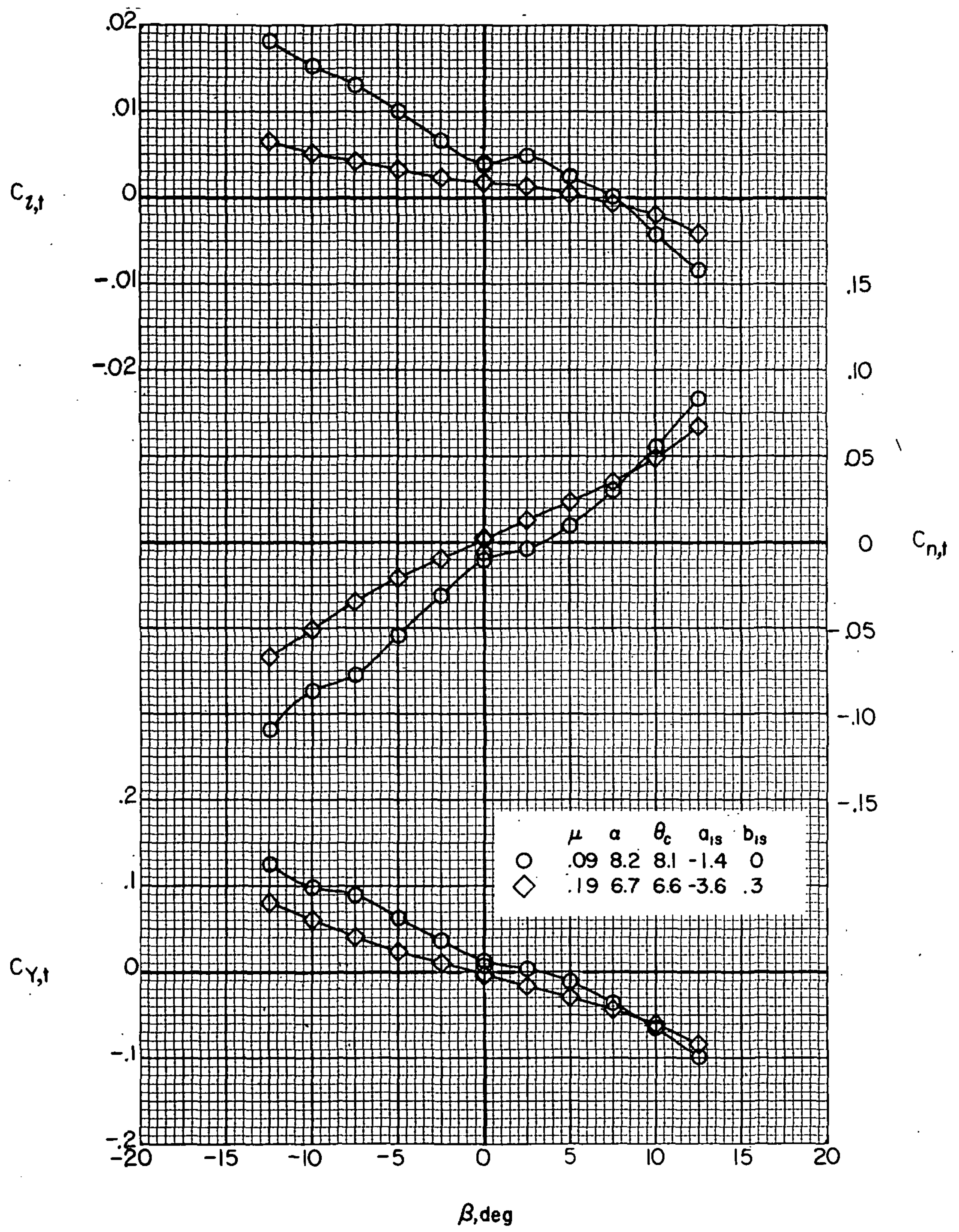

(b) $F_1M_RVH_C$.

Figure 63.- Continued.

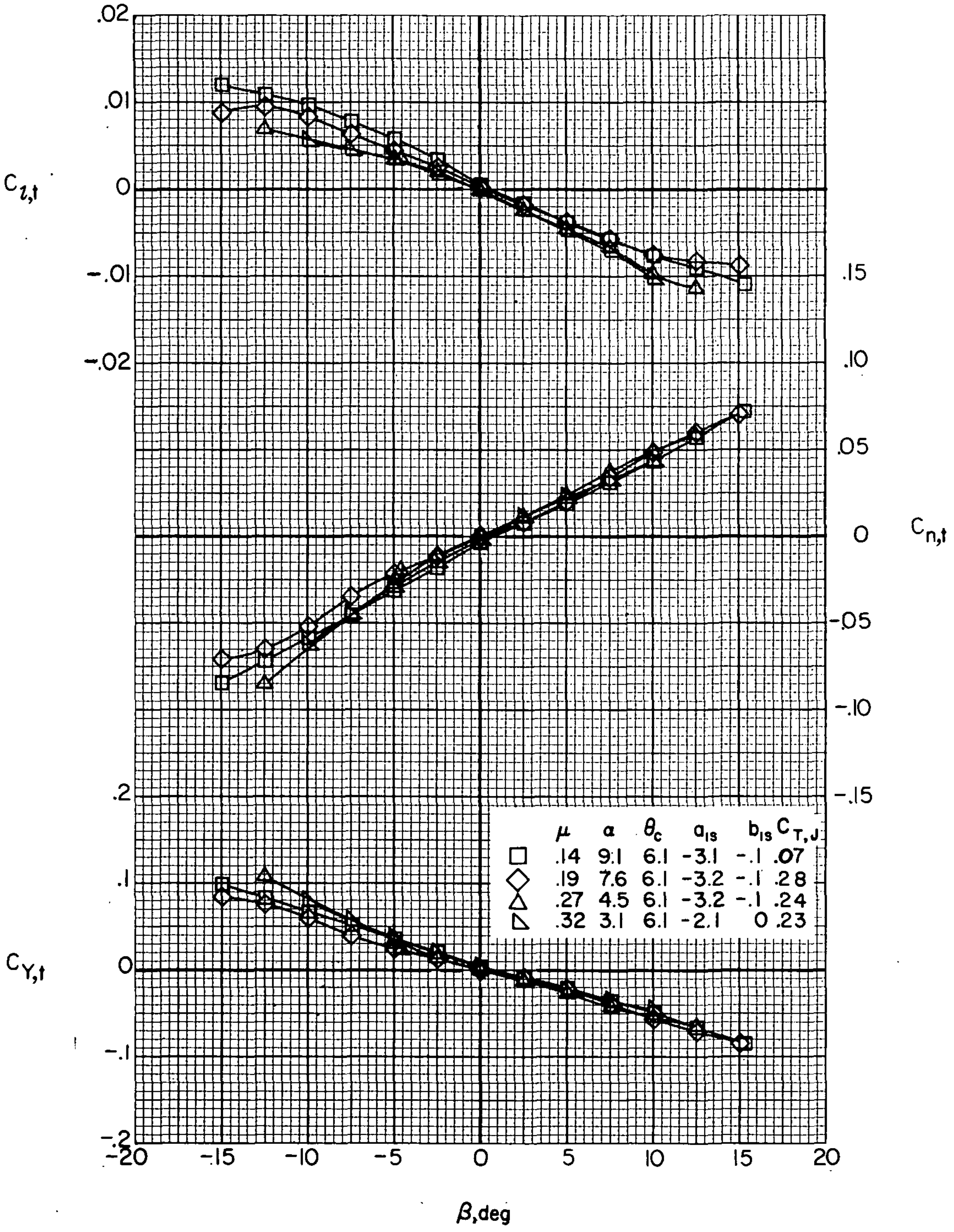

(c) $F_1M_RW_1VH_CJ_2$; high wing lift.

Figure 63.- Continued.

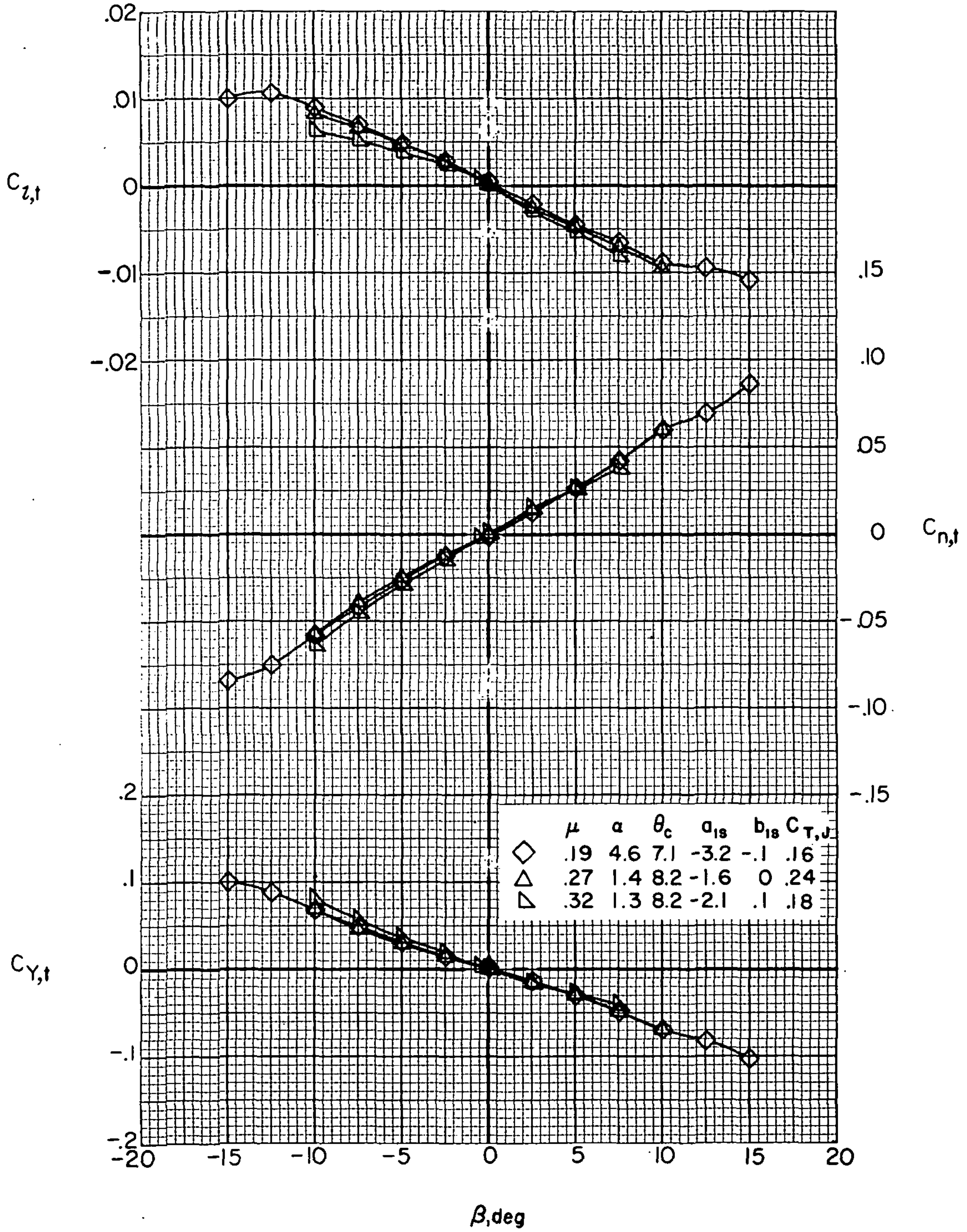

(d) $F_1M_RW_1VH_CJ_2$; low wing lift.

Figure 63.- Continued.

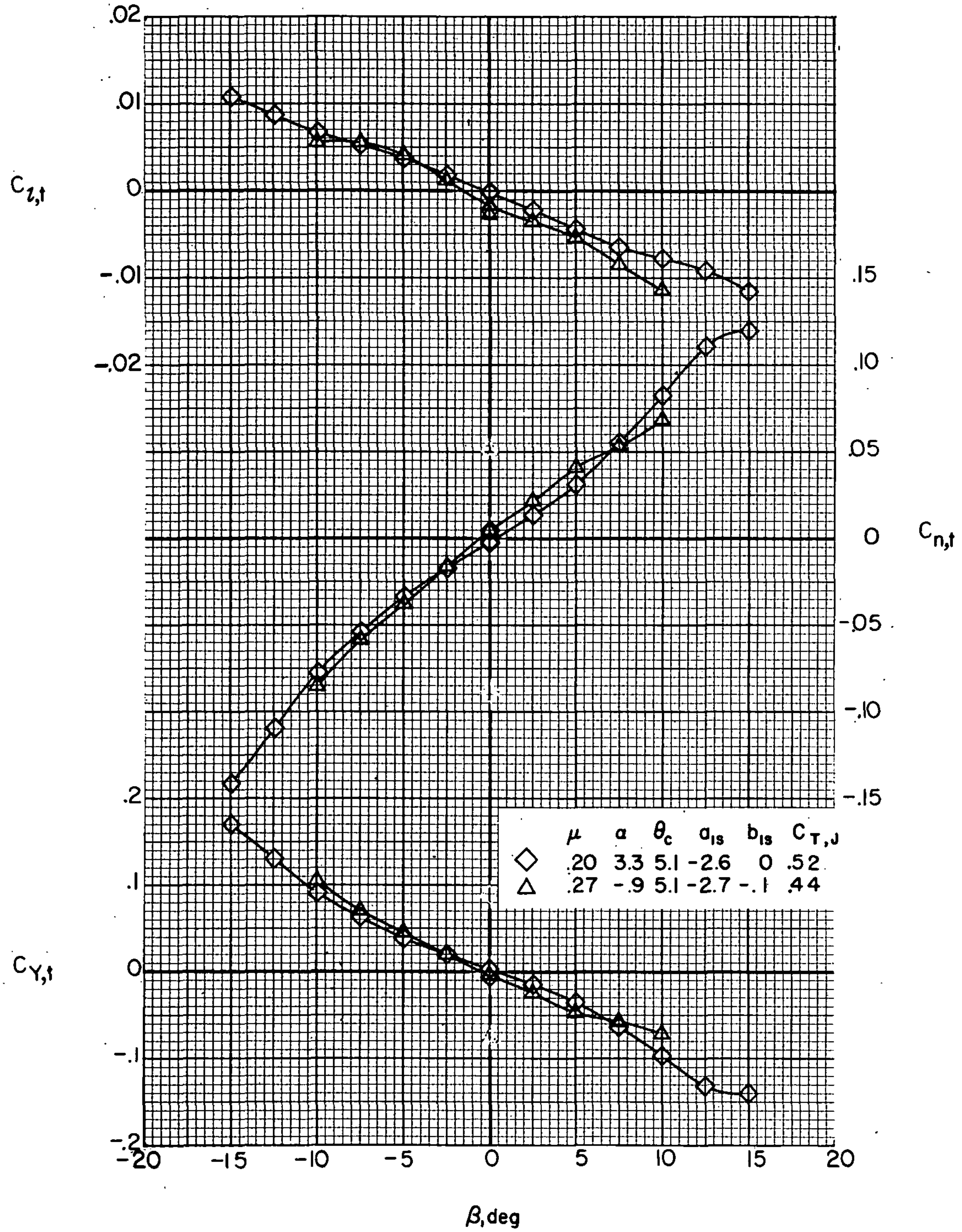

(e) $F_1M_RW_6VH_CJ_2$; high wing lift.

Figure 63. - Continued.

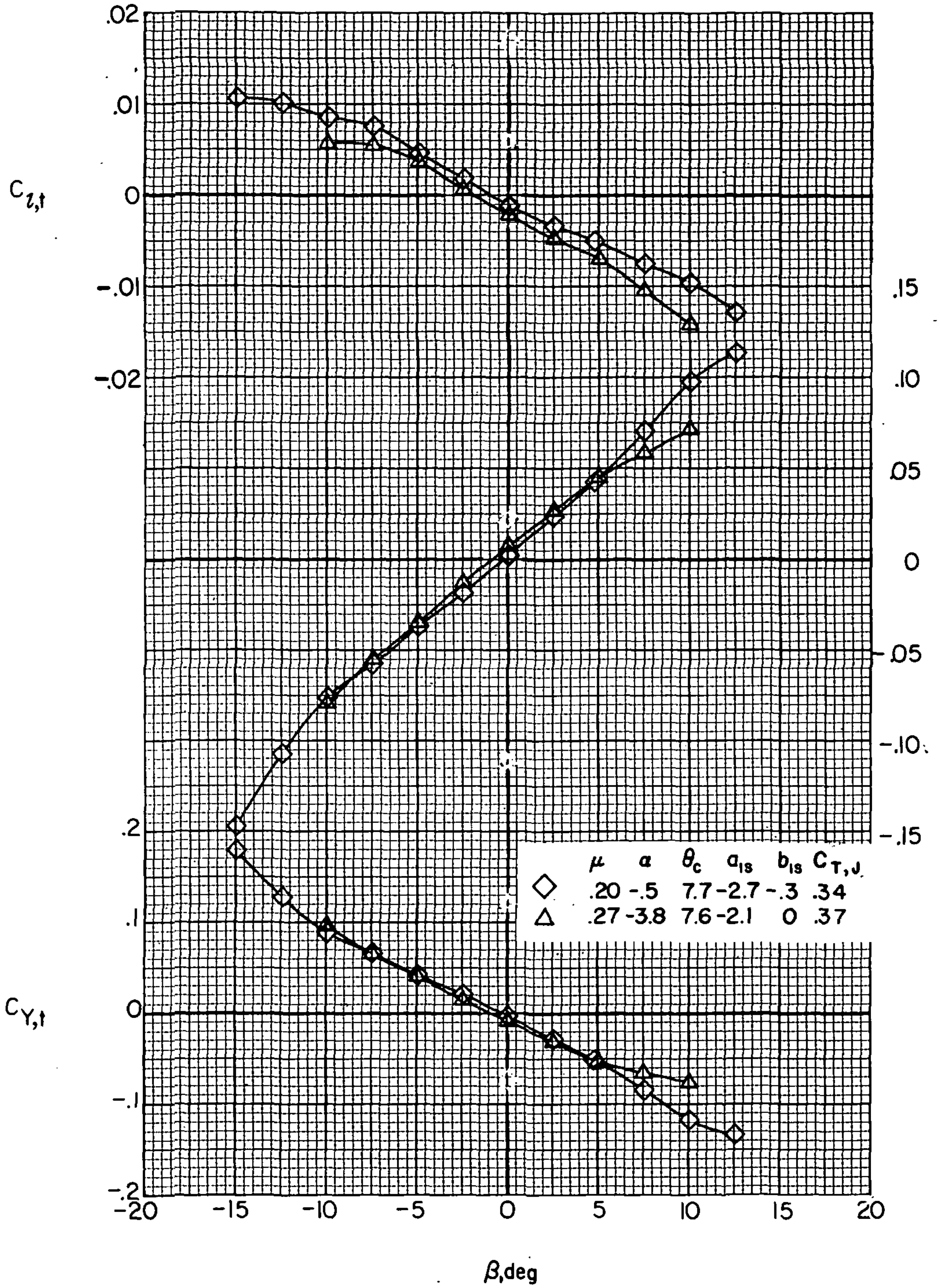

(f) $F_1M_RW_6VH_CJ_2$; low wing lift.

Figure 63.- Concluded.

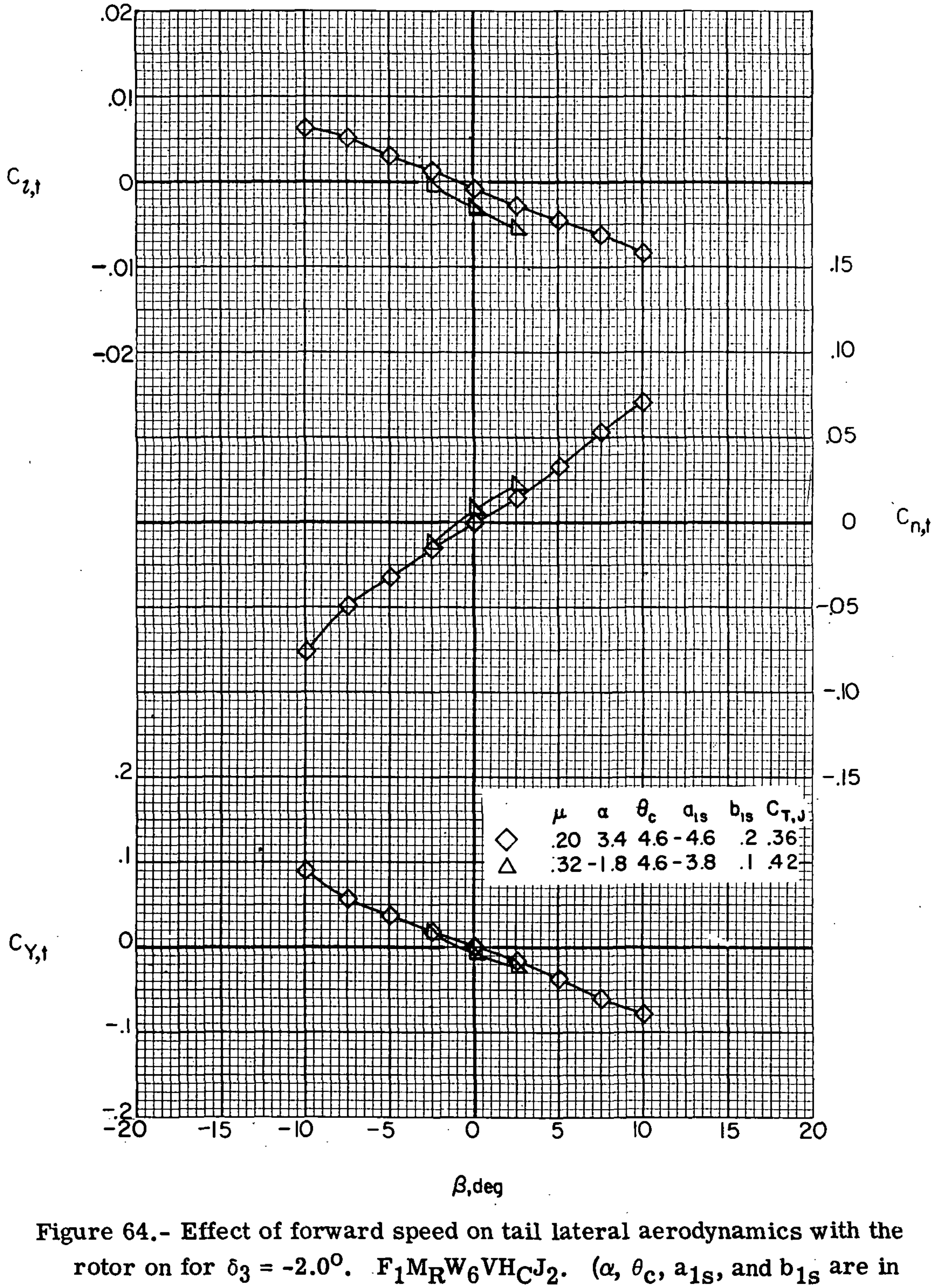

Figure 64.- Effect of forward speed on tail lateral aerodynamics with the rotor on for $\delta_3 = -2.0^{\circ}$. $F_1M_RW_6VH_CJ_2$. (α, θ_c, a_{1s}, and b_{1s} are in degrees.)

NASA-Langley, 1977 L-11287

> *"The aeronautical and space activities of the United States shall be conducted so as to contribute . . . to the expansion of human knowledge of phenomena in the atmosphere and space. The Administration shall provide for the widest practicable and appropriate dissemination of information concerning its activities and the results thereof."*
>
> —NATIONAL AERONAUTICS AND SPACE ACT OF 1958

NASA SCIENTIFIC AND TECHNICAL PUBLICATIONS

TECHNICAL REPORTS: Scientific and technical information considered important, complete, and a lasting contribution to existing knowledge.

TECHNICAL NOTES: Information less broad in scope but nevertheless of importance as a contribution to existing knowledge.

TECHNICAL MEMORANDUMS: Information receiving limited distribution because of preliminary data, security classification, or other reasons. Also includes conference proceedings with either limited or unlimited distribution.

CONTRACTOR REPORTS: Scientific and technical information generated under a NASA contract or grant and considered an important contribution to existing knowledge.

TECHNICAL TRANSLATIONS: Information published in a foreign language considered to merit NASA distribution in English.

SPECIAL PUBLICATIONS: Information derived from or of value to NASA activities. Publications include final reports of major projects, monographs, data compilations, handbooks, sourcebooks, and special bibliographies.

TECHNOLOGY UTILIZATION PUBLICATIONS: Information on technology used by NASA that may be of particular interest in commercial and other non-aerospace applications. Publications include Tech Briefs, Technology Utilization Reports and Technology Surveys.

Details on the availability of these publications may be obtained from:

SCIENTIFIC AND TECHNICAL INFORMATION OFFICE

NATIONAL AERONAUTICS AND SPACE ADMINISTRATION

Washington, D.C. 20546